Научном већу Института за физику у Београду
Предлог за Студентску награду Института за физику у Београду
Кандидат: др Милош Ранковић

За Студентску награду Инситута за најбољу докторску дисертацију урађену у Институту и одбрањену током претходне 2016. године предлажемо др Милоша Ранковића.

Прилог:

1. Биографија
2. Библиографија
3. Образложење предлога
4. Радове у часописима
5. Предавања на конференцијама са позивним писмима
6. Цитираност радова у Web of Science и Scopus
7. Докторска дисертација

Београд

15.03.2017.

Биографија др Милоша Ранковића

Ранковић Милош је рођен у Београду 17.06.1986. године, општина Савски Венац, Република Србија. Основну школу и средњу електротехничку школу "Никола Тесла" је похађао у Београду. Основне академске студије на Физичком факултету, Универзитет у Београду, смер Примењена физика и информатика, уписао је 2005. године. У јулу 2012. године је дипломирао са просечном оценом 8.97 и оценом 10 на дипломском испиту са темом "Примена акустичких мерења у волуметријској анализи". У децембру 2012. године је уписао докторске студије на Физичком факултету, Универзитет у Београду. Од априла 2013. године је запослен у Институту за физику, Универзитет у Београду, Центар за физику атомских сударних процеса, као истраживач-приправник на пројекту ОИ 171020 "Физика судара и фото процеса у атомским, (био) молекуларним и нанодимензионим системима", који финансира Министарство просвете, науке и технолошког развоја Србије. На Физичком факултету, Универзитета у Београду, 2. септембра 2016. године одбранио је доктроску дисертацију под називом: Фотонска и електронска акциона спектроскопија трапираних биомолекуларних јона - Од излованих до наносолватисаних честица".

Милош је аутор/коаутор девет радова у водећим међународним часописима, више саопштења са међународних и националних конференција, укључујући и четири предавања по позиву на међународним конференцијама.

Библиографија др Милоша Ранковића

Радови у изузетним међународним часописима (М21а)

А.1. Jenny Rackwitz, Janina Kopyra, Iwona Dabkowska, Kenny Ebel, **Miloš Lj. Ranković**, Aleksandar R. Milosavljević and Ilko Bald, "Sensitizing DNA towards low-energy electrons with 2-fluoroadenine", *Angew. Chem. Int. Ed.* **55,** 35 (2016). (IF=12.111) DOI: 10.1002/anie.201603464

А.2. A. R. Milosavljević, C. Nicolas, **M. Lj. Ranković**, F. Canon, C. Miron and A. Giuliani, "K-Shell Excitation and Ionization of a Gas-Phase Protein: Interplay Between Electronic Structure and Protein Folding", *J. Phys. Chem. Lett.* **6**, 16 (2015), pp 3132–3138 (IF=8.539) DOI: 10.1021/acs.jpclett.5b01288

А.3. Aleksandar R. Milosavljević, Viktor Z Cerovski, Francis Canon, **Miloš Lj. Ranković**, Nikola Škoro, Laurent Nahon, Alexandre Giuliani, "Energy-Dependent UV Photodissociation of Gas-Phase Adenosine Monophosphate Nucleotide Ions: The Role of a Single Solvent Molecule", *J. Phys. Chem. Lett.* **5**, 11 (2014), pp 1994–1999. (IF=7.536) DOI: 10.1021/jz500696b

Радови у врхунским међународним часописима (М21)

Б.1. **Miloš Lj. Ranković**, Alexandre Giuliani and Aleksandar R. Milosavljević, "Electron impact action spectroscopy of mass/charge selected macromolecular ions: inner-shell excitation of ubiquitin protein", *Appl. Phys. Lett.* **108**, 064101 (2016). (IF=3.293) DOI: 10.1063/1.4941798

Б.2. **M. Lj. Ranković**, F. Canon, L. Nahon, A. Giuliani, and A. R. Milosavljević, "VUV action spectroscopy of protonated leucine-enkephalin peptide in the 6-14 eV range", *J. Chem. Phys.* **143**, 244311 (2015). (IF=2.950) DOI: 10.1063/1.4939080

Б.3. A. R. Milosavljević, **M. Lj. Ranković**, D. Borka, J. B. Maljković, R. J. Bereczky, B. P. Marinković and K. Tőkési, "Study of electron transmission through a platinum tube", *Nucl. Instr. Meth.* **B,** 86-89 (2015). (IF=1.423) DOI: 10.1016/j.nimb.2014.11.087

Радови у међународним часописима (М23)

B.1. Jenny Rackwitz, **Miloš Lj. Ranković**, Aleksandar R. Milosavljević and Ilko Bald, "A novel setup for the determination of absolute cross sections for low-energy electron induced strand breaks in oligonucleotides – The effect of the radiosensitizer 5-fluorouracil",
Eur. Phys. J. D **71**, 32 (2017). (IF=1.224)
DOI: 10.1140/epjd/e2016-70608-4

B.2. **Miloš Lj. Ranković**, Alexandre Giuliani and Aleksandar R. Milosavljević, "Design and performance of an instrument for electron impact tandem mass spectrometry and action spectroscopy of mass/charge selected macromolecular ions stored in RF ion trap",
Eur. Phys. J. D **70,** 6 (2016). (IF=1.224)
DOI: 10.1140/epjd/e2016-70108-7

B.3. A. R. Milosavljević, V. Z. Cerovski, **M. Lj. Ranković**, F. Canon, L. Nahon, and A. Giuliani,
"VUV photofragmentation of protonated leucine-enkephalin peptide dimer below ionization energy",
Eur. Phys. J. D **68**, 68 (2014). (IF=1.240)
DOI:10.1140/epjd/e2014-40826-y

Предавање по позиву са међународног скупа штампано у целини (неопходно позивно писмо) (М31)

Г1. **M. Lj. Ranković**, F. Canon, L. Nahon, A. Giuliani and A. R. Milosavljević, "Photoinduced fragmentation of gas-phase protonated leucine-enkephalin peptide in the VUV range ",
Journal of Physics: Conference Series **635**, (2015) 012034
doi:10.1088/1742-6596/635/1/012034
http://iopscience.iop.org/article/10.1088/1742-6596/635/1/012034

Предавање по позиву са међународног скупа штампано у изводу (М32)

Д.1. ***M. Lj. Ranković**, F. Canon, L. Nahon, A. Giuliani and A. R. Milosavljević, "Photodissociation of hydrated peptide by synchrotron radiation in the VUV region",
Proc. 4th XLIC General Meeting, 14-16 march 2017, Prague, Czech Republic, Editors: Manuel Alcamí, Paola Bolognesi, Alicja Domaracka, Bernard Pireaux and Miroslav Polášek,Young Scientists Forum.
http://www.jh-inst.cas.cz/xlic2017/home

Д.2. **M. Lj. Ranković**, A. Giuliani and A. R. Milosavljević,
"Electron impact action spectroscopy of mass/charge selected macromolecular ions",
Proc. 28th Summer School and Int. Symp. on Physics of Ionized Gases – SPIG 2016, 29th august - 1st september 2016, Belgrade, Serbia, Editors: Dragana Marić Aleksandar Milosavljević, Bratislav Obradović and Goran Poparić, Progress report, p.9.
http://www.spig2016.ipb.ac.rs/

Д.3. **Miloš Lj. Ranković**, Alexandre Giuliani and Aleksandar R. Milosavljević,
"Design and performance of an instrument for gas phase electron spectroscopy of trapped molecular ions"
Proc.The 3rd CELINA Meeting, May 18-20, 2016, Kraków, Poland, Editors: Petra Swiderek and Janina Kopyra, Progress report, p.40.
http://celina.uni-bremen.de/celina/celina2016/

Д.4. **M. Lj. Ranković**, F. Canon, L. Nahon, A. Giuliani and A. R. Milosavljević,
"Photodissociation of protonated Leucine-Enkephalin peptide in the VUV range",
Proc. XXIX ICPEAC15 International Conference on Photonic, Electronic and Atomic Collisions, 22 July - 28 July 2015, Spain, Toledo, Editors: F. Martín, G. García, L. Méndez, L. Argenti and A. Palacios, Special Report, p.105.
http://www.icpeac2015.com/

*предавање одржано након одбране докторске дисертације

Научном већу Института за физику у Београду

Предлог и образложење за Студентску награду Института за физику у Београду

Кандидат: др Милош Ранковић

За Студентску награду Инситута за најбољу докторску дисертацију урађену у Институту и одбрањену током претходне 2016. године предлажемо др Милоша Ранковића.

Образложење

Др Милош Ранковић је завршио основне академске студије на Физичком факултету Универзитета у Београду 2012. године, на смеру Примењена физика и информатика са просеком 8,97. Добитник је награде *Проф. др. Љубомир Ћирковић* за најбољи дипломски рад (2012). Докторске студије је уписао децембра 2012. године на Физичком факултету Универзитета у Београду – смер Експериментална физика атома и молекула и завршио са средњом оценом 10,00. Докторску дисертацију под насловом „*Фотонска и електронска акциона спектроскопија трапираних биомолекуларних јона - Од излованих до наносолватисаних честица*" одбранио је на истом факултету дана 2. септембра 2016 под менторством др Александра Милосављевића. Од 1.04.2013. године је запослен у Институту за физику у Београду, Универзитет у Београду, у Лабораторији за физику атомских сударних процеса и ангажован је на пројекту основних истраживања ОИ 171020 „*Физика судара и фотопроцеса у атомским, (био)молекулским и нанодимензионим системима*".

Др Милош Ранковић је радио своју докторску дисертацију у области атомске, молекулске и хемијске физике, пре свега као експериментална истраживања процеса интеракција фотона из синхротронског радијационог извора са биомолекулима у гасном стању, као и интеракцији електрона са биомолекулима и површинама метала. Научни резултати др Милоша Ранковића представљају важан и оригиналан допринос истраживањима процеса интеракције синхротронског зрачења као и расејања електрона средњих енергија на великим органским биомолекулима. Др Ранковић је користио низ експериметалних метода као што су VUV и X-ray спектроскопија јона целих протеина у гасној фази која се базира на повезивању електроспреј (ESI) извора, линеарне јонске замке и синхротронског зрачења, затим методе електронске спектроскопије и спектрометрије примењене на биомолекулима и површинама. Др Милош Ранковић је успешно конструисао нов уређај који повезује јонску замку са електронским млазом.

Др Милош Ранковћ је до сада објавио девет радова у међународним часописима, више саопштења на међународним и националим конференцијама, укључујући и четири предавања по позиву на међународним скуповима. Радови су објављени у следећим часописима:

- 1 рад у *Angew. Chem. Int. Ed.* (2016) M21a, $иф_5$=12.111
- 2 рада у *J. Phys. Chem. Lett* (2014, 2015) M21a, $иф_5$=7,536; 8,539
- 1 рад у *Appl. Phys. Lett*. (2016) M21, $иф_5$=3,293
- 1 рад у *J. Chem. Phys.* (2015) M21, $иф_5$=2,950
- 1 рад у *Nucl. Instr. Meth. B* (2015) M21, $иф_5$=1,423
- 3 рада у *Eur. Phys. J. D* (2014, 2016, 2017) M23, $иф_5$=1,240; 1,224, 1,224)

Укупни импакт фактор радова кандидата у часописима категорија M21a до M23 је 39,540. Укупан број цитата без аутоцитата је 9 према Web of Knowledge [приступљено 14.03.2017] са h-index=2, а према бази SCOPUS укупан број цитата без аутоцитата је 11 [приступљено 14.03.2017].

Посебно вредан резултат представља позив и одржано предавање на престижној међународној конференцији из области атомских сударних процеса XXIX ICPEAC2015 International Conference on Photonic, Electronic and Atomic Collisions, 22 July - 28 July 2015, Spain, Toledo. Ту је одржао предавање под насловом *Photodissociation of protonated Leucine-Enkephalin peptide in the VUV range* које је уврштено у „вруће теме" (hot topics).

Такође, предавања су одржана и на међународним конференцијама: 28th Summer School and Int. Symp. on Physics of Ionized Gases – SPIG 2016 и The 3rd CELINA Meeting, док је још једно предавање на основу резултата из докторске дисертације добијено на COST 4th General Meeting у Прагу које се одржава од 14. до 16. марта ове године.

Кандидат Милош Ранковић је развио широку међународну сарадњу и краће време боравио у иностраним лабораторијама:

- на синхротронском извору зрачења СОЛЕИЛ, Париз, Француска, на линијама DISCO и јонском трапу на линијама DESIRS и PLEIADES у више махова у периоду од 2012. до 2016.године.
- Institute of Chemistry—Physical Chemistry, University of Potsdam Немачка (2014-2016).

ЗАКЉУЧАК

На основу свих досадашњих постигнутих резултата кандидата, залагању и ефикасности при изради докторске дисертације, обима и квалитета резултата докторске дисертације, као и на основу чињенице да је кандидат одржао (и позван да одржи) предавања на националним и међународним конференцијама, велико нам је задовољство да **предложимо Комисији за доделу награда да овогодишњу Студентску награду Института за физику у Београду додели др Милошу Ранковићу**.

У Београду и Паризу,
14. март 2017.

Др Александар Милосављевић
Научни саветник

Др Братислав Маринковић
Научни саветник

DNA Radiosensitization

International Edition: DOI: 10.1002/anie.201603464
German Edition: DOI: 10.1002/ange.201603464

Sensitizing DNA Towards Low-Energy Electrons with 2-Fluoroadenine

*Jenny Rackwitz, Janina Kopyra, Iwona Dąbkowska, Kenny Ebel, MiloŠ Lj. Ranković, Aleksandar R. Milosavljević, and Ilko Bald**

Abstract: *2-Fluoroadenine (^{2F}A) is a therapeutic agent, which is suggested for application in cancer radiotherapy. The molecular mechanism of DNA radiation damage can be ascribed to a significant extent to the action of low-energy (< 20 eV) electrons (LEEs), which damage DNA by dissociative electron attachment. LEE induced reactions in ^{2F}A are characterized both isolated in the gas phase and in the condensed phase when it is incorporated into DNA. Information about negative ion resonances and anion-mediated fragmentation reactions is combined with an absolute quantification of DNA strand breaks in ^{2F}A-containing oligonucleotides upon irradiation with LEEs. The incorporation of ^{2F}A into DNA results in an enhanced strand breakage. The strand-break cross sections are clearly energy dependent, whereas the strand-break enhancements by ^{2F}A at 5.5, 10, and 15 eV are very similar. Thus, ^{2F}A can be considered an effective radiosensitizer operative at a wide range of electron energies.*

Radiation therapy using high-energy photons, electrons, or ions belongs to the most important methods used to treat cancer. As was shown in recent years, the radiation damage induced by the high-energy primary radiation is mostly due to the effect of low-energy secondary particles generated along the ionization track.[1,2] Low-energy electrons (LEEs) belong to the most important intermediates, since they are produced in significant quantities[2,3] and can directly attach to DNA and other biomolecules to form transient negative ions, which are unstable towards dissociation.[4] In DNA, dissociative electron attachment (DEA) can result in effective single and double strand breaks.[5,6]

In radiation therapy, radiosensitizers are used as therapeutics to enhance the radiation damage to the tumor tissue.[7] On a physicochemical level the radiosensitization can be ascribed to an enhanced reactivity towards LEEs.[8] The most important administered drugs in chemoradiotherapy are cisplatin and its derivatives,[9] 5-fluorouracil[10], and gemcitabine,[11] whose reactivities towards LEEs have been clearly shown.

Fludarabine, a nucleoside containing 2-fluoroadenine (^{2F}A), is an established chemotherapeutic,[12] but is also considered as a potential radiosensitizer.[13] Herein, we analyze the reactivity of ^{2F}A towards low-energy electrons. We investigate the change of the absolute strand-break cross section when ^{2F}A is incorporated into an oligonucleotide to replace adenine (A) and analyze the observations in terms of negative ion resonances revealed by DEA spectroscopy in the gas phase.

The response of single model compounds of DNA to LEEs has been studied in great detail,[1,14] but thus far it was unclear whether such gas-phase results can be transferred to the condensed phase and the situation in an oligonucleotide; that is, how the anion resonances observed in gas-phase experiments can be connected to an actual DNA strand-break process. In the present study we compare the gas phase results to absolute strand-break cross sections obtained at three different electron energies using our recently established DNA origami-based technique.[15,16] In this way we accurately quantify the effect of the incorporation of radiosensitizers into oligonucleotides and, hence, can assess the quality of potential radiosensitizers.

Figure 1a shows the general approach for the determination of the absolute cross sections for DNA strand breakage induced by LEEs (detailed experimental procedures can be found in Ref. [15–17] and in the Supporting Information). Two different biotinylated target sequences are attached to the DNA origami platforms, which are immobilized on Si/SiO_2 substrates. After electron irradiation, the remaining intact oligonucleotides are visualized by atomic force microscopy (AFM) with streptavidin (SAv). In Figure 1b, a non-irradiated control sample is shown, and in the expanded area, the two different positions of two target sequences (central and side positions, respectively) can be clearly distinguished. As the target sequence we chose 5′-d(TT(ATA)$_3$TT) (side position) and 5′-d(TT(^{2F}AT^{2F}A)TT) (central position) to directly compare the strand-break yields of a non-modified DNA sequence and a DNA sequence modified with ^{2F}A. It was demonstrated previously that 5′-d(TT(ATA)$_3$TT) is particularly sensitive to damage by LEEs.[15] For comparison we have also determined strand-break cross sections upon

[*] J. Rackwitz, K. Ebel, Prof. Dr. I. Bald
Institute of Chemistry—Physical Chemistry, University of Potsdam
Karl-Liebknecht-Str. 24–25, 14476 Potsdam (Germany)
E-mail: ilko.bald@uni-potsdam.de
Dr. J. Kopyra
Faculty of Sciences, Siedlce University
3 Maja 54, 08-110 Siedlce (Poland)
Dr. I. Dąbkowska
Department of Chemistry, University of Gdańsk
80-952 Gdańsk (Poland)
M. Ranković, Prof. Dr. A. R. Milosavljević
Institute of Physics Belgrade, University of Belgrade
Pregrevica 118, 11080 Belgrade (Serbia)
Prof. Dr. A. R. Milosavljević
SOLEIL, l'Orme des Merisiers, St. Aubin
BP48, 91192, Gif sur Yvette Cedex (France)
Prof. Dr. I. Bald
Department 1—Analytical Chemistry and Reference Materials
BAM Federal Institute for Materials Research and Testing
Richard-Willstätter Str. 11, 12489 Berlin (Germany)

Supporting information for this article can be found under: http://dx.doi.org/10.1002/anie.201603464.

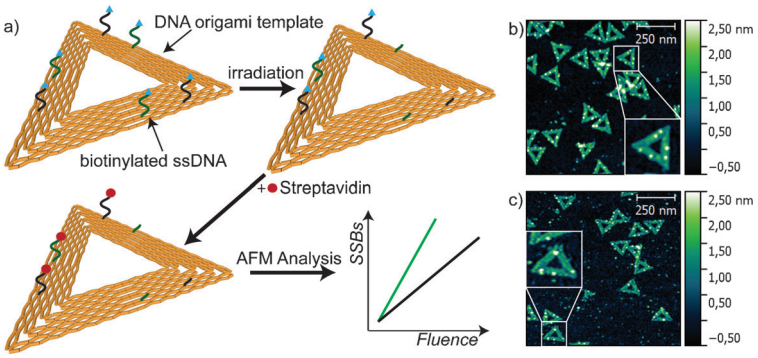

Figure 1. a) Experimental procedure to determine the absolute cross sections of DNA strand breakage. b), c) Examples of AFM images of b) a non-irradiated control sample and c) a sample irradiated with 10 eV electrons for 60 s at 5.5 nA.

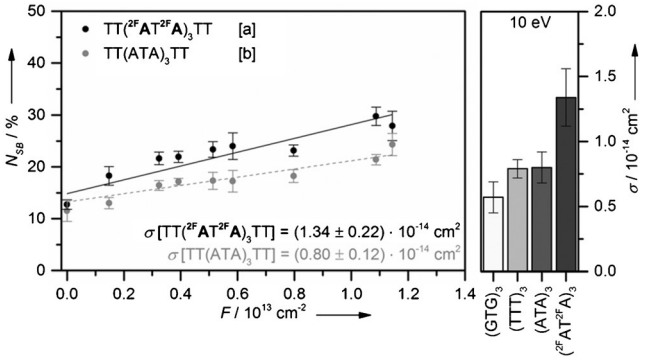

Figure 2. Left: Fluence dependence of strand breakage of the two oligonucleotide sequences 5′-d(TT(^{2F}AT^{2F}A)$_3$TT) (sequence a) and 5′-d(TT(ATA)$_3$TT) (sequence b). Irradiation was performed at 10 eV electron energy. Right: Absolute strand-break cross sections σ obtained from the linear fit of the fluence dependence of strand breakage in different sequences. For clarity only the central sequence is shown.

10 eV electron irradiation for the sequences 5′-d(TT(GTG)$_3$TT) and T$_{12}$ (Figure 2 Right and Figure S1 in the Supporting Information). Figure 1c shows a typical AFM image after LEE irradiation. From the AFM images the relative number of strand breaks (N_{SB}) is determined for various electron fluences (see the Supporting Information). The fluence is chosen to be small enough that no saturation of N_{SB} is reached as it was observed in earlier experiments.[15] From the slope of the linear fit of the exposure response curve the absolute cross sections for strand breakage for the two target sequences are obtained as shown in Figure 2 for 10 eV electrons. 10 eV was chosen because in previous experiments using plasmid DNA the highest strand break yield was found at this energy.[5,18] For the non-modified DNA sequence 5′-d(TT(ATA)$_3$TT) we find a strand-break cross section of $\sigma = (0.80 \pm 0.12) \times 10^{-14}$ cm^2, whereas for the modified sequence 5′-d(TT(^{2F}AT^{2F}A)TT) we obtain a value of $\sigma = (1.34 \pm 0.22) \times 10^{-14}$ cm^2. This results in a strand-break enhancement factor (EF) of 1.7 ± 0.5. This value corresponds to the highest EF found in previous studies of BrU-modified oligonucleotides.[16] Very recently, an EF of approximately 1.5 was reported for SSBs in plasmid DNA mixed with cisplatin and derivatives irradiated with 10 eV electrons.[19] This indicates that ^{2F}A is an effective radiosensitizer in terms of enhancement of strand breakage. The modified sequence 5′-d(TT(^{2F}AT^{2F}A)TT) also shows a higher sensitivity towards 10 eV electrons compared to the sequences 5′-d(TT(GTG)$_3$TT) and 5′-dT$_{12}$, which have strand break cross sections of $(0.57 \pm 0.12) \times 10^{-14}$ cm^2 and $(0.79 \pm 0.07) \times 10^{-14}$ cm^2, respectively (Figure 2).

The absolute cross sections for strand breakage are in the same order of magnitude as the effective and absolute cross sections found in earlier studies for strand breakage in plasmid DNA ($(2.7 \pm 1.8) \times 10^{-14}$ cm^2 and $(3.8 \pm 1.2) \times 10^{-14}$ cm^2, respectively).[20]

To obtain more information on the involved negative ion resonances and specific DEA reactions, we have studied DEA to ^{2F}A in the gas phase using a crossed electron-molecular beam experimental setup to record fragment anion yields as a function of electron energy (see the Supporting Information for more detailed information on the experimental procedure). The anion yield curves of selected fragmentation products are shown in Figure 3.

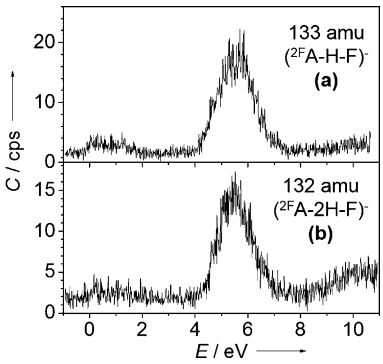

Figure 3. Ion count rate C for fragment anions detected at m/z 133 and 132 resulting from electron attachment to ^{2F}A. These fragmentation products are mainly observed within broad resonances at 4.5–7.0 eV. E = electron energy.

In total, fragment ions have been observed within resonant features located at 0.3–3 eV, 4–7 eV, and weakly around 10 eV (see below). Two fragment anions at m/z 133 ($(^{2F}A-H-F)^-$) and m/z 132 ($(^{2F}A-2H-F)^-$) have been observed, both within a broad resonance centered at 5.5 eV (Figure 3a,b). The fragment anion at m/z 132 appears additionally around 10 eV with a lower intensity. The fragment anions are formed by the loss of F and one or two H atoms, respectively, from the transient negative ion $^{2F}A^{\#-}$. The same m/z ratios have previously been observed in A, at 7.0 and 10.5 eV for the loss of two H atoms and at 6.5 and 10.9 eV for the loss of three H atoms.[21] Due to the presence of F in ^{2F}A, the negative-ion states of ^{2F}A are shifted to lower energies compared to A resulting in lower vertical attachment energies. The ion yield curves in Figure 3 clearly show the pronounced resonance around 5.5 eV and only a weak signal around 10 eV. This situation is in contrast to the ion yield

curves obtained for the same m/z ratios from A.[21] There, a clear signal at 10.5 eV was observed at m/z 133, which is even more dominant at m/z 132. Both resonances are assigned to a core-excited resonance. The formation of the m/z 133 and m/z 132 ions can also be accompanied by the formation of neutral HF, which has a high binding energy and can then thermodynamically drive the reaction. Indeed, it is frequently observed that the formation of fragment anions in the case of halo-nucleobases is driven by the formation of a neutral stable molecule of a halogen acid. This has been recently reported for 5-chlorouracil, 6-chlorouracil[22], and ^{2Cl}A.[23] In contrast, for 5-bromouracil (^{5Br}U) only the loss of the Br atom resulting in $(^{5Br}U-Br)^-$ was observed.[24] This can be easily attributed to the difference of the binding energy of H–X (X = F, Cl or Br), which decreases substantially from HF (5.9 eV) to HCl (4.5 eV) and HBr (3.8 eV).[25]

To test whether the anion resonance observed in the gas phase at 5.5 eV also leads to higher strand-break cross sections, a further condensed-phase experiment has been performed at 5.5 eV, which corresponds to the maximum of the resonance shown in Figure 3.

As shown in Figure 4, both sequences 5′-d(TT(ATA)$_3$TT) and 5′-d(TT(^{2F}AT^{2F}A)$_3$TT) indeed have a higher strand-break cross section at 5.5 eV than at 10 eV indicating a higher sensitivity of both sequences towards 5.5 eV electrons. However, the EF is again 1.6 ± 0.1 at 5.5 eV, which is the same (within the error bars) as that determined for 10 eV. In DEA to gas-phase ^{2F}A, the anion fragment $(^{2F}A-2H-F)^-$ appears at 5.5 eV and with lower intensity at 10 eV. This correlates well with the observed strand break cross sections. In DEA to A, the anion fragment $(A-2H)^-$ and a number of smaller fragment anions are formed at 5.0–6.0 eV and around 10 eV. The present results indicate that the LEE-induced strand breakage is particularly effective using the resonances at around 5.5 eV. This is also in accordance with recent experiments using plasmid DNA, in which the maximum strand breakage was found at 5.5 eV.[26] Additionally, we have determined strand-break cross sections at 15 eV for the same sequences (Figure 4 and Figure S2 in the Supporting Information), which are clearly lower than those at 10 eV. Nevertheless, the enhancement is the same within the error of the experiment (EF = 1.7 ± 0.9). The EF accounts for the more efficient decomposition of ^{2F}A compared to A within the oligonucleotide, which is true for each electron energy considered herein.

The discussion above is focused on the electron-energy regime > 5 eV. However, it should be noted that the most intense ion observed in DEA to ^{2F}A is the dehydrogenated molecular anion [Eq. (1)]:

$$^{2F}A + e^- \rightarrow {}^{2F}A^{\#-} \rightarrow (^{2F}A-H)^-(m/z\ 152) + H \quad (1)$$

The corresponding ion yield curve is shown in Figure 5a revealing a broad signal at 0.3–3.5 eV, which is composed of at least three resonances located at 0.8, 1.29, and 2.0 eV. At these low electron energies, the extra electron occupies a formerly empty molecular orbital without changing the initial electron configuration. Since the potential energy curve of such MOs is typically repulsive, the electron must be captured in a metastable state through a centrifugal energy

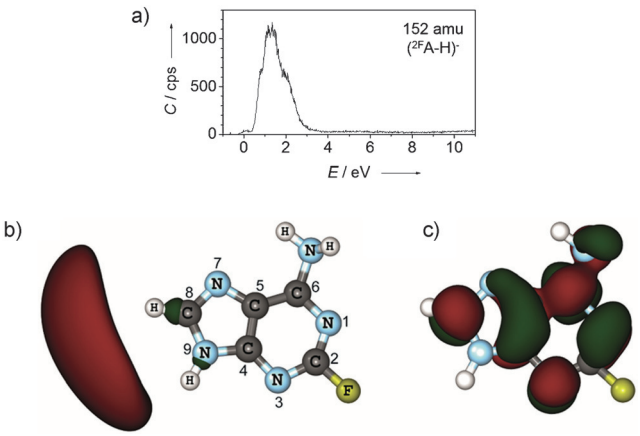

Figure 5. a) Ion count rate C for the fragment anion detected at m/z 152 within the energy regime of 0.3–3.5 eV resulting from electron attachment to ^{2F}A. b), c) Results of ab initio calculations of the anion of ^{2F}A. b) Dipole-bound anion state of ^{2F}A (MP2/CCSD(T)) showing also the molecular structure and the atom labeling of ^{2F}A, and c) the valence-bound anion of ^{2F}A (MP2).

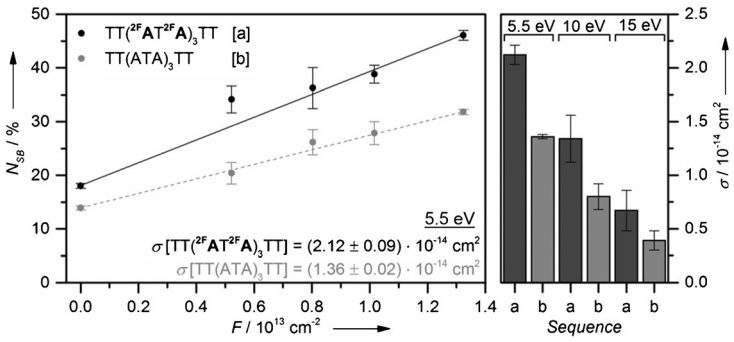

Figure 4. Left: Fluence dependence of the strand breakage of the two oligonucleotide sequences 5′-d(TT(^{2F}AT^{2F}A)$_3$TT) (sequence a) and 5′-d(TT-(ATA)$_3$TT) (sequence b). Irradiation was performed at 5.5 eV electron energy. Right: Comparison of the absolute strand-break cross sections σ obtained from the linear fit of the fluence dependence of strand breakage from 10 and 5.5 eV.

barrier (denoted here as $^{2F}A^{\#-}$).[27] A dehydrogenated parent ion was previously also observed in DEA to adenine (A) and 2-chloroadenine (^{2Cl}A) within several overlapping resonances between approximately 0.7 and 2.2 eV.[21,23,28,29] By using different methylated A derivatives, the resonances below 1.5 eV were assigned to an H loss from N9 (see Figure 5b a for the typical atom labelling in purine bases).[28] In both A and ^{2Cl}A the lowest energy resonances were assigned to vibrational Feshbach resonances (VFRs), whereas the signals between 1.1 and 2.2 eV were assigned to π* resonances.[23,28]

Taking the previous measurements on A and ^{2Cl}A into account, the 0.8 eV signal in the ion yield curve of $(^{2F}A-H)^-$ is assigned to a VFR, and the signals at 1.29 eV and 2.0 eV are assigned to π* resonances.

Compared to A, the resonance positions are slightly shifted to lower energies in ^{2F}A owing to the presence of the F atom. In ^{2F}A, the H abstraction can take place from N9, from the NH_2 group, or from C8. Based on the previous findings on A[28] and ^{2Cl}A,[23] the H loss below 2.0 eV is ascribed to a cleavage of the N9–H bond.

This is supported by ab initio calculations that we have performed at the DFT/B3LYP, MP2 and MP2/CCSD(T) levels of theory. The calculations predict metastable molecular valence-bound anions of ^{2F}A, which are adiabatically unbound with an electron affinity of −0.71 eV (MP2) and −0.67 eV (CCSD(T)), respectively. The MO representation of the valence bound anion (MP2) is shown in Figure 5c. However, the calculations indicate that ^{2F}A possesses a very high dipole moment (4.6 Debye), suggesting that an excess electron may be bound by the dipole force.[30] Indeed, adding extra diffuse functions to the aug-cc-pVDZ basis set allows us to render the dipole-bound anion state (DBS) stable (at Koopman's theory level). However, only CCSD(T) correction to the electron energy leads to positive values of the adiabatic electron affinity (0.02 eV). The DFT calculations predict only a geometrically stable DBS with an electron affinity of −0.24 eV. In both DBS anionic states (MP2/CCSD(T) and DFT), an extra electron localizes close to the N9–H bond in ^{2F}A, (see Figure 5b). This is most likely the precursor state for the H loss from ^{2F}A$^-$, in agreement with previous findings on A and ^{2Cl}A.[23,28] In the present case, the energy thresholds for hydrogen loss from ^{2F}A$^-$ from N9, C8, and N6 are 0.83, 1.90, and 3.08 eV, respectively (determined at DFT level), corresponding well to the broad feature on the DEA spectrum in Figure 5a. In conclusion, the lowest energy signals (peaking at 0.8 eV) are tentatively assigned to H loss from N9 most likely through a DBS, whereas the signals peaking at 1.29 and 2.0 eV are most likely due to π* valence states.

In addition to the fragment anions shown in Figures 3 and 5, we have also observed the smaller fragments FCN_2^- (at 0.55 eV), FCN^- (at 0.07 eV), and CN^- (at 1.61 eV and weakly around 6.3 eV), which are shown in Figure S1 in the Supporting Information. FCN^- is formed with considerable intensity and could therefore represent an important precursor for strand breakage induced by very low-energy electrons close to zero eV.

In conclusion, the present gas- and condensed-phase experiments indicate that ^{2F}A is an efficient radiosensitizer as a result of its increased reactivity towards LEEs. The condensed-phase experiments have shown a pronounced energy dependence of strand-break cross sections. The anion resonances observed at 5.5 eV in the gas phase are very likely the precursors of the strand break process observed in oligonucleotides in the condensed phase. Remarkably, the strand-break enhancement factor is 1.6–1.7 at all investigated energies, that is, 5.5, 10, and 15 eV. It needs to be explored in further experiments whether the strand-break cross sections follow a similar resonant profile as suggested by the gas-phase DEA data by recording a detailed energy dependence of the strand break cross section. In the future, we will extend our study to double-stranded DNA to explore the effect of ^{2F}A on double-strand breaks. This physicochemical insight into the mechanism of radiosensitization supports the use of ^{2F}A as a radiosensitizer in tumor radiation therapy.

Acknowledgements

This research was supported by the Federal Institute for Materials Research and Testing (BAM), by the Polish Ministry of Science and Higher Education, a Marie Curie FP7 Integration Grant within the 7th European Union Framework Programme, by the Deutsche Forschungsgemeinschaft (DFG) and the University of Potsdam. J.R. acknowledges a travel grant to Siedlce University, Siedlce (Poland) from the European Union via the COST Action MP1002 (Nano-IBCT). I.D. was supported by the Foundation for Polish Science (POMOST/2012-6/3 cofunded from POIG 2007–2013). M.Lj.R. and A.R.M. acknowledge support by the MESTD of the Republic of Serbia under Project No. #171020.

Keywords: ab initio calculations · dissociative electron attachment · DNA origami · DNA radiation damage · fludarabine

How to cite: *Angew. Chem. Int. Ed.* **2016**, *55*, 10248–10252
Angew. Chem. **2016**, *128*, 10404–10408

[1] I. Baccarelli, I. Bald, F. A. Gianturco, E. Illenberger, J. Kopyra, *Phys. Rep.* **2011**, *508*, 1–44.
[2] E. Alizadeh, L. Sanche, *Chem. Rev.* **2012**, *112*, 5578–5602.
[3] a) T. Jahnke, H. Sann, T. Havermeier, K. Kreidi, C. Stuck, M. Meckel, M. Schöffler, N. Neumann, R. Wallauer, S. Voss, et al., *Nat. Phys.* **2010**, *6*, 139–142; b) M. Mucke, M. Braune, S. Barth, M. Förstel, T. Lischke, V. Ulrich, T. Arion, U. Becker, A. Bradshaw, U. Hergenhahn, *Nat. Phys.* **2010**, *6*, 143–146.
[4] M. Neustetter, J. Aysina, F. F. da Silva, S. Denifl, *Angew. Chem. Int. Ed.* **2015**, *54*, 9124–9126; *Angew. Chem.* **2015**, *127*, 9252–9255.
[5] B. Boudaiffa, P. Cloutier, D. Hunting, M. A. Huels, L. Sanche, *Science* **2000**, *287*, 1658–1660.
[6] a) T. M. Orlando, D. Oh, Y. Chen, A. B. Aleksandrov, *J. Chem. Phys.* **2008**, *128*, 195102; b) S. V. K. Kumar, T. Pota, D. Peri, A. D. Dongre, B. J. Rao, *J. Chem. Phys.* **2012**, *137*, 045101.
[7] T. Y. Seiwert, J. K. Salama, E. E. Vokes, *Nat. Clin. Pract. Oncol.* **2007**, *4*, 86–100.
[8] a) J. Rak, L. Chomicz, J. Wiczk, K. Westphal, M. Zdrowowicz, P. Wityk, M. Żyndul, S. Makurat, Ł. Golon, *J. Phys. Chem. B* **2015**, *119*, 8227–8238; b) Q.-B. Lu, Q.-R. Zhang, N. Ou, C.-R. Wang, J. Warrington, *EBioMedicine* **2015**, *2*, 544–553; c) R. Schürmann, I. Bald, *J. Phys. Chem. C* **2016**, *120*, 3001–3009.
[9] a) J. Kopyra, C. Koenig-Lehmann, I. Bald, E. Illenberger, *Angew. Chem. Int. Ed.* **2009**, *48*, 7904–7907; *Angew. Chem.* **2009**, *121*, 8044–8047; b) M. Rezaee, E. Alizadeh, P. Cloutier, D. J. Hunting, L. Sanche, *ChemMedChem* **2014**, *9*, 1145–1149.
[10] H. Abdoul-Carime, M. A. Huels, E. Illenberger, L. Sanche, *Int. J. Mass Spectrom.* **2003**, *228*, 703–716.
[11] J. Kopyra, A. Keller, I. Bald, *RSC Adv.* **2014**, *4*, 6825–6829.
[12] F. Ricci, A. Tedeschi, E. Morra, M. Montillo, *Ther. Clin. Risk Manage.* **2009**, *5*, 187–207.
[13] V. Grégoire, N. Hunter, W. A. Brock, L. Milas, W. Plunkett, W. N. Hittelman, *Int. J. Radiat. Oncol. Biol. Phys.* **1994**, *30*, 363–371.
[14] a) P. Swiderek, *Angew. Chem. Int. Ed.* **2006**, *45*, 4056–4059; *Angew. Chem.* **2006**, *118*, 4160–4163; b) I. Bald, I. Dabkowska,

E. Illenberger, *Angew. Chem. Int. Ed.* **2008**, *47*, 8518 – 8520; *Angew. Chem.* **2008**, *120*, 8646 – 8648; c) I. Bald, J. Kopyra, I. Dąbkowska, E. Antonsson, E. Illenberger, *J. Chem. Phys.* **2007**, *126*, 074308; d) J. Kopyra, *Phys. Chem. Chem. Phys.* **2012**, *14*, 8287 – 8289.

[15] A. Keller, I. Bald, A. Rotaru, E. Cauet, K. V. Gothelf, F. Besenbacher, *ACS Nano* **2012**, *6*, 4392 – 4399.

[16] A. Keller, J. Rackwitz, E. Cauet, J. Lievin, T. Körzdörfer, A. Rotaru, K. V. Gothelf, F. Besenbacher, I. Bald, *Sci. Rep.* **2014**, *4*, 7391.

[17] a) A. Keller, J. Kopyra, K. V. Gothelf, I. Bald, *New J. Phys.* **2013**, *15*, 083045; b) S. Vogel, J. Rackwitz, R. Schürman, J. Prinz, A. R. Milosavljević, M. Réfrégiers, A. Giuliani, I. Bald, *J. Phys. Chem. Lett.* **2015**, *6*, 4589 – 4593.

[18] M. A. Huels, B. Boudaïffa, P. Cloutier, D. Hunting, L. Sanche, *J. Am. Chem. Soc.* **2003**, *125*, 4467 – 4477.

[19] M. Rezaee, D. J. Hunting, L. Sanche, *Int. J. Radiat. Oncol. Biol. Phys.* **2013**, *87*, 847 – 853.

[20] a) R. Panajotovic, F. Martin, P. Cloutier, D. Hunting, L. Sanche, *Radiat. Res.* **2006**, *165*, 452 – 459; b) M. Rezaee, P. Cloutier, A. D. Bass, M. Michaud, D. J. Hunting, L. Sanche, *Phys. Rev. E* **2012**, *86*, 031913.

[21] D. Huber, M. Beikircher, S. Denifl, F. Zappa, S. Matejcik, A. Bacher, V. Grill, T. D. Märk, P. Scheier, *J. Chem. Phys.* **2006**, *125*, 084304.

[22] S. Denifl, S. Matejcik, S. Ptasinska, B. Gstir, M. Probst, P. Scheier, E. Illenberger, T. D. Mark, *J. Chem. Phys.* **2004**, *120*, 704 – 709.

[23] F. Kossoski, J. Kopyra, M. T. do N. Varella, *Phys. Chem. Chem. Phys.* **2015**, *17*, 28958 – 28965.

[24] R. Abouaf, J. Pommier, H. Dunet, *Int. J. Mass Spectrom.* **2003**, *226*, 397 – 403.

[25] *CRC Handbook of Chemistry and Physics* (Ed.: D. R. Lide), CRC, Boca Raton, **1992**.

[26] S. Kouass Sahbani, P. Cloutier, A. D. Bass, D. J. Hunting, L. Sanche, *J. Phys. Chem. Lett.* **2015**, *6*, 3911 – 3914.

[27] I. Bald, J. Langer, P. Tegeder, O. Ingólfsson, *Int. J. Mass Spectrom.* **2008**, *277*, 4 – 25.

[28] S. Denifl, P. Sulzer, D. Huber, F. Zappa, M. Probst, T. D. Märk, P. Scheier, N. Injan, J. Limtrakul, R. Abouaf, et al., *Angew. Chem. Int. Ed.* **2007**, *46*, 5238 – 5241; *Angew. Chem.* **2007**, *119*, 5331 – 5334.

[29] H. Abdoul-Carime, J. Langer, M. A. Huels, E. Illenberger, *Eur. Phys. J. D* **2005**, *35*, 399 – 404.

[30] a) T. Sommerfeld, *J. Chem. Phys.* **2007**, *126*, 124301; b) H. Hotop, M.-W. Ruf, M. Allan, I. I. Fabrikant in *Advances in Atomic, Molecular and Optical Physics*, *Vol. 49* (Eds.: B. Bederson, H. Walther), Elsevier, Amsterdam, **2003**.

Received: April 8, 2016
Revised: June 16, 2016
Published online: August 2, 2016

THE JOURNAL OF PHYSICAL CHEMISTRY Letters

Letter

pubs.acs.org/JPCL

K-Shell Excitation and Ionization of a Gas-Phase Protein: Interplay between Electronic Structure and Protein Folding

Aleksandar R. Milosavljević,[*,†,#] Christophe Nicolas,[‡] Miloš Lj. Ranković,[†] Francis Canon,[§] Catalin Miron,[‡,∥] and Alexandre Giuliani[‡,⊥]

[†]Institute of Physics Belgrade, University of Belgrade, Pregrevica 118, 11080 Belgrade, Serbia

[‡]SOLEIL, l'Orme des Merisiers, St. Aubin, BP48, 91192 Gif sur Yvette Cedex, France

[§]INRA, UMR1324 Centre des Sciences du Goût et de l'Alimentation, F-21000 Dijon, France

[∥]Extreme Light Infrastructure - Nuclear Physics (ELI-NP), "Horia Hulubei" National Institute for Physics and Nuclear Engineering, 30 Reactorului Street, RO-077125 Măgurele, Jud. Ilfov, Romania

[⊥]INRA, UAR1008, CEPIA, Rue de la Géraudière, BP 71627, 44316 Nantes, France

Supporting Information

ABSTRACT: Understanding the correlation between proteins' tertiary and electronic structures is a great challenge, which could possibly lead to a more efficient prediction of protein functions in living organisms. Here, we report an experimental study of the interplay between electronic and tertiary protein structure, by probing resonant core excitation and ionization over a number of charge-state selected precursors of electrically charged proteins. The dependence of the core ionization energies on the protein charge state shows that the ionization of a protonated protein is strongly correlated to its tertiary structure, which influences its effective Coulomb field. On the other hand, the electronic core-to-valence shell transition energies are not markedly affected by the unfolding of the protein, from compact to totally elongated structures, suggesting that frontier protein orbitals remain strongly localized. Nevertheless, the unfolding of a protein seems to influence the cross section ratio between different resonant electronic transitions.

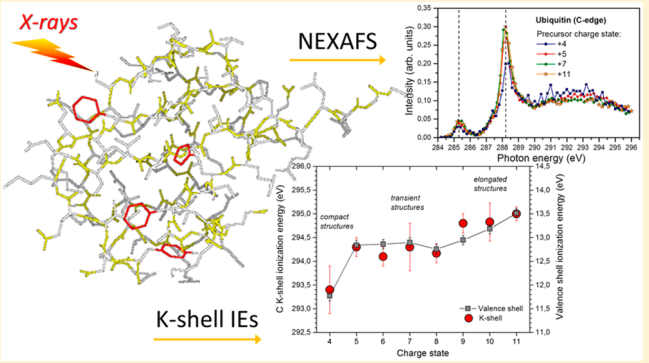

Proteins are essential for living organisms, as they accomplish numerous vital biological functions. Constituted by different polypeptide chains, proteins have in common that their functions are closely related to their three-dimensional molecular structures.[1] Therefore, long-standing research, stimulated at the same time by outstanding technological development, has been devoted to determine the average structure of a protein.[2] However, both the structural and the dynamical properties of proteins should be considered to rationalize their behavior and accurately predict their biological function.[3] The electronic structure of a protein is fundamentally correlated with its atomistic representation. Therefore, it appears important to gain a deeper understanding of the interplay between the protein electronic structure and its folding, as it could help develop methods to predict protein activity.[4,5] In order to achieve this goal, we propose an experimental approach to probe, by near edge X-ray absorption fine structure (NEXAFS) action spectroscopy,[6] the electronic structure of isolated protein ions, with some control on their three-dimensional structure provided by their level of protonation.[7] For this we use the high sensitivity and selectivity of the tandem mass spectrometry (MS^2) with the high brightness of a third-generation tunable soft X-ray synchrotron radiation source.

NEXAFS has already been established as a very sensitive method to probe the electronic structure of a wide range of samples, including biologically relevant molecules and biopolymers.[8] In recent years, proteins have come into the focus of NEXAFS, and several studies have been reported on the potential of the method to investigate protein electronic properties and even to elucidate (at least tentatively) their primary structure in combination with modeled spectra.[9,10] In NEXAFS studies of biomolecules, the X-ray absorption efficiency is probed by scanning the photon energy throughout the K-shell absorption edges. Therefore, the NEXAFS spectral features correspond to resonant excitation of a core electron to unoccupied molecular orbitals. Nevertheless, all mentioned studies with proteins were performed on thin organic films, thereby preventing control of the target's charge state and

Received: June 17, 2015
Accepted: July 28, 2015

DOI: 10.1021/acs.jpclett.5b01288
J. Phys. Chem. Lett. 2015, 6, 3132−3138

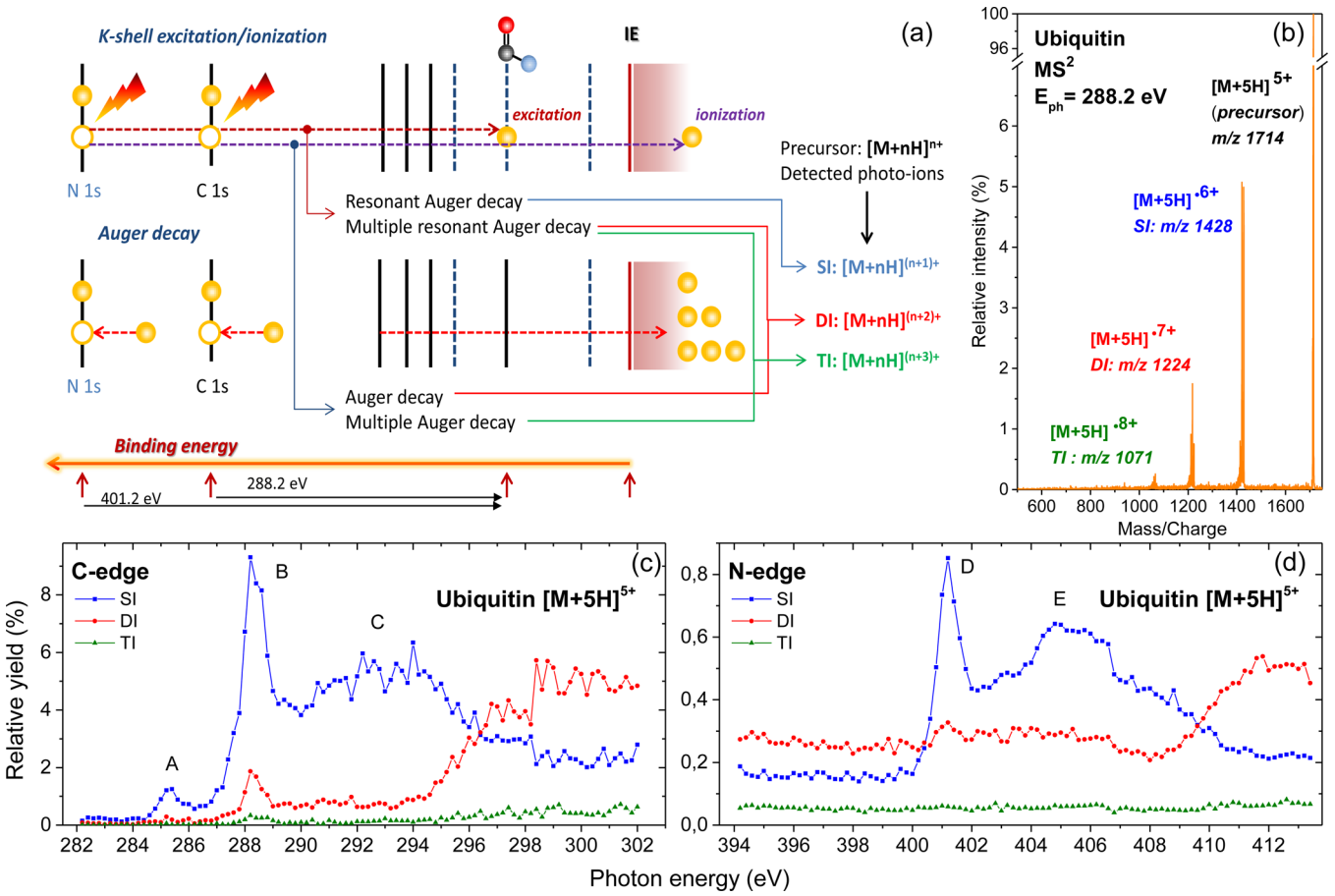

Figure 1. (a) Schematic representation of the X-ray K-shell excitation/ionization of a protein, followed by Auger decay and production of ionized cations, which are detected in the experiment. (b) Tandem ESI/photoionization mass spectrum of 5+ (m/z 1714) ion of ubiquitin protein, obtained after 500 ms of irradiation at a photon energies of 288.2 eV. (c,d) Single (SI, $[M+5H]^{6+}$, 6+ charge state, m/z 1427−1429), double (DI, $[M+5H]^{7+}$, 7+ charge state, m/z 1223−1225), and triple (TI, $[M+5H]^{8+}$, 8+ charge state, m/z 1071−1073) C and N K- edge photoionization yields of the 5+ charge state precursor $[M+5H]^{5+}$ of equine ubiquitin protein.

structure. To overcome these limitations, gas-phase study of proteins should be performed instead.

In the past two decades, mass spectrometry appeared as a very efficient tool to study the structure of proteins from their primary structure[11] up to the structure of their supramolecular edifices.[12] Recently, the introduction of the vacuum-ultraviolet (VUV) activation MS^2 has allowed determination of the binding site of a ligand on an intrinsically disordered protein, whereas classical techniques failed.[13] Among the different applications of this technique, one of the most exciting possibilities offered by such *in vacuo* spectroscopy of biological macromolecules is the investigation of their fundamental physicochemical properties.

As a proof of principle for our proposed method, we produced desolvated ubiquitin protein, in gas-phase, in different charge states ranging from +4 to +11, by means of electrospray ionization. Subsequent isolation of a selected cation, with a specific charge state, in an ion trap mass spectrometer allows us to manipulate, at least partly, its tertiary structure from a compact to an elongated geometry.[7,14] After activation of the ionic precursor by soft X-ray synchrotron radiation, a mass analysis of the produced ions is achieved (MS^2). Finally, from the recorded MS^2, a relative yield of the ionization products can be determined as a function of the photon energy, thus enabling construction of the NEXAFS action spectra (X-ray ion yields) for a desired charge-state precursor (see details below). The relationship between protein structure and charge states is now established.[15] Particularly, the case of ubiquitin has been extensively studied by ion mobility.[16] It appears that the most important structural transitions occur for states at the boundary of the elongated region. It is important to note that, in our experiments, the ion storage times are long enough to ensure that the sample has already reached equilibrium. Indeed, it requires several tenths of milliseconds from the ionization to the storage of the target ion, which is much longer than the folding dynamics of ubiquitin.[17]

In our previous work in the VUV domain, we have found a strong correlation between the folding of a gas-phase protein and its valence-shell ionization energy (IE).[7] We have also reported that an electrostatic model could be used to relate the valence-shell IE of an isolated-charge protein to its charge state and the effective radius.[7] An interesting question logically arises: Is a similar correlation seen for K-shell IEs? If the measured K-shell IEs shift in the same way, it would suggest that the unfolding of a protein changes the screening Coulomb field that affects only the ionized electron; that is, the measured correlation is a final state effect that generally relates protein's tertiary structure with its ability to be ionized by any means. Along this line, the gas-phase action NEXAFS spectroscopy can be also used to probe the protein's structure. In this letter, we demonstrate a strong correlation between K-shell and valence-shell IE dependence on the protein's charge state, suggesting

DOI: 10.1021/acs.jpclett.5b01288
J. Phys. Chem. Lett. 2015, 6, 3132−3138

that the electrostatic model reported in Giuliani et al.[7] also holds for inner-shell ionization. Moreover, unlike in the valence-shell ionization studies where only the IE can be measured, the analysis of the pre-edge features in soft X-ray absorption spectroscopy could be an additional guide to understand the interplay between electronic and tertiary protein structure.

The ionization of the photoexcited precursor at photon energies below the inner-shell ionization energy (IE) is the consequence of resonant Auger decay,[6,18] which can be briefly summarized as follows (see Figure 1a): The core (1s) electron resonantly absorbs the photon and is promoted to an unoccupied, bound molecular orbital, forming a highly excited electronic state, which decays in the femtosecond time range.[19] A valence electron fills the core vacancy, and the target relaxes by the ejection of an electron. Depending on whether the initially excited electron participates in the decay process, the process may be qualified as a participator (usually much less efficient[18]) or as a spectator, respectively. Also, it is generally energetically possible that more than one valence electron is ejected, leading to multiple resonant Auger decay.[20,21] Therefore, the processes resulting from K-shell photoexcitation of the isolated n-time multiply charged protein precursor in the present experiment can be represented by the following formula:

$$[\mathrm{M} + n\mathrm{H}]^{n+} + h\nu \rightarrow ([\mathrm{M} + n\mathrm{H}]^{n+})^* \rightarrow [\mathrm{M} + n\mathrm{H}]^{(n+k)+\bullet} + k\mathrm{e}^- \quad (1)$$

(k = 1,2,...)

In the case where the photon energy is larger than the K-shell IE, the core 1s electron is ejected into the ionization continuum, forming a core vacancy that initiates the normal Auger decay resulting in at least doubly ionized precursor:

$$[\mathrm{M} + n\mathrm{H}]^{n+} + h\nu \rightarrow ([\mathrm{M} + n\mathrm{H}]^{(n+1)+})^* + \mathrm{e}^- \rightarrow [\mathrm{M} + n\mathrm{H}]^{(n+1+k)+\bullet} + (k+1)\mathrm{e}^- \quad (2)$$

(k = 1,2,...)

In both cases 1 and 2, the formed radical cation can undergo further fragmentation. However, as reported previously for cytochrome *c*,[6] the susceptibility of gas-phase proteins to soft X-ray-induced fragmentation appears to be drastically different than it is for their amino acid building blocks, and peptides.[22] Indeed, as seen in Figure 1b for an example of the 5+ charge state precursor of ubiquitin $[\mathrm{M+5H}]^{5+}$, the ionization process, accompanied by low-mass neutral losses, represents the dominant relaxation channel upon resonant (C 1s → π^*_{amide}) X-ray absorption by ubiquitin. In this respect, fragmentation to small ionic fragments below the presented cutoff of about m/z 500 is negligible. The neutral losses from the ionized species produce fragments at masses close to the precursor, which appear just next to the main single ionization (SI), double ionization (DI), etc. peaks toward lower m/z, clearly resolved in the present work. Based on this fact, the present communication is focused on the ionization process as a way to probe the protein electronic structure. The signal between SI, DI, etc. processes is due to the weak fragmentation channels, but discussing these processes would be out of scope of the present Letter.

The partial ion-yield X-ray absorption spectra have been obtained from the mass spectra recorded as a function of the photon energy, after normalizing the integrated intensity of the SI, DI, and triple ionization (TI) peaks to both the total ion current and the photon flux. As explained above (see eq 1 and Figure 1a), the SI is exclusively triggered by resonant 1s excitation to unoccupied molecular orbitals (and neglecting the valence-shell ionization in this photon energy range). Therefore, the measured SI partial ion-yield X-ray absorption spectra in the present experiment represent the action NEXAFS spectra. Indeed, as also reported in our previous work,[6] the SI curve exhibits a rich spectroscopic structure allowing one to clearly resolve features that match perfectly with previously reported results from NEXAFS spectroscopy of thin protein films.[9,10] For example, electronic transitions from C 1s to molecular orbitals corresponding to $\pi^*_{\mathrm{C=C}}$ (aromatic) at 285.3 eV and π^*_{amide} (peptide bond) at 288.2 eV, as well as from N 1s to π^*_{amide} at 401.2 eV (bands A, B and D, respectively, in Figure 1c,d). Note that the spectra in Figure 1c are not background subtracted; therefore the direct valence-shell photoionization remains low and will thus be neglected in the following discussion, as it is known that its cross section (CS) is monotonously decreasing with photon energy.

Figure 1c,d also presents DI partial ion-yield X-ray absorption spectra (red circles). In contrast to the SI ion-yields discussed just above (blue squares), the DI curves clearly show an onset at about 294 and 408 eV, for C and N K-edge, respectively. The onsets correspond to the opening of the direct ionization channel (see Figure 1a) above the K-shell IEs. Note that the double ionization of the precursor below the C K-shell IE is dominantly produced by multiple *resonant* Auger decay (Figure 1a), triggered by the resonant 1s excitation. Therefore, the shape of the relative $[\mathrm{M} + n\mathrm{H}]^{(n+2)+}$ ion yield curve (DI) below the onset should closely reproduce the one of the relative $[\mathrm{M}+n\mathrm{H}]^{(n+1)+}$ ion yield curve (SI), which is indeed shown in Figure 2 for the case of 5+ charge state precursor.

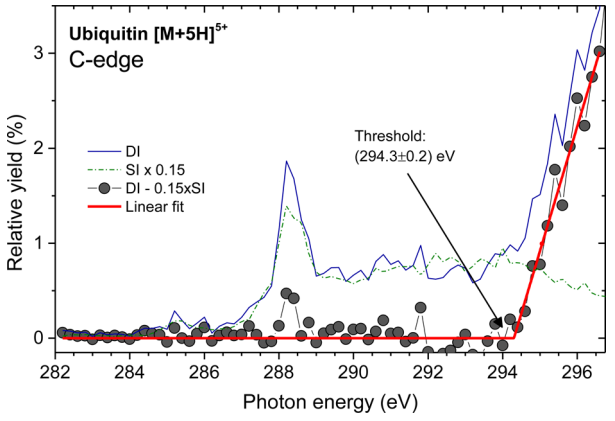

Figure 2. Normalized single (SI, $[\mathrm{M+5H}]^{6+}$, m/z 1427−1429) and double (DI, $[\mathrm{M+5H}]^{7+}$, m/z 1223−1225) C K-edge photoionization yields of the 5+ charge state precursor $[\mathrm{M+5H}]^{5+}$ of ubiquitin protein. Circles represent a difference DI − 0.15 × SI, resulting in normal Auger decay contribution of DI yields fitted to a linear threshold model (line).

Having this in mind, the subtraction of the normalized SI from the DI ion-yields should leave only a threshold curve that shows the contribution from the direct K-shell ionization (which is possible only above the IE). Figure 2 presents such a threshold curve for the case of 5+ charge state ubiquitin, together with a linear model fit that determines IE(5+) at 294.3 ± 0.2 eV (the error bars reflect the uncertainty due to both the fit and the selected fitting range). It is interesting to note that normalized SI and DI ion-yields, in fact, are different around the peak B, suggesting that the branching ratio might depend on the K-shell

DOI: 10.1021/acs.jpclett.5b01288
J. Phys. Chem. Lett. 2015, 6, 3132−3138

excitation energy (note that DI can include both double Auger ionization and Auger cascade processes). Still, this relatively small effect does not influence our adopted fitting procedure to determine IEs.

In order to determine the charge-state dependence of the C K-shell IE of ubiquitin, the C K-edge ion yields (as shown in Figure 1c) were measured for a number of charge states, in the range from 4+ to 11+ and the IEs were extracted following the procedure described above (see Figure 2). The obtained C K-shell IEs are plotted against the protein charge state in Figure 3,

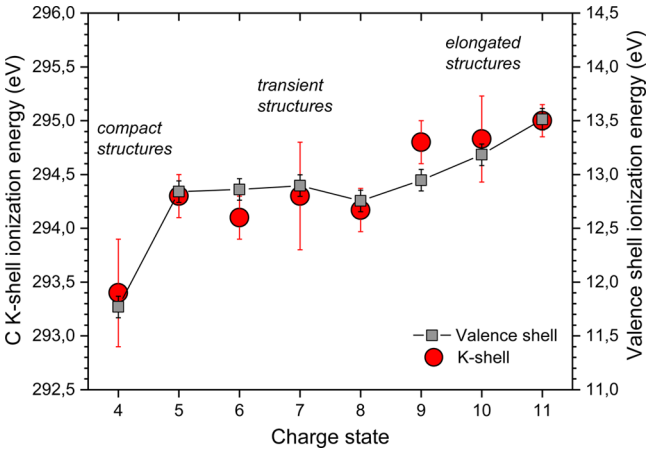

Figure 3. K-shell (circles) and valence-shell (squares)[7] ionization energies of protonated ubiquitin precursor as a function of the charge state.

together with the valence-shell IEs of ubiquitin reported recently.[7] Both curves show that an increase of the charge state of a folded protein (compact structures) would increase the IE, but as soon as the protein starts to unfold at higher protonation levels (transient structures), the effective IE remains more or less constant until the protein is totally unfolded[14] (elongated structures). Our results show that near K-edge X-ray spectroscopy has the ability to probe the tertiary structure of a protein *in vacuo*, simply by measuring the core IEs.

The C K-edge photoionization yields of ubiquitin for different precursor charge states in the overall range from +4 to +11 are compared in Figure 4a (see Supporting Information for all measured charge states). It is important to note that all curves in each panel in Figure 4a have been measured sequentially in the same experiment (see Experimental Section). This procedure ensures that the energy positions of spectral features relative to each other for different charge states are not affected by the absolute calibration of the energy scale (see Experimental section). Furthermore, the extracted spectra presented in Figure 4 are normalized to the same area (after subtraction of the background obtained as an average signal below 284 eV) in order to avoid a possible influence of different experimental conditions, particularly the target density in the trap. Indeed, according to the Thomas–Reiche–Kuhn sum rules, the area below the NEXAFS spectrum should be conserved along the charge states series.

The present measurements clearly show that the energies of the C 1s → $\pi^*_{C=C}$ (aromatics, 285.3 eV) and C 1s → π^*_{amide} (peptide bond, 288.2 eV) transitions are practically not affected by the increase of the precursor protonation from +4 to +11, at least within the limit of the present experimental uncertainty of about 0.1 eV. Supporting Figure 1 also shows that both the

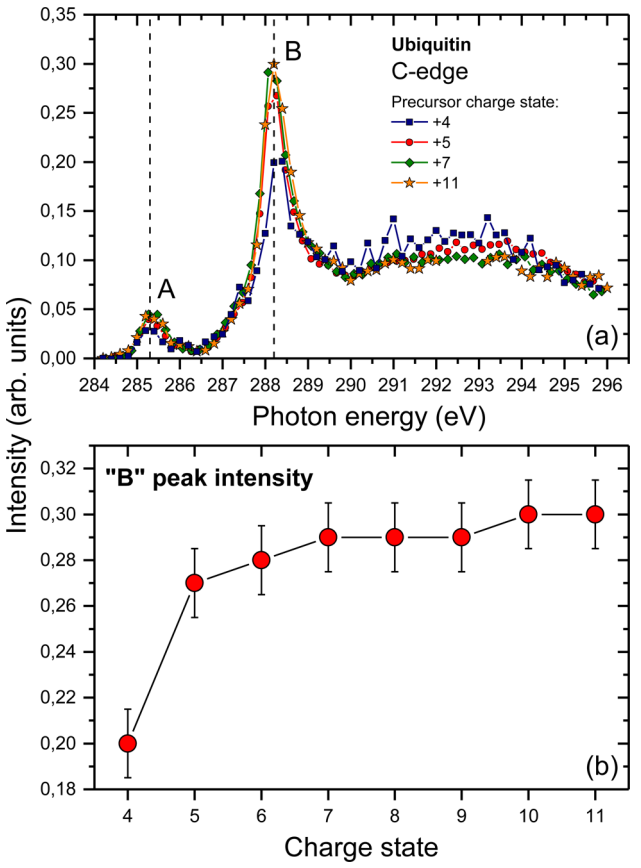

Figure 4. (a) Single C K-edge photoionization yields of the ubiquitin cation for different charge states. Dashed vertical lines mark the maximum of the A (1s → $\pi^*_{C=C}$ [aromatic]) and B (1s → π^*_{amide} [peptide bond]) bands. (b) The intensity at the maximum of the B peak as a function of the precursor charge state.

shape and the width of the dominant band are not affected by the protonation. The same conclusions stand for the N 1s → π^*_{amide} transition, as well, although less charge states have been probed in the case of N K-edge (see Supporting Figure S2). On the other hand, the relative intensity of the dominant C 1s → π^*_{amide} resonant transition (peak B in Figure 4a) markedly depends on the protonation level as shown in Figure 4b.

Our present finding, that the resonant excitation energies are not markedly affected by the protonation (Figure 4a), may be seen as a surprise. The protonation/deprotonation of amino acids affects the charge distribution in the vicinity of their functional groups; therefore it should have a strong influence on the energetics and electronic structure of biomolecules, indeed reported previously for smaller biomolecules.[23] On the other hand, the X-ray absorption spectroscopy (XAS) does not provide information on the absolute energies of the states involved in the absorption process.[24] Therefore, the measured core excitation energies may not apparently depend on the protonation if both the core and the unoccupied valence states are similarly affected. Brown et al.[24] have recently shown this effect for protonated formic acid by combining XAS and X-ray photon spectroscopy (XPS) in a liquid microjet study. However, it is important to point out that in the present case the target biopolymer is significantly larger and is not solvated. Indeed, ubiquitin is a 76-residue protein[4] (see Supporting Information, Figure S3), so in the whole range explored, from +4 to +11 charge, one can estimate that only about 5% to 15%,

DOI: 10.1021/acs.jpclett.5b01288
J. Phys. Chem. Lett. 2015, 6, 3132–3138

respectively, of all possible local core−electron transitions to π^*_{amide} are affected by the additional charge on the functional group. Therefore, even in the case of large energy shifts, the overall contribution to the measured signal may be intrinsically hidden by the signal associated with the rest of the protein.

Although the protonation itself should not affect significantly the core excitations in the present case of a large protein complex, it should also be considered that the level of protonation defines at the same time the protein's three-dimensional structure in the gas phase.[14,16] Therefore, we simultaneously probe the influence of protein folding on core−electron excitation. In this respect, two different effects can be studied according to the results presented in Figure 4 (and the Supporting Information): (a) the K-shell excitation energies—according to the position of the bands (thus the energy of the unoccupied molecular orbitals) and (b) the relative intensity of different types of transitions (e.g., excitation to π^* or σ^* orbitals). Considering the former case (a), the folding/unfolding of the protein apparently does not affect significantly the core excitation energies to unoccupied frontier molecular orbitals. Starting from the fact that core excitation is of a very local character,[8,25] the present experimental results suggest that the unoccupied frontier protein orbitals are practically unaffected by the change of the tertiary protein's structure, even in the whole range from compact to totally unfolded and elongated structures. This result is in agreement with the prediction of previously reported complex quantum mechanical calculations for ubiquitin[4] and enzymes[5] that frontier orbitals of a protein are very localized and not affected by its dynamics. It should be noted that the measured action NEXAFS spectra do not exclude a possibility that the protein unfolding affects both the core and the unoccupied molecular orbitals, thus not significantly affecting the resonant transitions[24] (note that photoelectron spectroscopy cannot be performed in the present experiment because electrons cannot be extracted from the radiofrequency ion trap to be analyzed). Indeed, the protonation clearly produces a shift of the K-shell ionization energies. Nevertheless, there is a very good correlation between the valence and the K-shell IEs (Figure 3), suggesting that both effects represent a final state effect, which is intrinsically related to the spatial rearrangement of the charged protein. The latter affects the effective Coulomb field that influences only the ionized electron, as shown in our previous work.

On the other hand, the relative intensity of the bands corresponding to C K-shell excitations to the π^* state, as seen in Figure 4b, appears lower for lower charge states and increases with the charge state, as the protein unfolds. Interestingly enough, this increase is most pronounced in the transition from compact to unfolded structures. And it should be noted that a similar dependence has been also found for the aromatic peak A. Therefore, the tertiary structure of the protein seems to affect the relative intensity of the core-to-valence π^* transitions, the latter being less pronounced in a folded protein. Previously, Zubavichus et al.[10] investigated the formation of a macromolecule that gave rise to a 20−25% attenuation of the π^* resonances in the spectra, which they tentatively interpreted as a manifestation of conformational flexibility. The authors suggested that the molecular mass and structural flexibility of biological macromolecules could influence the NEXAFS spectra, but further research was lacking to reach solid conclusions. Indeed, the present experimental results suggest that the folding of the ubiquitin protein may induce a noticeable suppression of the π^* resonances (about 10%) in its C K-edge ion yield spectra. Following previous studies,[26] this effect can be tentatively explained by a geometrical rearrangement of C atoms with respect to each other.

In conclusion, the present experimental results provide a very first demonstration of the interplay between electronic and tertiary protein structure, by probing resonant core excitation and ionization over a number of charge-state selected precursors. The dependence of core ionization energies on the protein charge states was found to be in strong correlation with valence-shell ionization, showing that, generally, the ionization of a protonated protein is strongly correlated to its tertiary structure that influences its effective Coulomb field. On the other hand, the unfolding of the protein, from compact to totally elongated structures, practically does not influence the resonant transition energies. This experimental result is in favor of recent theoretical predictions that frontier protein orbitals remain strongly localized in a protein[45]. Nevertheless, the unfolding of a protein seems to influence the intensity ratio of different core-to-valence resonant transitions.

Finally, an interesting perspective deserves to be mentioned: the high efficiency of the X-ray-induced resonant ionization, as experimentally shown in the present measurements, clearly confirms the possibility to raise-up the production of low-energy, secondary electrons in a protein sample by orders of magnitude, by simply tuning the photon energy near the C K-edge. As pointed out in a recent theoretical study,[18] this can be of particular importance in radiation damage-related research, since the low-energy secondary electrons that interact with neighboring molecules may be a very effective source of bond breaking.[27]

EXPERIMENTAL SECTION

SR/MS^2 Spectroscopy. A commercial linear quadrupole ion trap mass spectrometer was coupled to the soft X-ray beamline PLEIADES at the synchrotron radiation facility SOLEIL (France), as described previously.[6] The photon irradiation time of 500 ms was controlled by a mechanical shutter activated by a signal sent from the spectrometer through a pulse generator that ensures a short delay of ion recording in order to reduce background contributions. The ion injection time was set to 100 ms. The X-ray beam was introduced from the back side of the trap connected to the beamline via a dedicated differential pumping stage. The electrosprayed ions were injected from the front side into the trap. The tandem mass spectra were recorded as a function of the photon energy scanned in small steps. The photon energy calibration was performed in parallel for each measurement by using an online low-pressure ion yield setup installed upstream of the mass spectrometer. The relative ion yields were extracted from the mass spectra and normalized to the total ion current and to the photon flux. For the presented action NEXAFS spectroscopy, the mass resolution has been reduced to about 1500−2000 to achieve higher signal/noise ratio, but was still more than sufficient to clearly resolve SI and DI peaks. We had a very good reproducibility of the spectra over several days of data acquisition.

The Samples. Ubiquitin protein (from Sigma-Aldrich) has been placed in water/acetonitrile solution (70:30) at 10 μM. The photon energy calibration was performed with molecular CO_2 and N_2 gas from Air Liquide, with a stated purity of 99.998% and 99.9999%, respectively.

PLEIADES Beamline. A permanent magnet APPLE II type undulator, with a period of 80 mm, was used as synchrotron

DOI: 10.1021/acs.jpclett.5b01288
J. Phys. Chem. Lett. 2015, 6, 3132−3138

radiation source. The linear polarization of the light was kept perpendicular to the plane of the electrons' orbit in the storage ring. A high-flux, 600 l/mm grating was used to monochromatize the synchrotron radiation produced by the undulator for the different K-edge regions. The exit slit of the modified Pertersen plane grating monochromator was set to reach an average resolution of 320 meV at the C-edge and 300 meV at the N-edge. The average photon fluxes at the C-edge and at the N-edge were 1.3×10^9 photon/s and 2.4×10^{10} photon/s, respectively. These fluxes take into account the carbon contamination of some of the beamline optics, and also the reduction of the incident flux by the absorption due to a pressure of 5×10^{-7} mbar CO_2 or N_2 gas present in the chamber used for calibration purposes during the measurements. The calibration gas was introduced in the calibration chamber by an effusive jet crossing at right angle the SR beam. The ions created in the interaction region are extracted by a continuous electric field detected and counted at each step of a photon energy scan. The detector consists of two polarizable grids, which attract the cations, a multichannel plates chevron stack, and a 50 Ω-adapted full-metal anode. The photon energy was calibrated according to the $Ar(2p3/2^{-1}\ 4s)$ and N 1s → π^* in N_2 transitions.[19] The absolute accuracy of the energy calibration was estimated to be 50 meV for both C and N edges.

■ ASSOCIATED CONTENT

Supporting Information

The Supporting Information is available free of charge on the ACS Publications website at DOI: 10.1021/acs.jpclett.5b01288.

Additional action NEXAFS spectra for C and N K-edges, as well as adopted structure of ubiquitin protein (PDF).

■ AUTHOR INFORMATION

Corresponding Author

*E-mail: vraz@ipb.ac.rs.

Present Address

#A.R.M.: Radiation Laboratory, University of Notre Dame, Notre Dame, Indiana 46556, USA.

Notes

The authors declare no competing financial interest.

■ ACKNOWLEDGMENTS

This work was supported by the Agence Nationale de la Recherche, France, under Project ANR-08-BLAN-0065. A.R.M. and M.Lj.R. acknowledge support by the Ministry of Education, Science and Technical Development of Republic of Serbia (Projects No. 171020). A.R.M. and C.M. acknowledge support from COST action "XUV/X-ray light and fast ions for ultrafast chemistry − XLIC". The SOLEIL synchrotron radiation facility is acknowledged for providing beamtime under Project 20130382.

■ REFERENCES

(1) Rossmann, M. G.; Argos, P. Protein Folding. *Annu. Rev. Biochem.* **1981**, *50*, 497−532.

(2) Jones, N. Crystallography: Atomic Secrets. *Nature* **2014**, *505*, 602−603.

(3) Lindorff-Larsen, K.; Best, R. B.; Depristo, M. A.; Dobson, C. M.; Vendruscolo, M. Simultaneous Determination of Protein Structure and Dynamics. *Nature* **2005**, *433*, 128−132.

(4) Pichierri, F. Insights into the Interplay between Electronic Structure and Protein Dynamics: The Case of Ubiquitin. *Chem. Phys. Lett.* **2005**, *410*, 462−466.

(5) Fukushima, K.; Wada, M.; Sakurai, M. An Insight into the General Relationship between the Three Dimensional Structures of Enzymes and Their Electronic Wave Functions: Implication for the Prediction of Functional Sites of Enzymes. *Proteins: Struct., Funct., Genet.* **2008**, *71*, 1940−1954.

(6) Milosavljevic, A. R.; Canon, F.; Nicolas, C.; Miron, C.; Nahon, L.; Giuliani, A. Gas-Phase Protein Inner-Shell Spectroscopy by Coupling an Ion Trap with a Soft X-Ray Beamline. *J. Phys. Chem. Lett.* **2012**, *3*, 1191−1196.

(7) Giuliani, A.; Milosavljević, A. R.; Hinsen, K.; Canon, F.; Nicolas, C.; Réfrégiers, M.; Nahon, L. Structure and Charge-State Dependence of the Gas-Phase Ionization Energy of Proteins. *Angew. Chem., Int. Ed.* **2012**, *51*, 9552−9556.

(8) Hähner, G. Near Edge X-Ray Absorption Fine Structure Spectroscopy as a Tool to Probe Electronic and Structural Properties of Thin Organic Films and Liquids. *Chem. Soc. Rev.* **2006**, *35*, 1244−1255.

(9) Stewart-Ornstein, J.; Hitchcock, A. P.; Hernández Cruz, D.; Henklein, P.; Overhage, J.; Hilpert, K.; Hale, J. D.; Hancock, R. E. W. Using Intrinsic X-Ray Absorption Spectral Differences to Identify and Map Peptides and Proteins. *J. Phys. Chem. B* **2007**, *111*, 7691−7699.

(10) Zubavichus, Y.; Shaporenko, A.; Grunze, M.; Zharnikov, M. Is X-Ray Absorption Spectroscopy Sensitive to the Amino Acid Composition of Functional Proteins? *J. Phys. Chem. B* **2008**, *112*, 4478−4480.

(11) Aebersold, R.; Mann, M. Mass Spectrometry-Based Proteomics. *Nature* **2003**, *422*, 198−207.

(12) Van Duijn, E.; Bakkes, P. J.; Heeren, R. M. A; van den Heuvel, R. H. H.; van Heerikhuizen, H.; van der Vies, S. M.; Heck, A. J. R. Monitoring Macromolecular Complexes Involved in the Chaperonin-Assisted Protein Folding Cycle by Mass Spectrometry. *Nat. Methods* **2005**, *2*, 371−376.

(13) Canon, F.; Milosavljević, A. R.; van der Rest, G.; Réfrégiers, M.; Nahon, L.; Sarni-Manchado, P.; Cheynier, V.; Giuliani, A. Photodissociation and Dissociative Photoionization Mass Spectrometry of Proteins and Noncovalent Protein-Ligand Complexes. *Angew. Chem., Int. Ed.* **2013**, *52*, 8377−8381.

(14) Shelimov, K. B.; Clemmer, D. E.; Hudgins, R. R.; Jarrold, M. F. Protein Structure in Vacuo: Gas-Phase Conformations of BPTI and Cytochrome c. *J. Am. Chem. Soc.* **1997**, *119*, 2240−2248.

(15) Hall, Z.; Robinson, C. V. Do Charge State Signatures Guarantee Protein Conformations? *J. Am. Soc. Mass Spectrom.* **2012**, *23*, 1161−1168.

(16) Myung, S.; Badman, E. R.; Lee, Y. J.; Clemmer, D. E. Structural Transitions of Electrosprayed Ubiquitin Ions Stored in an Ion Trap over ∼ 10 Ms to 30 S. *J. Phys. Chem. A* **2002**, *106*, 9976−9982.

(17) Chung, H. S.; Ganim, Z.; Jones, K. C.; Tokmakoff, A. Transient 2D IR Spectroscopy of Ubiquitin Unfolding Dynamics. *Proc. Natl. Acad. Sci. U. S. A.* **2007**, *104*, 14237−14242.

(18) Gokhberg, K.; Kolorenč, P.; Kuleff, A. I.; Cederbaum, L. S. Site- and Energy-Selective Slow-Electron Production through Intermolecular Coulombic Decay. *Nature* **2014**, *505*, 661−663.

(19) Nicolas, C.; Miron, C. Lifetime Broadening of Core-Excited and -Ionized States. *J. Electron Spectrosc. Relat. Phenom.* **2012**, *185*, 267−272.

(20) Hitchcock, A. P.; Lablanquie, P.; Morin, P.; Lizon A Lugrin, E.; Simon, M.; Thiry, P.; Nenner, I. Ionic Fragmentation of K-Shell Excited and Ionized CO. *Phys. Rev. A: At., Mol., Opt. Phys.* **1988**, *37*, 2448.

(21) Journel, L.; Guillemin, R.; Haouas, a.; Lablanquie, P.; Penent, F.; Palaudoux, J.; Andric, L.; Simon, M.; Céolin, D.; Kaneyasu, T.; et al. Resonant Double Auger Decay in Carbon K-Shell Excitation of CO. *Phys. Rev. A: At., Mol., Opt. Phys.* **2008**, *77*, 042710.

(22) González-Magaña, O.; Reitsma, G.; Tiemens, M.; Boschman, L.; Hoekstra, R.; Schlathölter, T. Near-Edge X-Ray Absorption Mass

DOI: 10.1021/acs.jpclett.5b01288
J. Phys. Chem. Lett. 2015, 6, 3132−3138

Spectrometry of a Gas-Phase Peptide. *J. Phys. Chem. A* **2012**, *116*, 10745−10751.
(23) Ottosson, N.; Børve, K. J.; Spångberg, D.; Bergersen, H.; Sæthre, L. J.; Faubel, M.; Pokapanich, W.; Öhrwall, G.; Björneholm, O.; Winter, B. On the Origins of Core-Electron Chemical Shifts of Small Biomolecules in Aqueous Solution: Insights from Photoemission and Ab Initio Calculations of Glycine(aq). *J. Am. Chem. Soc.* **2011**, *133*, 3120−3130.
(24) Brown, M. A.; Vila, F.; Sterrer, M.; Thürmer, S.; Winter, B.; Ammann, M.; Rehr, J. J.; Van Bokhoven, J. a. Electronic Structures of Formic Acid (HCOOH) and Formate (HCOO-) in Aqueous Solutions. *J. Phys. Chem. Lett.* **2012**, *3*, 1754−1759.
(25) Miron, C.; Morin, P. High-Resolution Inner-Shell Coincidence Spectroscopy. *Nucl. Instrum. Methods Phys. Res., Sect. A* **2009**, *601*, 66−77.
(26) Zubavichus, Y.; Shaporenko, A.; Grunze, M.; Zharnikov, M. NEXAFS Spectroscopy of Homopolypeptides at All Relevant Absorption Edges: Polyisoleucine, Polytyrosine, and Polyhistidine. *J. Phys. Chem. B* **2007**, *111*, 9803−9807.
(27) Boudaïffa, B.; Cloutier, P.; Hunting, D.; Huels, M. A.; Sanche, L. Resonant Formation of DNA Strand Breaks by Low-Energy (3 to 20 eV) Electrons. *Science (Washington, DC, U. S.)* **2000**, *287*, 1658−1660.

DOI: 10.1021/acs.jpclett.5b01288
J. Phys. Chem. Lett. 2015, 6, 3132−3138

THE JOURNAL OF PHYSICAL CHEMISTRY Letters

Letter

pubs.acs.org/JPCL

Energy-Dependent UV Photodissociation of Gas-Phase Adenosine Monophosphate Nucleotide Ions: The Role of a Single Solvent Molecule

Aleksandar R. Milosavljević,*[,†] Viktor Z. Cerovski,[†] Francis Canon,[‡] Miloš Lj. Ranković,[†] Nikola Škoro,[†] Laurent Nahon,[§] and Alexandre Giuliani[§,∥]

[†]Institute of Physics Belgrade, University of Belgrade, Pregrevica 118, 11080 Belgrade, Serbia

[‡]INRA, UMR1324 Centre des Sciences du Goût et de l'Alimentation, F-21000 Dijon, France

[§]Synchrotron SOLEIL, L'Orme des Merisiers, Saint Aubin, 91192 Gif-sur-Yvette, France

[∥]UAR 1008 CEPIA, INRA, 44316 Nantes, France

Supporting Information

ABSTRACT: The photodissociation of gaseous protonated adenosine 5′-monophosphate (AMP) and the same system hydrated with one water molecule has been investigated in the 4 to 13 eV photon energy range by coupling a linear quadrupole ion trap with a synchrotron radiation beamline. The dissociation of the bare AMP cation upon absorption of a single ultraviolet (UV) photon below the ionization energy (IE) almost exclusively produces the protonated adenine base, with a measured photodissociation yield showing spectroscopic features with dominant absorption bands located at 4.75 and 6.5 eV, found in agreement with TD-DFT calculations. Nevertheless, the addition of a single water molecule to the system modifies the dissociation energy dependence and strongly suppresses the cleavage of the glycosidic CN bond below the IE. Both the experimental and theoretical results suggest that a single solvent molecule can intrinsically influence the structure and physicochemical properties of the AMP cation, including its UV induced dissociation pattern, beyond the simple water evaporation.

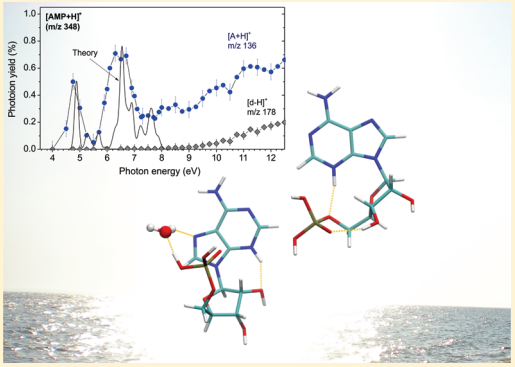

SECTION: Spectroscopy, Photochemistry, and Excited States

The photostability of DNA and RNA against ultraviolet (UV) radiation is a crucial issue for the understanding of life's development and evolution, particularly regarding the conservation of the genetic information. These molecules strongly absorb in the UV region,[1] which should make them vulnerable to photon-induced alteration. Although an immense number of publications have been devoted in recent years to photophysics of DNA building blocks,[1−5] this topic is still attracting a large scientific attention focusing on DNA photostability mechanisms. Particularly, 266 nm photodestruction of both protonated and deprotonated AMP nucleotide isolated in vacuo has been reported in 2003[6] and followed by intensive investigation of the AMP molecule. However, to our knowledge, the photodynamic of isolated nucleotides has not been studied over a broad UV and vacuum ultraviolet (VUV) domain.

Moreover, functions and properties of biomolecules are in nature intrinsically linked to their aqueous environment. The recent development of experimental techniques has allowed investigations of the effect of solvation down to a limit of only a few solvent molecules (nanosolvation or microsolvation). For example, it has been shown that even one, two, or three water molecules can strongly affect chemical reaction dynamics,[7] peptide structure,[8] or the stability of a fragile peptide dimer.[9] Recent pioneering experiments have investigated dissociation of electrosprayed nanosolvated deprotonated adenosine 5′-monophosphate (AMP) nucleotide anions, induced either by energetic collisions with neutral atoms (Ne, Na)[10] or by electron capture.[11] Nevertheless, although the latter studies[10,11] are relevant in the context of high-energy photon interaction with DNA and radiation damage due to secondary electrons,[12] they do not investigate directly the role of nanosolvation in ubiquitous high-energy photon interaction with DNA building blocks. It should be noted that there is a long-standing effort to understand solvent effects in DNA photophyics, including a number of results from solution (see refs1, 13, and references therein), as well as studies on DNA bases microhydration in the gas phase.[14]

In this Letter, we report on UV action spectroscopy of protonated AMP molecule (Figure 1) isolated in the gas phase and on the same system hydrated with a single water molecule,

Received: April 7, 2014
Accepted: May 20, 2014

   dx.doi.org/10.1021/jz500696b | J. Phys. Chem. Lett. 2014, 5, 1994−1999

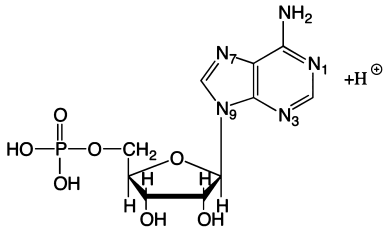

Figure 1. Schematic drawing of the protonated AMP molecule.

performed by coupling a linear ion trap with a VUV synchrotron radiation beamline.[15−17] The photodissociation yield of $[AMP + H]^+$ appears to be strongly energy-dependent, with structures observed on the action spectroscopy of AMP over a large UV energy domain (4−13 eV). Moreover, we found that hydration by a single water molecule significantly influences the precursor dissociation magnitude below the ionization energy (IE) as well as its energy dependence. Molecular dynamics (MD) and high-level density functional theory (DFT) calculations have been performed to understand the role of nanosolvation upon UV irradiation.

Figure 2a,b present tandem mass spectra (MS^2) upon collision induced dissociation (CID) of the bare $[AMP + H]^+$ and hydrated $[AMP + H_2O + H]^+$ precursors, respectively. For the hydrated precursor, one of the main CID fragmentation channels corresponds to the loss of the water molecule (m/z 348). It should be noted that we cannot exclude that some low-abundant peaks (Figure 2b,d,f) may indicate the presence of isobaric interfering ions but which are of lower abundance compared to the hydrated AMP protonated precursor and should not influence the discussion about UV induced fragmentation of AMP presented in the paper. For the following discussion, it is important to note that the hydrated cations can lose water by thermal evaporation during the trapping time even without any collisional or photon-induced activation, producing the m/z 348 fragment with a relative intensity of about 0.15%.

Figure 2c,e (left column) display MS^2 spectra of the bare protonated AMP precursor upon photon irradiation at two different energies below the IE. The results show that UV single-photon absorption practically exclusively leads to the cleavage of the glycosidic NC bond and formation of the protonated base fragment $[A + H]^+$. The present results are qualitatively in good agreement with the recent photodissociation studies at 266 nm (≈ 4.7 eV) and 260 nm (≈ 4.8 eV) of protonated AMP,[18,19] respectively. Still, some differences in fragmentation patterns, such as higher abundance of the fragment corresponding to the phosphate loss from protonated AMP,[19] might come from a different time scale of the experimental setups. Indeed, in ion traps, the ions are provided with much longer time to fragment than in sector instruments, which may affect the observed fragmentation patterns[20] (the time that ions have to fragment in the present case extends up to the irradiation time, which was about 500 ms). Note also that different abundance of fragments relative to the precursor may be due to different photon fluxes of synchrotron monochromatic and pulsed laser beams. Considering the present results at two different resonant energies, the fragmentation pattern appears to be very similar. Still, the abundance of protonated base increases, whereas traces of additional fragments can be seen at 6.5 eV.

The present experiment confirms a fundamentally different nature of UV photodissociation of the protonated AMP with respect to that of the deprotonated one,[18,22] for which a rich fragmentation pattern has been measured.[3,18,23] The latter results for $[AMP - H]^-$ anion suggests a mechanism that begins with a $\pi\pi^*$ electronic transition, followed by fast internal conversion to a vibrationally hot electronic ground state that ends up with a number of thermal fragmentation channels.[3] In contrast to the deprotonated case, $[AMP + H]^+$ exclusively

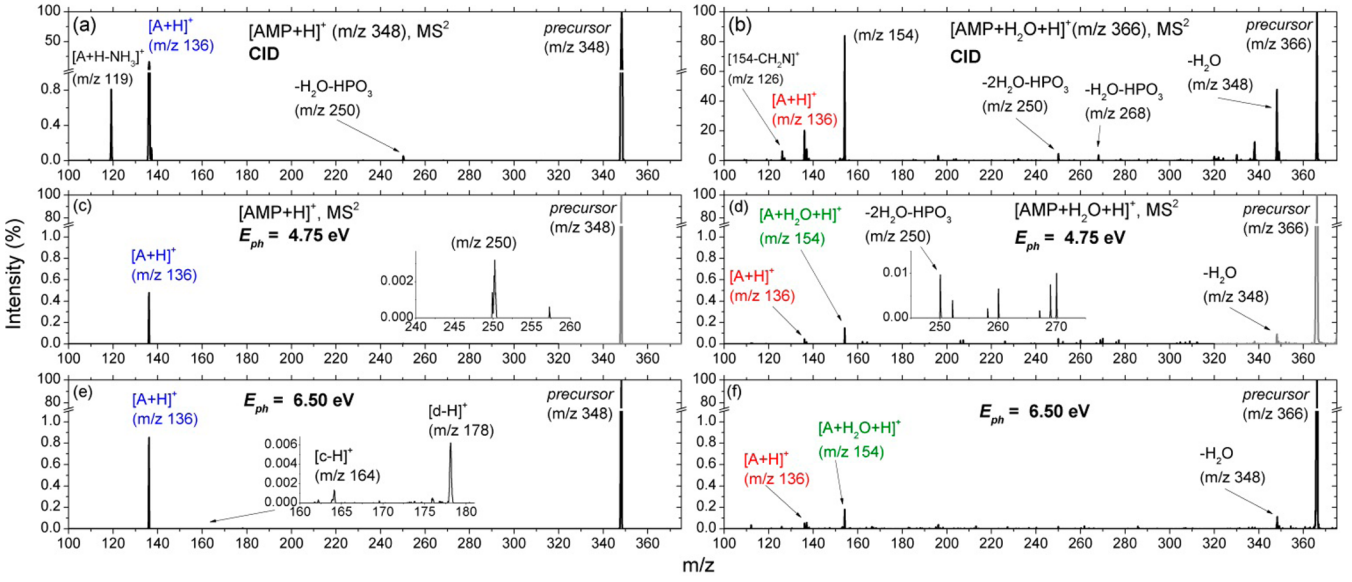

Figure 2. (a,b) Tandem mass spectra (MS^2) of the $[AMP + H]^+$ (m/z 348) (a) and $[AMP + H_2O + H]^+$ (m/z 366) (b) precursor cations upon collisional induced dissociation (CID). (c−f) MS^2 of bare protonated precursor $[AMP + H]^+$ (c,e) and the hydrated one (d,f) upon photon activation at 4.75 and 6.50 eV. The lower part of the spectra (black line) up to m/z 320 at the energy of 4.75 eV (c,d), corresponding to photofragmentation, has been normalized to the photon flux with respect to 6.50 eV (the photon flux at 6.5 eV was about 5 times higher). The insets show a zoom-in of the selected m/z regions. The structures of "c" and "d" fragments formed upon sugar moiety decomposition are given elsewhere.[21]

dx.doi.org/10.1021/jz500696b | J. Phys. Chem. Lett. 2014, 5, 1994−1999

photodissociates through the direct cleavage of the CN glycosidic bond, suggesting a possible fast fragmentation directly from the excited electronic state.

The addition of one water molecule to the protonated AMP markedly influences the photodynamic of the nucleotide. First, photodissociation yields of the hydrated precursor seems to be about 3−4 times lower than of the bare precursor. Second, photon absorption leads to the dissociation into both the bare protonated base $[A + H]^+$ and the protonated base bound to a solvent water molecule $[A + H_2O + H]^+$ (m/z 154, see Supporting Information Figure S2), as confirmed in an MS^3 scheme experiment (Supporting Information Figure S1). Clearly, the latter fragment represents the dominant fragmentation channel. Third, though CID of $[AMP + H_2O + H]^+$ leads to an intensive loss of H_2O (Figure 2b), this process is barely detectable upon VUV photon absorption (see below). It should be noted that the previous work has shown that the photofragmentation of an organic compound can be strongly affected by clustering with even a single Xe atom;[24] therefore, the present results are important for further elucidating the role of the gradual water solvation in photochemistry of biomolecules.

Theoretical description of $[AMP + H]^+$ with and without H_2O was carried out in order to better understand the experimental results. The geometries of low-energy conformers (CFs) were found by using the genetic algorithm approach with classical force field geometry optimization followed by DFT optimizations at the M06-2X/6-311G(d,p) level,[25,26] where about 50 low-energy CFs were considered.

Figure 3 shows the lowest-energy geometries of the hydrated and nonhydrated CFs (see Supporting Information Figures S3 and S4). Both DFT and MP2[27] give the same geometry as the lowest-energy CF for both precursors, and the obtained energy difference between CF1′ and CF2′ is within the uncertainty of the calculations. Furthermore, all low-energy CFs found have their highest occupied molecular orbital (HOMO) and lowest unoccupied molecular orbital (LUMO) centered upon the adenine base (A), with only a small electronic density extending over the rest of the ion. It is important to note that upon hydration, there are two qualitatively different water H-bondings: (i) to the P-group away from the base A (CF1′ in Figure 3) and (ii) by forming a bridge between the P-group and A (CF2′ in Figure 3). Therefore, upon single photon absorption by adenine chromophore, leading to NC bond cleavage, two main fragments are expected: bare protonated base from CF1′ and hydrated protonated base from CF2′, which is in agreement with our experimental findings (Figure 2d,f). Still, significantly lower intensity has been measured for the $[A + H]^+$ fragment, suggesting much smaller abundance of CF1′ type conformers or intensive competitive production of small fragments that cannot be detected. The calculated vertical ionization energies (VIEs) of CF1, CF1′, and CF2′ are 12.53, 12.48, and 12.12 eV, respectively. The binding energies of water in the two CF's are 69 and 69.5 kJ/mol, respectively (~0.72 eV).

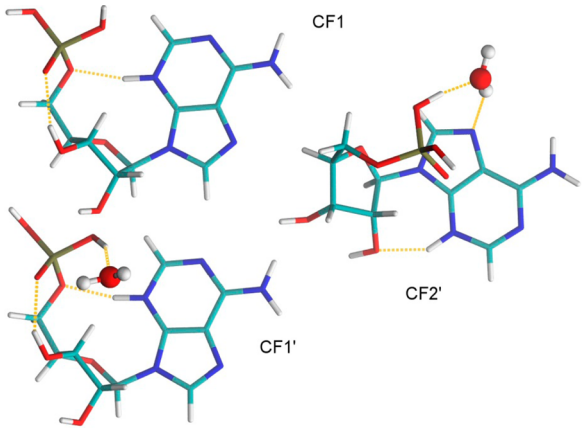

Figure 3. Lowest energy conformers structure found for $[AMP + H]^+$ (CF1) and $[AMP + H_2O + H]^+$ (CF1′, CF2′) at M06-2X/6-311G(d,p) level of DFT. The protonated AMP (CF1) has the N3 protonation site.

The energy dependence of the photodissociation of $[AMP + H]^+$ and $[AMP + H_2O + H]^+$ precursors is presented in Figure 4a,b. The photodissociation of $[AMP + H]^+$ below IE into $[A + H]^+$ (dominant channel) is strongly resonant. The first absorption band at about 4.75 eV (≈260 nm), corresponding to the strong $1(\pi\pi^*)$ transition,[1] is well known for the adenine base and has been extensively investigated in laser based experiments. Particularly, the most recent paper by Pedersen et al.[19] reports the action spectra up to 5.8 eV of protonated AMP, the photodissociation yield of $[A + H]^+$ fragment showing a broad band centered at about 4.7 eV, in very good agreement with the present results.

Furthermore, the present results also reveal a second absorption band centered at about 6.5 eV, which appears to correspond to the dominant photodissociation channel for the bare precursor. Experimental results are in a very nice agreement with the present theoretical absorption spectrum calculated using time-dependent B3LYP/6-31+G(d,p) (Figure 4a,d for CF1), confirming that $[AMP + H]^+$ strongly dissociate only upon $\pi\pi^*$ type transition at adenine site (it should be noted that there can be several different conformers present in the experiment at room temperature). On the other hand, fragmentation into the $[d - H]^+$ ion, which involves cleavage of several bonds,[21] starts to be important only at higher energies. It should be noted that previous calculations report $3(\pi\pi^*)$, $4(\pi\pi^*)$ excitations of adenine to be in the range from 6.2 to 6.7 eV.[28] Higher energies, where both more electronic transitions (due to increased density of states) and the ionization process become available, were not included in the present theoretical modeling.

The photoion yields upon excitation of hydrated precursor (Figure 4b) reveal the absorption bands at about the same positions as for the bare one, in line with the most recent measurements of the absorption spectra of protonated bare and monohydrated adenine, where no difference was seen upon water addition.[19] However, there is a lowering of the resonant photodissociation of protonated AMP in the whole UV and far-UV energy region, induced by the presence of a single solvent molecule. This might be regarded as a surprise considering both the present CID experiment (Figure 2b) and the previous studies on nanosolvated deprotonated AMP,[10,11] where 12 water molecules were needed to protect deprotonated AMP against energetic collisions with neutrals,[10] whereas the electron capture induced dissociation even increased with increasing solvation.[11] Furthermore, previous studies in solutions have shown that solvent did not seem to influence ultrafast de-excitation through conical intersections.[1]

Nevertheless, the photodissociation of protonated AMP is not likely to proceed through an ultrafast de-excitation followed by vibrational cooling from the hot ground state. Indeed, if this

dx.doi.org/10.1021/jz500696b | J. Phys. Chem. Lett. 2014, 5, 1994−1999

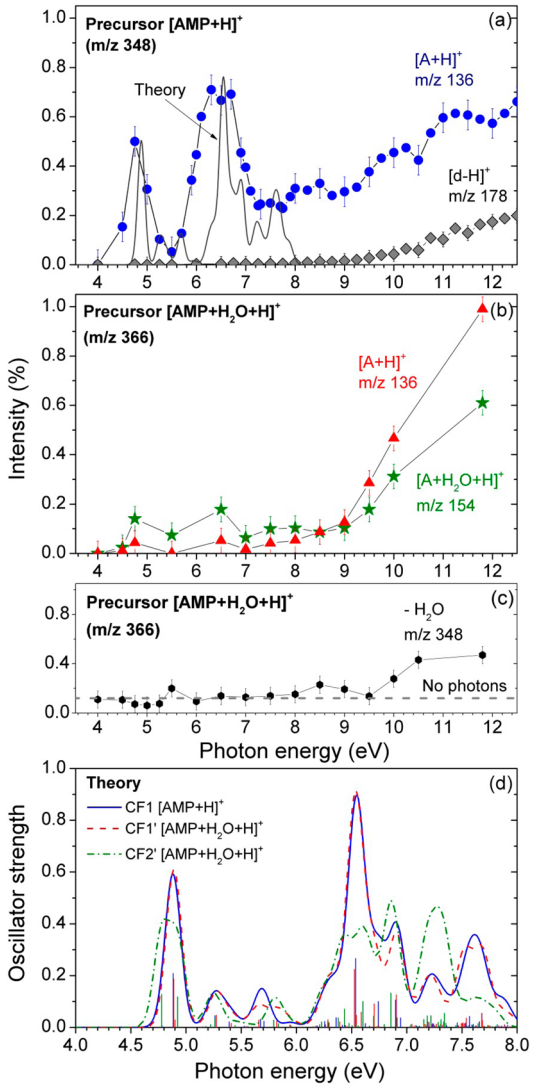

Figure 4. Photodissociation yields of protonated adenine base $[A + H]^+$ (circles) and $[d - H]^+$ (diamonds) fragments from the bare protonated adenosine monophosphate $[AMP + H]^+$ precursor (a) as well as $[A + H]^+$ (up triangles) and $[A + H_2O + H]^+$ (down triangles) from the hydrated protonated AMP precursor $[AMP + H_2O + H]^+$ (b). (c) The yield of $[AMP + H]^+$ fragment from $[AMP + H_2O + H]^+$ precursor, corresponding to the loss of a single water molecule as a function of the photon energy. The dashed line marks the average water loss upon thermal evaporation from the ion precursor, without photon irradiation. (d) Time-dependent B3LYP/6-31+G(d,p) calculated absorption spectra of CFs from Figure 3. Curves are obtained from the sticks by a 0.1 eV Gaussian convolution of the calculated transitions, providing a guide to the eye (the curve for CF1 is also plotted in panel a as a full line, normalized to experiment at 4.75 eV).

mechanism would become operative upon hydration, one would expect an intensive loss of the noncovalently attached water molecule, as measured in the present CID experiment (Figure 2b). The most recent paper by Pederesen et al.[19] also reports the water loss to be the dominant fragmentation channel upon UV (260 nm) photodissociation of monohydrated protonated adenine base (note that de-excitation of protonated adenine is an ultrafast process[19]). On the contrary, no photon-induced water loss from the protonated monohydrated AMP can be detected below the IE in the present experiment (see Figure 4c). We should note that low m/z ions, such as NH_4^+, H_3O^+, or H^+, cannot be detected with the present setup. Although the adenine base possesses higher proton affinity than the water,[29] this might not be crucial when such large amount of energy is dumped into the ion; thus, we cannot exclude that part of it is channeled into ejection of small fragments. Still, it should be noted that the recent results[19] do not show signal from H_3O^+ ion upon dissociation of monohydrated protonated adenine. Therefore, although we cannot completely exclude that part of the absorbed energy is channeled into ejection of low-mass fragments (due to monohydration-induced change in the precursor fragmentation pattern), the single-water solvation-induced frustrated UV photodissociation of the protonated AMP may be intrinsically related to the structure of the hydrated complex.

The calculated absorption spectra for the lowest-energy hydrated CFs are also shown in Figure 4d. The spectra for CF1 and CF1′ geometries are nearly identical in terms of both intensity and spectral distribution, clearly indicating that hydration on the phosphate site has only a minor effect on photoabsorption. Hence, there could be either a very low abundance of CF1′ type precursor or the dissociation to protonated base from CF1′ is not a preferential channel (as discussed above). At the opposite, the bridge-hydration (CF2′) significantly modifies the UV absorption properties of AMP. First, instead of a particular strong narrow band, the oscillator strengths (OSs) are redistributed over more numerous transitions, thus effectively reducing the resonant absorption. Furthermore, this OS redistribution can increase transition probabilities from nonbonding orbitals, thus again effectively reducing the dissociation yield. For example, CF2′ shows a double peak at ∼4.8 eV, where about 50% OS corresponds to the transition from a nonbonding (HOMO-1) to LUMO.

It should be noted that the lowest-energy protonated AMP CF found (Figure 3) has the N3 protonation site (see Figure 1), in agreement with the previous study by Touboul et al.[30] reporting that the N3 position is the most favorable site of protonation for adenosine, in contrast with adenine (N1). Interestingly, the absorption bands of protonated AMP and adenine molecules overlap,[19] although previous UV measurements showed red-shifted absorption of N3 protonated adenine in reference to N1 adenine (see ref 19 and references therein).

The current understanding of the fragmentation mechanisms of gas phase bare and hydrated AMP ions is briefly summarized as follows. The CID occurs on the ground electronic state after statistical redistribution of the absorbed energy over vibrational modes. Photoexcitation can lead to both statistical and nonstatistical fragmentation: (a) $[AMP - H]^-$ undergoes fast internal conversion to a vibrationally hot electronic ground state, followed by thermal (statistical) fragmentation;[3] (b) $[AMP + H]^+$ dissociates directly from the excited electronic state (according to the present study and refs 18 and 19); (c) $[AMP + H_2O + H]^+$, we propose that the dissociation also occurs from the excited states, before vibrational energy redistribution.

In summary, UV/VUV photodissociation of both bare and monohydrated protonated AMP nucleotide isolated in the gas phase has been measured as a function of the photon energy. The experimental results show strong $[AMP + H]^+$ dissociation bands centered at ca. 4.75 and 6.5 eV, in agreement with calculations. Nevertheless, our study shows that a single-water solvation inhibits dissociation, this effect being more likely due to intrinsic structural changes than to the vibrational cooling from the hot ground state. It should be noted that before the

dx.doi.org/10.1021/jz500696b | J. Phys. Chem. Lett. 2014, 5, 1994−1999

(mainly) biogenic oxygenation[31] of the early Earth, its atmosphere was transparent to VUV. Therefore, the present study on UV-induced AMP degradation is of particular importance regarding radiation damage of biomaterial and DNA photostability.

EXPERIMENTAL SECTION

Our experimental setup for VUV tandem mass spectrometry (MS^2) and action spectroscopy of large biomolymer ions isolated in the gas phase has been described in recent publications.[15,16] Briefly, it includes a commercial linear quadrupole ion trap mass spectrometer (LTQ XL; Thermo Fisher) coupled to the DESIRS VUV beamline[17] at the SOLEIL synchrotron facility. The ions are produced by an electrospray ion (ESI) source and introduced into the trap from the front side. After isolation of a desired precursor, the monochromatic photon beam, with a typically bandwidth of 12 meV and an absolute energy calibration of ±10 meV, is introduced from the backside of the trap during a well-defined period (500 ms in the present case). High harmonics of the undulator are filtered off by using a gas filter,[17] as well as MgF_2 or Suprasil windows, depending on the photon energy region. After irradiation, action mass spectra for the desired precursor ion were recorded as a function of the photon energy and normalized to the photon flux.

Both protonated AMP (Sigma-Aldrich) and hydrated protonated AMP ions were generated by the ESI source from a pure water solution at 100 μM. An appropriate combination of parameters, such as the concentration of the solution, transfer tube temperature, voltages, and sheath gas flow rate, was optimized in order to maximize the production of hydrated clusters.

ASSOCIATED CONTENT

Supporting Information

Mass spectrometry, calculated structures of the protonated hydrated adenine fragment and the bare and hydrated AMP conformers. This material is available free of charge via the Internet at http://pubs.acs.org.

AUTHOR INFORMATION

Corresponding Author

*E-mail: vraz@ipb.ac.rs (A.R.M.).

Notes

The authors declare no competing financial interest.

ACKNOWLEDGMENTS

This work was supported by the French ANR (project no. ANR-08-BLAN-0065), the "Pavle Savic" bilateral scientific project between Serbia and France (No. 27482TE) and the COST Action MP1002 (Nano-IBCT). A.R.M. and M.Lj.R., V.Z.C., and N.Š. acknowledge support by the Ministry of Education, Science and Technological Development of the Republic of Serbia under projects 171020, 171033 and 171037, and 41011, respectively. We are grateful to the SOLEIL general staff for providing beamtime under project no. 20120874 and 20130388.

REFERENCES

(1) Middleton, C. T.; de La Harpe, K.; Su, C.; Law, Y. K.; Crespo-Hernández, C. E.; Kohler, B. DNA Excited-State Dynamics: From Single Bases to the Double Helix. *Annu. Rev. Phys. Chem.* **2009**, *60*, 217−239.

(2) Marcum, J. C.; Halevi, A.; Weber, J. M. Photodamage to Isolated Mononucleotides–Photodissociation Spectra and Fragment Channels. *Phys. Chem. Chem. Phys.* **2009**, *11*, 1740−1751.

(3) Marcum, J. C.; Kaufman, S. H.; Weber, J. M. UV-Photodissociation of Non-Cyclic and Cyclic Mononucleotides. *Int. J. Mass Spectrom.* **2011**, *303*, 129−136.

(4) Gabelica, V.; Rosu, F.; Tabarin, T.; Kinet, C.; Antoine, R.; Broyer, M.; De Pauw, E.; Dugourd, P. Base-Dependent Electron Photodetachment from Negatively Charged DNA Strands upon 260-Nm Laser Irradiation. *J. Am. Chem. Soc.* **2007**, *129*, 4706−4713.

(5) Nielsen, L. M.; Pedersen, S. Ø.; Kirketerp, M.-B. S.; Nielsen, S. B. Absorption by DNA Single Strands of Adenine Isolated In Vacuo: The Role of Multiple Chromophores. *J. Chem. Phys.* **2012**, *136*, 064302.

(6) Brøndsted Nielsen, S.; Andersen, J. U.; Forster, J. S.; Hvelplund, P.; Liu, B.; Pedersen, U. V.; Tomita, S. Photodestruction of Adenosine 5′-Monophosphate (AMP) Nucleotide Ions In Vacuo: Statistical versus Nonstatistical Processes. *Phys. Rev. Lett.* **2003**, *91*, 048302.

(7) Otto, R.; Brox, J.; Trippel, S.; Stei, M.; Best, T.; Wester, R. Single Solvent Molecules Can Affect the Dynamics of Substitution Reactions. *Nat. Chem.* **2012**, *4*, 534−538.

(8) Nagornova, N. S.; Rizzo, T. R.; Boyarkin, O. V. Interplay of Intra- and Intermolecular H-Bonding in a Progressively Solvated Macrocyclic Peptide. *Science* **2012**, *336*, 320−323.

(9) Milosavljević, A. R.; Cerovski, V. Z.; Canon, F.; Nahon, L.; Giuliani, A. Nanosolvation-Induced Stabilization of a Protonated Peptide Dimer Isolated in the Gas Phase. *Angew. Chem., Int. Ed. Engl.* **2013**, *52*, 7286−7290.

(10) Liu, B.; Brøndsted Nielsen, S.; Hvelplund, P.; Zettergren, H.; Cederquist, H.; Manil, B.; Huber, B. a. Collision-Induced Dissociation of Hydrated Adenosine Monophosphate Nucleotide Ions: Protection of the Ion in Water Nanoclusters. *Phys. Rev. Lett.* **2006**, *97*, 133401.

(11) Liu, B.; Haag, N.; Johansson, H.; Schmidt, H. T.; Cederquist, H.; Brondsted Nielsen, S.; Zettergren, H.; Hvelplund, P.; Manil, B.; Huber, B. A. Electron Capture Induced Dissociation of Nucleotide Anions in Water Nanodroplets. *J. Chem. Phys.* **2008**, *128*, 075102.

(12) Boudaïffa, B.; Cloutier, P.; Hunting, D.; Huels, M. A.; Sanche, L. Resonant Formation of DNA Strand Breaks by Low-Energy (3 to 20 eV) Electrons. *Science* **2000**, *287*, 1658−1660.

(13) Pluharrová, E.; Jungwirth, P.; Bradforth, S. E.; Slavícek, P. Ionization of Purine Tautomers in Nucleobases, Nucleosides, and Nucleotides: From the Gas Phase to the Aqueous Environment. *J. Phys. Chem. B* **2011**, *115*, 1294−1305.

(14) Belau, L.; Wilson, K. R.; Leone, S. R.; Ahmed, M. Vacuum-Ultraviolet Photoionization Studies of the Microhydration of DNA Bases (Guanine, Cytosine, Adenine, and Thymine). *J. Phys. Chem. A* **2007**, *111*, 7562−7568.

(15) Milosavljević, A. R.; Nicolas, C.; Lemaire, J.; Dehon, C.; Thissen, R.; Bizau, J.-M.; Réfrégiers, M.; Nahon, L.; Giuliani, A. Photoionization of a Protein Isolated In Vacuo. *Phys. Chem. Chem. Phys.* **2011**, *13*, 15432−15436.

(16) Milosavljević, A. R.; Nicolas, C.; Gil, J.-F.; Canon, F.; Réfrégiers, M.; Nahon, L.; Giuliani, A. VUV Synchrotron Radiation: A New Activation Technique for Tandem Mass Spectrometry. *J. Synchrotron Radiat.* **2012**, *19*, 174−178.

(17) Nahon, L.; de Oliveira, N.; Garcia, G. a; Gil, J.-F.; Pilette, B.; Marcouillé, O.; Lagarde, B.; Polack, F. DESIRS: A State-of-the-Art VUV Beamline Featuring High Resolution and Variable Polarization for Spectroscopy and Dichroism at SOLEIL. *J. Synchrotron Radiat.* **2012**, *19*, 508−520.

(18) Aravind, G.; Antoine, R.; Klærke, B.; Lemoine, J.; Racaud, A.; Rahbek, D. B.; Rajput, J.; Dugourdb, P.; Andersen, L. H. Sub-Microsecond Photodissociation Pathways of Gas Phase Adenosine 5′-Monophosphate Nucleotide Ions. *Phys. Chem. Chem. Phys.* **2010**, *12*, 3486−3490.

(19) Pedersen, S. Ø.; Støchkel, K.; Byskov, C. S.; Baggesen, L. M.; Nielsen, S. B. Gas-Phase Spectroscopy of Protonated Adenine,

Adenosine 5′-Monophosphate and Monohydrated Ions. *Phys. Chem. Chem. Phys.* **2013**, *15*, 19748−19752.
(20) Gabelica, V.; De Pauw, E. Internal Energy and Fragmentation of Ions Produced in Electrospray Sources. *Mass Spectrom. Rev.* **2005**, *24*, 566−587.
(21) Bagag, a.; Giuliani, a.; Laprévote, O. Atmospheric Pressure Photoionization Mass Spectrometry of Nucleic Bases, Ribonucleosides and Ribonucleotides. *Int. J. Mass Spectrom.* **2007**, *264*, 1−9.
(22) Brøndsted Nielsen, S.; Sølling, T. I. Are Conical Intersections Responsible for the Ultrafast Processes of Adenine, Protonated Adenine, and the Corresponding Nucleosides? *ChemPhysChem* **2005**, *6*, 1276−1281.
(23) Kumar, S. S.; Pérot-Taillandier, M.; Lucas, B.; Soorkia, S.; Barat, M.; Fayeton, J. A. UV Photodissociation Dynamics of Deprotonated 2′-Deoxyadenosine 5′-Monophosphate [5′-dAMP-H]-. *J. Phys. Chem. A* **2011**, *115*, 10383−10390.
(24) Lipciuc, M. L.; Wang, F.; Yang, X.; Kitsopoulos, T. N.; Fanourgakis, G. S.; Xantheas, S. S. Cluster-Controlled Photofragmentation: The Case of the Xe-Pyrrole Cluster. *ChemPhysChem* **2008**, *9*, 1838−1841.
(25) Zhao, Y.; Truhlar, D. G. A New Local Density Functional for Main-Group Thermochemistry, Transition Metal Bonding, Thermochemical Kinetics, and Noncovalent Interactions. *J. Chem. Phys.* **2006**, *125*, 194101.
(26) Valiev, M.; Bylaska, E. J.; Govind, N.; Kowalski, K.; Straatsma, T. P.; Van Dam, H. J. J.; Wang, D.; Nieplocha, J.; Apra, E.; Windus, T. L.; et al. NWChem: A Comprehensive and Scalable Open-Source Solution for Large Scale Molecular Simulations. *Comput. Phys. Commun.* **2010**, *181*, 1477−1489.
(27) Moller, C.; Plesset, M. S. Note on an Approximation Treatment for Many-Electron Systems. *Phys. Rev.* **1934**, *46*, 618.
(28) Szalay, P. G.; Watson, T.; Perera, A.; Lotrich, V. F.; Bartlett, R. J. Benchmark Studies on the Building Blocks of DNA. 1. Superiority of Coupled Cluster Methods in Describing the Excited States of Nucleobases in the Franck-Condon Region. *J. Phys. Chem. A* **2012**, *116*, 6702−6710.
(29) NIST Chemistry WebBook. http://webbook.nist.gov/chemistry/ (accessed May 16, 2014).
(30) Touboul, D.; Bouchoux, G.; Zenobi, R. Gas-Phase Protonation Thermochemistry of Adenosine. *J. Phys. Chem. B* **2008**, *112*, 11716−11725.
(31) Crowe, S. A.; Døssing, L. N.; Beukes, N. J.; Bau, M.; Kruger, S. J.; Frei, R.; Canfield, D. E. Atmospheric Oxygenation Three Billion Years Ago. *Nature* **2013**, *501*, 535−538.

AIP | Applied Physics Letters

Electron impact action spectroscopy of mass/charge selected macromolecular ions: Inner-shell excitation of ubiquitin protein

Miloš Lj. Ranković, Alexandre Giuliani, and Aleksandar R. Milosavljević

Citation: Applied Physics Letters **108**, 064101 (2016); doi: 10.1063/1.4941798
View online: http://dx.doi.org/10.1063/1.4941798
View Table of Contents: http://scitation.aip.org/content/aip/journal/apl/108/6?ver=pdfcov
Published by the AIP Publishing

Electron impact action spectroscopy of mass/charge selected macromolecular ions: Inner-shell excitation of ubiquitin protein

Miloš Lj. Ranković,[1] Alexandre Giuliani,[2,3,a)] and Aleksandar R. Milosavljević[1,4,a)]
[1]*Institute of Physics Belgrade, University of Belgrade, Pregrevica 118, 11080 Belgrade, Serbia*
[2]*SOLEIL, l'Orme des Merisiers, St. Aubin, BP48, 91192 Gif sur Yvette Cedex, France*
[3]*INRA, UAR1008, CEPIA, Rue de la Géraudière, BP 71627, 44316 Nantes, France*
[4]*Radiation Laboratory, University of Notre Dame, Notre Dame, Indiana 46556, USA*

(Received 7 December 2015; accepted 28 January 2016; published online 11 February 2016)

We have performed inner-shell electron impact action spectroscopy of mass and charge selected macromolecular ions. For this purpose, we have coupled a focusing electron gun with a linear quadrupole ion trap mass spectrometer. This experiment represents a proof of principle that an energy-tunable electron beam can be used in combination with radio frequency traps as an activation method in tandem mass spectrometry (MS^2) and allows performing action spectroscopy. Electron impact MS^2 spectra of multiply protonated ubiquitin protein ion have been recorded at incident electron energies around the carbon 1 s excitation. Both MS^2 and single ionization energy dependence spectra are compared with literature data obtained using the soft X-ray activation conditions. © *2016 AIP Publishing LLC*. [http://dx.doi.org/10.1063/1.4941798]

There has been a long standing effort to develop experimental techniques to investigate photon and electron interaction with large molecular species and complex systems under controllable, well-defined and single-collision conditions.[1–4] In this respect, an important breakthrough has been made in recent years by successful coupling of synchrotron radiation sources with ion traps, to perform photon activation of mass over charge (m/z) selected ions confined in the gas phase.[5–9] Indeed, by using electrospray ionization (ESI) technique[10] to extract macromolecular ions from solution, tandem mass spectrometry (MS^2)[11] and action spectroscopy[3,12] of unprecedentedly large species could be performed. Recently, we have applied near-edge X-ray fine structure (NEXAFS) action spectroscopy to investigate interplay between the electronic and the three-dimensional structure of gas phase ubiquitin protein.[13]

However, electron impact activation MS^2 of large biopolymer ions trapped in a radio frequency (RF) ion trap, and corresponding electron impact action spectroscopy, is considerably more challenging. Indeed, in contrast to photons, electrons are very sensitive to the oscillating electric field. Depending on the incident electron energy, RF can strongly influence spatial and energy profiles of an electron beam and ultimately prevent the electrons entering the trapping region. Moreover, both primary and scattered electrons (from background gases and surrounding surfaces) can be extracted towards ion detectors (as composed of conversion dynodes and electron multipliers), inducing a significant noise in the recorded mass spectra or even damage the detectors. All these issues have certainly penalized the use of an energy-tunable focused electron beam as activation technique in MS^2 based on RF ion traps. It should be noted, however, that since the invention of electron capture dissociation (ECD),[14] low-energy electron attachment to macromolecular ions has become a widely used activation method in MS^2 increasing the potential of top-down protein sequencing.[15] Using higher energy electrons, electron impact ionization of multiply protonated ions could be also achieved in Fourier transform ion cyclotron resonance (FT-ICR) ion trap instruments.[16] Although electron activation techniques were originally performed using the FT-ICR trap, a great deal of research has been devoted in recent years to development of technical solutions allowing for efficient ECD in RF traps (see Refs. 17–20 and references therein). Still, all these reports are concerned with bringing low energy (close to 0 eV) electrons into an RF trap, in order to produce efficient fragmentation of macromolecular ions via electron attachment. Recently, Voinov and coworkers reported the implementation of a radio frequency-free analyzer-independent cell[21] allowing ECD in triple quadrupole instruments. The method was also demonstrated in hybrid quadrupole time of flight instruments.[22] Interestingly, low energy electron impact ionization could be achieved using this setup.

However, high-energy electron impact activation/spectroscopy of trapped ionic species has not been reported yet. This is surprising considering that the scientific community is appealing for a technique that would allow controllable investigation of electron interaction with macromolecular systems. Such measurements could open new spectroscopic investigations and shed new light on radiation damage research.[1] Also, profound understanding of electron interaction with complex exotic molecules could help development of new applications, such as Focused Electron Beam Induced Deposition (FEBID).[23] Finally, energy-tunable electron impact activation MS^2 allows fragmentation via selective inner-shell excitation of a macromolecule. This could open new possibilities for advanced top-down sequencing by loading incident energy into specific parts of the macromolecule or inducing preferential type of fragmentation via chosen resonant excitation.

In this letter, we present a system allowing energy resolved electron impact activation MS^2 of m/z selected protein ions confined in a RF linear quadrupole ion trap. The

[a)]Authors to whom correspondence should be addressed. Electronic addresses: alexandre.giuliani@synchrotron-soleil.fr and vraz@ipb.ac.rs

instrument is based on an energy-tunable focused electron beam providing incident electron energies around C K-shell excitation. We recorded MS^2 spectra at selected electron activation energies and performed action electron spectroscopy of trapped protein ions. Moreover, we report a comparative study of inner-shell protein ionization by electron impact and X-ray absorption.

The experiment was performed by coupling a commercial linear quadrupole ion trap mass spectrometer (Thermo Scientific LTQ XL), equipped with an ESI source, to a differentially pumped vacuum stage including a custom-made electron gun assembly. The electron gun and the corresponding assembly were developed at the Institute of Physics Belgrade (IPB), Serbia. The experiment was conducted at the DISCO beamline of the synchrotron SOLEIL, France, where the electron-LTQ XL assembly was constructed. Fig. 1 presents a schematic drawing of the experimental setup. Six-way CF100 cross was used as a vacuum chamber, which was mounted on a movable support, and connected to the backside of the LTQ XL mass spectrometer. The assembly holding the electron gun was mounted on a custom made CF100 flange, with electrical feed-through. The remaining flanges of the cross were used to fit a turbomolecular pump, a cold cathode ionization gauge, and a viewport. During the experiment, the pressure was 4×10^{-6} mbar in the cross and 1×10^{-5} mbar in the vacuum manifold of the LTQ XL. The coupling of the CF100 cross with the back plate of the mass spectrometer was achieved using a bellows, to allow precise alignment of the electron gun axis with respect to the ion trap axis. The LTQ XL mass spectrometer was also mounted on a dedicated custom-made movable frame allowing a fine tuning of the ion trap position, as previously used for alignment with the photon beam.[24] Therefore, optimal overlap between the electron beam and ion packet was achieved by both fine positioning of the mounting frames and steering of the electron beam using the XY deflectors. Prior to the experiment, a pre-alignment was performed by measuring incident electron current on an electrode installed temporarily behind the trap, downstream the electron beam (see Fig. 1).

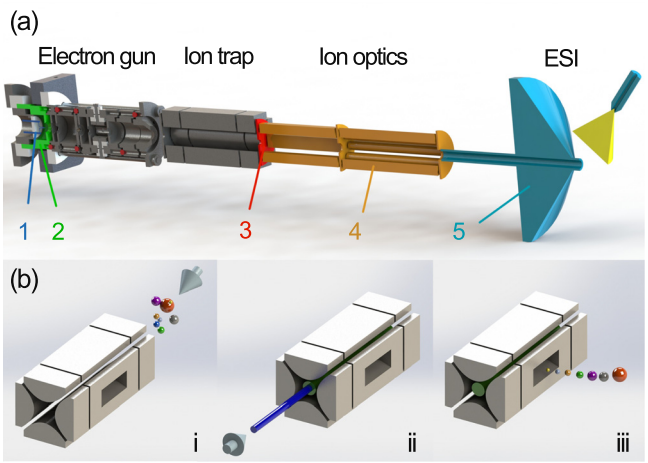

FIG. 1. Schematic representation of the experimental setup. (a) 1–tungsten filament, 2–Wehnelt electrode, 3–disc plate for current measurement, 4–quadrupole and octopole filters, 5–electrospray ion source. (b) i–ion injection and selection, ii–electron activation of selected ions, and iii–detection of fragments.

The electron gun was described in details previously.[25] Briefly, it consists of an extraction part and a focusing part (also including semi-cylindrically shaped XY deflectors to steer the beam). The electrons are emitted from a thoriated-tungsten cathode. The electron energy and all focusing voltages are controlled by a custom-made electronic board. The irradiation time was controlled by applying a variable DC pulse voltage on the Wehnelt electrode of the electron gun (see Fig. 1) that otherwise suppresses an electron emission from the filament. A dedicated electronic shutter circuit was designed in order to trigger and control the electron beam pulses by using the transistor-transistor logic (TTL) signal from the LTQ XL. The measurement procedure consisted of: ion production and injection into the trap, precursor isolation, electron irradiation, ion ejection, and detection, as previously used for photon irradiation.[5,7,24] The shortest irradiation time can be set to a few tens of ms, but 500 ms was used in the present experiment. In order to reduce background contributions, the TTL signal from the LTQ XL was sent through a digital delay generator (DG645, Stanford Research Systems, Sunnyvale, CA, USA) that provides a short delay (usually adjusted to 200 ms) of the ion ejection, after the electron irradiation was stopped.

The main issue in this experimental concept is that a focused electron beam is introduced into a RF field, which can, in principle, strongly influence the beam properties. The LTQ XL quadrupole ion trap uses a combination of DC and RF voltages. The DC component is ± 100 V. The RF electric field has an amplitude of 400 V peak-to-peak and a frequency of 1 MHz.[26] Therefore, even for the shortest electron pulses of a few tens of ms, the electron beam appears as continuous for the RF performance (a full RF cycle is 1 μs). Nevertheless, at the energy of about 300 eV, which is of interest for the present study (vicinity of C K-edge), an electron travels a half-length distance (34 mm) of the ion trap in about 5 ns. Therefore, we expect that a dominant portion of the incident electron current reaches the interaction volume almost undisturbed, while only small part is lost on the trap electrodes.

To investigate propagation and characteristics of the electron beam passing through the LTQ ion trap during 1 RF period, we performed electron tracing simulations using SIMION 8.2 program package[27] (Fig. 2). A continuous electron beam is simulated by a train of 1 ns pulses with 121 electrons arranged in a 0.5 mm square grid, which simulates a realistic electron current of 75 nA. Figs. 2(b) and 2(c) show simulated radial and kinetic energy distributions, respectively, of the electrons that can reach the center of the trap, for the starting energy of 300 eV and the initial beam radius of 0.5 mm. The simulations show that both the geometrical beam profile and the initial energy spread (limited to about 0.5 eV due to the emission from a hot cathode) are largely preserved in the interaction region, even though some disturbance due the RF field is inevitable.

Fig. 3(a) presents an electron activation MS^2 spectrum of multiply protonated ubiquitin protein ion (precursor charge state 7+) after electrospray ionization measured at 288 eV incident electron energy. Besides the peak corresponding to the precursor ion $[M+7H]^{7+}$ at m/z 1225, the dominant peak in the electron impact MS^2 lies at m/z 1071,

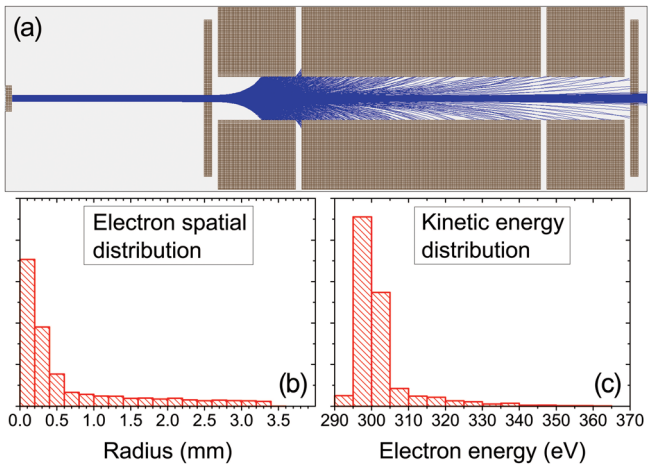

FIG. 2. Simulation of pulsed electron beam propagation in a linear quadrupole ion trap under influence of RF (1 MHz, 400 V) and DC (100 V) potentials. A total of 1.2×10^5 electrons, during a pulse width of 1 μs, at the energy of 300 eV and with a beam diameter of 0.5 mm, was directed along the axis of the ion trap. (a) The simulation of the propagation of the electron beam; (b) the spatial distribution, and (c) the energy distribution of electrons recorded at the center of the ion trap.

which represents a radical singly ionized cation $[M+7H]^{8+}$. We ascribe the other closely positioned intensive peak at about m/z 1066 to a small neutral loss from the ionized 8+ ion. Due to limited mass resolution for such high charge states, we cannot exactly define the mass of the neutral loss. We can tentatively assume that it could be due to amino acids side chain losses.[12] Finally, besides the single

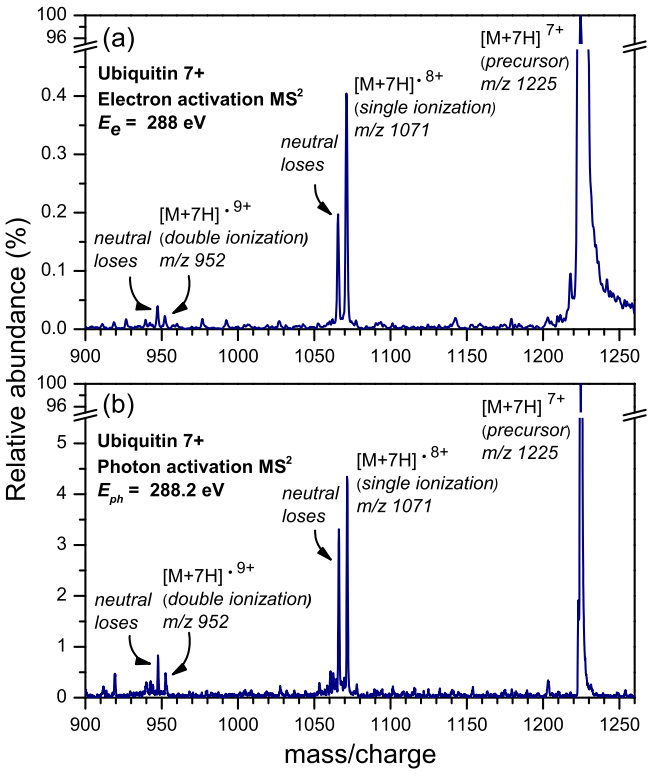

FIG. 3. Comparison of tandem mass spectra of Ubiquitin 7^+ precursor for energies near carbon K-edge activated with: (a) electrons (isolated m/z 1222.8–1225.8) and (b) photons (isolated m/z 1223.4–1226.4). The electron irradiation was performed during 500 ms (200 ms acquisition delay), with estimated 10^{13} electrons/second. The photon irradiation was performed during 600 ms (50 ms acq. delay), with estimated 10^{12} photons/second.

ionization (SI) process, which is clearly the dominant relaxation channel upon inner-shell electron impact excitation of ubiquitin, the peak corresponding to doubly ionized cation $[M+7H]^{9+}$ can also be traced down in the MS^2 at m/z 952. And the latter is accompanied by intensive neutral losses, as well. The abundances of other fragments are much lower and thus will not be discussed in the present study. It should be noted, however, that low-mass background was also detected (not shown here) and removed, most probably originated from electron ionization of neutral gasses present in traces in the trap and the electron-induced noise.

For comparison, Fig. 3(b) presents X-ray activation MS^2 of the same 7+ precursor and at practically the same photon energy of 288.2 eV. The results are extracted from recent X-ray inner-shell spectroscopy of gas-phase proteins by coupling the same ion trap to the PLEIADES soft X-ray beamline at the SOLEIL facility[13] (note that the X-ray spectrum was measured with higher m/z resolution). The correspondence between the two spectra is striking. Indeed, the ionization of the protein is the result of the resonant Auger decay process, triggered by carbon 1 s electron excitation to a frontier molecular orbital and a core hole formation. The ionization/fragmentation pattern, however, does not depend significantly on the triggering process itself.[13] This finding is also important for the studies on radiation damage of proteins, particularly considering recent results suggesting that proteins were damaged by X-ray radiation at a faster rate than is DNA.[28]

Nevertheless, it should be pointed out that the two discussed processes—electron and photon inner-shell excitation—are intrinsically different. In the case of X-ray activation, an incident photon is resonantly absorbed at the energy that corresponds to the transition involving a core electron. In the case of electron impact activation, the incident electron transfers part of its energy to the system triggering the electronic transition and is scattered out suffering the corresponding energy loss. Furthermore, in the present experiment, the incident electron energy is only slightly above the transition energy. Therefore, the electron excitation is performed under so-called near-threshold conditions.[29] Consequently, the acquisition of MS^2 as a function of the electron energy, in the same way as we measured action NEXAFS spectra of gas phase protein,[7,13] will yield in the present case the action near-edge electron excitation function (NEEEF).

Fig. 4 presents NEEEF (circles) and NEXAFS (dashed line)[13] action spectra of ubiquitin 7+ precursor. In both cases, an area under the peak in MS^2 corresponding to singly ionized radical $[M+7H]^{8+}$ (see Fig. 3) has been normalized to the total ion current, and plotted as function of the activation electron or photon energy, respectively. In the case of the NEEEF spectrum, the focal properties of the electron gun are adjusted as a function of the electron energy to preserve a constant beam profile. These focusing voltages have been determined prior to MS^2 experiment by measuring electron current passing through the ion trap. Experimental details about the NEXAFS spectra are given in the previous publication.[13] The spectra presented in Fig. 4 are normalized to the same area under the curve.[13] The electron-induced SI yield is measured with lower energy resolution, which is due to

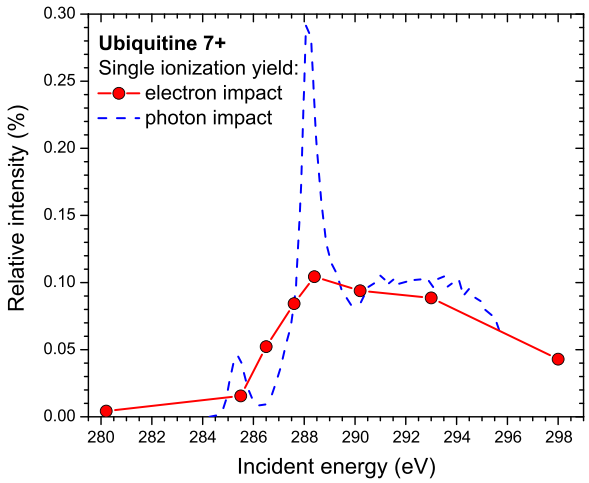

FIG. 4. Comparison of single ionization yield from Ubiquitin 7^+ precursor activated with electrons (red circles) and soft X ray photons[13] (blue dashed curve).

both using of an electron gun (without an electron monochromator) and additional beam energy broadening inside an RF trap (see Fig. 2).

The electron impact SI yield of ubiquitin protein (Fig. 4, circles) shows strong incident energy dependence. The cross section starts increasing at the energy that corresponds to C $1s \rightarrow \pi^*_{aromatic}$ transition at about 284.5 eV and steeply rises reaching a maximum at about 288 eV, which corresponds to $1s \rightarrow \pi^*_{amide}$ transition. The SI yield slowly decreases with further increasing of the impact electron energy. There is a clear correspondence between the two sets of results obtained using X-ray or electron irradiation. Indeed, in both cases, the SI of the precursor proceeds from carbon core excited molecular transient state via Auger decay. Nevertheless, as already pointed out, the excitation processes itself is essentially different. Therefore, the electron energy dependence may be distinctly different, since in the electron impact case, a triggering process is due to near-threshold electron collision. Moreover, scattered electrons carry out some residual energy and the core excitation does not have to be resonant, so at a particular impact energy, it depends on the redistribution of excitation cross sections. It should be noted that previously, Cooper *et al.*[30] performed the inner shell electron energy-loss spectroscopy of a condensed protein, but recorded under scattering conditions where electric dipole transitions dominate (2.5 keV residual electron energy and 2° scattering angle). Such spectra, however, are to be compared with X-ray absorption data, as represented here by action NEXAFS spectrum (blue curve).

In conclusion, we have demonstrated energy-tunable focused electron beam activation of m/z selected trapped protein ions by coupling an electron gun to a linear quadrupole ion trap mass spectrometer. We have shown that both electron and X-ray activation produce very similar MS^2 patterns, which is defined by resonant Auger decay process regardless of triggering process. However, the energy dependences are not to be directly compared, since in the case of electron action spectroscopy, an electron impact near-threshold excitation takes place. Therefore, the present experiment suggests a possibility to perform a comparative study of electron and photon induced excitation of macromolecular ions and to discuss intrinsic differences between the two processes, which will be undertaken in future publications.

The present results pave a way to developing methods for investigation of electron interaction with macromolecules, complex systems and nanoparticles, under well-defined conditions, and in a wide energy range. Moreover, we demonstrate a proof of principle for an activation method for MS^2 top-down macromolecular sequencing using high-energy electron impact activation of trapped ions. This may be a complementary low-cost method that allows investigating only specific fragmentation processes, depending on the activation energy.

This work was supported by the ANR, France, under Project No. ANR-08-BLAN-0065. M.Lj.R. and A.R.M. acknowledge support by the MESTD of Republic of Serbia under Project No. #171020. The Notre Dame Radiation Laboratory is supported by the U.S. Department of Energy Office of Science, Office of Basic Energy Sciences under Award No. DE-FC02-04ER15533 (this is document number NDRL 5095). A.R.M. and M.Lj.R. acknowledge support from the COST Actions CM1204 (XLIC) and CM1301 (CELINA). We thank Dr. Christophe Nicolas for his help to assemble the experiment and the general staff of the DISCO, DESIRS, and PLEIADES beamlines of the SOLEIL synchrotron radiation facility for the technical support.

[1]J. Gu, J. Leszczynski, and H. F. Schaefer, Chem. Rev. **112**, 5603 (2012).
[2]D. Touboul, F. Gaie-Levrel, G. A. Garcia, L. Nahon, L. Poisson, M. Schwell, and M. Hochlaf, J. Chem. Phys. **138**, 094203 (2013).
[3]A. R. Milosavljević, A. Giuliani, and C. Nicolas, in *X-ray and Neutron Techniques for Nanomaterials Characterization*, edited by Challa S. S. R. Kumar (Springer-Verlag, Berlin, Heidelberg, 2016), ISBN: 978-3-662-48604-7.
[4]E. Antonsson, H. Bresch, and R. Lewinski, Chem. Phys. Lett. **559**, 1 (2013).
[5]A. R. Milosavljević, C. Nicolas, J. Lemaire, C. Dehon, R. Thissen, J.-M. Bizau, M. Réfrégiers, L. Nahon, and A. Giuliani, Phys. Chem. Chem. Phys. **13**, 15432 (2011).
[6]S. Bari, O. Gonzalez-Magaña, G. Reitsma, J. Werner, S. Schippers, R. Hoekstra, and T. Schlathölter, J. Chem. Phys. **134**, 024314 (2011).
[7]A. R. Milosavljevic, F. Canon, C. Nicolas, C. Miron, L. Nahon, and A. Giuliani, J. Phys. Chem. Lett. **3**, 1191 (2012).
[8]A. Giuliani, A. R. Milosavljević, F. Canon, and L. Nahon, Mass Spectrom. Rev. **33**, 424 (2014).
[9]O. González-Magaña, G. Reitsma, M. Tiemens, L. Boschman, R. Hoekstra, and T. Schlathölter, J. Phys. Chem. A **116**, 10745 (2012).
[10]J. B. Fenn, M. Mann, C. K. Meng, S. F. Wong, and C. M. Whitehouse, Mass Spectrom. Rev. **9**, 37 (1990).
[11]R. Aebersold and M. Mann, Nature **422**, 198 (2003).
[12]F. Canon, A. R. Milosavljevic, L. Nahon, and A. Giuliani, Phys. Chem. Chem. Phys. **17**, 25725 (2015).
[13]A. R. Milosavljević, C. Nicolas, M. L. Ranković, F. Canon, C. Miron, and A. Giuliani, J. Phys. Chem. Lett. **6**, 3132 (2015).
[14]R. Zubarev, N. L. Kelleher, and F. W. McLafferty, J. Am. Chem. Soc **120**, 3265 (1998).
[15]N. L. Kelleher, Anal. Chem. **76**, 196A (2004).
[16]R. A. Zubarev and H. Yang, Angew. Chem. Int. Ed. Engl. **49**, 1439 (2010).
[17]L. Ding and F. L. Brancia, Anal. Chem. **78**, 1995 (2006).
[18]T. Baba, J. L. Campbell, J. C. Y. Le Blanc, J. W. Hager, and B. A. Thomson, Anal. Chem. **87**, 785 (2015).
[19]O. A. Silivra, F. Kjeldsen, I. A. Ivonin, and R. A. Zubarev, J. Am. Soc. Mass Spectrom. **16**, 22 (2005).
[20]T. Baba, Y. Hashimoto, H. Hasegawa, A. Hirabayashi, and I. Waki, Anal. Chem. **76**, 4263 (2004).

[21]V. G. Voinov, M. L. Deinzer, and D. F. Barofsky, Anal. Chem. **81**, 1238 (2009).
[22]V. G. Voinov, M. L. Deinzer, J. S. Beckman, and D. F. Barofsky, J. Am. Soc. Mass Spectrom. **22**, 607 (2011).
[23]W. F. van Dorp and C. W. Hagen, J. Appl. Phys. **104**, 081301 (2008).
[24]A. R. Milosavljević, C. Nicolas, J.-F. Gil, F. Canon, M. Réfrégiers, L. Nahon, and A. Giuliani, J. Synchrotron Radiat. **19**, 174 (2012).
[25]A. R. Milosavljević, S. Madžunkov, D. Šević, I. Čadež, and B. P. Marinković, J. Phys. B: At., Mol. Opt. Phys. **39**, 609 (2006).
[26]J. C. Schwartz and M. W. Senko, J. Am. Soc. Mass Spectrom. **13**, 659 (2002).
[27]See http://simion.com/ for information about SIMION field and particle trajectory simulator software.
[28]C. Bury, E. F. Garman, H. M. Ginn, R. B. G. Ravelli, I. Carmichael, G. Kneale, and J. E. McGeehan, J. Synchrotron Radiat. **22**, 213 (2015).
[29]A. Hitchcock, J. Electron Spectrosc. Relat. Phenom. **112**, 9 (2000).
[30]G. Cooper, M. Gordon, D. Tulumello, C. Turci, K. Kaznatcheev, and A. P. Hitchcock, J. Electron Spectrosc. Relat. Phenomena **137–140**, 795 (2004).

VUV action spectroscopy of protonated leucine-enkephalin peptide in the 6-14 eV range

M. Lj. Ranković, F. Canon, L. Nahon, A. Giuliani, and A. R. Milosavljević

Citation: The Journal of Chemical Physics **143**, 244311 (2015); doi: 10.1063/1.4939080
View online: http://dx.doi.org/10.1063/1.4939080
View Table of Contents: http://scitation.aip.org/content/aip/journal/jcp/143/24?ver=pdfcov
Published by the AIP Publishing

VUV action spectroscopy of protonated leucine-enkephalin peptide in the 6-14 eV range

M. Lj. Ranković,[1] F. Canon,[2] L. Nahon,[3] A. Giuliani,[3,4] and A. R. Milosavljević[1,5,a)]
[1]*Institute of Physics Belgrade, University of Belgrade, Pregrevica 118, 11080 Belgrade, Serbia*
[2]*INRA, UMR1324 Centre des Sciences du Goût et de l'Alimentation, F-21000 Dijon, France*
[3]*SOLEIL, l'Orme des Merisiers, St Aubin, BP48, 91192 Gif sur Yvette Cedex, France*
[4]*INRA, UAR1008, CEPIA, Rue de la Géraudière, BP 71627, 44316 Nantes, France*
[5]*Radiation Laboratory, University of Notre Dame, Notre Dame, Indiana 46556, USA*

(Received 3 November 2015; accepted 15 December 2015; published online 29 December 2015)

We have studied the Vacuum Ultraviolet (VUV) photodissociation of gas-phase protonated leucine-enkephalin peptide ion in the 5.7 to 14 eV photon energy range by coupling a linear quadrupole ion trap with a synchrotron radiation source. We report VUV activation tandem mass spectra at 6.7, 8.4, and 12.8 eV photon energies and photodissociation yields for a number of selected fragments. The obtained results provide insight into both near VUV radiation damage and electronic properties of a model peptide. We could distinguish several absorption bands and assign them to particular electronic transitions, according to previous theoretical studies. The photodissociation yields appear to be very different for the various observed fragmentation channels, depending on both the types of fragments and their position along the peptide backbone. The present results are discussed in light of recent gas-phase spectroscopic data on peptides. © *2015 AIP Publishing LLC.* [http://dx.doi.org/10.1063/1.4939080]

I. INTRODUCTION

Investigation of the interaction of Vacuum Ultraviolet (VUV) radiation with polymers of amino acids, namely, peptides and proteins, is of essential importance. These molecules are ubiquitous in the biosphere and are involved in many important processes in living organisms. Their function and activity are intrinsically connected with their primary structure–the sequence of amino acids.[1] Therefore, any alteration of the primary sequence and degradation of the biopolymer, due to interaction with energetic photons such as UV, VUV, or X-rays, may lead to severe consequences and ultimately to cellular death. All these effects are commonly ascribed as radiation damage. In this respect, deep UV and VUV action spectroscopy of biopolymers isolated in the gas phase offers possibilities to investigate photon activation processes of particular mass-to-charge selected systems. Such experiments could help in reaching the fundamental understanding of radiation damage at the molecular level.

On the other hand, the availability of third generation synchrotron radiation facilities, providing high-resolution, tunable and high-brightness sources of energetic photons, as well as recent development of state-of-the-art spectroscopic experimental systems, allowed for detailed investigation of electronic and structural properties of biomolecules. However, until now the VUV spectroscopic and dynamical studies have been limited only to amino acids, since these relatively small molecules can be evaporated and thus introduced as neutrals into the gas phase (see, e.g., Refs. 2–4 and references therein), as well as some small peptides[5] and nucleobases.[6]

The study of the building blocks of biomolecules is certainly important to understand the physicochemical properties of a biopolymer that they form. However, this bottom-up approach is still insufficient to reach comprehensive knowledge about the complex biological systems such as proteins and DNA. Indeed, the electronic structure and physicochemical properties of biopolymers are built up from the properties of their building units as well as from the intramolecular interactions closely correlated with their primary, secondary and tertiary structures. For example, in a peptidic chain, amino-acids are connected to each other through peptide bonds, which crucially influence the protein's electronic structure. Moreover, biomolecules are not isolated in nature, and solvents can strongly affect their radiation response.[7–9] Therefore, the building blocks approach in the investigations of complex biomolecules may be of limited relevance in some aspects regarding their electronic structure, structural properties, function, and radiation damage sensitivity.

The recent development of experimental techniques that couple ion traps with synchrotron radiation sources has opened up possibilities to perform VUV action spectroscopy of protonated or deprotonated large biopolymers isolated in the gas phase.[10–13] The biomolecules are brought into the gas phase by electrospray ionization (ESI),[14] selected and stored in a radio frequency (RF) ion trap. The technique is based on tandem mass spectrometry, where a particular precursor ion is selected, activated by VUV radiation, and analyzed using mass spectrometry. A high sensitivity and selectivity of the mass spectrometry, a prolonged interaction time in the trap, and a high brightness of third generation SR sources provide a respectable signal to noise ratio, overcoming significantly lower target densities in comparison

a)Author to whom correspondence should be addressed. Electronic mail: vraz@ipb.ac.rs.

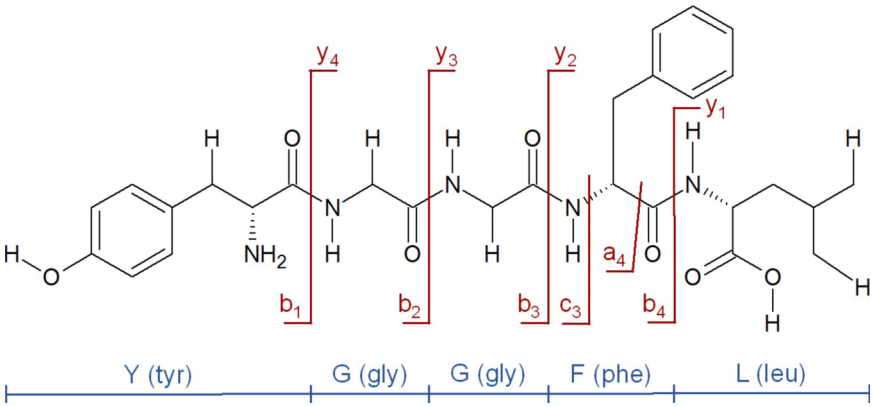

FIG. 1. The structure of the leucine-enkephaline peptide with its five amino acid constituents and imonium ions with mass-to-charge ratios of Y(136), F(120) and L(86).

with classic spectroscopy of neutral molecules.[12] The energy tunable SR sources enable recording of tandem mass spectra (MS^2) as a function of the photon energy. Therefore, action spectroscopy of desired target ions is performed by recording photoionization and photofragmentation ion yields.

Leucine-enkephaline (Leu-enk) consists of five amino acids arranged in the following sequence: Tyr-Gly-Gly-Phe-Leu (YGGFL) (see Fig. 1) and has been intensively investigated in recent years to become a standard model in mass spectrometry.[15] Recently, we have also investigated VUV photon interaction with both bare and nanosolvated Leu-enk dimers.[16,17] We have measured the backbone photofragment yields and thus mapped the electronic excitation bands of the Leu-enk dimer molecule that lead to molecular dissociation.[17] More interestingly, we have found a significant stabilization effect of only three water molecules, which has also been confirmed by Density Functional Theory (DFT) calculations.[16] Bari *et al.*[11] have reported the pioneering and detailed investigation of the photodissociation of gas-phase protonated Leu-enk trapped cations in the 8–40 eV photon energy range. They have discussed in detail photofragmentation patterns both below and above the ionization threshold and presented ion yields for a number of different fragments. However, the latter study[11] was fragmentary regarding the low VUV photon energies below 10 eV, as the authors probed only a few energies in this domain. Therefore, it was not possible to discuss spectroscopic features in the energy range below 10 eV and the corresponding lowest energy electronic transitions of the Leu-enk molecule.

The present study extends previous studies on model peptides and Leu-enk[11,16–18] in several directions. It reports novel results of the VUV action spectroscopy of an isolated peptide. This is an extension of our previous work on Substance P peptide (11 residues),[18] investigating the electronic structure of the Leu-enk molecule, which is a smaller 5-amino acid peptide with a simpler fragmentation pattern. Therefore, the present work allows for deep insight into general electronic properties of a peptide. On the other hand, we also significantly extend the previous study of VUV-induced energy-dependent fragmentation of Leu-enk molecule.[11] Indeed, this time we dominantly focus on the low-energy VUV domain, where the electronic excitations trigger molecular dissociation.

II. EXPERIMENTAL METHOD

A commercial linear quadrupole ion trap mass spectrometer (Thermo Finnigan LTQ XL) was used for both ion production and selection/isolation. It was previously modified and coupled[10,19] to the VUV beamline DESIRS[20] of the SOLEIL synchrotron radiation facility in France. The front side of the LTQ mass spectrometer was equipped with an ESI source. Ions produced by ESI were introduced through the system of ion lenses and stored in the linear ion trap. Singly protonated precursor ions $[Leu\text{-}Enk+H]^+$ (m/z 556) were selected and stored in the ion trap, where they were irradiated using monochromatic VUV photon beam for 500 ms. The control of the irradiation time has been achieved, by installing a fast rotating mechanical shutter in the path of the photon beam,[21] inside a dedicated vacuum chamber on the back side of LTQ.

The VUV photon beam was produced by an electromagnetic undulator (OPHELIE II) feeding the DESIRS beamline and further monochromatized using a normal incidence monochromator, resulting in a typical bandwidth of 12 meV in the present case.[20] The absolute photon energy uncertainty was a few tens of meV, as calibrated against the zero order. A monochromator grating of 200 gr mm^{-1} in combination with a 200 μm exit slit was used, allowing for a high photon flux of 10^{12}–10^{13} ph/s. In order to obtain high spectral purity, higher harmonics from the undulator were removed using a krypton gas filter (cutoff above 14 eV) and MgF_2 window filter (cutoff above 10.6 eV). A pressure difference between the synchrotron beamline (10^{-8} mbar) and the LTQ mass spectrometer (10^{-5} mbar) was accommodated with a custom made differential pumping stage, in assembly with a mechanical shutter and a movable photodiode. The latter was used to measure the photon flux just before the ion trap. The LTQ mass spectrometer was mounted on a custom-made supporting frame with several degrees of freedom, for rotational and translational position adjustment. A precise alignment of the photon beam with respect to the ion trap axis was essential for achieving a high ion activation efficiency and signal to noise ratio.

Leu-enk was provided by Sigma-Aldrich in a powder form and was dissolved in a water/acetonitrile (75:25 v/v) mixture at a concentration of 10 μM. After photon activation of the isolated ions, all fragments were ejected from each side of the trap towards detectors, and tandem mass spectrum (MS^2) was

recorded for particular photon energy. Each sequence of ion isolation, photon activation and mass spectrum recording was repeated for different photon energies. A home-made software was used to control and synchronize the ion isolation, the opening of mechanical shutter, the beamline photon energy adjustment and the mass spectra recording. Automated data acquisition scans lasting up to several hours resulted in 30-50 mass spectra with a 0.2 eV energy step for a desired precursor.

The photodissociation ion yields were extracted from the recorded mass spectra by plotting the area under the peak of interest against the photon energy, and normalizing to the photon flux and the total ion current (TIC). The photon flux was measured in a separate energy scan with a photodiode (AXUV100, International Radiation Detectors) under the same experimental conditions. For the present experiment, two scans of the photon flux were performed, one with a krypton gas filter and one with an MgF_2 glass window filter. In order to cover the whole energy range of interest, three separate action scans of the $[M+H]^+$ precursor, within partly overlapping energy domains (5.7-8.5) eV, (7.2-10.2) eV, and (10-14) eV, were performed. The first energy range of (5-8) eV was measured with the MgF_2 glass window filter, whereas the other two ranges were measured with the krypton gas filter. Extraction and normalization of all ion yields have been performed separately for each energy range. The final energy yield for each fragment ion, in the overall range from 5.7 to 14 eV, was obtained by coupling three separately obtained normalized relative ion yields. An additional normalization procedure to couple the lowest energy fragment ion yields of (5.7-8.5) eV with the other two is as follows. All fragment ion yields in the higher energy ranges (7.2-10.2 and 10-14 eV domains) were multiplied with the independent factor for each fragment ion to achieve the best overlap with the same fragment ion yield in the lowest energy range. In other words, fragment yields from the two higher ranges were down-scaled to match the yields from the first energy range, each ion fragment having its own scale factor.

III. RESULTS AND DISCUSSION

A. Tandem mass spectrometry

The schematic structure of the Leu-enk molecule is presented in Fig. 1. Upon VUV photon absorption, the electronic excitation and the ionization of the precursor can both induce bond cleavages (photodissociation and dissociative ionization, respectively) leading to different fragment ions. As for peptide backbone cleavage, depending on both which particular bond has been cleaved along the backbone and where the remaining charge stays upon this bond cleavage, there is a standard nomenclature[22,23] of the fragments: a_n, b_n, and c_n for N-terminal and x_n, y_n, and z_n for C-terminal, where subscripts indicate the number of amino acid residues left in a particular fragment. Additionally, the photon absorption can induce detachment of neutral groups (e.g., amino acid residues) and multiple bond cleavages.

Fig. 2 presents the MS^2 obtained at three prominent photon energies: at 6.7 eV (below the ionization threshold), at 8.4 eV (near, just below the threshold) and at 12.8 eV (above the threshold). The ionization energy (IE) of the protonated molecule has been predicted from DFT calculations to be

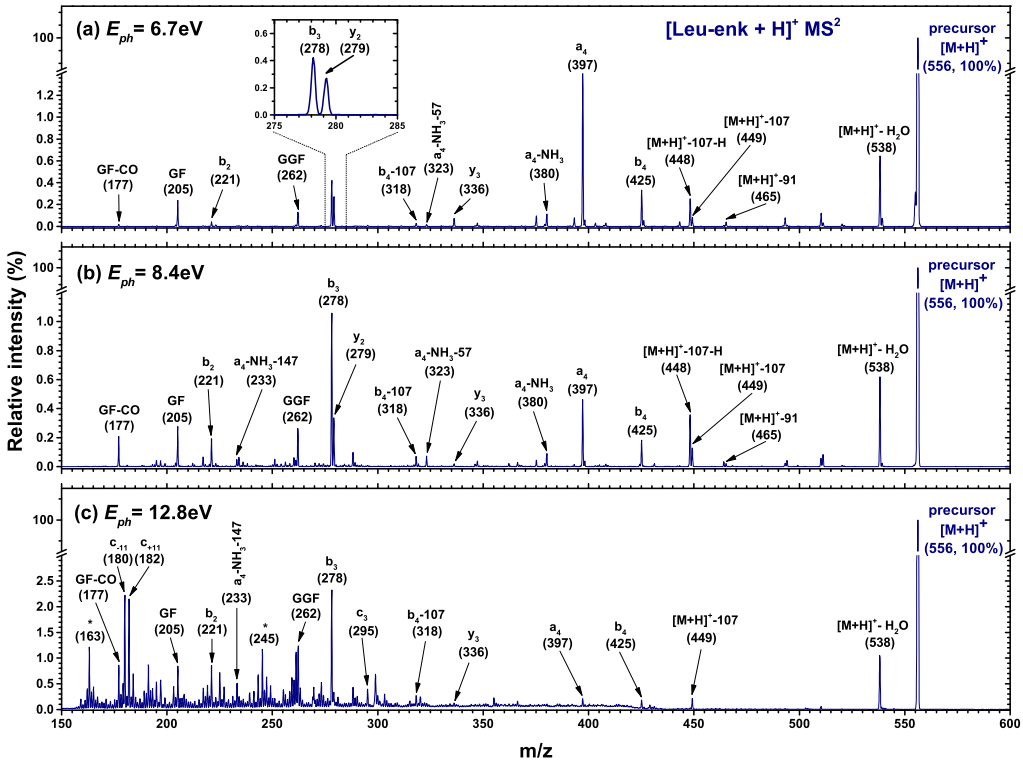

FIG. 2. Photo-activation tandem mass spectra of leucine-enkephalin, after 500 ms irradiation of $[Leu\text{-}Enk+H]^+$ precursor at: (a) 6.7 eV, (b) 8.4 eV, and (c) 12.8 eV photon energies. The proposed assignments of the most important fragments are given in the figure while "M" denotes the pseudomolecular ion.

at 8.87 eV.[11] The peak designated at a mass-to-charge ratio (m/z) of 556 corresponds to the parent cation of protonated Leu-enk $[M+H]^+$. For energies lower than IE (Figs. 2(a) and 2(b)), the fragmentation pattern appears to be very similar to MS^2 recorded in collision-induced dissociation (CID) experiments.[15] At these energies, photo-induced fragmentation mainly proceeds through cleavage of a peptide backbone that yields *a*, *b*, and *y* fragments, which are clearly visible in the mass spectrum at 6.7 eV (Fig. 2(a)). Dominant Leu-enk fragments in the mass spectra recorded at incident photon energies below IE are a_4 (m/z 397), b_3 (m/z 278), y_2 (m/z 279) and b_4 (m/z 425). Fragments assigned to the precursor's loss of one water molecule $[M+H]^+$-H_2O (m/z 538) and the tyrosine side chain $[M+H]^+$-107 (m/z 449) are also clearly visible, while the precursor's loss of the phenylalanine side chain $[M+H]^+$-91 (m/z 465) is of much less abundance. Fragments b_3 (m/z 278) and y_2 (m/z 279) could not be separated in the previous VUV photodissociation study,[11] but are clearly resolved in the present mass spectra (see the inset in Fig. 2(a)). Further internal fragmentation of a_4 and b_4 can lead to fragments with ammonia loss a_4-NH_3 (m/z 380), loss of glycine a_4-NH_3-57 (m/z 323), loss of tyrosine side chain b_4-107 (m/z 318), GGF (m/z 262), GF (m/z 205), and loss of carbon monoxide GF-CO (m/z 177).

Very similar MS^2 fragmentation patterns of present sub-IE VUV-induced dissociation (Figs. 2(a) and 2(b)) and CID[15] of protonated Leu-enk suggest that absorption of photons by Leu-enk molecular ions leads to electronic excitations after which intramolecular vibrational redistribution and/or internal conversion leading to a hot ground state dominantly take place. Still, it should be noted that at the energy of 8.4 eV (Fig. 2(b)), which is near IE, we observe a substantial change of the intensities of main peaks in the MS^2. The intensity of fragment b_3 (m/z 278) markedly increases, while quite opposite stands for the fragments a_4 (m/z 397) and b_4 (m/z 425). The intensity of fragment GF (205) slightly increased whereas its loss of carbon monoxide CO, namely, fragment GF-CO (m/z 177), becomes stronger. Other fragments b_2 (m/z 221), GGF (m/z 262), $[M+H]^+$-107 (m/z 449), and b_4-107 (m/z 318) exhibit moderate intensity increase.

At the energy of 12.8 eV, which is well above the IE, the MS^2 spectrum significantly changes. As a result of the formation of the doubly charged radical precursor at the first instance, more fragmentation channels become open, resulting in a rich mass spectrum in the low m/z range of 150-350. A sequence fragment c_3 (m/z 295) appears. There are also unassigned fragments, which can be due to the photoionization of neutral contaminants present in the ion trap in traces. Fragments that dominated the sub-ionization mass spectrum: a_4 (m/z 397), b_4 (m/z 425) and $[M+H]^+$-107 (m/z 449) are barely visible at 12.8 eV. On the other hand, the production of the fragment corresponding to the water loss $[M+H]^+$-H_2O (m/z 538) is two-fold enhanced as compared to lower energies. After internal fragmentation of a_4-NH_3 (m/z 380), due to loss of phenylalanine residue (−147), a remaining fragment a_4-NH_3-147 (m/z 233) is also visible above IE. A doubly ionized precursor ion $[M+H]^{2+}$ (m/z 278) shows up at the same position in the mass spectrum as the fragment b_3 (278); therefore, it is difficult to claim if the doubly ionized precursor can be seen in the spectrum. Even if this ion is formed, it may quickly dissociate before detection, due to a high Coulomb potential energy. In our previous work, the doubly ionized Leu-enk dimer could not be seen in the MS^2, but the nanosolvation-induced stabilization effect allowed for tracing down the doubly ionized hydrated precursor with three water molecules. In the present measurements the relative intensity of the b_3 (m/z 278) fragment increases more rapidly above the IE in comparison with other backbone fragments, as can be seen in the mass spectra presented in Fig. 2 (see also below). However, we cannot provide a definite conclusion if this is due to the contribution of the $[M+H]^{2+}$ dication formed above IE.

Present fragmentation patterns are in a very good agreement with the recent work of Bari *et al.*[11] in the overlapping m/z and photon energy domains. All fragments assigned in the later article[11] at the photon energy of 8 eV are also found in the present mass spectrum at the photon energy of 8.4 eV. Additionally, owing to improvement in the signal to noise ratio and mass resolution, we could resolve additional important backbone fragments such as b_2, y_2, y_3, and b_4 (see Fig. 2(b)). Similarly, we could assign all fragments reported in Ref. 11 at 15 eV and resolve additional species originating from Leu-enk.

B. Photodissociation ion yields

In this section, we study the spectroscopic structures of several selected abundant fragments. This is made possible because of the high signal to noise ratio and improved mass resolution for accurate and detailed measurements of desired photofragmentation yields in small energy steps and with a high photon energy resolution. The aim is to investigate the electronic structure of Leu-enk and specific fragmentation processes resulting from the electronic excitation. Particularly, we compare the backbone sequence specific photofragmentation yields of: (a) the same type of *b* fragments (C–N bond cleavage) along the peptide backbone, (b) fragments resulting from the same bond cleavage (C–N) but formed with a charge at N- or C-terminus (b_2/y_3 and b_3/y_2) and (c) the fragments formed with a charge at N-terminus but resulting from neighboring bond cleavages (C–C_α a_4 and C–N b_4). We also compare the spectroscopic signatures of fragments resulting from detachment of different neutral groups.

Figs. 3 and 4 present selected photodissociation ion yields of singly protonated Leu-enk ions in the 5.7–14 eV energy range. The shown absolute uncertainties (Δ) were obtained as the biggest mismatch between overlapping points of different energy ranges, according to the normalization procedure described in the experimental section. Note, however, that low statistics and possible higher influence of a background in the case of very less-abundant fragments could increase the overall uncertainty of the curve shape (e.g., Fig. 3(d), the 8-10 eV region). The extracted ion yields show rich spectroscopic features, which will be discussed in more detail below.

Fig. 3 compares relative photodissociation ion yields of the most abundant sequence specific fragments resulting

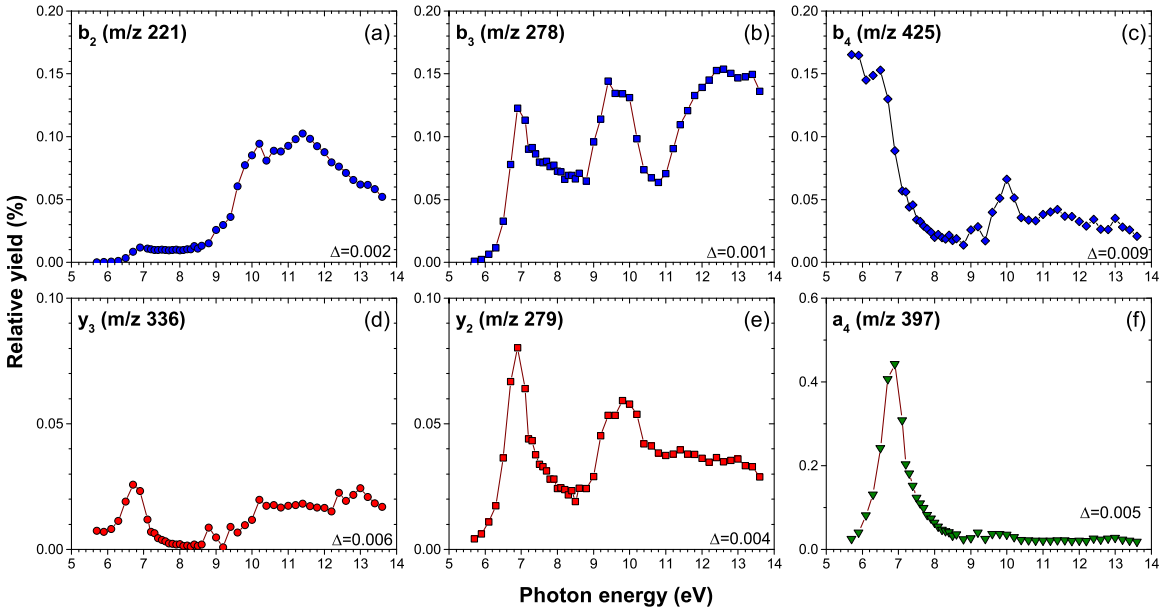

FIG. 3. Normalized relative ion yields from the photodissociation of precursor $[Leu\text{-}Enk+H]^+$ in the range from 5.7 to 14 eV. Integrated mass ranges are: (a) b_2 (m/z = 220.5-221.5), (b) b_3 (m/z = 277.5-278.5), (c) b_4 (m/z = 424.5-425.5), (d) y_3 (m/z = 335.5-336.5), (e) y_2 (m/z = 278.5-279.5), and (f) a_4 (m/z = 396.5-397.5). The absolute uncertainties of the experimental points obtained as the biggest mismatch between overlapping values of different energy ranges upon normalization are shown on the right bottom corner of each panel as Δ values.

from the peptide backbone dissociation. According to previous studies,[18,24–27] the electronic structure of a dipeptide backbone can be described as a four-level system. Hence, the lowest energy excited states responsible for VUV photon absorption by the backbone involve: $n_0\pi_3^*$ (W), $\pi_2\pi_3^*$ (NV_1), and $\pi_1\pi_3^*$ (NV_2).[18,24–27] Except for the a_4 fragment (Fig. 3(f)), all sequence fragments presented in Fig. 3 result from cleavage of the C–N bond (b/y fragmentation). The most prominent structure in Fig. 3 is a band centered at the photon energy of about 6.9 eV. The latter band can be ascribed to the peptide $\pi_2\pi_3^*$ (NV_1) transition, most probably followed by a non-radiative decay to a vibrationally excited ground state resulting in C–N bond cleavages.[18] The second band centered at about 9.6 eV clearly appears for b_3 and y_2 sequence fragments (Figs. 3(b) and 3(e), respectively). It should correspond to the peptide $\pi_1\pi_3^*$ (NV_2) transition followed by either direct C–N type fragmentation from the electronically excited state or upon non-radiative decay to the hot ground state.[18] The increased yield above 9 eV of all other sequence fragments shown in Fig. 3 is also notable, although it should be noted that this effect is very weak for b_4 and a_4 fragments (Figs. 3(c) and 3(f), respectively) relative to the low-energy part. However, the second band is clearly distinguished only in the case of b_3 and y_2 fragments.

According to our knowledge, there is only one existing study on VUV action spectroscopy of gas-phase Leu-enk published by Bari *et al.*[6] to compare with. However, Bari et al. performed measurements at only few points in the energy region overlapping with the present measurements, which cannot provide insight into the excitation bands. Still, the trends of their reported Leu-enk sequence specific fragment photodissociation yields, in the energy region of 8-14 eV, are in good agreement with the present results. On the other hand, it is also interesting to compare the energy dependences of backbone dissociation for different peptides: Leu-enk (the present case) and Substance P.[18] Assuming that a peptide backbone can be generally described by a four-level electronic system, as discussed above, one would expect at least some corresponding spectroscopic features (related to photon absorption by the backbone). Indeed, the a-ion yield in the previous study for Substance P[18] clearly showed a band centered at about 6.8 eV that is very well comparable with the

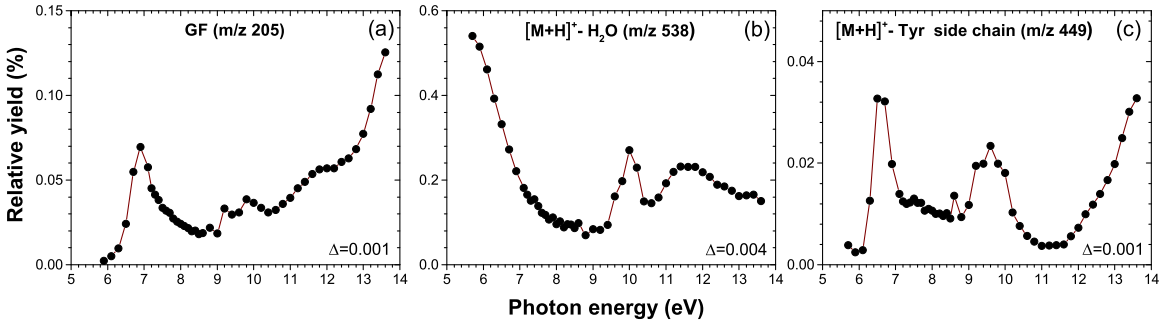

FIG. 4. Normalized relative ion yields from the photodissociation of precursor $[Leu\text{-}Enk+H]^+$ in the range from 5.9 to 14 eV. Integrated mass ranges are: (a) GF (m/z = 203.5-204.5), (b) $[M+H]^+$-H_2O (m/z = 537.5-538.5) and (c) $[M+H]^+$-tyrosine side chain (m/z = 448.5-449.5).

present a_4-ion yield (Fig. 3(f)). The additional higher-energy structures are also visible for *a*-ions, as well as *x*, *b* and *y* ions in the previous study[18] above 8 eV and peaking somewhere between 10 and 12 eV. The latter features may correspond to the present band at about 9.6 eV as well as broad features found for *b* and *y* fragments above 10 eV. However, it is interesting that in the previous study of Substance P, *b* fragments appear only above about 8 eV, while in the present case of protonated Leu-enk, there is a very strong band for *b* fragments at the energy of 6.9 eV, as found for the *a* fragment. Moreover, even in the case of *a* and *y* fragments of Substance P, where the first 6.9 eV band can be clearly resolved, its intensity is still considerably inferior to the signal above 8 eV. In contrast, for Leu-enk, the band at 6.9 eV represents a dominant feature for most of the *b* and *y* fragments in the spectra and particularly for the a_4 fragment. In a previous study, González-Magaña *et al.*[28] have reported an effect of the peptide chain length on the fragmentation patterns. Short peptides bearing up to 7 residues appeared to have a different behavior than the longer one (with 12 residues), which was assigned to charge migration following the photoionization. In the present case, we also observe a very different photochemistry below the ionization threshold for Leu-Enk (5 residues) with respect to Substance P (11 residues).

Figs. 3(a)–3(c) (blue curves—in the first raw) present VUV photodissociation yields of *b* fragments (cleavage of C–N bond with charge left on N-terminus). The latter offer an exciting insight into the energy dependence of the cleavage of the peptide linkage as a function of its site along the Leu-enk peptide backbone. Since all *b* yields correspond to the same C–N bond cleavage, their different energy dependences steam from different VUV absorption efficiency, which correspond to the change of the electronic density of the biopolymer along its backbone. Indeed, (a)-(c) show that the relative ion yields strongly depend on the position of the C–N bond cleavage on the peptide. Clearly, by approaching the C-terminus (and increasing the fragment size), the low-energy part of the action spectra becomes more important. Particularly, the low-energy absorption at about 6.9 eV, assigned to NV_1 electronic transition, appears to be weak for b_2 fragment (Fig. 3(a)) relative to the fragmentation intensity at photon energies above 8 eV, which is very similar to the previous case found for Substance P. However, already for b_3 fragment (Fig. 3(b)), the 6.9 eV band is very strong. Moreover, for b_4 fragment (Fig. 3(c)), the photodissociation yield still increases with decreasing the photon energy below 6 eV suggesting that peptide dissociation to b_4 may be triggered even by the lowest energy $n_0\pi_3^*$ (*W*) transition previously suggested to be at about 5.5 eV.[18] VUV photodissociation to *b* and *y*-type fragments of protonated Substance P has not been observed below 6 eV, although it was reported for *a*-type fragments. Still, it is interesting to note that the present b_2 relative photodissociation yield corresponds very well to the measured energy dependences for small neutral losses; for example, $-H_2O$ in the present case of protonated Leu-enk (Fig. 4(b)) or $-NH_3$ in the previously investigated Substance P.[18] Significant differences in relative photodissociation yields corresponding to the same bond cleavage along the peptide backbone suggest a strong influence of the protonation site on the frontier peptide orbitals and a redistribution of the electronic density along the peptide backbone upon protonation.

The present results also offer a possibility to compare the photodissociation yields of different fragments that are directly produced by the cleavage of the same bond (see Fig. 1). In Fig. 3, we compare the yields of b_2 (a) and y_3 (d), as well as of b_3 (b) and y_2 (e). A pair of fragments produced by the same bond scission is expected to have similar photodissociation yields, which is indeed shown in Fig. 3 for b_2/y_3 and b_3/y_2. Still, it is interesting that in both cases *y* fragments appear to have somewhat higher relative intensity at lower photon energies. The other notable difference is a strong increase of b_3 fragment yield above 11 eV (Fig. 3(b)), which is not seen for the corresponding y_2 fragment (Fig. 3(e)). It has been already noted above that b_3 (m/z 278) cannot be resolved from the doubly charged precursor $[M+H]^{2+}$, which should strongly increase above the IE. However, the doubly charged precursor may not survive until detection. Finally, for both pairs of b/y fragments, the abundance of *b* fragments is much higher over the whole photon energy range, which is expected since N-terminus should represent the preferential protonation site of the gas-phase protonated Leu-enk.[29]

In the last column of Fig. 3, we compare the photodissociation yields of fragments produced by cleavage of neighboring bonds from the same carboxyl C atom (see Fig. 1), and with the charge left at the N-terminus; namely, b_4 (Fig. 3(c)) is produced by a C–N cleavage and a_4 (Fig. 3(f)) is produced by a C_α–C cleavage. Clearly, in both cases, fragmentation into these ionic species dominantly occurs at low photon energies. The formation of the latter fragments is preferentially triggered by $\pi\pi^*$ electronic transitions. Both dissociation yields show a strong band at about 6.9 eV as well as an increased yield at photon energies between 9 and 10.5 eV. The a_4 fragment is significantly more abundant at low energies and its action spectrum shows a strong absorption band centered at about 6.9 eV, which is typically seen for most of the other fragments. However, interestingly, the C_α–C bond cleavage producing a_4 does not seem to be important below 6 eV in contrast to the cleavage of closely situated C–N bond producing b_4.

Besides sequence specific fragments, we also study the energy dependence of the formation of fragments involving breaking of multiple bonds and neutral losses. In Fig. 4, we compare photodissociation yields of the fragment GF (m/z 205) with the fragments produced by the loss of the water molecule (m/z 538) and the tyrosine side chain (m/z 449). According to the previous study, the formation of GF fragment is not associated with substantial rearrangements of the system and proceeds along an entropically favored pathway.[30] Furthermore, it has been suggested according to the same surface-induced dissociation study[30] that the GF fragment was formed from y_3 (mainly) and a_4 fragments. Therefore, one would expect that significant formation of GF can already occur at lower VUV photon energies below the IE and that the relative photodissociation yield of GF (Fig. 4(a)) is similar to the yields of y_3 (Fig. 3(d)) and a_4 (Fig. 3(f)). Indeed, the dominant feature of GF yield appears at about 6.9 eV (assigned above to NV_1), as found for y_3

and particularly for a_4. Also, as for y_3 and a_4, additional features can be seen between 9 and 10.5 eV (assigned to NV_2). However, it is interesting to note that, in contrast to y_3 and a_4, the yield of GF strongly increases above the IE. We can therefore tentatively explain the depletion of b, y and a fragments at higher photon energies as being due to increased formation of other internal fragments. In this particular case, for example, GF represents a favored channel at higher photon energies. Note that this domination is even more pronounced with the further increase of the photon energy above 14 eV.[31]

The loss of the water molecule from protonated Leu-enk has been detected as a relatively strong fragmentation channel upon both CID[15] and surface-induced dissociation,[30] but this process was not discussed in detail. Moreover, in the previous study of VUV photodissociation of protonated Leu-enk by Bari *et al.*,[11] the fragment formed upon the loss of water was above the m/z cutoff presented by the authors. Therefore, according to our knowledge, we report for the first time the energy dependence of VUV-induced loss of water from protonated Leu-enk peptide. Interestingly, the present study shows (Fig. 4(b)) that $-H_2O$ photodissociation yield appears to be markedly different at low photon energies from the yields of other neutral losses (Fig. 4(c)), internal fragment GF (Fig. 4(a)) and sequence fragments (Fig. 3), except for the b_4 fragment yield for which the curve also shows an intense abundance at low photon energy, well below the 6.9 eV band. Therefore, we can tentatively assume that loss of water can proceed from the lowest $n_0\pi_3^*$ (W) peptide excitation, similarly as for b_4 fragment. Note that b_4 fragment is formed by the cleavage of the C–N bond close to the C–terminal of Leu-enk, so in close vicinity to a carboxyl group, which could be the site from where the water molecule is extracted. It should be noted that a similar strong increase of the yield towards low photon energies has been seen for a small methionine residue loss (−15) in the previous study with Substance P;[18] however, methionine absorbs at rather low energies in contrast to carbonyl chromophores.

The loss of tyrosine side chain has been already studied before[11] but with large energy steps. The present results discover a rich spectroscopic structure corresponding to protonated Leu-enk dissociation to this fragment. Two bands are clearly resolved at about 6.9 eV and 9.8 eV. With this respect, the spectrum is comparable with b and y sequence fragments (Fig. 3), suggesting that loss of Tyr side chain can be triggered by backbone photon absorption. The spectrum is similar to most of the neutral losses from Sub P.

IV. CONCLUSION

We presented a detailed study on energy dependent fragmentation of protonated Leu-enk peptide in the VUV photon domain from 5.7 eV (217.5 nm) to 14 eV (88.56 nm) with unprecedented spectral details, owing to the very small steps between the photon energies. The fragment ion yields exhibit rich features which have been assigned to the lowest energy excited states. The most prominent structure appeared at the photon energy of about 6.9 eV. The latter band is ascribed to the peptide $\pi_2\pi_3^*$ ($NV1$) transition. The fragmentation pattern at low photon energy is similar to that produced under CID excitation conditions. Thus, based on this argument, we propose that the photofragmentation below the threshold proceeds on the hot ground electronic state after internal conversion. However, we have also found significant differences between relative photodissociation yields that correspond to the cleavage of the C–N bond along the peptide backbone. Moreover, interestingly, the photochemical behavior of protonated Leu-enk is very different from the one reported recently for substance P. This observation is in line with previous investigations on the length effects on VUV fragmentation of peptides.[28] Although the origin of such differences is not yet explained and requires further work, it clearly appears that the photochemical and photophysical properties of small peptides cannot be simply extended and serve as a model to longer systems such as bigger peptides and proteins. Indeed, there is a strong interplay between the length of a biopolymer and its electronic structure.

ACKNOWLEDGMENTS

This work was supported by the Agence Nationale de la Recherche, France, under Project No. ANR-08-BLAN-0065. M.Lj.R. and A.R.M. acknowledge support by the Ministry of Education, Science and Technological Development of Republic of Serbia under Project No. 171020. The Notre Dame Radiation Laboratory is supported by the U.S. Department of Energy Office of Science, Office of Basic Energy Sciences under Award No. DE-FC02-04ER15533 (this is Document No. NDRL 5093). We thank the general staff of the SOLEIL synchrotron radiation facility for running the beam smoothly and for providing beamtime under Project No. 20131031.

[1]C. B. Anfinsen, Science **181**, 223 (1973).
[2]O. Plekan, V. Feyer, R. Richter, M. Coreno, M. De Simone, K. C. Prince, and V. Carravetta, J. Phys. Chem. A **111**, 10998 (2007).
[3]F. Gaie-Levrel, G. a Garcia, M. Schwell, and L. Nahon, Phys. Chem. Chem. Phys. **13**, 7024 (2011).
[4]M. Tia, B. Cunha de miranda, S. Daly, F. Gaie-Levrel, G. A. Garcia, L. Nahon, and I. Powis, J. Phys. Chem. A **118**, 2765 (2014).
[5]K. R. Wilson, M. Jimenez-Cruz, C. Nicolas, L. Belau, S. R. Leone, and M. Ahmed, J. Phys. Chem. A **110**, 2106 (2006).
[6]M. Schwell and M. Hochlaf, Top. Curr. Chem. **355**, 155 (2015).
[7]L. Belau, K. R. Wilson, S. R. Leone, and M. Ahmed, J. Phys. Chem. A **111**, 7562 (2007).
[8]E. Pluhařová, P. Slavíček, and P. Jungwirth, Acc. Chem. Res. **48**, 1209 (2015).
[9]J.-W. Ho, H.-C. Yen, H.-Q. Shi, L.-H. Cheng, C.-N. Weng, W.-K. Chou, C.-C. Chiu, and P.-Y. Cheng, Angew. Chem., Int. Ed. **54**, 14772 (2015).
[10]A. R. Milosavljević, C. Nicolas, J. Lemaire, C. Dehon, R. Thissen, J.-M. Bizau, M. Réfrégiers, L. Nahon, and A. Giuliani, Phys. Chem. Chem. Phys. **13**, 15432 (2011).
[11]S. Bari, O. Gonzalez-Magaña, G. Reitsma, J. Werner, S. Schippers, R. Hoekstra, and T. Schlathölter, J. Chem. Phys. **134**, 024314 (2011).
[12]A. Giuliani, A. R. Milosavljević, F. Canon, and L. Nahon, Mass Spectrom. Rev. **33**, 424 (2014).
[13]C. Brunet, R. Antoine, A.-R. Allouche, P. Dugourd, F. Canon, A. Giuliani, and L. Nahon, J. Phys. Chem. A **115**, 8933 (2011).
[14]P. Kebarle and U. H. Verkerk, Mass Spectrom. Rev. **28**, 898 (2009).
[15]K. V. Judit sztáray, A. Memboeuf, and L. Drahos, Mass Spectrom. Rev. **30**, 298 (2011).
[16]A. R. Milosavljević, V. Z. Cerovski, F. Canon, L. Nahon, and A. Giuliani, Angew. Chem., Int. Ed. Engl. **52**, 7286 (2013).
[17]A. R. Milosavljević, V. Z. Cerovski, M. Lj. Ranković, F. Canon, L. Nahon, and A. Giuliani, Eur. Phys. J. D **68**, 68 (2014).
[18]F. Canon, A. R. Milosavljevic, L. Nahon, and A. Giuliani, Phys. Chem. Chem. Phys. **17**, 25725 (2015).

[19]A. R. Milosavljević, C. Nicolas, J.-F. Gil, F. Canon, M. Réfrégiers, L. Nahon, and A. Giuliani, J. Synchrotron Radiat. **19**, 174 (2012).
[20]L. Nahon, N. de Oliveira, G. a Garcia, J.-F. Gil, B. Pilette, O. Marcouillé, B. Lagarde, and F. Polack, J. Synchrotron Radiat. **19**, 508 (2012).
[21]A. R. Milosavljević, C. Nicolas, J.-F. Gil, F. Canon, M. Réfrégiers, L. Nahon, and A. Giuliani, Nucl. Instrum. Methods Phys. Res., Sect. B **279**, 34 (2012).
[22]K. Biemann, Methods Enzymol. **193**, 455 (1990).
[23]P. Roepstorff and J. Fohlman, Biomed. Mass Spectrom. **11**, 601 (1984).
[24]L. Serrano-Andrés and M. P. Fülscher, J. Am. Chem. Soc. **118**, 12190 (1996).
[25]L. Serrano-Andrés and M. P. Fülscher, J. Am. Chem. Soc. **118**, 12200 (1996).
[26]L. Serrano-Andrés and M. P. Fülscher, J. Am. Chem. Soc. **120**, 10912 (1998).
[27]L. Serrano-Andrés and M. P. Fülscher, J. Phys. Chem. B **105**, 9323 (2001).
[28]O. González-Magaña, G. Reitsma, S. Bari, R. Hoekstra, and T. Schlathölter, Phys. Chem. Chem. Phys. **14**, 4351 (2012).
[29]N. C. Polfer, J. Oomens, S. Suhai, and B. Paizs, J. Am. Chem. Soc. **129**, 5887 (2007).
[30]J. Laskin, J. Phys. Chem. A **110**, 8554 (2006).
[31]M. Lj. Ranković, F. Canon, L. Nahon, A. Giuliani, and A. R. Milosavljević, J. Phys.: Conf. Ser. **635**, 012034 (2015).

Nuclear Instruments and Methods in Physics Research B xxx (2014) xxx–xxx

Contents lists available at ScienceDirect

Nuclear Instruments and Methods in Physics Research B

journal homepage: www.elsevier.com/locate/nimb

Study of electron transmission through a platinum tube

A.R. Milosavljević [a,*], M.Lj. Ranković [a], D. Borka [b], J.B. Maljković [a], R.J. Bereczky [c], B.P. Marinković [a], K. Tőkési [c]

[a] Institute of Physics Belgrade, University of Belgrade, Pregrevica 118, 11080 Belgrade, Serbia
[b] Vinča Institute of Nuclear Sciences, University of Belgrade, P.O. Box 522, 11001 Belgrade, Serbia
[c] Institute for Nuclear Research, Hungarian Academy of Sciences, H-4001 Debrecen, Hungary

ARTICLE INFO

Article history:
Received 18 July 2014
Received in revised form 21 November 2014
Accepted 26 November 2014
Available online xxxx

Keywords:
Electrons
Transmission
Platinum capillary

ABSTRACT

We have measured 200 eV electron transmission through a single platinum tube of a diameter of 3.3 mm. We find that the transmission of electrons can be detected even at large tilt angles, where the tube is not transparent geometrically. The transmission drops down exponentially with increasing the tilt angle. The energy spectrum of detected electrons behind the tube contain contributions at lower energies due to both inelastic scattering and secondary electron emission. The spectrum is qualitatively in good agreement with the calculations performed for the flat Pt surface in order to understand and model the electron interaction processes that define the transmission and the energy spectrum at the exit.

1. Introduction

There has been a large interest in recent years to investigate transmission of low-energy electrons (up to 1 keV) through nano(-micro) capillaries made of insulating materials. This investigation was triggered by the highly charge ions (HCI) *guiding* phenomenon, which was first discovered by Stolterfoht and coauthors in 2002 [1]. The HCI guiding is well explained presently and is based on the fact that the beam of charged particles dynamically deposits charge on the inner capillary surface, thus forming a Coulomb field that deflects the forthcoming particles (preventing close interaction with the surface) and efficiently guides them towards the capillary exit. A large number of papers have been published so far on this phenomenon, which offers possibilities both to study fundamental particle–surface interaction processes and to develop interesting applications such as HCI beam for nanometer-scale fabrication and MeV proton microbeams for irradiating single cells [2,3]. A comprehensive review on the subject can be found in the recent paper by Lemell et al. [4].

The first studies on electron guiding through insulating capillaries have been reported in 2007 [5,6], and followed by more detailed investigations [7–9]. The electron transmission through the capillaries appears to be fundamentally different from the simple picture of HCI guiding governed solely by Coulomb deflection [8,9]. Beside the Coulomb interaction that can also exist (although not necessary repulsive, but rather attractive due to the secondary electron emission [9]), electrons can be both elastically and inelastically scattered upon close interaction with the surface (primary projectiles) and can produce secondary electrons. Note also that electrons cannot change their charge state (in contrast to HCI), therefore it is impossible to distinguish between original and scattered projectiles. Moreover, since the dominant process upon electron transmission may be elastic electron–surface scattering, it has been suggested that even metallic (conductive) capillaries may be used for the electron guiding [8]. Following this idea, we have recently started an investigation on electron transmission through single metallic capillaries. The aim of the research is to learn about fundamental properties of both the electron guiding by metallic capillaries and the processes of electron–surface interaction that define guiding properties, as well as to investigate possible applications.

In the present paper, we report the study on the transmission of 200 eV incident electrons through a single Pt macrocapillary (3.3 mm diameter and 40.8 mm length – the aspect ratio of about 12.4). A large-diameter tube has been used, therefore the obtained results can be tested and analyzed according to the calculations made for the electron scattering by a flat Pt surface (which is more trivial), whereas the tube aspect ratio is large enough to test electron transmission at large tilt angles. The intensity of the outgoing electron current has been measured as a function of both the incident beam angle with respect to the capillary axis (the tilt angle) and the kinetic energy of outgoing electrons.

* Corresponding author.
E-mail address: vraz@ipb.ac.rs (A.R. Milosavljević).

http://dx.doi.org/10.1016/j.nimb.2014.11.087
0168-583X/

2. Experiment

The experiment has been performed at the Institute of Physics Belgrade. The experimental system has been already described in detail elsewhere [5,7]. Additional small modifications have been made for the present study. A schematic view of the experimental setup is given in Fig. 1(a).

The system consists of an electron gun, a Pt tube attached to a 4-electrode electrostatic lens, a double cylindrical mirror analyzer (DCMA) followed by a single channel multiplier (channeltron) and a Faraday cup. Fig. 1(b) shows the realistic model of the Pt tube fitted in the 4-electrode lens, as well as electric field distributions for typically used electrode voltages, made in SIMION program [10]. Note that a penetration of the electric field inside the Pt tube, thus possible influence to electron transmission, is negligible.

The electron gun produces a well collimated electron beam with an energy spread of about 0.5 eV, which is directed into a Pt tube of 3.3 mm diameter and 40.8 mm length (the aspect ratio of about 12.4). The angle between the incident electron beam direction and the tube axis, referred as the tilt angle, can be adjusted by rotating the electron gun. At the tilt angle of 90°, the electron beam is directed into the Faraday cup, which is attached to an X–Y manipulator allowing the measuring of both the incident electron current intensity and the beam profile. The characteristic parameters of the electron beam – the diameter and the pencil angle (divergence) – are retrieved according to the simulated profile (for the identical geometry) where these parameters are adjusted to have the best fit to the experimental points. Fig. 1(c) shows a typical beam profile measured at 200 eV and the corresponding simulated curve obtained with a diameter of 0.9 mm and a divergence of 0.3°. Therefore, the incident electron beam is very well collimated and enters the Pt tube without losses.

The energy of electrons escaping the backside of the tube was analyzed using the DCMA working in a constant pass-energy mode – therefore, the count rates were recorded as a function of the retarding potential (V_R in Fig. 1(a)). It should be noted that this mode of operation provides a constant overall energy resolution, which was about 1 eV (full width at half maximum-FWHM), as measured in the elastic peak. However, the transmission of the entrance 4-electrode lens depends on the retarding potential. Therefore, the recorded kinetic electron energy distributions were corrected according to the transmission function estimated by electron ray-tracing simulations made in SIMION program [10]. The base pressure in the experimental chamber was about 7×10^{-7} mbar.

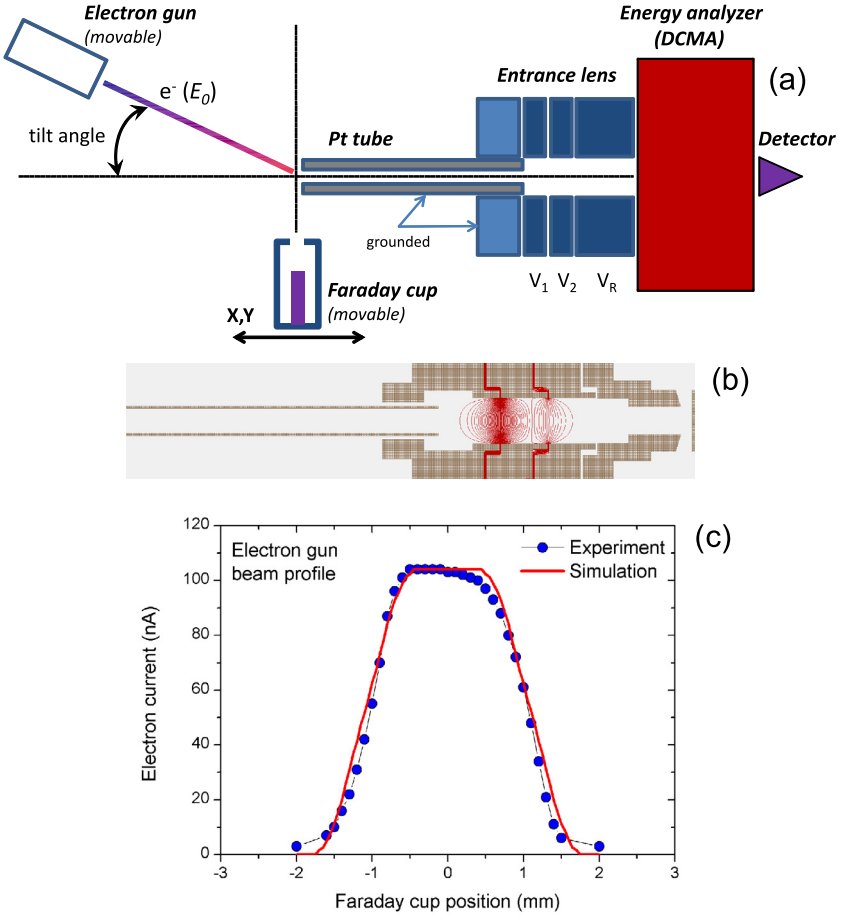

Fig. 1. (a) Experimental setup used in the present work. Electrons produced by the rotatable electron gun are directed into a Pt tube. Electrons escaping the tube are energy-analyzed. The intensity of the incident electron current and the electron beam profile are measured by using a movable Faraday cup with an entrance hole of 2 mm. (b) The realistic model of the Pt tube fitted in the 4-electrode lens made in SIMION program. The distribution of the electric field for electrode potentials typically used in the experiment are shown by red lines. (c) The 200 eV electron beam profile measured by the Faraday cup (blue circles) and the corresponding SIMION simulation (red line) obtained with the parameters: diameter = 0.9 mm; pencil angle = 0.3°. (For interpretation of the references to color in this figure legend, the reader is referred to the web version of this article.)

Please cite this article in press as: A.R. Milosavljević et al., Study of electron transmission through a platinum tube, Nucl. Instr. Meth. B (2014), http://dx.doi.org/10.1016/j.nimb.2014.11.087

3. Electron–surface scattering calculations

We also present calculated kinetic energy spectra of 200 eV electrons scattered from a flat Pt surface. Calculation is performed using Monte Carlo Simulation (MCS) of low energy electrons backscattered from platinum (Pt) surface [11]. In this simulation we take into account both elastic and inelastic collisions. For elastic collisions of electrons by Pt atoms, we use static field approximation with non-relativistic Schrödinger partial wave analysis [12].

For the case of inelastic scattering we use a dielectric response formalism [13–16]. According to the dielectric theory, a dielectric function $\epsilon(q,\omega)$ describes the response of a medium, as an assembly of interacting electrons and atoms, to the disturbance from an external point charge. The dielectric function $\epsilon(q,\omega)$ is the momentum (q) and energy (ω) dependent. The energy loss function $Im(-1/\epsilon(q,\omega))$, determines the probability of such an event. For the case of bulk material the energy loss function is given by the relation $Im(-1/\epsilon(q,\omega))$ and in the case of a surface it is given by the relation $Im(-1/(\epsilon(q,\omega)+1))$. For low energies, like in the present case, it is more convenient to use the surface energy loss function. The dielectric function for Pt is obtained from Refs [17,18].

We have performed MCS and calculated the backscattered electron energy loss distributions for primary and secondary electrons. Details about calculation can be found in papers [11,19] and in references there in.

4. Results and discussion

Fig. 2(a) presents a typical dependence of the detected count rate of the electrons escaping the Pt tube without an energy loss on the tilt angle. In order to avoid a saturation of the channeltron at small tilt angles, the incident current intensity was reduced to below 1 nA (such low electron currents were not measurable with the present setup). The measurements show a very narrow angular distribution of the detected electron current, which practically corresponds to the primary electron beam. Note that the aspect ratio of the Pt tube defines the maximum acceptance angle of 4.6°. Therefore, the measured angular distribution presented in Fig. 2(a) is also influenced by the electrostatic field (i.e. the focal properties of the lens – in the present case, the focus was on the elastic channel), as well as the transmission of the whole analyzer system, including the 4-element entrance lens, the double cylindrical mirror analyzer and a 3-element lens placed at the exit (see [20] for details).

Clearly, at low incident electron currents only the direct beam is detected, therefore the scattered (guided) electrons cannot be measured and studied. Still the measurements presented in Fig. 2(a) are important for the adjustment of the incident electron beam profile and the calibration of the angular scale.

In order to test a possibility of electrons being directed along the capillary axis due to the close interaction with the inner walls, as well as to measure the kinetic energy distribution of scattered electrons, the electron gun was positioned at large tilt angles and the incident electron current was increased to about 100 nA (as measured in the Faraday cup – see Fig. 1(b)). Fig. 2(b) presents a kinetic energy distribution of electrons escaping the tube at the incident energies or with small energy losses (up to about 8 eV). Clearly, the elastic peak can be detected even at very large tilt angles above the maximum value of 4.6° as defined by the tube aspect ratio. As expected, the intensity of the transmitted (guided) electron current strongly decreases with increasing the tilt angle; the dependence is practically exponential (see the inset in Fig. 2(b)). Since the incident beam direction is far from the capillary acceptance angle, the measured signal of electrons escaping the capillary at incident energies (200 eV) must be due to the elastic

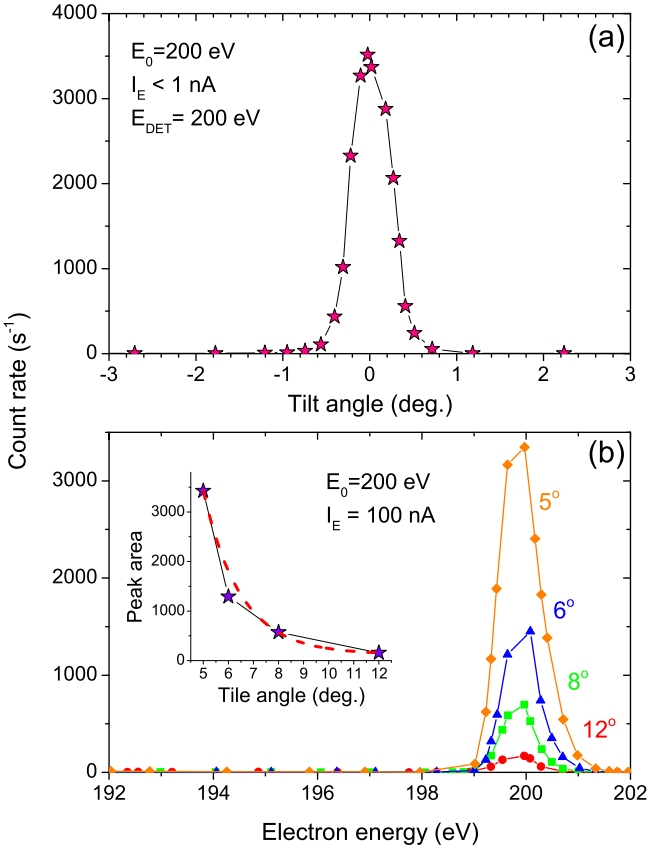

Fig. 2. (a) The intensity of the electron current escaping the Pt tube at the energy of 200 eV, as a function of the tilt angle, for the incident electron energy of 200 eV and the incident electron current intensity lower than 1 nA. (b) Experimentally obtained kinetic energy spectra of electrons escaping the Pt tube, for the incident electron energy of 200 eV, the incident electron current intensity of 100 nA and the tilt angles of 5 (diamonds), 6 (triangles), 8 (squares) and 12 (circles) degrees. The inset shows the area of the peaks presented in (b), in the energy domain from 198 to 202 eV, as a function of the tilt angle The red curve represents the exponential decay fit to the experimental points. (For interpretation of the references to color in this figure legend, the reader is referred to the web version of this article.)

electron scattering from the Pt capillary surface, thus enabling the transmission along the axis.

The close electron interaction with the inner Pt surface should also lead to both inelastic scattering and secondary electrons emission. Therefore, in contrast to the HCI guiding by insulating capillaries provided by Columbic mirror, a very broad kinetic energy distribution of escaping electrons is expected. A typical distribution obtained at the tilt angle of 6°and with the incident electron energy of 200 eV, is presented in Fig. 3(a), in a broad energy domain down to 50 eV. Apart from the sharp elastic peak that corresponds to the dominant fraction of the transmitted electrons, there is a large number of electrons at lower energies.

Fig. 3(b) shows the calculated kinetic energy distribution of electrons upon scattering of 200 eV incident electron beam from a plane Pt surface at an angle of 6°(it should be noted that the calculated distribution is not strongly dependent on the incident beam angle). The theoretical curves also separately present the yield of both the primary (due to elastic and inelastic scattering) and the secondary electrons, down to the energy of 80 eV. The experimental results are compared with the calculations by normalizing the measured curve at the energy of 185 eV. There is a good qualitative agreement between the theory and the experiment, particularly in the energy domain down to about 170 eV. Moreover, the constant increase of the secondary electrons yield as their energy decreases is also in agreement with the trend found

Please cite this article in press as: A.R. Milosavljević et al., Study of electron transmission through a platinum tube, Nucl. Instr. Meth. B (2014), http://dx.doi.org/10.1016/j.nimb.2014.11.087

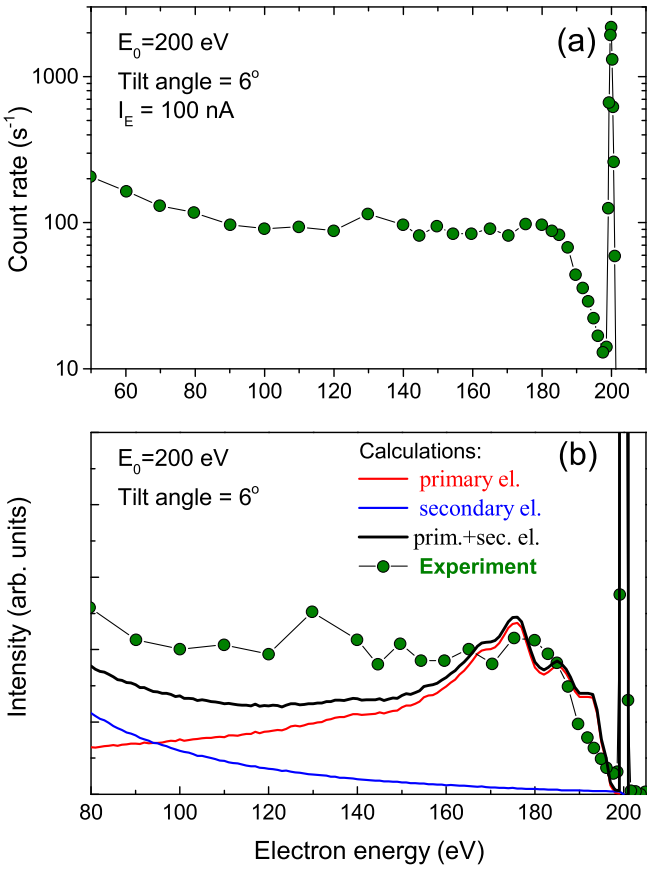

Fig. 3. (a) Experimentally obtained kinetic energy spectrum of electrons escaping the Pt tube, for the incident electron energy of 200 eV, the incident electron current intensity of 100 nA and the tilt angle 6°. (b) Calculated kinetic energy spectra of electrons scattered from a flat Pt surface, for the incident electron energy of 200 eV and the scattering angle of 6°. The experimentally obtained kinetic energy spectrum of electrons escaping the Pt tube, for the incident electron energy of 200 eV is normalized at 185 eV.

in the experiment. However, the calculated curve appears to be more structured, with pronounced shoulders, which cannot be resolved in the measured electron energy spectrum. Also, although both energy distributions are characterized by a pronounced elastic peak, the inelastic/elastic ratios are different.

The disagreement between the calculated and the measured spectra can be due to several reasons. The calculations were performed for a flat surface (to the best of our knowledge, there are no experimental results for a flat Pt surface), while in the experiment the electrons interact with the capillary surface and can suffer multiple scattering events before reaching the capillary exit and being detected. Therefore, this multiple scattering (including inelastic scattering of inelastically scattered projectiles) can smear out the respective structures seen in the theoretical spectrum. Furthermore, although the experimental spectrum has been corrected for the transmission function, the real transmission may be somewhat different from the calculated one that is based on an ideal uniform beam leaving the Pt tube and takes into account only the entrance electrostatic lens. It should be also taken into account that, in contrast to the theoretical case, the Pt surface in the experiment may be polluted from the adsorbed residual gas in the vacuum chamber. Finally, there is also an uncertainty of the calculated spectrum, dominantly because we have used a dielectric function for Pt that has been obtained by fitting the experimental results. It has been found in the present work that the calculated energy spectra were sensitive to the applied dielectric functions. However, overall, there is a good accordance between the experiment and the calculations, suggesting that the theory can be used to predict and select good candidates as materials to be used for electron transport by metallic capillaries.

5. Conclusion

In summary, we have presented a joint experimental and theoretical study on 200 eV electron transmission through a single platinum tube. We find that the transmission of electrons at their incident energies can be detected even at large tilt angles, where the tube is not transparent geometrically. The transmission drops down exponentially with increasing the tilt angle. The energy spectrum of detected electrons behind the tube contain contributions at lower energies due to both inelastic scattering and secondary electron emission. The spectrum is qualitatively in good agreement with the calculations performed for the flat Pt surface in order to understand and model the electron interaction process that define the transmission and the energy spectrum at the exit.

Although more studies with micro and nano capillaries should be performed, the present results suggest a possibility of using metallic capillaries to investigate fundamental properties of a conductive material inside a high aspect ratio pores, by use of the electron spectroscopy under ultra-high vacuum conditions. Moreover, there are potentials for interesting applications, such as the use of nano and micro high-aspect ratio metallic capillaries as a robust, spatially well-determined low-energy electron source/transporter. This could be applied, for example, to study electron driven molecular processes under different environmental conditions.

Acknowledgments

The work was supported by the Ministry of education, science and technological development of Republic of Serbia under the Grants OI 171020 and 45005, by the Hungarian SRF OTKA No. NN 103279, and by the Bilateral Cooperation Program between the Hungarian and Serbian Academies. This work was conducted within the framework of the COST Action CM1301 (CELINA).

References

[1] N. Stolterfoht, J.-H. Bremer, V. Hoffmann, R. Hellhammer, D. Fink, A. Petrov, B. Sulik, Phys. Rev. Lett. 88 (2002) 133201.
[2] T. Ikeda, Y. Kanai, T.M. Kojima, Y. Iwai, T. Kambara, Y. Yamazaki, M. Hoshino, T. Nebiki, T. Narusawa, Appl. Phys. Lett. 89 (2006) 163502.
[3] T. Ikeda, T.M. Kojima, T. Kobayashi, W. Meissl, V. Mckel, Y. Kanai, Y. Yamazaki, J. Phys. Conf. Ser. 399 (2012) 012007.
[4] C. Lemell, J. Burgdörfer, F. Aumayr, Prog. Surf. Sci. 88 (2013) 237.
[5] A.R. Milosavlević, Gy. Víkor, Z.D. Pešić, P. Kolarž, D. Šević, B.P. Marinković, S. Mátéfli-Tempfli, M. Mátéfli-Tempfli, L. Piraux, Phys. Rev. A 75 (2007) 030901(R).
[6] S. Das, B.S. Dassanayake, M. Winkworth, J.L. Baran, N. Stolterfoht, J.A. Tanis, Phys. Rev. A 76 (2007) 042716.
[7] A.R. Milosavlević, J. Jureta, Gy. Víkor, Z.D. Pešić, D. Šević, M. Mátéfli-Tempfli, S. Mátéfli-Tempfli, B.P. Marinković, Europhys. Lett. 86 (2009) 23001.
[8] K. Schiessl, K. Tőkési, B. Solleder, C. Lemell, J. Burgdörfer, Phys. Rev. Lett. 102 (2009) 163201.
[9] A.R. Milosavljević, K. Schiessl, C. Lemell, K. Tokési, M. Mátéfli-Tempfli, S. Mátéfli-Tempfli, B.P. Marinković, J. Burgdörfer, Nucl. Instr. Meth. B 279 (2012) 190.
[10] D.J. Manura, D.A. Dahl, SIMION Version 8.0, User Manual, Scientific Instruments Services, Inc., 2007.
[11] Z.-J. Ding, R. Shimizu, Surf. Sci. 222 (1989) 313.
[12] F. Salvat, R. Mayol, Comput. Phys. Commun. 74 (1993) 358.
[13] D. Pines, Elementary Excitations in Solids, Benjamin, New York, 1964. p. 127.
[14] H. Ritchie, Phys. Rev. 106 (5) (1957) 874.
[15] H. Ritchie, A.L. Marusak, Surf. Sci. 4 (1966) 234.
[16] F. Salvat-Pujol, W.S.M. Werner, Surf. Interface Anal. 45 (2013) 873.
[17] W.S.M. Werner, K. Glantschnig, C. Ambrosch-Draxl, J. Phys. Chem. Ref. Data 38 (4) (2009).
[18] W.S.M. Werner, private comunications.
[19] Z.-J. Ding (Ph.D. thesis), Osaka University, 1990.
[20] A.R. Milosavljević, S. Madžunkov, D. Šević, I. Čadež, B.P. Marinković, J. Phys. B: At. Mol. Opt. Phys. 39 (2006) 609.

Eur. Phys. J. D (2017) 71: 32
DOI: 10.1140/epjd/e2016-70608-4

THE EUROPEAN PHYSICAL JOURNAL D

Regular Article

A novel setup for the determination of absolute cross sections for low-energy electron induced strand breaks in oligonucleotides – The effect of the radiosensitizer 5-fluorouracil*

Jenny Rackwitz[1], Miloš Lj. Ranković[2], Aleksandar R. Milosavljević[2,3], and Ilko Bald[1,4,a]

[1] Institute of Chemistry – Physical Chemistry, University of Potsdam, Karl-Liebknecht-Str. 24-25, 14476 Potsdam, Germany
[2] SOLEIL, l'Orme des Merisiers, St. Aubin, BP 48, 91192 Gif-sur-Yvette Cedex, France
[3] Institute of Physics Belgrade, University of Belgrade, Pregrevica 118, 11080 Belgrade, Serbia
[4] Department 1 – Analytical Chemistry and Reference Materials, BAM Federal Institute of Materials Research and Testing, Richard-Willstätter Str. 11, 12489 Berlin, Germany

Received 30 September 2016 / Received in final form 20 December 2016
Published online 14 February 2017 –

Abstract. Low-energy electrons (LEEs) play an important role in DNA radiation damage. Here we present a method to quantify LEE induced strand breakage in well-defined oligonucleotide single strands in terms of absolute cross sections. An LEE irradiation setup covering electron energies <500 eV is constructed and optimized to irradiate DNA origami triangles carrying well-defined oligonucleotide target strands. Measurements are presented for 10.0 and 5.5 eV for different oligonucleotide targets. The determination of absolute strand break cross sections is performed by atomic force microscopy analysis. An accurate fluence determination ensures small margins of error of the determined absolute single strand break cross sections σ_{SSB}. In this way, the influence of sequence modification with the radiosensitive 5-Fluorouracil (^{5F}U) is studied using an absolute and relative data analysis. We demonstrate an increase in the strand break yields of ^{5F}U containing oligonucleotides by a factor of 1.5 to 1.6 compared with non-modified oligonucleotide sequences when irradiated with 10 eV electrons.

1 Introduction

In cancer treatment by high energy radiation the simulation of dose distributions in patients is required to optimize the irradiation modalities [1]. These simulations must be based on the underlying fundamental physical processes in the interaction of high energy quanta with biological material [2]. This requires an accurate quantification of DNA radiation damage in terms of absolute cross sections for specific processes such as radiation induced DNA single and double strand breaks (SSBs and DSBs, respectively). Along the ionization track of high energy radiation secondary particles such as low-energy electrons (LEEs) and hydroxyl radicals are generated in copious amounts [3,4]. LEEs having an energy of roughly below 12 eV are able to induce DNA strand breaks by dissociative electron attachment (DEA) [5,6]. The electron then occupies a formerly unoccupied molecular orbital (MO) generating a transient negative ion (TNI), which is unstable towards autodetachment and dissociation [6]. Bond cleavage by DEA proceeds with high efficiency, i.e. high cross sections and often with pronounced site selectivity [7–9]. On the one hand research performed in the last couple of years on small model compounds focused on the question of where the excess charge is initially located and which specific bond cleavages finally lead to base losses and strand breaks [10,11]. In the condensed phase LEE induced strand breaks have mainly been studied using plasmid DNA. Since the early experiments by Boudaiffa et al. [5] in 2000 the LEE induced SSBs and DSBs have been studied by different groups, however, resulting in slightly different resonance profiles [12,13]. Effective cross sections for SSBs and DSBs have been determined by Boudaiffa et al. at electron energies of 10–50 eV [14] and by Panajotovic et al. in the energy regime 0.1–4.7 eV [15]. The determination of *absolute* strand break cross sections requires more sophisticated models such as the molecular survival model [16]. In general the determination of strand breaks induced by low-energy radiation in plasmid DNA is error-prone since the results depend on DNA film thickness and morphology, which is strongly influenced by experimental parameters [17–19]. Another draw-back of using plasmid DNA is the limited possibility to study the influence of DNA sequence and secondary structure on the strand breakage. Several novel experimental strategies have been proposed to study LEE

* Contribution to the Topical Issue "Low-Energy Interactions related to Atmospheric and Extreme Conditions", edited by S. Ptasinska, M. Smialek-Telega, A. Milosavljevic, B. Sivaraman.

[a] e-mail: bald@uni-potsdam.de

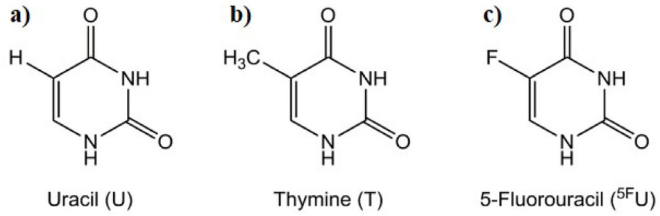

Fig. 1. Chemical structures of (a) the RNA nucleobase uracil; (b) the DNA nucleobase thymine and c) the radiosensitizer 5-fluorouracil (^{5F}U).

induced DNA damage in oligonucleotides including analysis by HPLC [20], surface-enhanced Raman scattering (SERS) [21,22], and the application of DNA microarrays and fluorescence spectroscopy as a read-out [23,24]. However, in all these approaches the quantification of DNA damage is limited to relative values. Recently, oligonucleotide target structures have been arranged on DNA origami nanostructures, which are analyzed by atomic force microscopy (AFM) after exposure to LEEs [25–27] or VUV photons [28]. The advantage of this method is that absolute strand break cross sections are readily accessible and that multiple sequences can be studied in a single irradiation experiment [27]. Furthermore, the target sequences can be freely chosen and even their secondary structure can be controlled in some way [29,30]. The control over the sequence enables the study of the modification of LEE induced strand break cross sections by radiosensitizers used in cancer radiation therapy [31,32].

In the present work we describe in detail the experimental setup used for LEE irradiation of oligonucleotides arranged on DNA origami substrates. We explore how absolute strand break cross sections can be determined using a reference sequence placed on the DNA origami substrate. Additionally, we study the effect of fluorinated nucleobase analogues on the strand break cross section after 10 eV electron irradiation. In particular, we focus on the radiosensitizer 5-fluorouracil (^{5F}U), which is a fluorinated derivative of uracil (U) and thymine (T) (Fig. 1). LEE induced reactions in ^{5F}U have been previously studied both in the gas phase [33,34] and in the condensed phase [35]. However, no strand break cross sections have been reported up to now. Finally, we compare the absolute strand break cross sections found for ^{5F}U containing oligonucleotides with those determined for 2-fluoroadenine (^{2F}A) containing oligonucleotides, which have recently been shown to effectively enhance the strand break cross sections upon LEE irradiation [32].

2 Experimental setup

2.1 The general setup of the electron irradiator

The LEE irradiator is shown in Figure 2 and consists of a high-vacuum chamber housing an electron gun and a sample holder. A DN100 six-way cross with CF flanges is the central element of the high-vacuum chamber. The

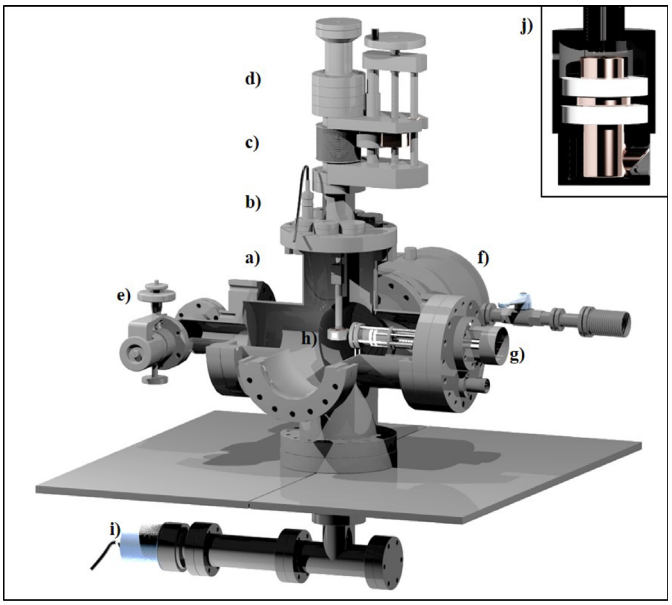

Fig. 2. 3D model of the setup with (a) the six-way cross, (b) the BNC feed through, (c) the z-translator, (d) the rotor, (e) the valve, (f) the turbomolecular pump, (g) the electron gun, (h) the sample stage, (i) the pressure gauge, and (j) the additional Faraday cup containing sample stage for beam characterization.

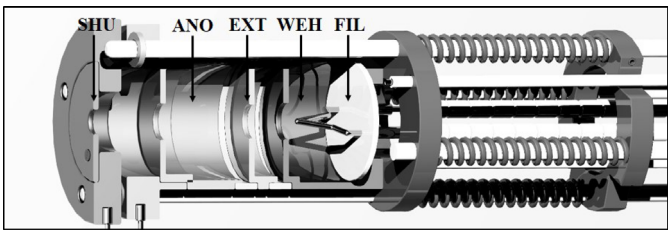

Fig. 3. 3D model of the electron gun with the filament FIL, the Wehnelt cylinder WEH, the electrostatic lens EXT between two ceramics, the modified electrostatic lens ANO, the ceramic spacer and the additionally implemented electrostatic lens SHU.

vacuum is generated by a turbomolecular pump (*Agilent* TwissTorr 304 FS) backed by a dual stage rotary vane pump (*Agilent* DS 102), resulting in a base pressure of 1.0×10^{-8} mbar. A full range combined pirani and inverted magnetron pressure gauge (*Agilent* FRG-700 CF35) measures the pressure inside the vacuum chamber and is attached at a remote position with respect to the electron gun to prevent the magnetic field disturbing the LEE beam. The electron gun (*Omnivac* FS100) is aligned horizontally at the six-way cross. A detailed illustration of the electron gun is shown in Figure 3. Thermal electrons are emitted from a tungsten hairpin filament (FIL) and collected by a Wehnelt cylinder (WEH). An aperture (EXT) in front of the Wehnelt cylinder extracts the electrons and accelerates them toward the sample. In order to defocus the beam, a low potential of around 1 V is applied to the next aperture (ANO). With decreasing kinetic energy the electrons are less focused. In result, fewer electrons reach

the sample and to keep the current at the sample constant, the voltage at ANO needs to be reduced. An additional aperture (SHU) is positioned in front of the electron flood gun serving as a shutter switching the electron beam on and off. If SHU is grounded, the electrons will pass the 4 mm diameter hole in the aperture. If a voltage of −14 V is applied, the beam will be totally defocused and no electrons will reach the sample.

The custom built sample stage is aligned vertically to the electron gun. It consists of an eight sided sample holder which is insulated from the chamber with a ceramic. The Si/SiO_2 substrates have a maximum size of 12×12 mm^2 and are fixed with conductive copper tape. The sample holder is electrically connected via a copper sliding contact (DN16 ring) and a BNC feed through with the picoamperemeter (*Keithley* 6485E). The electron current is measured in real-time during irradiation. The stage is positioned vertically with a z-translator over 50 mm travel distance and can be rotated by 360°.

For an accurate beam profile determination another sample stage was constructed. This stage is grounded on the outside along with the samples and contains an isolated faraday cup, held in position by two Teflon rings (Fig. 2j). An 8 mm diameter hole in the aluminum housing in front of the faraday cup allows to collect the complete electron beam. To determine the beam profile, a cover with a central hole of 1 mm diameter is attached to the sample stage. Since the sample stage is grounded, no real-time measurements during irradiation can be done in this configuration. Therefore, this stage is used only for beam characterization while the insulated stage is used for sample irradiation itself, since the electron current is in general not constant during irradiations.

A UHV dosage valve with gas inlet and sapphire seal (*Vacom* 11LVM-4016CF-MS-S) is used for slow venting to avoid decomposition of the DNA origami structures. It is connected to the main chamber by a DN40 T-flange, resulting in two 90° angles to create turbulences to avoid a pressure front hitting the sample surface. Additionally, the sample stage is moved up to the highest position during venting to take the sample out of the direct airflow.

2.2 Characterization of the electron beam

During the LEE irradiation of the DNA origami samples only a small electron current has been used to minimize sample charging [13]. At the same time the beam needs to be slightly defocused to increase the homogenously irradiated area. The following settings have been used: $I(\mathrm{FIL}) = 2.1$ A, $U(\mathrm{EXT}) = 65$ V and $U(\mathrm{ANO}) = 1.5$ V for 10 eV electron energy to defocus the electron beam.

Charging of the native SiO_2 layer on the silicon surface during the electron irradiation may result in an additional repulsive potential, slowing the approaching electrons down. To determine the surface charging, the origin of the electron energy scale and the electron energy distribution, the electron current has been recorded as a function of applied voltage around the current onset. Below 2.0 V no electrons passed the silicon surface, which defines the origin of the electron energy scale. The energy distribution can be obtained from the full width at half maximum (FWHM) of the gauss fit of the first derivative of the measured current, which is 1.2 ± 0.1 eV for the current setup.

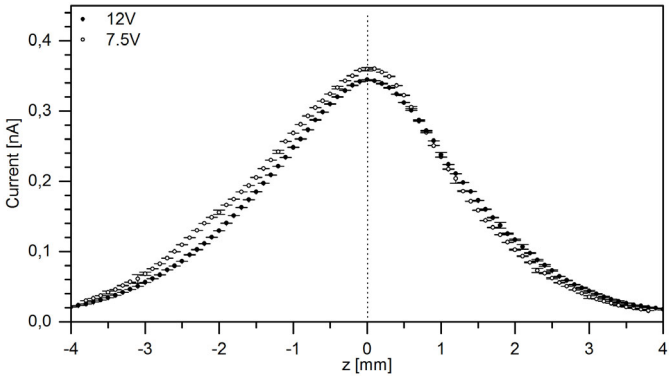

Fig. 4. Beam profile of two measurements with 12 V (•) and 7.5 V (○) ENG.

In order to accurately determine the strand break cross section the fluence needs to be determined at the position on the sample, on which AFM measurements are performed. The faraday cup has been used to determine the beam profile by moving it vertically through the beam at defined height increments of 0.2 mm. At each height position the current was measured and averaged over 15 s. The average and error of each current measurement was plotted as a function of the z coordinate to visualize the beam profile (Fig. 4). Here, $z = 0$ mm corresponds to a height position in which the faraday cup aperture is aligned with the axis of the electron gun. To account for aging of the filament, the beam profile was determined periodically.

2.3 Determination of the fluence

The fluence F is defined as the ratio of the total number of electrons N_e and the area of irradiation A (Eq. (1)). The number of electrons N_e is given by the time of irradiation t and the current I measured at the sample provided that no electrons are reflected from the surface

$$F = \frac{N_e}{A} = \frac{tI}{Ae}. \tag{1}$$

In real-time measurements during irradiation, the total current at the sample is measured. Thus, the area of irradiation A corresponds to the total area irradiated by the beam. According to the beam profile measurements the width of the beam profile is between 7 and 8 mm. Due to the Gaussian shape of the beam, more electrons reach the sample at the central region than at the outer regions. Therefore, if the fluence F is calculated with the total current I_{total} and the total area A_{total}, an average value for F results. The surface analysis is done using AFM images of 4×4 μm^2 size. Thus, even with several AFM images, only a small fraction out of the total irradiated area A_{total} can be analyzed in these single molecule studies.

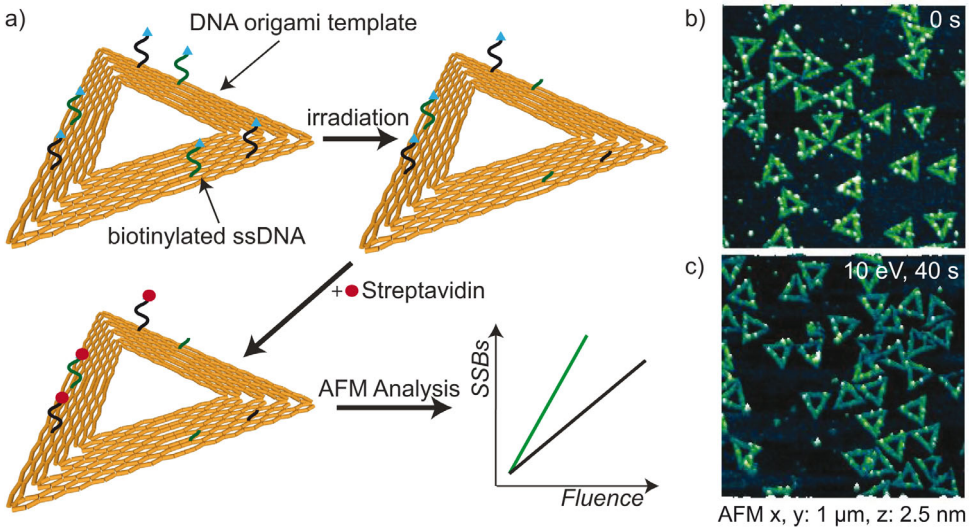

Fig. 5. (a) Scheme of the DNA origami structure and the experimental procedure. The DNA origami triangle consists of three trapezoids. On each trapezoid two different target sequences (one in the center (green) and one on the side (black)) are immobilized carrying a biotin (Bt) modification at its end. After irradiation some of the target sequences are broken due to LEE induced strand breakage. The samples are then incubated with streptavidin (SAv), which binds to the Bt modification of intact strands. The SAv can be easily identified in AFM images enabling the quantification of LEE induced strand breakage. (b) AFM image of a non-irradiated control sample. (c) AFM image of a sample irradiated with 10 eV electrons for 40 s.

Table 1. List of all modified sequences used during the experiments (Bt – biotin).

Protruding oligonucleotide sequence	Position on the DNA origami triangle (nomenclature according to Ref. [37])
5'-Bt-d(TT(ATA)$_3$TT)-3'	t7s8/18/28g
5'-Bt-d(TT(A^{5F}UA)$_3$TT)-3'	t1s8/18/28i
5'-Bt-d(TT(^{2F}AT^{2F}A)$_3$TT)-3'	t1s8/18/28i
5'-Bt-d(TT(^{5F}UT^{5F}U)$_3$TT)-3'	t-5s8/18/28g

Thus, it is necessary to precisely determine the fluence at the position of the AFM image within the beam profile. For this, the irradiated area is divided into constant sub areas A_i, for which the partial current I_i arriving on this area is determined [36]. The area A_i is small enough to assume that the fluence is homogeneous on A_i. The current I_i is determined from the beam profile using the Faraday cup as described above. By scanning the electron beam profile with the Faraday cup, a current percentage $I_{\%}$ has been determined for each sub area A_i: $I_{\%} = I_i/I_{total}$. The AFM measurements are performed in the center of the electron beam within a sub area corresponding to a circle with a diameter of 1.0 mm, for which the current percentage is $I_{\%} = 5.95\%$. This method allows for the direct calculation of the fluence at a certain sample subarea A_i from measured current values along the z-axis. Thus, no further theoretical models or fits are required.

The experiments were done with very short irradiation times of below 2 min, thus the beam profile can be assumed to be constant over this short time. With an electron gun warm-up period of exactly 30 min, the determined beam profile can be used for $I_{\%}$ calculation of the sub areas on the samples irradiated with identical conditions.

2.4 Preparation and irradiation of DNA origami structures

The DNA origami triangles are assembled according to the original protocol by Rothemund [37]. The circular single stranded genome m13mp18 with 7249 nucleotides is used as the scaffold. The viral strand is folded into the triangle pattern by a set of designed artificial staple strands. As shown in Figure 5 the triangle is formed from three trapezoids. The staple strands can be extended with a protruding DNA strand sequence representing the target sequence. Table 1 contains all protruding DNA strand sequences used in the experiments of this work. Since the DNA origami triangle has a symmetric geometry, the three trapezoids cannot be distinguished in the AFM images. On one trapezoid two protruding strands are attached. One strand is positioned in the center and one in the corner of the trapezoid, with a distance of 30 nm between both. The distance between these positions is sufficient to reliably distinguish both streptavidin (SAv) molecules at the end of the protruding strands in the AFM images. The asymmetric pattern is identical for all three trapezoids.

The modified target strands (Tab. 1) and unmodified staple strands are combined to a mixture containing

0.15 μL of each strand. Additionally, 5 μL of the viral DNA strand m13mp18 (100 nM in 10 mM Tris and 1 mM EDTA), 10 μL buffer (10 × TAE with 200 mM $MgCl_2$), and 41.65 μL deionized water are added to the solution. For annealing the prepared solution is heated up to 80 °C and cooled down stepwise over 2 h to 4 °C. Subsequently, the annealed DNA origami triangle solution is spin filtered two times with 300 μL 1 × TAE buffer containing 20 mM $MgCl_2$ with 6000 rpm for 5 minutes using 100 kDa molecular cutoff centrifugal filters (*Millipore*). The DNA origami containing filtrate is isolated and stored at 4 °C.

The silicon wafers are cut into 8 × 8 mm^2 pieces, marked with a central cross and cleaned with air plasma for 5 min, directly before DNA origami immobilization on the surface. From the freshly prepared DNA origami solution one drop of 0.8 μL is placed directly at the cross marker. To prevent drying effects, instantly afterwards 15 μL of 10 × TAE buffer with 200 mM $MgCl_2$ is added. The sample is incubated for 1 h at room temperature in an incubation chamber containing water to maintain high humidity to prevent drying. Subsequently, the sample is cleaned once with 1 mL of 1:1 deionized water/ethanol, and instantly placed in 10 mL ethanol for 1 h. Afterwards, the sample is dried with air and mounted on the sample stage for irradiation. The UHV chamber is evacuated slowly down to 10^{-3} mbar, before the turbomolecular pump is started. At a base pressure below 1.0×10^{-7} mbar the electron gun is switched on and warmed up for 30 min with 2.1 A filament current. Subsequently, the sample stage is positioned in the electron beam and the samples are irradiated for several seconds. Afterwards, the sample stage is lifted up, and the electron gun is switched off and cooled down for 1 h. The UHV chamber is vented slowly to atmospheric pressure using the dosage valve. The irradiated samples are removed from the sample stage and incubated with a 50 nM solution of SAv in 1 × TAE buffer with 20 mM $MgCl_2$. After 2 min of incubation the sample is rinsed with 0.5 mL 1:1 water/ethanol and dried with air.

2.5 AFM analysis

AFM imaging is performed with an *Agilent* 5500 instrument and Tap150-Al-G cantilevers by *Budget Sensors*. Using the top-view camera of the AFM, the images are taken at (300 ± 100) μm from the center of the marker, to coincide with the central circular area of 1 mm diameter, for which the fluence is calculated. At least one AFM image is taken in each quadrant separated by the cross marker with 4×4 μm image size, usually containing between 1000 and 2000 DNA origami structures.

Within each AFM image, all intact DNA origami triangles are analyzed. The number of intact strands is counted, corresponding to their position on the DNA origami. If all protruding strands are intact, three SAv molecules at the corners of the triangle and three SAv molecules at the central positions of the DNA origami trapezoids are visible. In case that one or more single strand breaks occur, the protruding strand is no longer labelled with biotin (Bt) and thus, no SAv can bind at the protruding strand. In result, the number of target strands on top of the origami will decrease. The number of strand breaks (N_{SB}) is calculated as

$$N_{SB} = \left(1 - \frac{\sum N_{SAv}}{3\ N_{Origami}}\right) \times 100 \tag{2}$$

with N_{SAv} being the number of still intact strands and $N_{Origami}$ being the number of analyzed DNA origami. N_{SB} is then plotted as a function of the fluence F.

3 Results and discussion

The absolute cross sections for strand breakage of oligonucleotides σ_{SSB} can be determined using two different methods. Initial values of σ_{SSB} need to be determined by recording the fluence dependence of strand breaks. In the following, this is referred to as the absolute method. By using an oligonucleotide sequence with known value of σ_{SSB} this sequence can be used as a reference, and the strand break cross section for another sequence can be determined relative to it. In the following, this is referred to as the relative method.

3.1 Absolute method

In the absolute method two different sequences are positioned on one DNA origami design. From AFM analysis, the number of strand breaks N_{SB} is determined as a function of fluence F:

$$N_{SB} = \sigma_{SSB} F + N_{SB0} \tag{3}$$

with N_{SB0} being the number of strand breaks without irradiation. For low fluences, the dose response curve is linear [5]. Thus, the absolute strand break cross section can be obtained from the instrumental weighted linear fit to the data. The resulting strand break cross section σ_{SSB} is then obtained from:

$$\sigma_{SSB} = (N_{SB} - N_{SB0})/F. \tag{4}$$

In a single irradiation experiment the strand break cross sections of at least two different sequences is obtained. A fluence dependency needs to be recorded, thus at least two different sample series are irradiated under identical conditions to prove repeatability. The total amount of samples irradiated with different fluence values has been at least ten samples to improve the accuracy of the determined absolute strand break cross sections. To reduce the number of irradiated samples, the relative method is applied by using one target sequence as a reference.

3.2 Relative method

The relative method allows to reduce the amount of samples which need to be irradiated to determine the strand

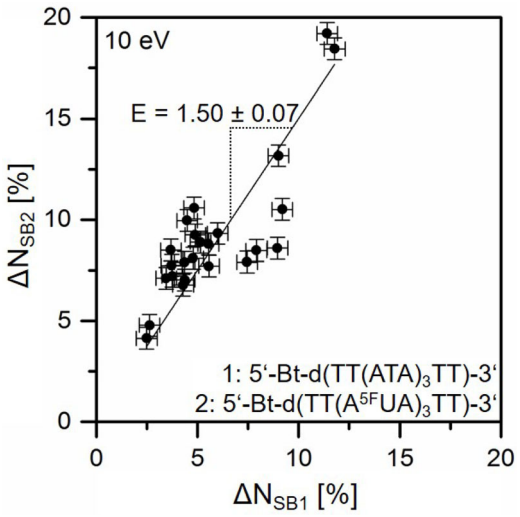

Fig. 6. Graphical correlation of the LEE induced strand breakage at 10 eV between the known 5'-Bt-d(TT(ATA)$_3$TT)-3' sequence and the unknown 5'-Bt-d(TT(A^{5F}UA)$_3$TT)-3' sequence, to determine the ratio E from the slope of the linear fit.

break cross section for a given sequence. A sequence with known σ_{SSB} at a certain energy is used as an internal reference. In combination with the reference sequence, the strand break cross section for an unknown sequence is determined. Both sequences are placed on one DNA origami and thus irradiated under identical conditions. The fluence F is therefore identical for both sequences:

$$(N_{SB} - N_{SB0})/\sigma_{SSB} = F = (N_{SB,ref} - N_{SB0,ref})/\sigma_{SSB,ref}. \quad (5)$$

The unknown strand break cross section σ_{SSB} can then be calculated based on the reference strand break cross section $\sigma_{SSB,ref}$:

$$\sigma_{SSB} = \sigma_{SSB,ref}\,(N_{SB} - N_{SB0})\,/\,(N_{SB,ref} - N_{SB0,ref}) = \sigma_{SSB,ref} E \quad (6)$$

with

$$E = (N_{SB} - N_{SB0})\,/\,(N_{SB,ref} - N_{SB0,ref}) = \Delta N_{SB}/\Delta N_{SB,ref}. \quad (7)$$

The value E is obtained as the slope of the plot of ΔN_{SB} against $\Delta N_{SB,ref}$ (Fig. 6). For this method, rather few samples are needed. To ensure reproducibility, at least three samples are irradiated. This method is independent of the fluence, as long as all irradiations are performed in the linear response regime. Thus, all samples have been irradiated with rather short times at low current. At very short irradiation times, the N_{SB} is very similar to N_{SB0}, resulting in stronger variations for E. Over all experiments, the error of E is quite small. Yet this error is added to the error of the reference strand break cross section $\sigma_{SSB,ref}$. Thus, it is useful to apply the absolute method to determine absolute strand break cross sections with an error around 10%. Then, the less time consuming relative method can be used for further strand break cross section determination for a variety of sequences.

The margin of error of the absolute strand break cross section is higher when the relative method is used, since the error of the reference sequence is taken into account as well. Yet compared to the error of the strand break cross sections obtained with the absolute method, the additional error through the relative method is rather small. This indicates that the error of the strand break cross section using the absolute method arises from fluence variations. These variations can occur through an off-center irradiation position and AFM images taken at different distances from the center of irradiation.

3.3 Biotin label for oligonucleotide visualization

Since in the above described experiments Bt is irradiated just like the oligonucleotide sequences, its stability towards 10 eV electrons over the analyzed fluence range needs to be confirmed. Therefore, only the Bt label was attached to the sequences 5'-Bt-t-1s4i-3', -t-1s14i and -t-1s24i on the DNA origami triangle and analyzed with the absolute method. With an obtained damage cross section of $(0.26 \pm 0.92) \times 10^{-15}$ cm^2 Bt remains stable with no detectable fragmentation at 10 eV up to a fluence of at least 10^{13} cm^{-2}.

3.4 Strand breaks in modified oligonucleotides

Previously, we have studied the radiosensitizing effect of ^{2F}A [32]. In the present work we have determined the absolute cross sections for single strand breakage upon irradiation with 10 eV electrons for oligonucleotides containing the radiosensitizer ^{5F}U using the relative method and reference sequences that have been analyzed previously using the absolute method [32].

The sequence 5'-Bt-d(TT(A^{5F}UA)$_3$TT)-3' has been irradiated together with the T containing 5'-Bt-d(TT(ATA)$_3$TT)-3' sequence with 10 eV electrons. The ratio E between the sequence containing ^{5F}U and the known reference sequence has been obtained from all ΔN_{SB} values as $E = 1.50 \pm 0.07$ (Fig. 6). This ratio was then multiplied with the absolute strand break cross section of the 5'-Bt-d(TT(ATA)$_3$TT)-3' sequence of $(0.80 \pm 0.12) \times 10^{-14}$ cm^2 [32], resulting in a strand break cross section of $(1.20 \pm 0.20) \times 10^{-14}$ cm^2 for the 5'-Bt-d(TT(A^{5F}UA)$_3$TT)-3' sequence.

To compare the radiosensitizing effect of both ^{5F}U and ^{2F}A, the nucleotide sequence of 5'-Bt-d(TT(^{2F}AT^{2F}A)$_3$TT)-3' at the center positions of the DNA origami triangle was combined with the ^{5F}U containing sequence 5'-Bt-d(TT(^{5F}UT^{5F}U)$_3$TT)-3' at the corner positions. In both sequences the amount of F containing nucleobases is identical with each modified nucleobase being flanked by T. The experiment yields a ratio $E = 0.98 \pm 0.03$, resulting in an absolute strand

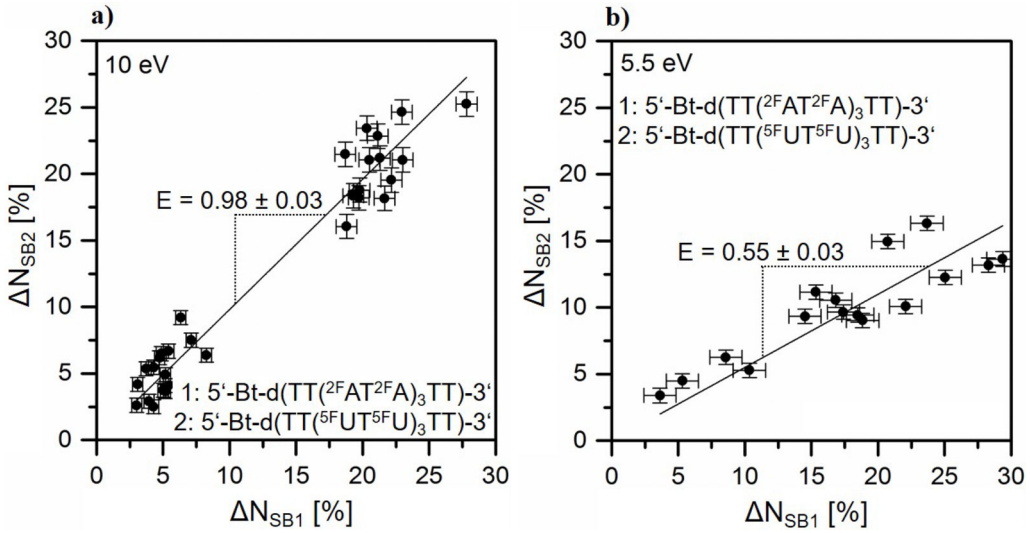

Fig. 7. Correlation between ΔN_{SB} values of the sequences 5'-Bt-d(TT(^{5F}UT^{5F}U)$_3$TT)-3' and 5'-Bt-d(TT(^{2F}AT^{2F}A)$_3$TT)-3' (a) at 10 eV and (b) at 5.5 eV. The x-axis corresponds to the reference sequences. The ratios E have been obtained from the slopes of the linear fits.

Table 2. Overview of the absolute strand break cross sections σ_{SSB} of the ^{2F}A and ^{5F}U containing oligonucleotides at 10 eV and 5.5 eV (results from Ref. [32] included).

5'-Bt-d(TTXTT)-3'	σ_{SSB} (at 10 eV)	σ_{SSB} (at 5.5 eV)
X = (ATA)$_3$	$(0.80 \pm 0.12) \times 10^{-14}$ cm^2	$(1.36 \pm 0.02) \times 10^{-14}$ cm^2
X = (^{2F}AT^{2F}A)$_3$	$(1.34 \pm 0.22) \times 10^{-14}$ cm^2	$(2.12 \pm 0.09) \times 10^{-14}$ cm^2
X = (^{5F}UT^{5F}U)$_3$	$(1.31 \pm 0.25) \times 10^{-14}$ cm^2	$(1.17 \pm 0.11) \times 10^{-14}$ cm^2
X = (A^{5F}UA)$_3$	$(1.20 \pm 0.20) \times 10^{-14}$ cm^2	
X = T$_8$	$(0.79 \pm 0.07) \times 10^{-14}$ cm^2	

break cross section of $(1.31 \pm 0.25) \times 10^{-14}$ cm^2 for 5'-Bt-d(TT(^{5F}UT^{5F}U)$_3$TT)-3', based on the strand break cross section for 5'-Bt-d(TT(^{2F}AT^{2F}A)$_3$TT)-3' of $(1.34 \pm 0.22) \times 10^{-14}$ cm^2 (Fig. 7a) [32].

The same DNA origami design with oligonucleotides containing ^{5F}U and ^{2F}A was also irradiated with 5.5 eV electrons, and analyzed with the relative method (Fig. 7b). Based on the strand break cross section for 5'-Bt-d(TT(^{2F}AT^{2F}A)$_3$TT)-3' of $(2.12 \pm 0.09) \times 10^{-14}$ cm^2 and a ratio $E = 0.55 \pm 0.03$ the absolute strand break cross section for 5'-Bt-d(TT(^{5F}UT^{5F}U)$_3$TT)-3' was determined to be $(1.17 \pm 0.11) \times 10^{-14}$ cm^2 (Fig. 7b).

All the obtained values of σ_{SSB} are summarized in Table 2 and compared in Figure 8. At 10 eV the absolute strand break cross section for 5'-Bt-d(TT(A^{5F}UA)$_3$TT)-3' is $(1.20 \pm 0.20) \times 10^{-14}$ cm^2 and thus only slightly below the strand break cross section for 5'-Bt-d(TT(^{5F}UT^{5F}U)$_3$TT)-3', which is $(1.31 \pm 0.25) \times 10^{-14}$ cm^2. Both strand break cross sections are identical within the margin of error. Thus, the sensitivity towards electrons of 10 eV energy is independent of the amount of ^{5F}U in the oligonucleotide and the neighboring nucleobases A or T in the oligonucleotide sequence. The latter observation is also supported by the comparison of 5'-Bt-d(TT(ATA)$_3$TT)-3' and 5'-Bt-d(T)$_{12}$-3' [32]. Within the margin of error, both sequences have identical strand break cross sections of (0.80 ± 0.12) and $(0.79 \pm 0.07) \times 10^{-14}$ cm^2, respectively. However, both aspects, the neighboring nucleobase A or T and the amount of ^{5F}U in the sequence (either 3 or 6 times), can have an opposite influence on the sensitivity of the sequence,

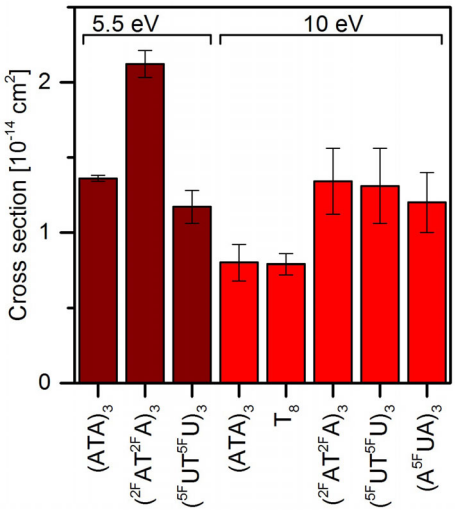

Fig. 8. Comparison of all obtained absolute strand break cross sections for the oligonucleotides 5'-Bt-d(TTXTT)-3', with X = (ATA)$_3$, T$_8$, (^{2F}AT^{2F}A)$_3$, (^{5F}UT^{5F}U)$_3$ and (A^{5F}UA)$_3$ at 5.5 eV and 10 eV.

resulting in an identical strand break cross section for both sequences 5'-Bt-d(TT(A^{5F}UA)$_3$TT)-3' and 5'-Bt-d(TT(^{5F}UT^{5F}U)$_3$TT)-3'. Although it is rather unlikely that these two very different aspects influence the strand break cross section with similar intensity in opposite directions, it is not utterly out of question.

At 10 eV, both sequences containing ^{5F}U showed an enhancement factor of 1.5 ± 0.1 and 1.6 ± 0.5, compared to 5'-Bt-d(TT(ATA)$_3$TT)-3'. Thus, both have similar sensitivities towards 10 eV electrons also compared to the ^{2F}A containing nucleotide. Therefore, it can be concluded, that the fluorination at the nucleobase is more important for the sensitivity than the type of the nucleobase itself. This is rather surprising since the fragmentation of the pyrimidine base ^{2F}A in DEA gas phase experiments is quite different from that of the purine base ^{5F}U [33,34]. In addition, none of them show relevant resonances around 10 eV. Yet both F containing nucleobases showed significant SSB enhancement in oligonucleotides. The higher electronegativity of F compared to H might draw electron density from the nucleobase, improving the antenna effect for the electrons and leading to DNA backbone decomposition by electron delocalization.

Comparing energies of 5.5 eV and 10 eV, no change in the strand break cross section of 5'-Bt-d(TT(^{5F}UT^{5F}U)$_3$TT)-3' is observed. The ratio of the respective strand break cross sections was calculated to be 0.9 ± 0.2. Thus, although significant resonances were observed for gas phase ^{5F}U around 5 eV and none at 10 eV [33,38], these fragmentations do not lead to an increase in strand breaks. This is in contrast to the ^{2F}A containing nucleotide, in which an increase of 1.6 ± 0.3 was obtained also at 5.5 eV [32].

4 Conclusion

We have assembled a LEE irradiation setup dedicated for the irradiation of oligonucleotides attached to DNA origami substrates. The setup and the experimental procedure are described in detail. A particular focus is put on an accurate determination of the fluence, which is critical for the quantification of DNA strand breaks. By AFM analysis of the irradiated samples the absolute cross sections for strand breakage (σ_{SSB}) can be determined for specific oligonucleotide sequences. We have compared different ^{5F}U containing oligonucleotides with their non-fluorinated analogues and with sequences containing ^{2F}A using two different electron energies (5.5 eV and 10 eV). The absolute strand break cross sections determined here are summarized in Figure 7. We find identical σ_{SSB} values (within the error bars) at 10 eV for the non-fluorinated sequences 5'-Bt-d(TT(ATA)$_3$TT)-3' and 5'-Bt-dT$_{12}$-3'. Compared to these sequences all fluorinated single strands show a similar enhancement of σ_{SSB} of 1.5–1.6 at 10 eV. The amount of ^{5F}U appears to have no significant influence on the strand break cross section, as similar values are obtained for the oligonucleotide containing three or six ^{5F}U molecules, respectively. At 5.5 eV the situation is slightly different compared to 10 eV: Both, 5'-Bt-d(TT(ATA)$_3$TT)-3' and 5'-Bt-d(TT(^{2F}AT^{2F}A)$_3$TT)-3' have clearly higher strand break cross sections at 5.5 eV than at 10 eV, whereas 5'-Bt-d(TT(^{5F}UT^{5F}U)$_3$TT)-3' shows even slightly lower values for σ_{SSB} at 5.5 eV than at 10 eV. This implicates that ^{2F}A should be a more effective radiosensitizer than ^{5F}U (which is routinely used in tumor radiation therapy) because ^{2F}A is more reactive towards LEEs within a wider range of electron energies.

This research was supported by the Federal Institute of Materials Research and Testing (BAM), a Marie-Curie FP7 Integration Grant within the 7th European Union Framework Programme, by the Deutsche Forschungsgemeinschaft (DFG) and the University of Potsdam. We acknowledge a bilateral grant between Serbia and Germany through the German Academic Exchange Service (DAAD, project No. 57055766) supported by the German Federal Ministry of Education and Research. M.Lj.R. and A.R.M. acknowledge support by the MESTD of Republic of Serbia under Project No. #171020.

References

1. D.W.O. Rogers, Phys. Med. Biol. **51**, R287 (2006)
2. L.H. Toburen, Int. J. Radiat. Biol. **88**, 2 (2012)
3. S.M. Pimblott, J.A. LaVerne, Radiat. Res. **150**, 159 (1998)
4. I. Baccarelli, I. Bald, F.A. Gianturco, E. Illenberger, J. Kopyra, Phys. Rep. **508**, 1 (2011)
5. B. Boudaiffa, P. Cloutier, D. Hunting, M.A. Huels, L. Sanche, Science **287**, 1658 (2000)
6. I. Bald, J. Langer, P. Tegeder, O. Ingólfsson, Int. J. Mass Spectrom. **277**, 4 (2008)
7. I. Bald, I. Dabkowska, E. Illenberger, O. Ingólfsson, Phys. Chem. Chem. Phys. **9**, 2983 (2007)
8. I. Bald, J. Kopyra, E. Illenberger, Angew. Chem. Int. Ed. **45**, 4851 (2006)
9. S. Ptasinska, S. Denifl, P. Scheier, E. Illenberger, T.D. Märk, Angew. Chem. Int. Ed. **44**, 6941 (2005)
10. I. Bald, I. Dabkowska, E. Illenberger, Angew. Chem. Int. Ed. **47**, 8518 (2008)
11. S. Ptasinska, S. Denifl, S. Gohlke, P. Scheier, E. Illenberger, T.D. Märk, Angew. Chem. Int. Ed. **45**, 1893 (2006)
12. Y. Chen, A. Aleksandrov, T.M. Orlando, Int. J. Mass Spectrom. **277**, 314 (2008)
13. S.V.K. Kumar, T. Pota, D. Peri, A.D. Dongre, B.J. Rao, J. Chem. Phys. **137**, 45101 (2012)
14. B. Boudaiffa, P. Cloutier, D. Hunting, M.A. Huels, L. Sanche, Radiat. Res. **157**, 227 (2002)
15. R. Panajotovic, F. Martin, P. Cloutier, D. Hunting L. Sanche, Radiat. Res. **165**, 452 (2006)
16. M. Rezaee, P. Cloutier, A.D. Bass, M. Michaud, D.J. Hunting, L. Sanche, Phys. Rev. E **86**, 31913 (2012)
17. M.A. Smiałek, S.A. Moore, N.J. Mason, D.E.G. Shuker, Radiat. Res. **172**, 529 (2009)
18. M.A. Smiałek, R. Balog, N.C. Jones, D. Field, N.J. Mason, Eur. Phys. J. D **60**, 31 (2010)
19. M.A. Smiałek, N.C. Jones, R. Balog, N.J. Mason, D. Field, Eur. Phys. J. D **62**, 197 (2011)

20. Z. Li, P. Cloutier, L. Sanche, J.R. Wagner, J. Am. Chem. Soc. **132**, 5422 (2010)
21. A.N. Sidorov, T.M. Orlando, J. Phys. Chem. Lett. **4**, 2328 (2013)
22. R. Schürmann, I. Bald, J. Phys. Chem. C **120**, 3001 (2016)
23. T. Solomun, C. Hultschig, E. Illenberger, Eur. Phys. J. D **35**, 437 (2005)
24. T. Solomun, H. Seitz, H. Sturm, J. Phys. Chem. B **113**, 11557 (2009)
25. A. Keller, I. Bald, A. Rotaru, E. Cauët, K.V. Gothelf, F. Besenbacher, ACS Nano **6**, 4392 (2012)
26. A. Keller, J. Kopyra, K.V. Gothelf, I. Bald, New J. Phys. **15**, 83045 (2013)
27. A. Keller, J. Rackwitz, E. Cauët, J. Liévin, T. Körzdörfer, A. Rotaru, K.V. Gothelf, F. Besenbacher, I. Bald, Sci. Rep. **4**, 7391 (2014)
28. S. Vogel, J. Rackwitz, R. Schürman, J. Prinz, A.R. Milosavljević, M. Réfrégiers, A. Giuliani, I. Bald, J. Phys. Chem. Lett. **6**, 4589 (2015)
29. I. Bald, A. Keller, Molecules **19**, 13803 (2014)
30. L. Olejko, P.J. Cywinski, I. Bald, Angew. Chem. Int. Ed. **54**, 673 (2015)
31. J. Kopyra, A. Keller, I. Bald, RSC Adv. **4**, 6825 (2014)
32. J. Rackwitz, J. Kopyra, I. Dąbkowska, K. Ebel, M.Lj. Ranković, A.R. Milosavljević, I. Bald, Angew. Chem. Int. Ed. Engl. **55**, 10248 (2016)
33. H. Abdoul-Carime, M.A. Huels, E. Illenberger, L. Sanche, Int. J. Mass Spectrom. **228**, 703 (2003)
34. R. Abouaf, H. Dunet, Eur. Phys. J. D **35**, 405 (2005)
35. P.-C. Dugal, H. Abdoul-Carime, L. Sanche, J. Phys. Chem. B **104**, 5610 (2000)
36. J. Rackwitz, *A novel approach to study low-energy electron-induced damage to DNA oligonucleotides. Influence of DNA sequence, topology and nucleobase modification* (Dissertation, University of Potsdam, 2016)
37. P.W.K. Rothemund, Nature **440**, 297 (2006)
38. G. Hanel, B. Gstir, S. Denifl, P. Scheier, M. Probst, B. Farizon, M. Farizon, E. Illenberger, T.D. Märk, Phys. Rev. Lett. **90**, 188104 (2003)

EPJ D
Atomic, Molecular, Optical and Plasma Physics
EPJ.org
your physics journal

Eur. Phys. J. D (2016) 70: 125 DOI: 10.1140/epjd/e2016-70108-7

Design and performance of an instrument for electron impact tandem mass spectrometry and action spectroscopy of mass/charge selected macromolecular ions stored in RF ion trap

Milos Lj. Ranković, Alexandre Giuliani and Aleksandar R. Milosavljević

edp sciences
Società Italiana di Fisica
Springer

Eur. Phys. J. D (2016) 70: 125
DOI: 10.1140/epjd/e2016-70108-7

THE EUROPEAN PHYSICAL JOURNAL D

Regular Article

Design and performance of an instrument for electron impact tandem mass spectrometry and action spectroscopy of mass/charge selected macromolecular ions stored in RF ion trap*

Milos Lj. Ranković[1], Alexandre Giuliani[2,3], and Aleksandar R. Milosavljević[1,2,4,a]

[1] Institute of Physics Belgrade, University of Belgrade, Pregrevica 118, 11080 Belgrade, Serbia
[2] SOLEIL, l'Orme des Merisiers, St Aubin, BP48, 91192 Gif sur Yvette Cedex, France
[3] INRA, UAR1008, CEPIA, Rue de la Géraudière, BP 71627, 44316 Nantes, France
[4] Radiation Laboratory, University of Notre Dame, Notre Dame, Indiana 46556, USA

Received 16 February 2016 / Received in final form 23 April 2016
Published online 2 June 2016 –

Abstract. A new apparatus was designed, coupling an electron gun with a linear quadrupole ion trap mass spectrometer, to perform m/z (mass over charge) selected ion activation by electron impact for tandem mass spectrometry and action spectroscopy. We present in detail electron tracing simulations of a 300 eV electron beam inside the ion trap, design of the mechanical parts, electron optics and electronic circuits used in the experiment. We also report examples of electron impact activation tandem mass spectra for Ubiquitin protein, Substance P and Melittin peptides, at incident electron energies in the range from 280 eV to 300 eV.

1 Introduction

The electron interaction with atoms and molecules in the gas phase has been studied for more than a century and has undergone several revivals [1]. Over the years, the electrons were used as a probe to reveal fundamental properties of atoms and molecules such as their electronic structure and chemical reactivity. The gas phase electron spectroscopy also discovered some important electron-collision phenomena such as low-energy resonances [2,3] and crucially helped to reach an intrinsic understanding of the complex electron-atom (molecule) collision processes, as well as their proper theoretical modeling [4]. Also, inner-shell electron spectroscopy of gas phase molecules found wide applications in different research fields [5].

In recent decades, however, the use of the gas-phase electron spectroscopy to investigate fundamental properties of matter has been challenged by the photon spectroscopy, due to the development of extremely bright photon sources with ultra-high energy resolution, such as lasers and accelerator based facilities (e.g. synchrotrons and free electron lasers). Still, a new wave of studies of electron interaction with isolated atoms and molecules was triggered at the beginning of the 21st century by a need to better understand the role of secondary electrons, intensively produced along the track of high-energy primary particles, in the radiation damage of biological material. Motivated by the finding that low-energy secondary electrons can induce resonant single and double strand breaks in a plasmid DNA film [6], a plethora of experimental studies on gas phase electron interaction with different relatively small molecules representing building blocks of biopolymers, have been performed [7]. The idea was to extrapolate the results of these studies to more complex systems and, hopefully, to reach a better understanding of electron-induced processes in the real biological environment. However, it is questionable to what extent this premise stands, which is also a point of a long-standing discussion within the scientific community. Clearly, there is a gap between the studies of electron interaction with small gaseous molecules performed under well-defined single-collision conditions and the processes in real biological systems. To bridge this gap, studies with isolated macromolecules and complex molecular systems are needed.

The development of experimental techniques for gas phase electron spectroscopy has faced a number of challenges. One of the earliest was the need for devices that allow for electron spectroscopy with high energy resolution, which leads to the development of different types

* Contribution to the Topical Issue "Advances in Positron and Electron Scattering", edited by Paulo Limao-Vieira, Gustavo Garcia, E. Krishnakumar, James Sullivan, Hajime Tanuma and Zoran Petrovic.

[a] e-mail: aleksandar.milosavljevic@synchrotron-soleil.fr

of energy selectors [8]. The other example is the development of magnetic angular changer that allows measurements of differential cross sections for electron scattering in the backward hemisphere [9]. Then, with growing interest in low-energy electron-induced processes, there was a need to develop methods to perform low-energy electron collision studies, down to practically 0 eV, with the high energy resolution, while preserving a high sensitivity (signal to noise ratio). In this respect, the work of Allan and Buckman are of profound interest for the field. They have developed, conducted, supervised or inspired measurements with an unprecedented combination of high electron energy resolution and sensitivity, and in the extended angular and energy ranges, allowing new insights into low-energy electron-induced processes and molecular properties (see [3,10–16] and references therein).

On the other hand, a permanent challenge in the field of gas phase electron spectroscopy was to increase the complexity of the targets. There has been a long-standing effort to perform gas phase single-collision studies of (bio)macromolecules, nanoparticles, clusters, solvated systems, radicals, ionic species and other exotic species. Several groups, including those of Allan and Buckman, made pioneering contributions in this respect. For example, Maddern et al. [17,18] and Brunton et al. [19,20] reported measurements of absolute differential cross sections (DCSs) for molecular radicals in the gas phase. Also, low-energy electron interaction and dissociative electron attachment (DEA) to highly reactive species and radicals has been investigated by Haughey et al. [21] and Field et al. [22]. There were also experiments with clusters and doped clusters [23–25] and references therein), as well as DEA to molecules brought into the gas phase by laser-induced acoustic desorption (LIAD) [26]. So far, electron interaction with small gaseous biomolecules has been extensively investigated [7,27]. For these studies, effusive target molecular beams under high vacuum were usually produced by using ovens. However, these sources are limited considering the size and complexity of the produced targets, since the target molecules may undergo thermal dissociation [28].

In 2010, Milosavljević et al. [29], followed by Bari et al. [30] in 2011, have reported experimental systems coupling a radio frequency (RF) ion trap, fitted with an electrospray ionization (ESI) source, with the synchrotron beamline, allowing VUV and X-ray gas-phase action spectroscopy of mass over charge (m/z) selected macromolecular ions stored in the ion trap [31–35]. By using ESI, large macromolecules (e.g. proteins) and complex systems (e.g. nanosolvated peptides) could be isolated in the ion trap in the desired charge state and studied using tandem mass spectrometry (MS^2) [36] and action spectroscopy [35,37]. Therefore, it would be of interest if such setup could also be used to study electron interaction with trapped macromolecular ions, in a wide range of electron energies. However, in contrast to photons, electrons are charged particles, thus affected by both DC and RF fields that provide ion trapping. Depending on the incident energy, an electron beam can be significantly disturbed even before reaching the target ion packet. Moreover, bouncing electrons in the ion trap produce noise, background ionization and could even be extracted towards ion detectors (composed of conversion dynodes and electron multipliers) and affect their performance. All these factors could drastically reduce signal to noise (s/n) ratio and even prevent measurements, thus discouraging any attempt of such experiments.

On the other hand, the mass spectrometry community has been developing for years methods for electron induced dissociation of large biopolymers by using electron capture dissociation (ECD) [38]. This technique is increasingly popular as an activation method in MS^2 for top-down protein sequencing [39]. Originally, electron activation techniques were performed in ion cyclotron resonance (ICR) traps, as the strong magnetic field used for these devices could also confine and guide low-energy (close to 0 eV) electrons into the ion trap. Nevertheless, in recent years, there is a large interest to develop devices that could provide ECD in RF ion traps, as well (see [40–43] and references therein). Also, Voinov and coworkers reported the implementation of a radio frequency-free analyzer independent cell [44] allowing ECD in triple quadrupole instruments. However, all these techniques are concerned with bringing electrons at energies close to 0 eV into an RF trap, providing efficient fragmentation of macromolecular ions via dissociative electron attachment.

We have recently reported a novel experimental system allowing electron activation of trapped macromolecular biopolymer ions stored in a linear RF ion trap, by using incident electron energies of several hundred of eVs [45]. We could record inner-shell electron activation MS^2 of multiply charged ubiquitin protein. Moreover, by measuring MS^2 spectra at different incident electron energies around the C K threshold, we could extract near-edge electron excitation function (NEEEF), that is, perform action inner-shell electron spectroscopy of a gas-phase m/z selected protein ion [45]. The later work also paves the way to action electron spectroscopy of isolated macromolecular species in a wide range of electron energies and the electron activation MS^2 for top-down protein sequencing. In the present paper, we describe in detail design and performance of this instrument [45] and present test measurements for different target molecular species. We also discuss possible future improvements, particularly regarding a decrease of the electron impact energy.

2 Design of the experimental setup

2.1 Electron tracing simulations

In order to assess the feasibility of focusing an electron beam on the trapped ion packet, without significant disturbance of beam properties due to the RF field, we have performed extensive electron tracing simulations by using the commercial program SIMION 8.2 [46]. The quadrupole linear ion trap that was used in our experiment is an integral part of the LTQ XL mass spectrometer (Thermo Scientific). A model of this trap made in the SIMION

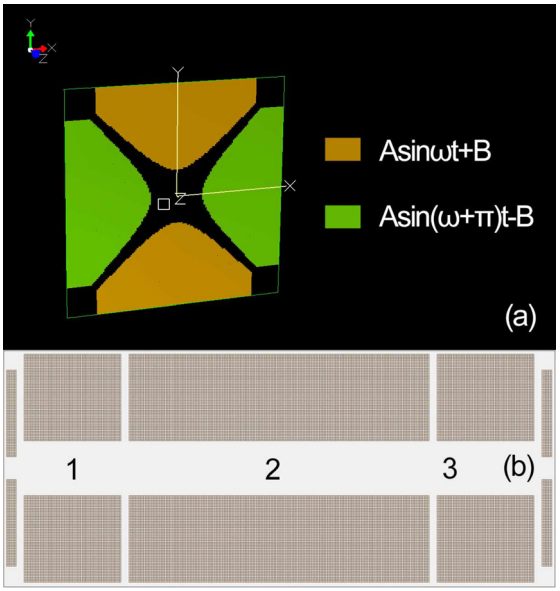

Fig. 1. Lateral (a) and longitudinal (b) cross sections of the model of a linear quadrupole ion trap made in SIMION. The ion trap comprises four hyperbolic electrodes of minimal radius of $r_0 = 4$ mm. RF voltage amplitude is $A = 400$ V, DC amplitude is $B = 100$ V and a circular frequency is $\omega = 2\pi \times 10^6$ Hz. The ion trap consists of three axial sections and two disc electrodes with a 2 mm aperture. DC voltages in Sections 1 and 3 are 10 V higher relative to the central Section 2, whereas potentials on disc electrodes are kept grounded.

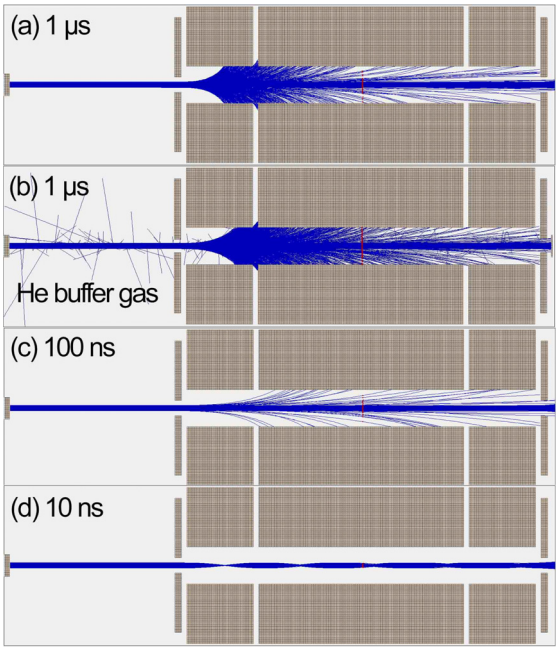

Fig. 2. Simulation of 300 eV pulsed electron beam in a linear quadrupole ion trap, for 400 V RF and 100 V DC, for three different pulse widths of: (a) 1 μs, (b) 1 μs with He buffer gas, (c) 100 ns and (d) 10 ns. The buffer gas was at the pressure of 5×10^{-3} mbar and temperature of 300 K, while the total electron-He interaction cross section of $\sigma = 5.56 \times 10^{-21}$ m^2 [47] was taken as the collisional cross section in the SIMION collisional hard-sphere model [46].

program is presented in Figure 1. It consists of four hyperbolic electrodes, divided into three sections in the axial direction. The ion trap is 68 mm long, 30 mm wide and has a minimal hyperbolic radius of 4 mm. Electrodes in all sections have both DC and RF voltages applied. The maximal amplitude of RF voltage is 400 V with a frequency of 1 MHz while maximal DC voltages are +100 V and –100 V in reference to the ground. Actual amplitudes of RF and DC voltages are the function of mass over charge (m/z) ratio of ions isolated in the trap and are usually lower. In order to estimate the highest possible perturbation of the electron beam, maximal values are used in the simulation. A polarity and a shape of DC and RF voltages through electrode sections is defined with equations displayed in Figure 1a. This configuration of voltages only enables radial ion trapping, but in order to obtain axial ion trapping as well, Section 2 has up to 10 V lower DC potentials relative to the DC potentials in Sections 1 and 3 (see Fig. 1b).

Simulations of 300 eV pulsed electron beam propagation inside the ion trap are presented in Figures 2 and 3, for three different Gaussian distribution pulse widths of 1 μs, 100 ns, and 10 ns. The electron current per pulse was 75 nA. The initial radius of the beam was 0.5 mm, with a uniform distribution of starting electrons. Electrons are generated on a disc at a 30 mm distance from the ion trap, with initial trajectories parallel to trap axis. Space charge effects of the electron beam were not included in the simulation. The space between the electrodes was assumed to be an absolute vacuum (Figs. 2a, 2c and 2d) occupied by time-dependent 3D electric field generated by the ion trap electrodes. We also performed a simulation where the surrounding of the ion trap as well as the region between the ion trap electrodes was filled with He buffer gas (Fig. 2b).

A full period of RF electric field is 1 μs, thus the simulation with the electron beam pulse width of 1 μs (Fig. 2a) effectively represents a continuous electron beam. The center of the Gaussian time distribution for electrons is set at 0.5 μs with respect to the RF sine wave. Even though electrons are highly scattered at the beginning of the trap, a significant percentage of around 65% manage to pass through the entire trap. Spatial and energy distributions of electrons at the half length of the trap are recorded and presented in Figure 3a. Although both distributions are clearly broadened in the middle of the trap, we could conclude that majority of electrons still have unperturbed energies corresponding to the initial one of 300 eV. Also, about 90% of electrons recorded at the center of the trap still have radial positions less than 0.5 mm, while the rest is scattered over the electrodes. Still, it should be noted that in the real experiment the ion trap is filled with He buffer gas at a pressure of about 10^{-3} mbar, in order to cool the ions and improve the trapping efficiency. Therefore, the buffer gas could in principle affect the transmission and the focusing of the electron beam. However, considering the low

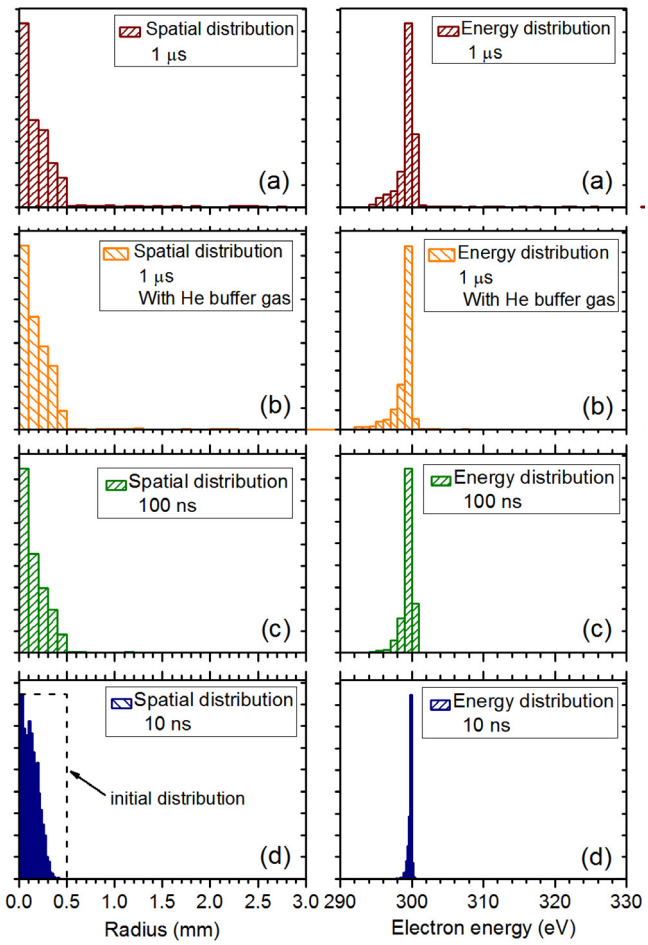

Fig. 3. Simulation of 300 eV pulsed electron beam in a linear quadrupole ion trap, for 400 V RF and 100 V DC, for three different pulse widths of: (a) 1 μs, (b) 1 μs with He buffer gas, (c) 100 ns and (d) 10 ns. Spatial (left column) and energy (right column) electron distributions were recorded at the center of ion trap. The buffer gas was at the pressure of 5×10^{-3} mbar and temperature of 300 K, while the total electron-He interaction cross section of $\sigma = 5.56 \times 10^{-21}$ m^2 [47] was taken as the collisional cross section in the SIMION collisional hard-sphere model [46].

total cross section for 300 eV electron interactions with He of 5.56×10^{-21} m^2 [47], as well as dominantly forward elastic scattering, this influence should not be significant. Figure 2b shows the SIMION electron tracing simulations that included a standard collisional hard-sphere model [46] for the ion trap filled with the gas at the pressure of 5×10^{-3} mbar, the temperature of 300 K, and taking the collision cross section in the model as the total electron-He interaction cross section of 5.56×10^{-21} m^2 [47]. The simulations show that the focal properties of the electron beam are still qualitatively well preserved, although the presence of the gas causes a slightly lower transmission of 62% compared to 65% obtained in the simulations performed in vacuum. The spatial and energy distributions depicted in Figure 3b are also very similar to those obtained without the buffer gas (Fig. 3a). It should be stressed that the used model is only an approximation, in order to obtain a qualitative picture. Indeed, in a real experiment, the electron-He interactions include both the elastic and inelastic (excitation and ionization) process, and should dynamically take into account the corresponding differential cross sections, which depend on the electron energy. Such simulations are rather complex and out of the scope of the present work. However, we can tentatively conclude that the presence of the He buffer gas at about 10^{-3} mbar dos not influence significantly the 300 eV electron beam propagation through the RF ion trap, which was also confirmed experimentally according to the signal to noise ratio in the action spectra.

Narrowing the electron pulse width to 100 ns and fine tuning of the center of the time distribution of starting electrons to 0.6 μs with respect to the RF sine wave, yields around 80% of the electron transmission through the trap, which can be seen in Figure 2c. The spatial and the electron energy distributions in Figure 3c are also broadened, but at lower extent compared to the previous case of 1 μs pulse width. Only a small number of electrons around is scattered towards the electrodes, whereas the rest pass through a full length of the trap with the transmission of about 80%.

The electron beam does not seem to be affected at all if the pulse widths are decreased down to an order of 10 ns, Figure 2d. The electron energy distribution presented in Figure 3d reveals relatively small broadening of 1–2 eV. It should be noted that the thermo-electron emission process introduces an energy spread of 0.5 eV to the initial electron beam in the real experiment. However, geometrical properties of the electron beam are almost unaffected. The spatial distribution is smeared out, resembling a bell like Gaussian shape. For comparison, the square profile for the uniform spatial distribution of the initial electrons is presented by dashed lines in Figure 3d (left side). The electron beam effectively falls into a spatial resonance and at a few points along the trap axis becomes compressed, yielding an even smaller beam radius then the initial one. However, for the pulse widths of this order of magnitudes, the synchronization of the pulse propagation with the RF field oscillation is crucial. According to our simulation, if this synchronization is shifted for more than $\pm$25 ns, the electron transmission is practically blocked.

To conclude, the SIMION simulations demonstrate that a pulsed electron beam, with a train of short pulses of the order of 10 ns synchronized with the trap RF field, would allow 100% transmission at 300 eV and even a very efficient electron transmission at lower electron energies. Unfortunately, such experimental conditions could not be obtained in the present work, so the electron beam appears as continues regarding the ion trap performance. Still, the electron tracing simulations also show that at the energy of about 300 eV, as used in the present measurements, both the spatial profile and the energy spread of the continuous electron beam are well preserved in the trap. Therefore, the pulsing procedure is used in the present experiment only to define the irradiation time and block the stream of electrons during the ion acquisition, as described below.

2.2 Timing procedure

The experiment is performed through several temporally spaced sequences. These sequences are: (1) ion production and selection; (2) ion activation by electrons; and (3) fragment detection. An electrospray ion source (ESI) is used to produce the molecular ionic targets of the interest. Through the system of ion optic lenses, comprised of octopole and quadrupole mass filters, ions are guided into the linear quadrupole ion trap from the front side. Precursor ions of the desired charge state are selected and stored in the trap. In order to increase the efficiency of the trapping, ion trap is filled with Helium buffer gas at the pressure of 10^{-3} mbar. Stored ions are then activated in collisions with the focused beam of electrons during a defined irradiation time. To be able to activate ions only for a desired period, the electron beam has to be switched on and off. Therefore, a pulsed mode of operation of the electron gun was required, instead of the standard continuous mode of operation where a steady stream of electrons is produced. To stop the electron emission from the hot cathode inside the electron gun, an electronic circuit called *shutter circuit* was designed (more details can be found in Sect. 2.5). This circuit was synchronized with the mass spectrometer by the use of transistor-transistor logic (TTL) signals, generated by the mass spectrometer. The length of the TTL signal is defined by the irradiation (activation) time, specified by the user in the mass spectrometer software.

Once the irradiation of ions has finished by stopping the electron beam, all ion products are ejected from both sides of the ion trap and detected in electron multiplier detectors. Between the actual ion detection and the end of the irradiation, a time window called *acquisition delay* is introduced. It enables fragmentation processes of contaminants that take place during the irradiation to reduce quickly. This in turn has the result of fairly reducing the noise and improving the signal to noise ratio of the instrument. The length of the acquisition delay is usually a fraction of the irradiation time and depends on a selected target. Practical realization of the acquisition delay was achieved by the inserting a delay generator in the path of a TTL signal line, before the shutter circuit. For each ion fragment detection, a tandem mass spectrum (MS^2) is recorded for a given selected precursor ion, at a defined electron energy. The entire process is then repeated for different electron energies until an *energy scan* is completed. The best mass resolution in the present experiment was about 5000, although it depends on the applied working mode of the LTQ XL spectrometer, to reach a satisfactory signal/noise ratio for the particular precursor.

2.3 Coupling the electron source with the LTQ XL mass spectrometer

In order to perform electron activation of the trapped ions, a custom made electron gun is coupled to the commercial linear ion trap mass spectrometer LTQ. Figure 4 presents a 3D model of the coupling of the electron gun with the LTQ XL.

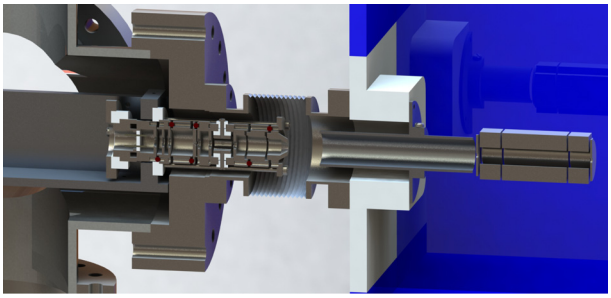

Fig. 4. 3D model of the experimental setup. The electron gun (on the left-hand side) is connected to the ion trap (on the right-hand side) by an edge welded bellows. The aluminum shielding is located in the middle.

The electron gun is fitted in a dedicated CF100 six-way cross vacuum chamber, rested on a rigid position tunable support and connected to the back plate of the LTQ XL through flexible bellows. The assembly with the electron gun was mounted on an L-shaped support attached to a custom made CF100 flange, with two CF16 electrical feed-through flanges on its back for electrical contacts (see Fig. 5b).

The remaining vacuum connections of the six-way CF100 cross were used to fit a turbo pump, a high vacuum cold-cathode gauge, and a glass window. The pressure gauge is connected via extended flexible bellows at about 1 m from the electron gun, to reduce the magnetic disturbance of the electron beam. The coupling of the six-way cross vacuum chamber with a Plexiglas window on the back side of the mass LTQ XL spectrometer was made through by using a reducer CF100-40 flange and a CF40 edge welded bellows. This flexible connection allows for precise alignment of the electron beam with respect to the ion trap axis.

2.4 Electron optics

The electron gun used in the present experiment has been designed at the Institute of Physics Belgrade [48]. It consists of six cylindrical electrodes and a thoriated-tungsten cathode. A 3D model of the electron gun is presented in Figure 6. It also comprises two pairs of cylindrical deflectors inside the S electrode (X-Y in Fig. 6), for fine adjustment of X and Y electron beam positions at the target plane. Electrons are produced through a thermo-electron emission process from a resistively heated hairpin cathode. The cathode potential is set to a negative voltage relative to the ground potential of the interaction region. This voltage, therefore, defines the incident electron energy. The energy resolution is defined by the temperature of the cathode, which yields an energy uncertainty of about 0.5 eV for the initial electron beam.

In the present experiment, cathode is heated by 2.3 A, from a high power external DC source. At maximally rated heating currents close to 3.5 A, it can produce electron

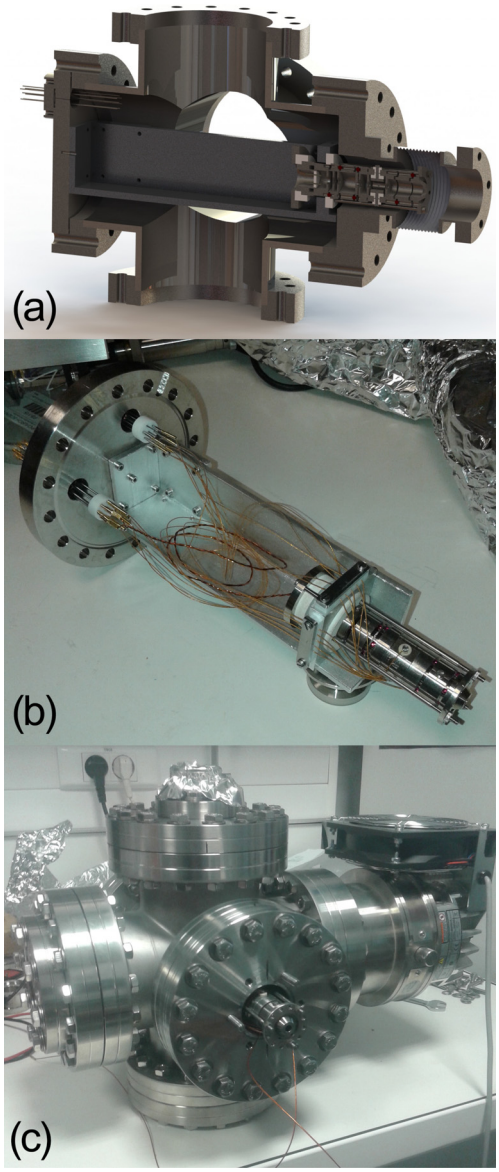

Fig. 5. Electron gun vacuum stage: (a) 3D model of the vacuum stage assembly, (b) CF100 flange in the assembly with electron gun and L-shaped support frame and (c) completed vacuum stage with fitted turbo pump, electron gun and a glass window.

emission of a few tens of μA, but at the expense of a shorter lifespan. Optimally adjusted electrode voltages for selected cathode current of 2.3 A and an electron energy of 150 eV, yield an electron beam of around 10 μA. This is the current measured in a Faraday cup, at a distance of 72 mm from the last grounded electrode M (Fig. 6). According to the best fit of simulated electron beam profiles to experimental electron current distributions measured with a movable Faraday cup, the electron beam spot size at this distance was estimated to be 1 mm, with the pencil (divergence) angle of 0.3°. A schematic of the electron gun with a shutter circuit and a TTL input is presented in Figure 7.

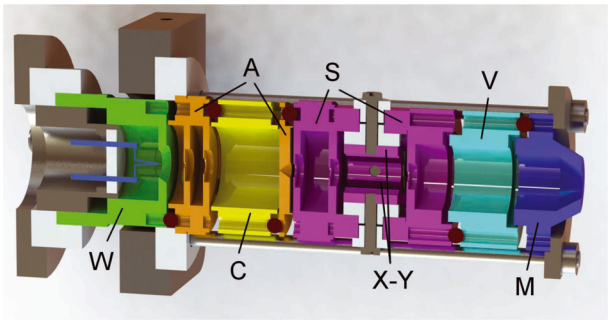

Fig. 6. 3D model of the electron gun: W – Wehnelt, A – anode, C – image inverting electrode, S – deflector housing electrode, X – horizontal deflectors, Y – vertical deflectors, V – focusing electrode, M – exit electrode (grounded). A pulsed voltage is applied to W electrode to stop the thermo-electron emission from the hairpin cathode on the left.

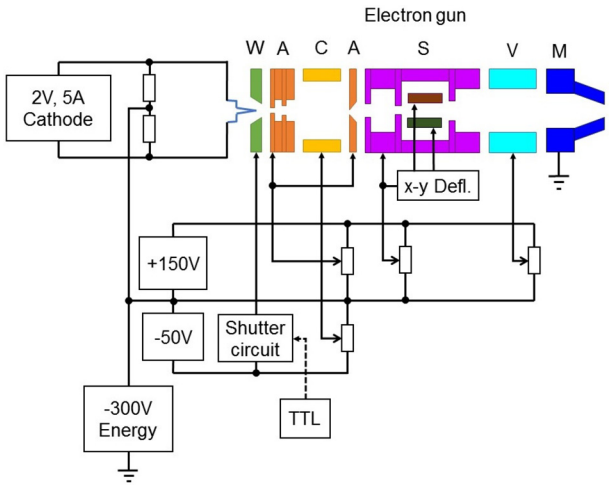

Fig. 7. Electric schematic of the electron gun used in the experiment to activate trapped ions. Shutter circuit pulses the voltages on the extractor electrode W, triggered by the TTL signal from a mass spectrometer.

A pulsed mode of the electron gun was established by applying a variable DC pulsed voltage on the Wehnelt (W) electrode (see Figs. 6 and 7). In the present experiment, an operating voltage of $W = -14$ V was needed for optimal electron beam focusing. The electron beam shut off was provided by polarizing the W electrode with –50 V relative to the cathode, thus completely stopping the electron emission. A special shutter circuit has been designed to switch between two W voltages (–14 V – "beam on" and –50 V – "beam off"), triggered by a TTL output from the LTQ XL mass spectrometer. Focusing of the electron beam at a given distance, for selected energy is done by tuning only one electrode – V (see Figs. 6 and 7).

2.5 The experimental procedure

LTQ XL mass spectrometer, equipped with an ESI source, is the main instrument that drives the experiment. By original design, it produces ions from a solution, stores

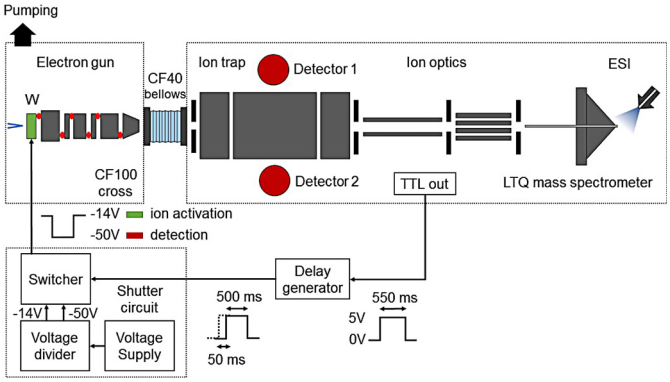

Fig. 8. Simplified schematic representation of the experimental setup. The potential of the W electrode of the electron gun is controlled by through a TTL signal from the LTQ XL mass spectrometer. All other electrodes of the gun are connected to fixed voltage supplies (not presented in this figure). Green color indicates the "electron beam on" state – the activation of the trapped ions while red color represents the "beam off" state – during which ionic fragments are detected.

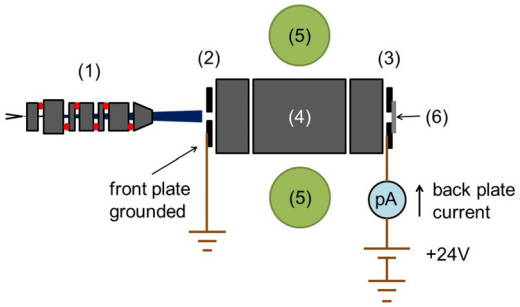

Fig. 9. Electrical scheme of the setup for the electron gun testing: (1) electron gun, (2) LTQ front plate – grounded, (3) LTQ back plate – connected to the pico-ampere meter, (4) ion trap, (5) ion detectors and (6) aluminum foil.

them in an ion trap, activate ions through collision-induced dissociation (CID) with Helium buffer gas and finally detect ion fragments and record mass spectra. However, in the present experiment, the feature of activating ions with CID is bypassed by setting up the excitation energy to 0 eV, so that ions can be activated by the external electron beam instead. For this purpose, TTL signal line is traced inside the mass spectrometer and connected to the shutter circuit input. Schematic of the entire setup with TTL synchronization of the pulsed electron gun is depicted in Figure 8.

Ions were generated by ESI from a solution. By tuning ESI parameters and solution properties, a wide range of precursor charge states can be obtained. After optimal density of desired precursor ions in the trap is reached, a TTL signal that triggers ion activation goes into the high state (5 V) until predefined activation time runs out. During this time, a focused beam of electrons of a defined energy is introduced from the back side into the trap (left side in Fig. 8).

Shutter circuit presented in the lower part of Figure 8, comprises of three stages: voltage supply, a voltage divider, and a switcher stage. Relative to the ground potential, voltage supply generates –50 V DC, which is separated by the voltage divider stage on two voltages. One of them is fixed –50 V and the other is tunable –14 V. Switcher stage operates as a simple switch by utilizing two field effect transistors (FETs). Their connection is such that only one FET can be active at all times, and each of them is connected to one voltage. State of the TTL signal defines which FET will be active. In the present experiment, high state or 5 V in the TTL signal enables the FET with –14 V to be active. This voltage is then applied to the W electrode of the electron gun. Thus electrons can be emitted from a constantly heated cathode and form an electron beam. TTL low state of 0 V, has a consequence of entirely blocking the cathode electron emission since the –50 V is applied to the W electrode.

Activation time is defined by the length of the high state of TTL signal, whereas start of ion detection is defined as when TTL signal goes into the low state. To introduce the acquisition delay or the delay between the ion activation and fragment detection, TTL signal is first sent to the digital delay generator (DG645, Stanford 150 Research Systems, Sunnyvale, CA, USA). It generates another TTL signal on the rising edge of the first one, with a length shorter by the amount of acquisition delay with respect to the first signal. In this way, the electron emission is stopped before the actual detection takes place.

2.6 Test measurements

The initial testing of the performance of the electron gun and the characterization of the electron beam profile were performed in the continuous mode. For this purpose, a disc plate electrode of the ion trap from the ESI side has been temporarily disconnected and wired as depicted in Figure 9, to measure the electron current passing through the ion trap. The electron current is measured on a thin foil (6) attached to the back electrode (3) (Fig. 9), which was polarized to +24 V and connected to a pico-ampere meter. Figure 10a shows an energy dependence of the measured current, provided that for each electron energy the electron beam was refocused by adjusting an optimal voltage on the V electrode (see Fig. 6). By using this procedure, the incident electron current in the interaction region inside the ion trap could be kept practically constant in the electron energy range of interest for the present experiment (280–300) eV, indicated by dashed lines (see Fig. 9a). Therefore, an additional normalization of ion fragment yield intensities relative to this current was not essential. Figure 9b presents measurements of the electron beam profile, performed by X-axis translation of the entire LTQ mass spectrometer, which was mounted on a dedicated custom-made supporting frame with 6 degrees of freedom [29].

Based on the geometry properties of the setup and the measured beam profile, we can roughly estimate the electron beam width to 3 mm at the front LTQ plate

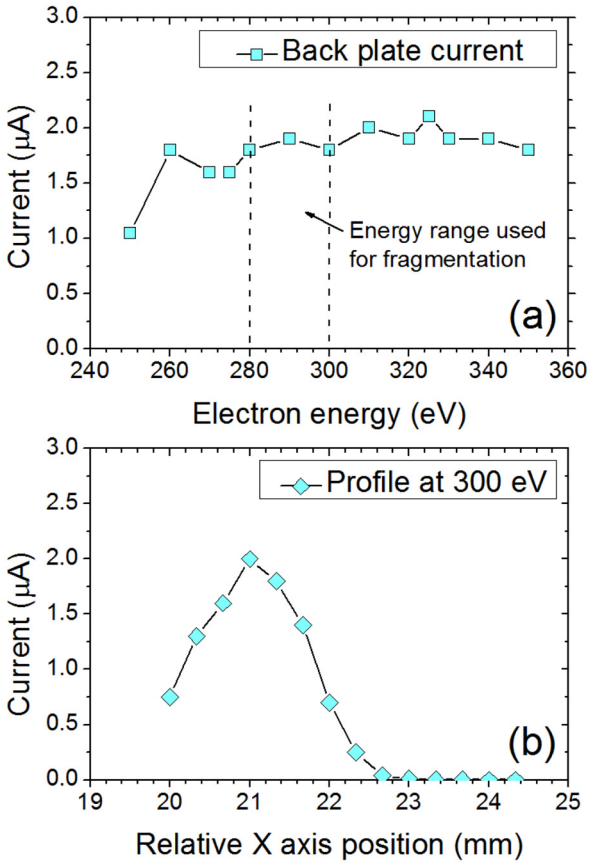

Fig. 10. Electron current measured at the back plate of the ion trap: (a) plot of the back plate current versus the electron energy and (b) electron beam profile recorded by moving the electron gun sideways relative to the LTQ.

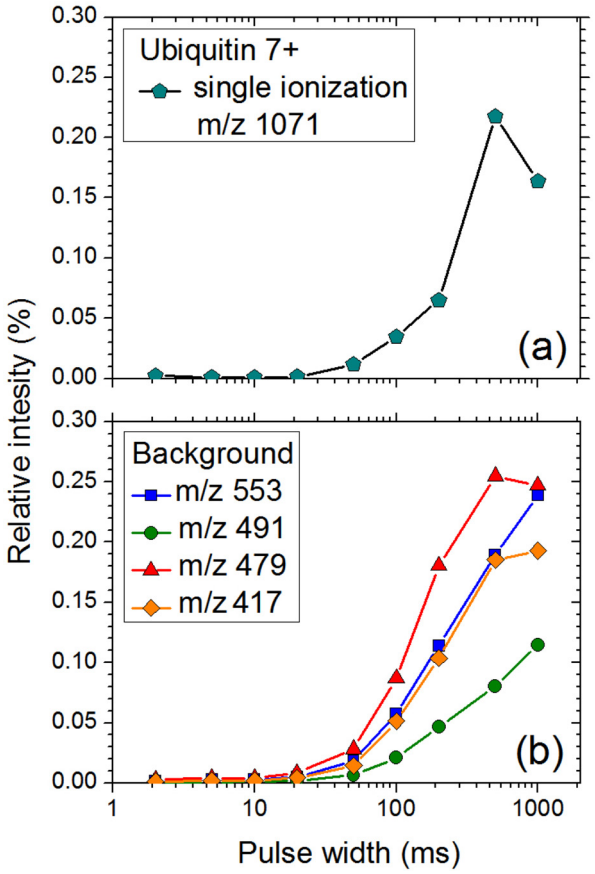

Fig. 11. Ion signal plot versus pulse widths, measured for Ubiquitin 7+ precursor: (a) peak at m/z 1071 corresponding to the single ionization of the parent ion and (b) fragments originating from electron background noise.

(see Fig. 8). It should be noted that an influence of the stray magnetic fields to the electron beam could not be completely avoided, as concluded from the known optimal adjustment of the setup in photon experiments. This influence will be prevented in future measurements by using a Mu-metal shield. In the present experiment, an aluminum tubing located between the electron gun and the front plate of the ion trap (see Fig. 4) provides only an electrostatic shielding of the electron beam.

During the activation period, electrons transfer part of their energy through collisions with ions, leading to fragmentation and ionization. The important question is for how long should this interaction be allowed to happen before reaching a saturation of the signal intensity, or even damaging detectors? To establish an optimal electron activation time of the trapped ions, different electron beam pulse widths were probed. For this purpose, ubiquitin ions of the charge state 7+ were isolated in the ion trap and activated with a short burst of 288 eV electrons. Several MS^2 were acquired during 3 min, for each electron pulse width. Averaged mass spectra were obtained for pulse widths of 2, 5, 10, 20, 50, 100, 200, 500 and 1000 ms. MS^2 acquisition delay for each pulse width was set to one-half of the given pulse width. The intensity of the peaks originating from several fragment ion products was extracted from these MS^2, normalized to precursor intensity and plotted against pulse widths in Figure 11.

From Figure 11, we can see that both the precursor ionization (Fig. 11a) and the background fragments (Fig. 11b) intensities increase with the increasing the electron pulse width. The final point corresponding to 1000 ms was omitted from Figure 11, since the created noise exceeded by far the ion signal. Based on this test, we took the 500 ms as the optimal electron activation time for the Ubiquitin 7+ protein precursor. Interestingly, this activation time turned out to be the same as the one we used previously for soft X-ray activation of the same target [49].

3 Results – inner-shell electron impact activation MS^2

The present instrument was tested by measuring electron impact activation MS^2 for several different molecular precursors produced by ESI. For each precursor, several MS^2 were recorded as a function of electron energies. Each scan was performed three times: (1) electrons + precursor ions, (2) no electrons + precursor ions and (3) electrons

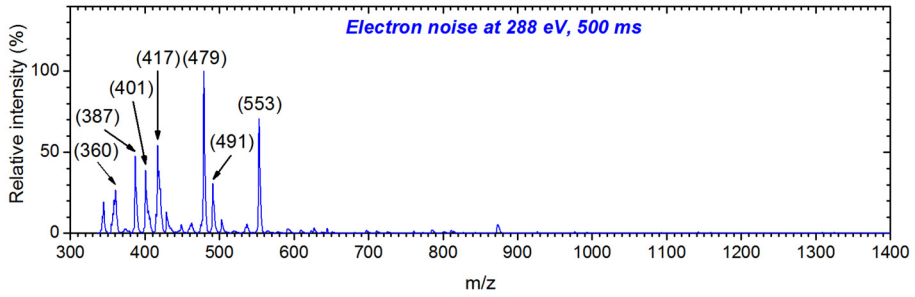

Fig. 12. Tandem mass spectrum recorded with no isolated ions, for electron impact energy of 288 eV, 500 ms pulse width.

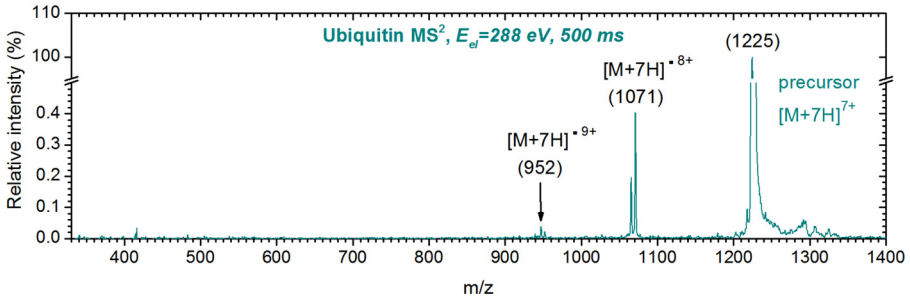

Fig. 13. Tandem mass spectrum recorded for 288 eV electron impact with protein Ubiquitin, 7+ charge state precursor.

+ no precursor ions, for background noise analysis. During measurements, an ultimate pressure inside the vacuum chamber (CF100 cross) with the electron gun, was 4.0×10^{-6} mbar.

An example of MS^2 recorded for 288 eV electrons while no precursor ions were isolated in the trap is presented in Figure 12. The low mass range is dominated by ionic fragments produced by electron ionization of residual neutral background present in the trap. The ion fragments that are not originating from selected ions are considered as background noise. In Figure 12, they occupy m/z range from 350 up to the 553.

Origin of the background is probably due to ionization of residual impurities in the trap and on the ion trap surfaces, or maybe from a false signal in the detectors. Ion detectors in the LTQ mass spectrometer have conversion dynodes which eject electrons after ion impact. The latter are then multiplied by electron multipliers. Therefore, it is possible that some of the electrons from the incident beam are also extracted towards detectors and directly detected. However, this effect is significantly reduced by an acquisition delay (see Experimental part), which was about (100–200) ms from falling edge of the electron pulse to the start of MS^2 recording.

It should also be noted that the presence of the He buffer gas could produce additional background due to the scattering of the incident beam, which may release secondary electrons in a broad energy distribution. However, as already discussed previously for X-ray action spectroscopy of proteins [33], this effect should not significantly influence the results.

Ubiquitin protein, precursor $[M+7H]^+$ at m/z 1225, was subjected to the electron energy of 288 eV, for 500 ms pulse width and 200 ms acquisition delay. The averaged mass spectrum recorded during 3 min acquisition, is presented in Figure 13. The background signal (presented in Fig. 12) has been subtracted from the spectrum. It should be noted that the subtracted background was of similar intensity as the ionization peaks. For example, the dominant background peak m/z 479 was 0.3% of the precursor.

The energy of 288 eV corresponds to the maximum in measured C 1s near-edge electron excitation function of the Ubiquitin protein [45]. After background noise subtraction and normalization to the precursor intensity, a low mass range is almost completely clear. Peaks designated at m/z 1071 and 952, are indeed originating from parent ions and correspond to single and double K-shell ionization of the precursor ion, respectively. Interestingly, the electron activation MS^2 has a remarkable similarity to soft X-ray activation MS^2 (see [49] for more details).

Substance P (SubP) singly charged precursor ions $[M+H]^+$ at m/z 1347, were isolated in the trap and subjected to 293 eV pulsed electron beam activation. The pulse width had to be raised to 900 ms in order to obtain measurable ion signal. The acquisition delay for each mass spectrum was set to 100 ms. The averaged mass spectrum is presented in Figure 14. A peak at m/z 673 corresponds to radical dication $[M+H]^{\bullet 2+}$, produced by ionization of the parent ions after a resonant Auger decay [49]. Furthermore, we have observed a neutral loss of CH_2CHSCH_3 (m/z 636) from the radical cation, corresponding to methionine residue. These losses were also observed in the recent comprehensive fragmentation study of Substance P involving VUV photons, reported by Canon et al. [37].

Melittin is a peptide consisting of 26 amino acids, larger than the 11 amino acid Substance P. Precursor ions of double charge state $[M+2H]^{2+}$, were produced by ESI and isolated in the trap. The trapped ions were subjected

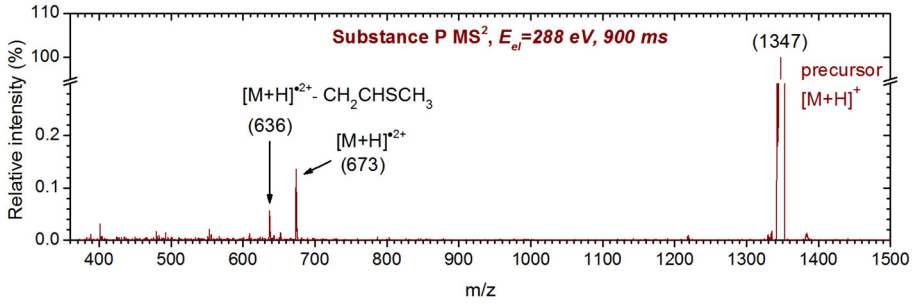

Fig. 14. Tandem mass spectrum recorded for 293 eV electron impact with peptide Substance P, singly charged precursor.

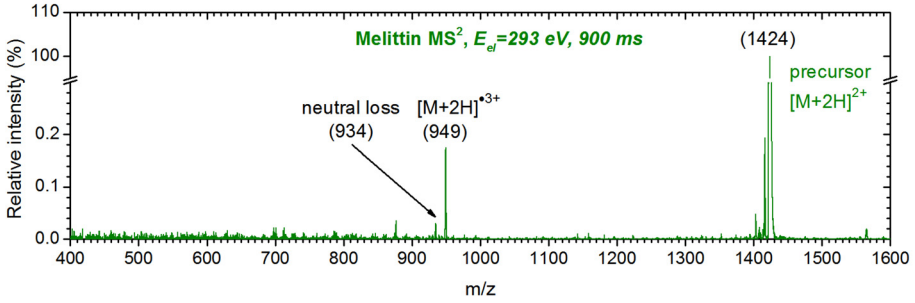

Fig. 15. Tandem mass spectrum recorded for 293 eV electron impact with peptide Melittin, doubly charged precursor.

to electron pulses of 900 ms, at 293 eV incident energy, Mass spectra were recorded after 100 ms delay of each electron pulse, yielding an averaged mass spectrum presented in Figure 15. Mass spectrum was normalized to precursor ion intensity, after electron noise subtraction. There was still some noise left in the lower mass region bellow m/z 873, but free of any distinctive fragments. Designated at m/z 949, we observe the radical cation $[M+2H]^{\bullet 3+}$, originating from the ionization of the doubly charged parent ion. Also, a relatively strong peak can be seen at m/z 934 due to a neutral loss of about 45 amu.

4 Conclusions

In this article, we report the design and the performances of a novel instrument for electron impact tandem mass spectrometry and action spectroscopy of mass/charge selected ions stored in RF ion trap. The experimental setup is based on coupling a custom-made electron gun to a commercial quadrupole linear ion trap LTQ XL (Thermo Phinningan) and allowed for unprecedented electron-impact inner-shell action spectroscopy of large biomolecules.

We present a comprehensive study, from electron tracing simulations of electron beam properties upon transmission through the ion trap, to the design and realization of custom-made vacuum stage and the electronic components. Our simulations reveal that a pulse width of the electron beam has to be extremely narrow, down to 10 ns and synchronized with the RF field, for 300 eV electrons to pass through the ion trap unaffected by RF electric field. Still, even for an electron, continuous beam, simulated by a pulse width equal to the RF period of 1 μs, a reasonable transmission higher than 60% was obtained both in vacuum and when the trap is filled with He buffer gas. Moreover, the electron beam energy distribution was not perturbed significantly according to our simulations.

A custom-made electronic shutter circuit was used for applying a pulsed voltage to the extractor electrode (Wehnelt) of the electron gun. This circuit is synchronized with LTQ XL spectrometer through a TTL signal, which controls the irradiation time of trapped ions. Three large biomolecular targets – Ubiquitin $[M+H]^{7+}$, Substance P $[M+H]^{+}$ and Melittin $[M+H]^{2+}$, were subjected to collisions with electrons at incident energies in the range from (280–300) eV, which corresponds to near C K-shell ionization threshold region. For all three molecular precursors, the most intensive interaction channel corresponds to a single ionization leading to the production of a singly ionized radical cations. This process is also accompanied by intensive neutral losses. Double precursor ionization, accompanied by neutral losses could also be detected. A careful background noise subtraction was performed to distinguish the fragments originating from the precursor molecules.

The experimental setup presented in this article is still a work in progress and can be further improved. Further advances could be focused on the magnetic shielding of the electron gun, the lowering the pulse width of the electron packet, along with the synchronization of the pulse timing with the trap RF field. This would allow for both minimizing the overall background noise created in the ion trap and the using even lower incident electron energies. However, the present work shows that all samples that can be placed in the gas phase using the electrospray ionization can now be probed by electron spectroscopy.

This work was supported by the ANR, France, under project ANR-08-BLAN-0065. M.LJ.R. and A.R.M. acknowledge support by the MESTD of Republic of Serbia under project #171020. The Notre Dame Radiation Laboratory is supported by the U.S. Department of Energy Office of Science, Office of Basic Energy Sciences under Award Number DE-FC02-04ER15533 (this is document number NDRL 5105). A.R.M. and M.Lj.R. acknowledge support from the COST Actions CM1204 (XLIC) and CM1301 (CELINA). We thank Dr. Christophe Nicolas (SOLEIL) and Miroslav Maksimović (IPB) for their help to assemble the experiment and the general staff of the DISCO, DESIRS and PLEIADES beamlines of the SOLEIL synchrotron radiation facility for the technical support.

References

1. N.J. Mason, J. Phys.: Conf. Ser. **565**, 012001 (2014)
2. G.J. Schulz, Phys. Rev. Lett. **10**, 104 (1963)
3. S.J. Buckman, C.W. Clark, Rev. Mod. Phys. **66**, 539 (1994)
4. S. Trajmar, W. McConkey, I. Kanik, in *Springer Handbook of Atomic, Molecular, and Optical Physics*, edited by Gordon W.F. Drake (Springer Science + Business Media, Inc, Würzburg, 2006)
5. A. Hitchcock, J. Electron Spectros. Relat. Phenomena **112**, 9 (2000)
6. B. Boudaïffa, P. Cloutier, D. Hunting, M.A. Huels, L. Sanche, Science **287**, 1658 (2000)
7. J. Gu, J. Leszczynski, H.F. Schaefer, Chem. Rev. **112**, 5603 (2012)
8. J.H. Moore, C.C. Davis, M.A. Coplan, S.C. Greer, *Building Scientific Apparatus* (Cambridge University Press, New York, 2009)
9. M. Zubek, N. Gulley, G.C. King, F.H. Read, J. Phys. B **29**, L239 (1996)
10. R. Janeckova, D. Kubala, O. May, J. Fedor, M. Allan, Phys. Rev. Lett. **111**, 1 (2013)
11. M. Allan, Phys. Rev. Lett. **93**, 3 (2004)
12. S. Živanov, M. Allan, M. Čížek, J. Horáček, F.A.U. Thiel, H. Hotop, Phys. Rev. Lett. **89**, 073201 (2002)
13. M. Allan, Phys. Rev. Lett. **87**, 033201 (2001)
14. M. Allan, Phys. Rev. Lett. **98**, 1 (2007)
15. M.J. Brunger, S.J. Buckman, Phys. Rep. **357**, 215 (2002)
16. J.C. Gibson, D.R. Lin, L.J. Allen, R.P. McEachran, L.A. Parcell, S.J. Buckman, J. Phys. B **31**, 3949 (1998)
17. T.M. Maddern, L.R. Hargreaves, J.R. Francis-Staite, M.J. Brunger, S.J. Buckman, C. Winstead, V. McKoy, Phys. Rev. Lett. **100**, 1 (2008)
18. T.M. Maddern, L.R. Hargreaves, M. Bolorizadeh, M.J. Brunger, S.J. Buckman, Meas. Sci. Technol. **19**, 085801 (2008)
19. J.R. Brunton, L.R. Hargreaves, S.J. Buckman, G. García, F. Blanco, O. Zatsarinny, K. Bartschat, M.J. Brunger, Chem. Phys. Lett. **568-569**, 55 (2013)
20. J.R. Brunton, L.R. Hargreaves, T.M. Maddern, S.J. Buckman, G. García, F. Blanco, O. Zatsarinny, K. Bartschat, D.B. Jones, G.B. da Silva, M.J. Brunger, J. Phys. B **46**, 245203 (2013)
21. S.A. Haughey, T.A. Field, J. Langer, N.S. Shuman, T.M. Miller, J.F. Friedman, A.A. Viggiano, J. Chem. Phys. **137**, 54310 (2012)
22. T.A. Field, K. Graupner, S. Haughey, C.A. Mayhew, N.S. Shuman, T.M. Miller, J.F. Friedman, A.A. Viggiano, J. Phys.: Conf. Ser. **388**, 052086 (2012)
23. F. Gobet, B. Farizon, M. Farizon, M.J. Gaillard, J.P. Buchet, M. Carré, P. Scheier, T.D. Märk, Phys. Rev. Lett. **89**, 183403 (2002)
24. S. Denifl, F. Zappa, I. Mähr, J. Lecointre, M. Probst, T.D. Märk, P. Scheier, Phys. Rev. Lett. **97**, 1 (2006)
25. S. Denifl, M. Stano, A. Stamatovic, P. Scheier, T.D. Märk, J. Chem. Phys. **124**, 054320 (2006)
26. I. Bald, I. Dąbkowska, E. Illenberger, Angew. Chem. - Int. Ed. **47**, 8518 (2008)
27. I. Baccarelli, I. Bald, F.A. Gianturco, E. Illenberger, J. Kopyra, Phys. Rep. **508**, 1 (2011)
28. F. Gaie-Levrel, G.A. Garcia, M. Schwell, L. Nahon, Phys. Chem. Chem. Phys. **13**, 7024 (2011)
29. A.R. Milosavljević, A. Giuliani, C. Nicolas, J.-F. Gil, J. Lemaire, M. Réfrégiers, L. Nahon, J. Phys.: Conf. Ser. **257**, 012006 (2010)
30. S. Bari, O. Gonzalez-Magaña, G. Reitsma, J. Werner, S. Schippers, R. Hoekstra, T. Schlathölter, J. Chem. Phys. **134**, 24314 (2011)
31. A.R. Milosavljević, C. Nicolas, J. Lemaire, C. Dehon, R. Thissen, J.-M. Bizau, M. Réfrégiers, L. Nahon, A. Giuliani, Phys. Chem. Chem. Phys. **13**, 15432 (2011)
32. A.R. Milosavljević, C. Nicolas, J.F. Gil, F. Canon, M. Réfrégiers, L. Nahon, A. Giuliani, J. Synchrotron Radiat. **19**, 174 (2012)
33. A.R. Milosavljević, F. Canon, C. Nicolas, C. Miron, L. Nahon, A. Giuliani, J. Phys. Chem. Lett. **3**, 1191 (2012)
34. O. González-Magaña, G. Reitsma, M. Tiemens, L. Boschman, R. Hoekstra, T. Schlathölter, J. Phys. Chem. A **116**, 10745 (2012)
35. A.R. Milosavljević, A. Giuliani, C. Nicolas, in Nanoscience Nanotechnology, Vol. 5: *X-ray and Neutron Techniques for Nanomaterials Characterization*, edited by Prof. Dr. Challa S.S.R. Kumar (Springer-Verlag Berlin Heidelberg, 2016, in press)
36. R. Aebersold, M. Mann, Nature **422**, 198 (2003)
37. F. Canon, A.R. Milosavljevi, L. Nahon, A. Giuliani, Phys. Chem. Chem. Phys. **17**, 25725 (2015)
38. R. Zubarev, N.L. Kelleher, F.W. McLafferty, J. Am. Chem. Soc. **120**, 3265 (1998)
39. N.L. Kelleher, Anal. Chem. **76**, 197A (2004)
40. L. Ding, F.L. Brancia, Anal. Chem. **78**, 1995 (2006)
41. T. Baba, Y. Hashimoto, H. Hasegawa, A. Hirabayashi, I. Waki, Anal. Chem. **76**, 4263 (2004)
42. T. Baba, J.L. Campbell, J.C.Y. Le Blanc, J.W. Hager, B.A. Thomson, Anal. Chem. **87**, 785 (2015)
43. O.A. Silivra, F. Kjeldsen, I.A. Ivonin, R.A. Zubarev, J. Am. Soc. Mass Spectrom. **16**, 22 (2005)
44. V.G. Voinov, M.L. Deinzer, D.F. Barofsky, Anal. Chem. **81**, 1238 (2009)
45. M.L. Ranković, A. Giuliani, A.R. Milosavljević, Appl. Phys. Lett. **108**, 064101 (2016)
46. http://simion.com/, (n.d.).
47. J.C. Nickel, K. Imre, D.F. Register, S. Trajmar, J. Phys. B **18**, 125 (1985)
48. A.R. Milosavljević, S. Madžunkov, D. Šević, I. Čadež, B.P. Marinković, J. Phys. B **39**, 609 (2006)
49. A.R. Milosavljević, C. Nicolas, M.L. Ranković, F. Canon, C. Miron, A. Giuliani, J. Phys. Chem. Lett. **6**, 3132 (2015)

Eur. Phys. J. D (2014) 68: 68
DOI: 10.1140/epjd/e2014-40826-y

THE EUROPEAN PHYSICAL JOURNAL D

Regular Article

VUV photofragmentation of protonated leucine-enkephalin peptide dimer below ionization energy*

Aleksandar R. Milosavljević[1,a], Viktor Z. Cerovski[1], Miloš Lj. Ranković[1], Francis Canon[2], Laurent Nahon[3], and Alexandre Giuliani[3,4]

[1] Institute of Physics Belgrade, University of Belgrade, Pregrevica 118, 11080 Belgrade, Serbia
[2] INRA, UMR1324 Centre des Sciences du Goût et de l'Alimentation, 21000 Dijon, France
[3] Synchrotron SOLEIL, L'Orme des Merisiers, Saint-Aubin, 91192 Gif-sur-Yvette, France
[4] UAR 1008 CEPIA, INRA, 44316 Nantes, France

Received 23 December 2013 / Received in final form 28 January 2014
Published online 25 March 2014 –

Abstract. The experimental investigation of 5–8 eV photons induced dissociation of the leucine-enkephalin (Leu-Enk) peptide dimer, performed by coupling a linear ion trap with a synchrotron beamline, in combination with the tandem mass spectrometry, has been reported. The present work extends the existing results on Leu-Enk VUV-induced dissociation to lower sub-ionization photon energy range. The measured tandem mass spectra show that even at the photon energies below the ionization threshold, VUV irradiation of the protonated Leu-Enk dimer precursor can lead to a rich fragmentation pattern, including peptide sequence ions and neutral losses. The photodissociation yields of selected ionic fragments reveal the absorption bands at about 6.7–7.1 eV (185–175 nm). The experimental results have been supported by theoretical description of the $[2\text{Leu-Enk} + \text{H}]^+$ precursors, optimized at B3LYP/6-31+G(*d*,*p*) level of DFT.

1 Introduction

There has been a long standing effort to understand details of radiation damage of biomaterials at the molecular level. Particularly, a large amount of results have been published in the recent years on electron, ion and photon interaction with isolated molecules representing building blocks or parts of large biological macromolecules such as DNA and RNA [1]. The investigation of an isolated molecular system under well-defined conditions allows for a more detailed insight into fundamental biological processes initiated by the impact of a high-energy particle. Furthermore, this research could help developing important applications in medicine, such as optimizing the type and dose of the radiation in cancer therapy, in order to maximize killing of the cancer cells, while minimizing the damage to surrounding healthy tissues [2].

Although DNA and RNA have been mostly in the focus of the radiation damage research so far, protein damage is a very important issue that must be also taken into account for realistic modeling. Along this line, most of the existing results have been reported on vacuum ultraviolet (VUV) photon interaction with amino acids – the building blocks of proteins (see [3] and references therein). Nevertheless, the susceptibility of amino acids to energetic photon irradiation (VUV/X-ray) cannot necessarily be transferred directly to their polymers. For example, it has been shown recently that an isolated full protein was extremely resistant to fragmentation upon soft X-ray irradiation in comparison with amino acids [4]. Therefore, it is important to study the high-energy photon interaction with the isolated targets representing polymers of amino acids (peptides), as well as their non-covalent complexes. Unfortunately, this used to be experimentally very challenging – especially to bring the amino acids or their polymers intact into the gas phase [4]. The development of experimental techniques in recent years, particularly those coupling synchrotron radiation with ion traps, allowed for the use of novel ionization methods such as electrospray ionization (ESI) to produce and study gas-phase intact peptides, proteins and even non-covalent complexes [3–7].

In the present article, we report on the experimental investigation of 5–8 eV photon induced dissociation of the leucine-enkephalin (Leu-Enk) peptide dimer, performed by coupling a linear ion trap with a synchrotron beamline, in combination with the tandem mass spectrometry (MS^2) method [6]. The Leu-Enk pentapeptide (see Fig. 1) has been intensively studied previously and has become a

* Contribution to the Topical Issue "Nano-scale Insights into Ion-beam Cancer Therapy", edited by Andrey V. Solov'yov, Nigel Mason, Paulo Limão-Vieira and Malgorzata Smialek-Telega.

[a] e-mail: vraz@ipb.ac.rs

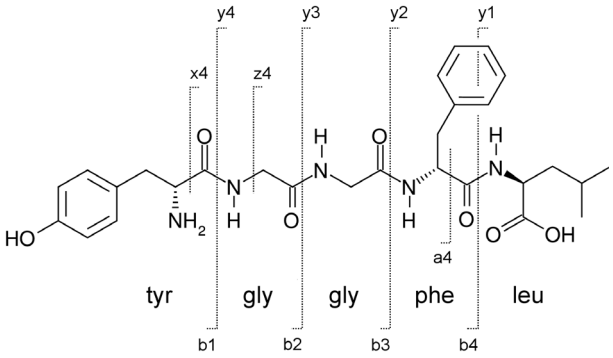

Fig. 1. Schematic drawing of leucine-enkephalin peptide (Leu-Enk) and the amino acid sequence.

standard model in mass spectrometry (see [3,8] and references therein). It has also been used as a model system for peptide-peptide interactions [9]. The existing results on high-energy photon interaction with gas phase Leu-Enk include the photodissociation study of protonated Leu-Enk monomer in the 8–40 eV VUV range [3,10] and soft X-ray [11], as well as the most recent study of both bare and nanosolvated Leu-Enk dimer in 7–10 eV range [9].

Therefore, the present work extends the existing results on Leu-Enk VUV-induced dissociation to lower sub-ionization photon energy range, which is particularly important regarding the intensive photoabsorption by peptides in the 4–7 eV region (300–180 nm) due to the strong electronic transitions associated with aromatics, disulfids, amides and the charge transfer [12]. Furthermore, the present work deals with the isolated gas phase Leu-Enk dimer, thus allowing an insight into the sub-ionization dissociation of non-covalent peptide complexes, a model system for the peptide-peptide interaction and ternary structure acquisition. In short, we could study the stability of fragile non-covalent peptide complexes against sub-ionization VUV irradiation by analyzing direct dissociation and backbone fragmentation as a function of the photon energy. Finally, extensive high-level molecular dynamics (MD) and density functional theory (DFT) calculations were performed in order to study the structure and physicochemical properties of the Leu-Enk dimer.

2 Experimental method

The experimental system [5,6] has been assembled by coupling a commercial linear quadrupole ion trap mass spectrometer (Thermo Finnigan LTQ XL) with the DESIRS VUV beamline [13] of the SOLEIL synchrotron radiation facility in France. Ions were produced from a solution by a detachable ESI source mounted on the mass spectrometer. The electrosprayed protonated Leu-Enk dimer ions were introduced from the front side of the mass spectrometer and guided through a transfer tube and a system of ion lenses into ion trap. Desired precursor ions $[2\text{Leu-Enk} + \text{H}]^+$ were isolated in the trap and irradiated during about 500 ms by a monochromatic VUV photon beam, which was introduced from the back side of the mass spectrometer. The photon beam is produced by an undulator and monochromatized by a normal incidence monochromator [13], with a typical bandwidth of 12 meV and an absolute energy calibration of ± 10 meV. High harmonics of the undulator producing the photons are filtered out by using a gas filter [13], as well as MgF_2 or Suprasil windows, depending on the photon energy region. A vacuum manifold with turbo pumping stage has been used to accommodate the pressure difference between the beamline (10^{-8} mbar) and mass spectrometer (10^{-5} mbar). A fast digitally activated rotating mechanical shutter has been fitted in the vacuum manifold in order to define the irradiation time [14]. The mass spectrometer was mounted on a home-made supporting frame which allows for a fine tuning of the position of the trapped ions packet with respect to the VUV photon beam, in order to have a high ion activation efficiency and an optimized signal to noise ratio.

Trapped ions were activated and fragmented in a repeated sequence, during which MS^2 spectra were recorded as a function of a particular photon activation energy. The ion trapping, the opening of the mechanical shutter, the recording of the spectra and the photon energy scanning are synchronized by a home-made software, in order to perform automated long-period acquisition. The photodissociation ion yields were obtained from the recorded mass spectra according to the intensity of a desired m/z region, and normalized to both the precursor intensity and the photon flux which has been measured separately under the same experimental conditions. Leucine-enkephalin (Leu-Enk : Try-Gly-Gly-Phe-Leu) was provided by Sigma Aldrich, from bovine erythrocytes in powder form and solvated with water/acetonitrile (75:25) solution at 10 μM concentration.

3 Results and discussion

3.1 Tandem mass spectrometry

Figure 2 presents the tandem mass spectrum of Leu-Enk dimer upon VUV photon activation at 6.7 eV. Clearly, the most intensive dissociation channel corresponds to the cleavage of non-covalent bonds between the monomers and production of the protonated Leu-Enk monomer $[\text{M} + \text{H}]^+$ at m/z 556.

Nevertheless, a zoom-in in the tandem mass spectrum reveals that the photon absorption also leads to an intensive peptide backbone (BB) fragmentation, as well as neutral losses. Figure 2b shows that both N-terminal (a,b) and C-terminal (x, y, z) sequence ionic fragments are formed upon photoactivation of the Leu-Enk dimer precursor. Moreover, the dissociation of the dimer produces fragments from BB fragmentation of one peptide which can stay attached to the other peptide, as can be clearly seen in the rich fragmentation pattern presented in Figure 2c. Finally, the most intensive fragmentation channels, beside the production of the charged monomer, correspond to the loss of neutral molecules, dominantly tyrosine (m/z 107) and phenyl (m/z 91), while more intensive loss of H_2O,

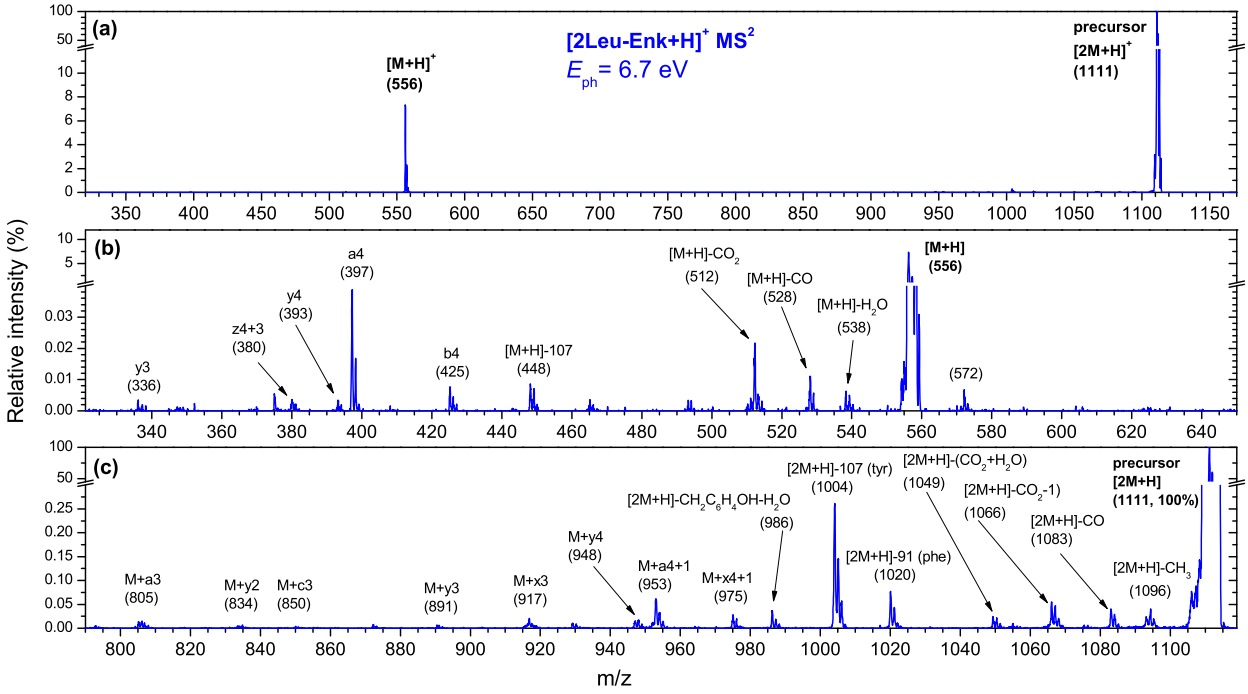

Fig. 2. Photo-activation tandem mass spectrum of leucine-enkephalin (Leu-Enk) peptide dimer recorded after irradiation of $[2\text{Leu-Enk} + \text{H}]^+$ precursors at 6.7 eV photon energy. The lower panels (b), (c) show close up of the mass regions up to (m/z 650) (b) and down to (m/z 800) (c), respectively. The proposed assignments of the fragments are given in the figure, where notation "M" corresponds to "Leu-Enk". The theoretical fragmentation of Leu-Enk peptide and the nomenclature of the fragments have been taken from reference [15].

m/z 28 and CO_2 accompanies the direct dissociation to the monomer units (Fig. 2b).

The measured tandem mass spectra show that even at the photon energies below the ionization threshold [9], VUV irradiation of the protonated Leu-Enk dimer precursor can lead to a rich fragmentation pattern, including peptide sequence ions and neutral losses. The mechanism should thus involve an electronic excitation of the precursor due to a resonant photon absorption, followed by a fast deexcitation to the hot ground state and subsequent fragmentation [9]. Therefore, the investigation of the energy dependence of the dissociation should allow for a direct mapping of the electronic transitions, as well as of the VUV photostability of this fragile non-covalent peptide complex.

3.2 Photodissociation ion yields

Figures 3–6 present photodissociation yields of the selected ionic fragments resolved in the tandem mass spectra, as indicated in Figure 2. The photodissociation intensity of the protonated Leu-Enk dimer is strongly energy dependent. The photodissociation yield of the dominant fragment – protonated monomer $[\text{M} + \text{H}]^+$ – reaches a maximum at about 7 eV (Fig. 3a). As indicated previously [9], this intensive sub-ionization photodissociation occurs from electronically excited states of the Leu-Enk dimer precursor. The relaxation of the electronically excited states and redistribution of energy among the vibrational degrees of freedom leads to the dissociation of the non-covalent complex from the hot ground state. Therefore, the maximum dissociation intensity directly points to the strongest electronic transition (absorption band). Furthermore, the slow decrease of the $[\text{M} + \text{H}]^+$ ion yield above 7 eV also indicates that several different absorption bands in the 6.5–8 eV energy region contribute to the dissociation. The electronic spectroscopy of small peptides has been theoretically investigated by Serrano-Andrés and Fülscher [12]. Briefly, electronic structure of the peptidic backbone may be approximated by a 4-level system including two π orbitals involving the amide bond, the oxygen lone pair and one virtual π orbital involving the amide [12]. The amide $\pi\pi*$ and charge transfer $n\pi*$ transitions have been tentatively assigned to the 6.5–8 eV spectral region. The contribution of different absorption bands is even more pronounced for the dissociation accompanied by loss of small neutral molecules H_2O and CO_2 (Figs. 3b and 3c, respectively).

Nevertheless, the loss of neutral amino acids phenyl and tyrosine is more resonant, as the corresponding photodissociation ion yields (Figs. 4a and 4b) reveal well defined absorption bands centered at about 6.9 eV. Therefore, sub-ionization site-specific covalent bond breaking and fragmentation of Leu-Enk dimer is conducted by a specific electronic transition from highest occupied molecular orbital (HOMO) to lowest unoccupied molecular orbital (LUMO). The similar photodissociation ion yields have been measured for the peptide sequence

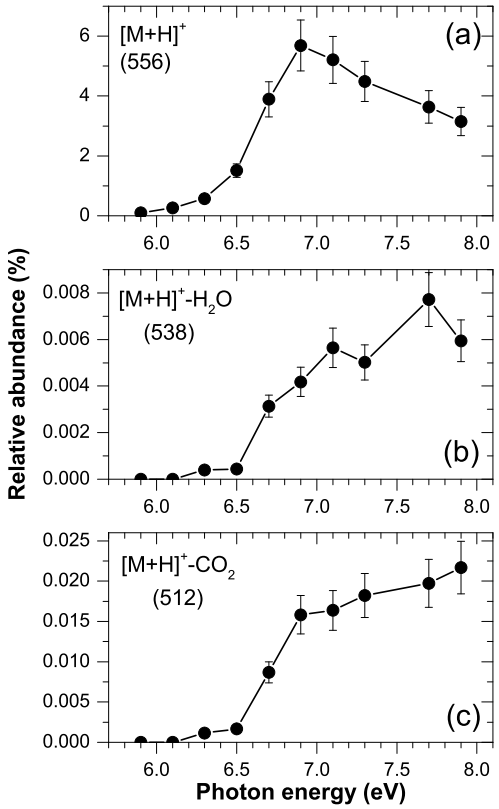

Fig. 3. Photodissociation yields of (a) $[M+H]^+$ (m/z 556.1–556.4), (b) $[M+H]^+$-H_2O (m/z 538.08–538.38) and (c) $[M+H]^+$-CO_2 (m/z 512.1–512.4) fragments.

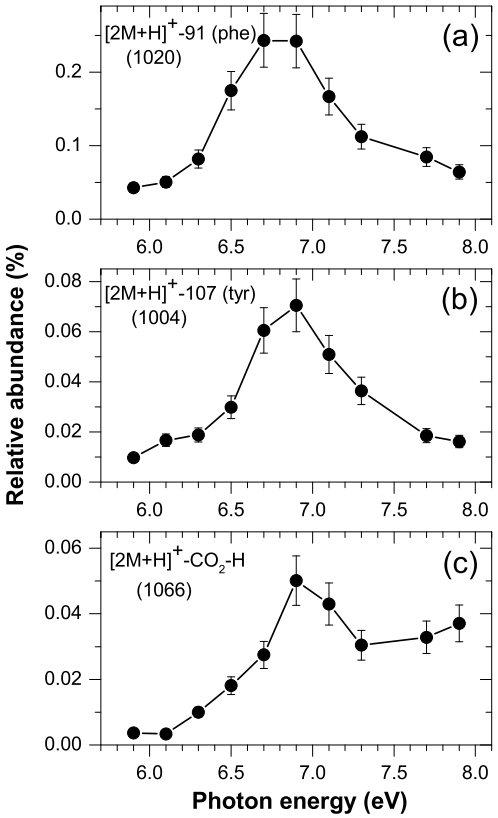

Fig. 4. Photodissociation yields of (a) $[2M+H]^+$-91 (phenyl) (m/z 1020.0–1020.3), (b) [2M+H]$^+$-107 (tyrosine) (m/z 1003.98–1004.28) and (c) $[2M+H]^+$-CO_2 (m/z 1066.0–1066.3) fragments.

fragments, both isolated and attached to the monomer (Figs. 5 and 6). The maxima of the measured ion yields, corresponding to the maximum absorption, are at about 6.8–7.1 eV. Still, the bands of the C-terminal fragments (x, y) seem to be slightly red-shifted in comparison to the N-terminal fragments (a,b), although a more detailed experimental study is needed for a definite conclusion.

3.3 Theoretical modeling of dimer electronic structure

Theoretical description of $[2\text{Leu-Enk}+H]^+$ was carried out in order to better understand the experimental results. The geometry of the lowest-energy conformer (CF) were obtained following reference [9], optimized at B3LYP/6-31+G(d,p) level of DFT after reference [16] using NWCHEM [17]. The calculated vertical ionization energy of this CF is 9.31 eV [9].

The geometry of the lowest-energy CF found of the bare Leu-Enk dimer is shown in Figure 7. Four HOMOs are all localized on aromatic groups, as shown in the figure (not shown HOMO-2 has the same localization as HOMO, on Phe(n)). LUMO, in contrast, is spread across the BB of the protonated monomer. LUMO+1 and LUMO+2, furthermore, also occupy about the same position as LUMO, with more weight on the Tyr(p) end of the monomer.

Given the obtained localization pattern, one could expect that some excitations of the type HOMO $-$ n $\rightarrow$ LUMO + m for $n = 0, 1, 2, 3$ and $m = 0, 1, 2$ consist of transfer of charge from aromatic ring to the BB(p). Taking into account the well-known electronic stabitility of the aromatic ring, the main effect of the transfer is weakening of the BB(p) due to the negative charge repulsion along the bone, leading to the conclusion that protonated monomer in the dimer is less stable than the neutral. Furthermore, it could be also argued that excitations involving a charge transfer from the neutral to the protonated monomer lead to the loss of Tyr(p), since the hole created by the excitation of electron on Phe(n) is well localized on the aromatic ring preventing the loss of Phe fragment. On the other hand, excitations involving transitions that take place only on the protonated monomer could additionally initiate loss of Phe fragment, due to the repulsion between positively charged Phe(p) and the NH^+. Nevertheless, a more detailed analysis and definite conclusions demand for time-dependent DFT theoretical calculations.

4 Conclusion

The present paper reports a detailed experimental study on photo-induced dissociation of protonated Leu-Enk peptide dimer isolated in the gas phase, at photon energies below the ionization threshold. The results show that photo-induced electronic excitation of the non-covalent dimer

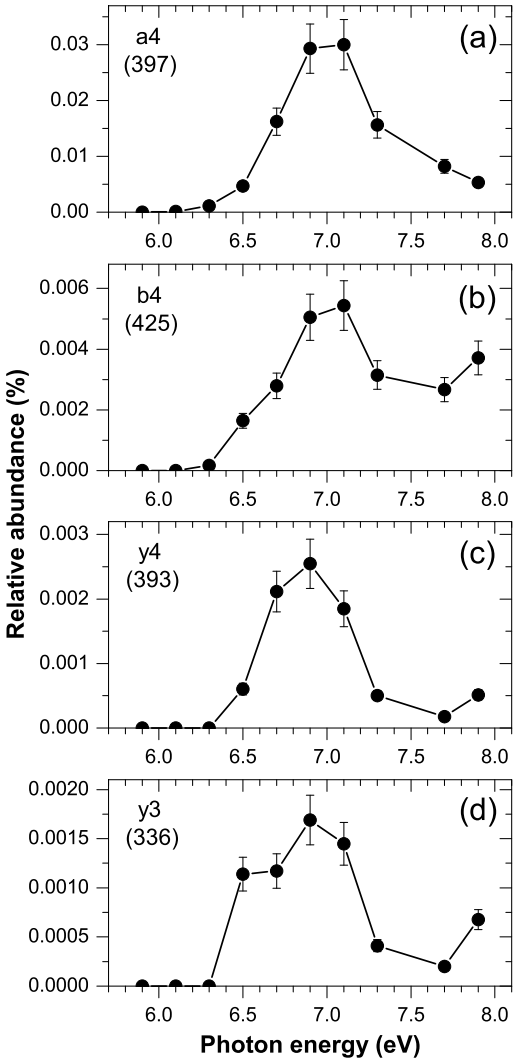

Fig. 5. Photodissociation yields of (a) a_4 (m/z 397.05–397.35), (b) b_4 (m/z 425.08–425.38), (c) y_4 (m/z 393.0–393.3) and (d) y_3 (m/z 336.0–336.3) fragments.

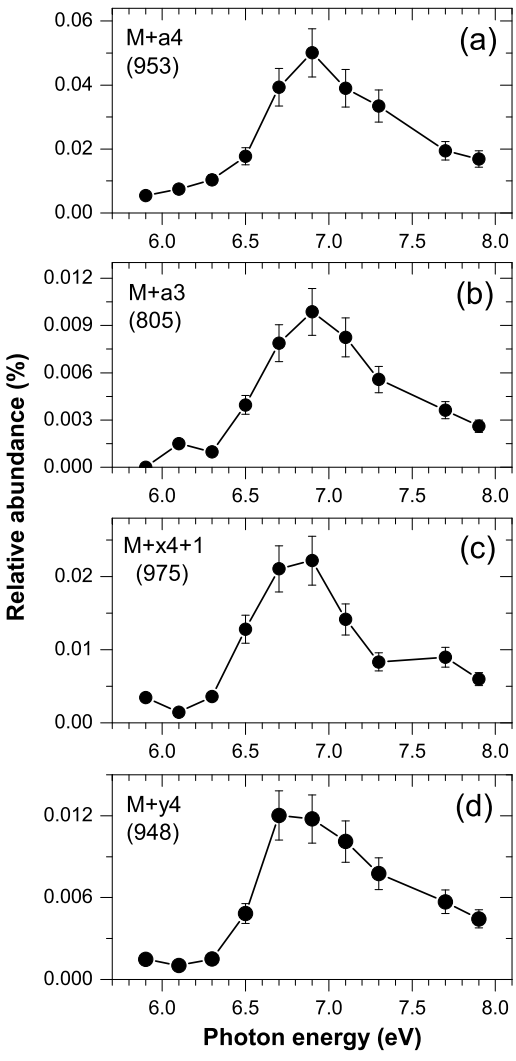

Fig. 6. Photodissociation yields of (a) $M + a_4$ (m/z 952.92–953.22), (b) $M + a_3$ (m/z 805.05–805.35), (c) $M + x_4 + 1$ (m/z 975.0–975.3) and (d) $M + y_4$ (m/z 948.0–948.3) fragments.

system leads to intensive dissociation to the monomer units (as expected), but also to backbone destruction and loss of neutral molecules. Furthermore, the fragmentation process can end up with the peptide sequence fragments both isolated and still attached to the monomer.

The intensity of the photo-induced fragmentation of the protonated Leu-Enk dimer is strongly dependent on the photon energy. The measured photodissociation yields of selected ionic fragments reveal the absorption bands at about 6.7–7.1 eV (185–175 nm). The experimental results have been supported by theoretical description of the $[2\text{Leu-Enk} + H]^+$ precursors, optimized at B3LYP/6-31+G(d,p) level of DFT. According to the calculated distribution of HOMO and LUMO, the experimental results and measured fragmentation pattern could be tentatively rationalized. Finally, the present work is important for the field of radiation damage and brings new results revealing the susceptibility of complex biopolymers to energetic photons.

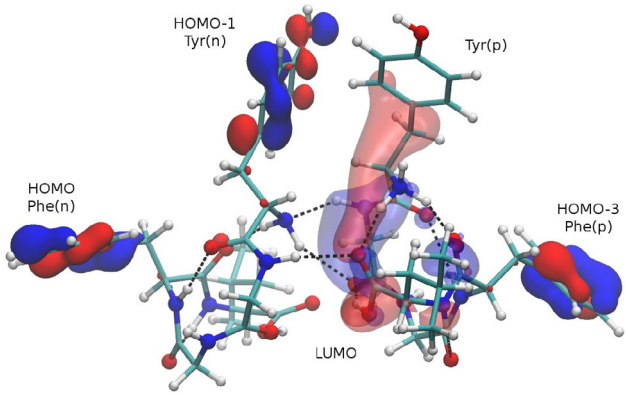

Fig. 7. Geometry of the lowest-energy CF found, shown together with several frontier orbitals, as indicated in the figure. HOMO-2 (not shown) is localized on Phe(n) just as HOMO. LUMO+1 and LUMO+2 (not shown) occupy about the same part of the molecule as LUMO. (n) and (p) next to the group name indicate whether the group belongs to the neutral or protonated monomer, respectivelly.

This work was supported by the French ANR (Project ANR-08-BLAN-0065), the "Pavle Savic" bilateral scientific project between Serbia and France (N27482TE) and the COST Action MP1002 (Nano-IBCT). A.R.M., M.Lj.R. and V.Z.C. acknowledge support by the Ministry of education, science and technological development of Republic or Serbia under Projects 171020 and 171033, respectively. We are grateful to the SOLEIL general staff for providing beamtime under Projects 20110324 and 20130388.

References

1. I. Baccarelli, F.A. Gianturco, A. Grandi, R.R. Lucchese, N. Sanna, Adv. Quantum Chem. **52**, 189 (2007)
2. ESF/COST action MP1002 Nano-scale insights in ion beam cancer therapy (Nano-IBCT), http://fias.uni-frankfurt.de/nano-ibct/overview/
3. S. Bari, O. Gonzalez-Magana, G. Reitsma, J. Werner, S. Schippers, R. Hoekstra, T. Schlatholter, J. Chem. Phys. **134**, 024314 (2011)
4. A.R. Milosavljević, F. Canon, C. Nicolas, C. Miron, L. Nahon, A. Giuliani, J. Phys. Chem. Lett. **3**, 1191 (2012)
5. A.R. Milosavljević, C. Nicolas, J. Lemaire, C. Déhon, R. Thissen, J.-M. Bizau, M. Réfrégiers, L. Nahon, A. Giuliani, Phys. Chem. Chem. Phys. **13**, 15432 (2011)
6. A.R. Milosavljević, C. Nicolas, J.-F. Gil, F. Canon, M. Réfrégiers, L. Nahon, A. Giuliani, J. Synchrotron Radiat. **19**, 174 (2012)
7. F. Canon, A.R. Milosavljević, G. van der Rest, M. Réfrégiers, L. Nahon, P. Sarni-Manchado, V. Cheynier, A. Giuliani, Angew. Chem. Int. Ed. **52**, 8377 (2013)
8. J. Sztáray, A. Memboeuf, L. Drahos, K. Vékey, Mass Spectrom. Rev. **30**, 298 (2010)
9. A.R. Milosavljević, V.Z. Cerovski, F. Canon, L. Nahon, A. Giuliani, Angew. Chem. Int. Ed. **52**, 7286 (2013)
10. O. González-Magaña, G. Reitsma, S. Bari, R. Hoekstra, T. Schlathölter, Phys. Chem. Chem. Phys. **14**, 4351 (2012)
11. O. González-Magaña, G. Reitsma, M. Tiemens, L. Boschman, R. Hoekstra, T. Schlathölter, J. Phys. Chem. A **116**, 10745 (2012)
12. L. Serrano-Andrés, M. Fülscher, J. Phys. Chem. B **105**, 9323 (2001)
13. L. Nahon, N. de Oliveira, G. Garcia, J.F. Gil, B. Pilette, O. Marcouille, B. Lagarde, F. Polack, J. Synchrotron Radiat. **19**, 508 (2012)
14. A.R. Milosavljević, C. Nicolas, J.-F. Gil, F. Canon, M. Réfrégiers, L. Nahon, A. Giuliani, Nucl. Instrum. Methods B **279**, 34 (2012)
15. http://prospector.ucsf.edu
16. N.C. Polfer, J. Oomens, S. Suhai, B. Paizs, J. Am. Chem. Soc. **129**, 5887 (2007)
17. M. Valiev, E.J. Bylaska, N. Govind, K. Kowalski, T.P. Straatsma, H.J.J. Van Dam, D. Wang, J. Nieplocha, E. Apra, T.L. Windus, W.A. de Jong Valiev, Comput. Phys. Commun. **181**, 1477 (2010)

28th Summer School and International Symposium on the Physics of Ionized Gases

Aug. 29 - Sep. 2, 2016, Belgrade, Serbia

CONTRIBUTED PAPERS
&
ABSTRACTS OF INVITED LECTURES, TOPICAL INVITED LECTURES, PROGRESS REPORTS AND WORKSHOP LECTURES

Editors:
Dragana Marić, Aleksandar Milosavljević,
Bratislav Obradović and Goran Poparić

University of Belgrade,
Faculty of Physics

Serbian Academy
of Sciences and Arts

28th Summer School and International Symposium on the Physics of Ionized Gases

Mr Miloš Ranković

Laboratory for atomic collision process
Institute of Physics,
University of Belgrade
Pregrevica 118,
11080 Belgrade,
Serbia

Belgrade, 23rd January 2016.

Dear Mr Ranković,

On behalf of the Scientific and Organizing Committees, we have a pleasure to invite you to attend the *28th Summer School and International Symposium on the Physics of Ionized Gases* (SPIG 2016) and present a **progress report** (20 min, including questions and discussions) aimed at the topics covered by the Section *1 (Atomic Collision Processes).*

The SPIG 2016 will be held from 29th August to 2nd September in Belgrade, Serbia. The details of the conference are available at www.spig2016.ipb.ac.rs. Unfortunately, due to the limited conference budget, the organizers cannot commit to any financial support.
We hope that you will be able to accept our invitation. Please let us know by the 1st of February and send us the title of your lecture.
We look forward to welcoming you to Belgrade.

Yours sincerely,

Dragana Marić
(Co-Chair of the Scientific Committee)

Goran Poparić
(Co-Chair of the Loc. Org. Committee)

Aleksandar R. Milosavljević
(Co-Chair of the Scientific Committee)

Bratislav Obradović
(Co-Chair of the Loc. Org. Committee)

Local organizing Committee:

Faculty of Physics, University of Belgrade
Studentski trg 12
11000 Belgrade, Serbia

Tel: +381 11 715-8151
Fax: +381 11 328-2 619

E-mail: spig2016@ff.bg.ac.rs
Web: www.spig2016.ipb.ac.rs

ELECTRON IMPACT ACTION SPECTROSCOPY OF MASS/CHARGE SELECTED MACROMOLECULAR IONS

Miloš Lj. Ranković [1], Alexandre Giuliani [2, 3] and Aleksandar R. Milosavljević [1,2]

[1] Institute of Physics Belgrade, University of Belgrade, Pregrevica 118, 11080 Belgrade, Serbia
[2] SOLEIL, l'Orme des Merisiers, St Aubin, BP48, 91192 Gif sur Yvette Cedex, France
[3]INRA, UAR1008, CEPIA, Rue de la Géraudière, BP 71627, 44316 Nantes, France

With the advent of modern mass spectrometry tools, as well as the electrospray ionization techniques, it has become possible to study large macromolecules in the gas phase. Recently Milosavljević et al [1] performed the action near edge X-ray absorption fine structure (NEXAFS) of a protein, by coupling the soft X-ray beamline PLEIADES at SOLEIL synchrotron with a linear quadrupole ion trap mass spectrometer. Here, we present the results from an electron impact action spectroscopy of trapped Ubiquitin protein, by coupling the same mass spectrometer with a focusing electron gun [2, 3]. We also compare the electron and photon impact results.

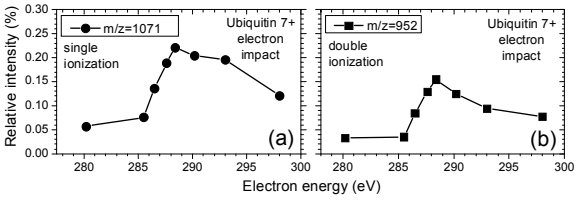

Figure 1. Single (a) and double (b) ionization yields from Ubiquitin 7+ precursor activated by electron impact.

Acknowledgements: This work was supported by ANR, France, under project ANR-08-BLAN-0065, MESTD of Republic of Serbia project #171020, and COST action STSM CM1301.

REFERENCES

[1] A. R. Milosavljević et al, *J. Phys. Chem. Lett.* 6, 16 (2015).
[2] M. Lj. Ranković, et al, *Appl.Phys. Lett.* 108, 064101 (2016).
[3] M. Lj. Ranković et al, *Eur. Phys. J.* D 70, 7 (2016).

CELINA

cost
EUROPEAN COOPERATION
IN SCIENCE AND TECHNOLO

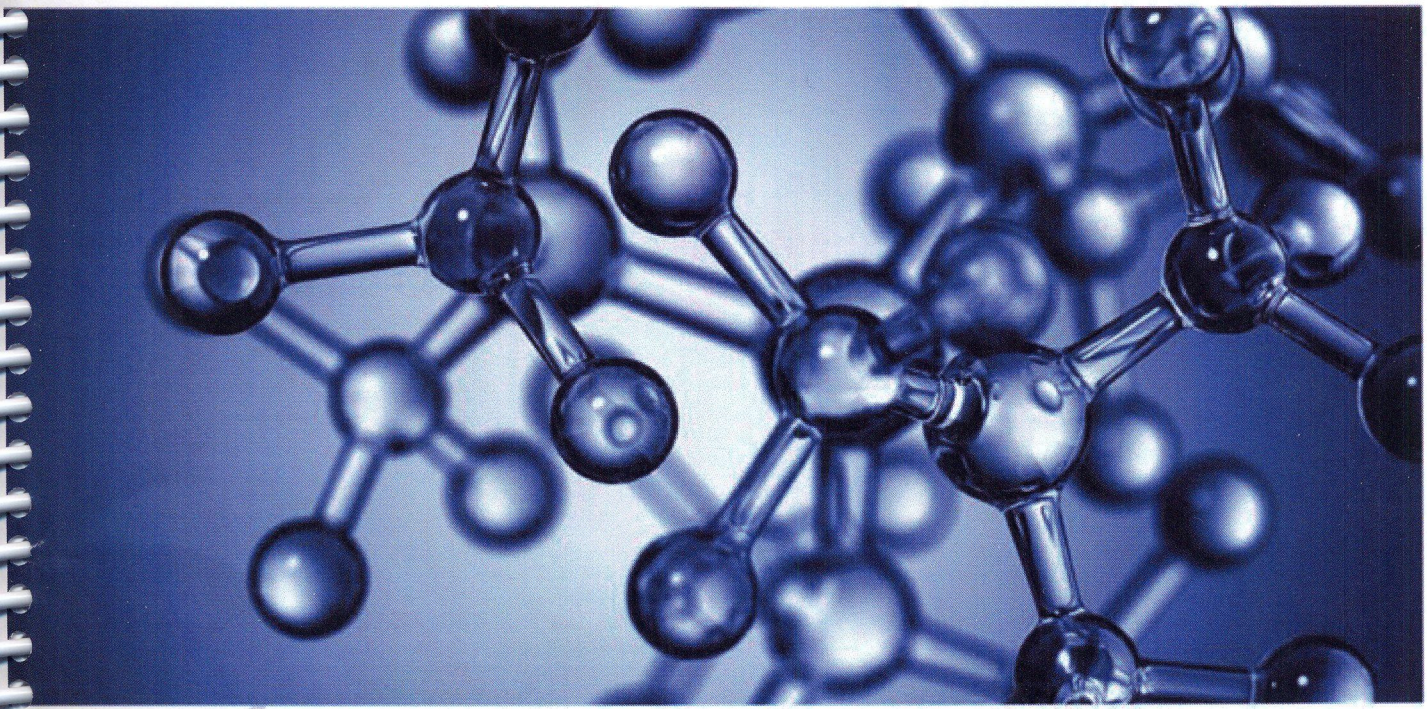

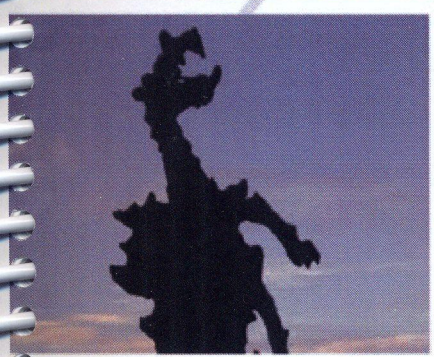

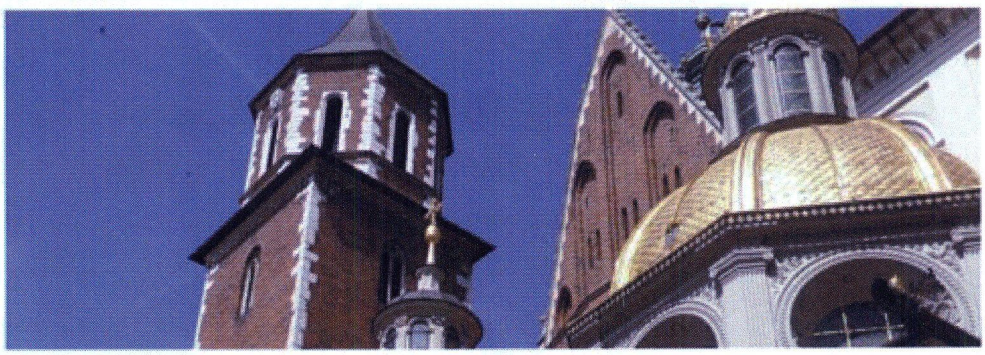

The 3rd CELINA Meeting

Kraków, May 18-20, 2016

The third Annual Meeting of COST Action CM1301 – Krakow, May 18-20, 2016

is organized by Siedlce University of Natural Sciences and Humaniteis jointly with the Academic Centre for Materials and Nanotechnology of the AGH University of Science and Technology in Krakow:

Organizers:

International Organizing Committee:

Petra Swiderek (University of Bremen, DE)

Cornelis W. Hagen (Delft University of Technology, NL)

Nigel Mason (The Open University, UK)

Janina Kopyra (Siedlce University, PL)

Oddur Ingolfsson (University of Iceland, IS)

Sven Barth (Vienna University of Technology, AT)

Patrik Hoffmann (EMPA Thun, CH)

Ivo Utke (EMPA Thun, CH)

Roser Valenti (University of Frankfurt, DE)

Local Organizing Committee:

Janina Kopyra (Siedlce University)

Aleksandra Szkudlarek (ACMIN)

Katarzyna Berent (ACMIN)

Katarzyna Hnida (ACMIN)

Kamila Kollbek (ACMIN)

Subject **COST CELINA 2016_Invitation**
From CELINA 2016 <celina2016@uph.edu.pl>
To <mrankovic@ipb.ac.rs>
Date 03/16/2016 12:21
Priority Normal

Dear Mr. Milos Rankovic,

On behalf of the organizers I would like to invite you to give a talk on your recent work at the annual meeting of the COST Action CM1301 on Chemistry for Electron-Induced Nanofabrication (CELINA). The meeting will be held in Krakow, Poland the 18th to 20th of May 2016.

http://www.celina.uni-bremen.de/celina/celina2016

Please notify me at the earliest opportunity if you can accept this invitation.

Yours sincerely,

Janina Kopyra
Chair of the organizing committee

Design and performance of an instrument for gas phase electron spectroscopy of trapped molecular ions

Miloš Lj. Ranković [1,*], Alexandre Giuliani [2, 3] and Aleksandar R. Milosavljević [1,2]

(1) Institute of Physics Belgrade, University of Belgrade, Pregrevica 118, 11080 Belgrade, Serbia
(2) SOLEIL, l'Orme des Merisiers, St Aubin, BP48, 91192 Gif sur Yvette Cedex, France
(3) INRA, UAR1008, CEPIA, Rue de la Géraudière, BP 71627, 44316 Nantes, France

e-mail: mrankovic@ipb.ac.rs

The electron interaction with atoms and molecules in the gas phase, has been studied for more than a century [1]. Over the years, electrons are used to probe the fundamental properties of atoms and molecules, such as electronic structure and chemical reactivity. Particularly, inner-shell electron spectroscopy of gas phase molecules, found its application in a wide area of research fields [2].

Recently we have designed a new experimental setup [3], for electron impact tandem mass spectrometry and action spectroscopy of electrosprayed macromolecules, by coupling a focused electron gun with a commercial linear ion trap mass spectrometer. Herein, we discuss the experimental details of this setup and the electron beam tracing simulations performed in SIMION to investigate the propagation of 300 eV energy electrons inside the RF linear quadrupole ion trap. We present the first results of electron-induced dissociation of peptides, as well as possibilities to probe trapped CELINA precursor $SiOEt_4$ by electron impact.

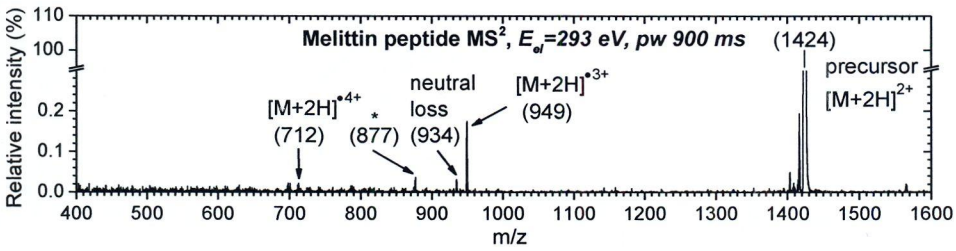

[1] N. J. Mason, *J. Phys. Conf. Ser.*, **565** (2014) 012001.
[2] A. P. Hitchcock, *J. Electron Spectros. Relat. Phenomena*, **112** (2000) 9.
[3] M. Lj. Ranković, A. Giuliani, A. R. Milosavljević, *Appl. Phys. Lett.*, **108 (2016)**064101.

CONFERENCE PROGRAM

ICPEAC 2015

XXIX INTERNATIONAL CONFERENCE on Photonic, Electronic and Atomic Collisions

22-28 JULY 2015 **TOLEDO** · SPAIN

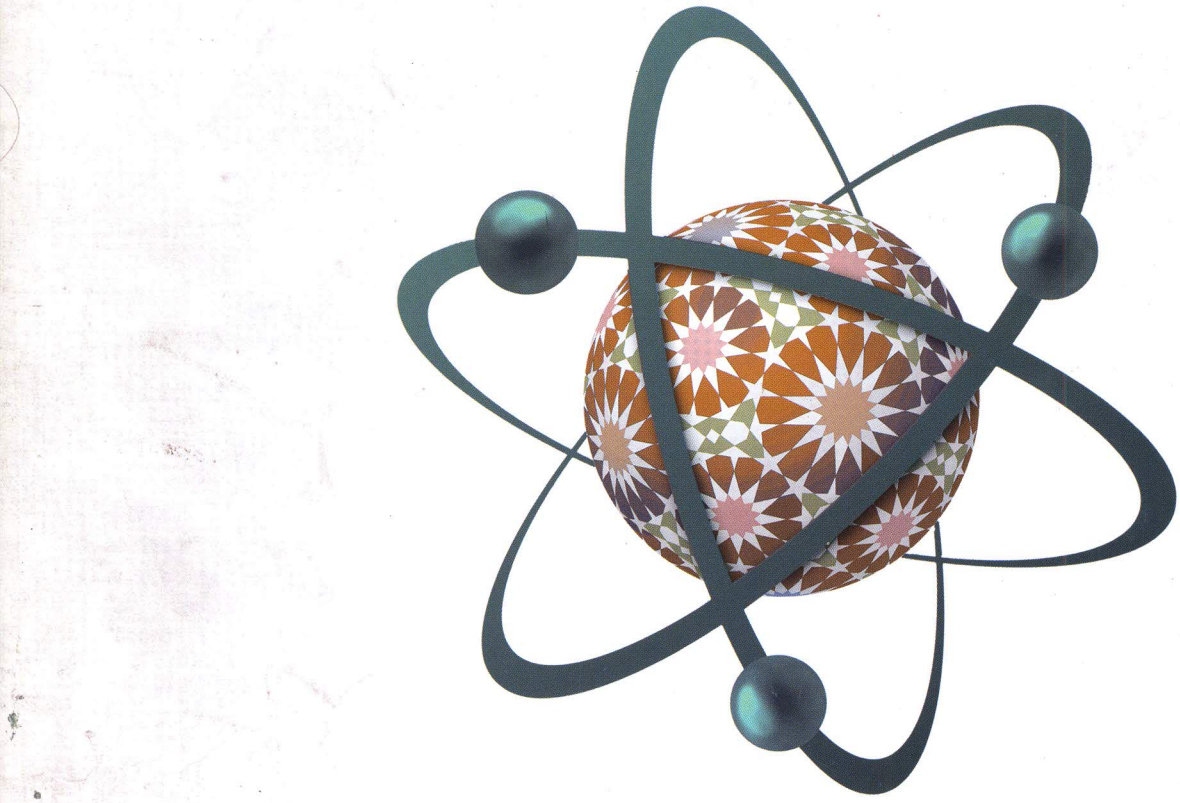

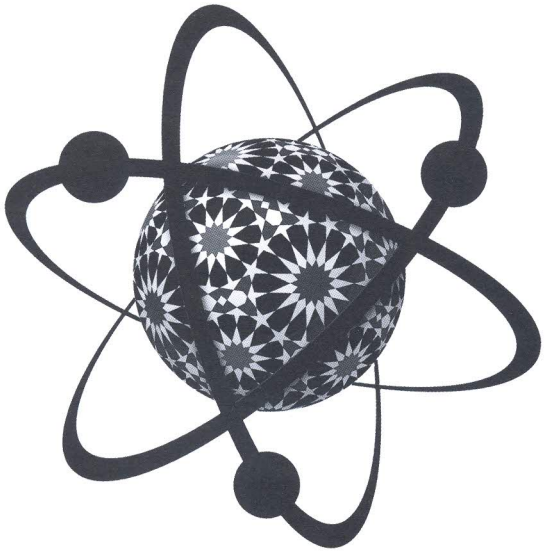

ICPEAC 2015

XXIX INTERNATIONAL CONFERENCE on Photonic, Electronic and Atomic Collisions

22-28 JULY 2015 TOLEDO · SPAIN

CONFERENCE PROGRAM

Edited By:

Fernando Martín, Gustavo García, Luis Méndez,
Luca Argenti, Alicia Palacios

XXIX ICPEAC Local Organizing Committee

Chair: Fernando Martín (UAM)

Co-Chairs: Gustavo García (CSIC)
Luis Méndez (UAM)

Secretaries: Luis Bañares (UCM)
Luis Roso (CLP)

Members: Manuel Alcamí (UAM)
Luca Argenti (UAM)
Enrique Conejero (US)
Inés Corral (UAM)
Gerardo Delgado (CSIC)
Cristina Díaz (UAM)
Sergio Díaz-Tendero (UAM)
Luis F. Errea (UAM)
Clara Illescas (UAM)
Otilia Mó (UAM)
Alicia Palacios (UAM)
Luis Plaja (US)
Rita Prosmiti (UAM)
Ismanuel Rabadán (UAM)
Paula Rivière (UAM)
Manuel Yáñez (UAM)

CLP	Centro de Láseres Pulsados, Salamanca
CSIC	Consejo Superior de Investigaciones Científicas, Madrid
UAM	Universidad Autónoma de Madrid
UCM	Universidad Complutense de Madrid
US	Universidad de Salamanca

Subject **Invitation for a Special Report oral presentation at ICPEAC 2015**
From Fernando Martín <fernando.martin@uam.es>
To <mrankovic@ipb.ac.rs>
Date 04/22/2015 13:47

To: Miloš Ranković Lj.
University of Belgrade
Serbia

Dear Miloš Ranković Lj.

On behalf of the ICPEAC 2015 International Programme Committee we are pleased to inform you that your communication entitled

"Photodissociation of protonated Leucine-Enkephalin peptide in the VUV range"

has been selected for a Special Report oral presentation at the XXIX International Conference on Photonic, Electronic and Atomic Collissions (XXIX ICPEAC), to be hel

Special Reports will be published in the J. Phys. Conference Series. We ask that speakers submit their papers at the conference so that the refereeing process can begi

For any query related to this invitation, please contact Alicia Palacios at alicia.palacios@uam.es.

We hope very much that you will be able to accept our invitation: please let us know by **1 May 2015** at the latest. Please be aware that this is a personal invitation that ca

We look forward to welcoming you to Toledo in 2015.

Yours sincerely

Roberto D. Rivarola
International Chair of XXIX ICPEAC
Instituto de Física de Rosario
Universidad Nacional de Rosario
Rosario Argentina

Fernando Martín
Local Chair of XXIX ICPEAC
Departamento de Química, Módulo 13
Universidad Autónoma de Madrid
28049 Madrid, Spain

SR

Photodissociation of protonated Leucine-Enkephalin peptide in the VUV range

M. Lj. Ranković[1*], V. Cerovski[1], F. Canon[2], L. Nahon[3], A. Giuliani[3,4] and A. R. Milosavljević[1]

[1]Institute of Physics Belgrade, University of Belgrade, Pregrevica 118, 11080 Belgrade, Serbia
[2]INRA, UMR1324 Centre des Sciences du Goût et de l'Alimentation, F-21000 Dijon, France
[3]SOLEIL, l'Orme des Merisiers, St Aubin, BP48, 91192 Gif sur Yvette Cedex, France
[4]INRA, UAR1008, CEPIA, Rue de la Géraudière, BP 71627, 44316 Nantes, France

Synopsis We present results of VUV action spectroscopy of gas-phase protonated Leucin-Enkephalin peptide. The experiment has been performed by coupling a linear quadrupole ion trap with a synchrotron radiation VUV beamline.

Recent development of experimental methods that use electrospray ion source (ESI) to bring macromolecules into gas phase and collect the ions in an ion trap, which is coupled to bright synchrotron radiation sources, has allowed the investigation of large biopolymers (proteins and nucleotides) under well-defined conditions. These studies can provide more detailed insight into fundamental properties of biopolymers and their interaction with high energy photons.

We present the results of VUV photon action spectroscopy of Leucin-Enkephalin (Leu-Enk) peptide in 5-15 eV energy domain. This peptide has been studied with wide range of spectrometry techniques and has become a standard biomolecular target [1].

The experiment has been performed at the beamline DESIRS [2] of the synchrotron radiation facility SOLEIL near Paris, France. More details about the experimental setup can be found in recent publications [3, 4]. Briefly, precursor ions $[Leu\text{-}Enk+H]^+$ were produced by ESI and injected into the ion trap from the front side. Ions were irradiated with monochromatized VUV photon beam, during 500 ms from the back side of the ion trap. After irradiation all ion fragment species were ejected from the ion trap and tandem mass spectra (MS^2) as a function of the photon energies were recorded. Leu-Enk molecules were provided from Sigma Aldrich and dissolved in water/acetonitrile at 10 μM.

Photodissociation ion yields were extracted from the MS^2 and normalized to the total ion current and the photon flux. The ion yields show spectroscopic structure allowing the studying of absorption-like bands of the peptide. Figure 1 shows the relative ion yield of one of the backbone fragments. The present experimental results are in good agreement with our time dependent density functional theory (TD DFT) calculations.

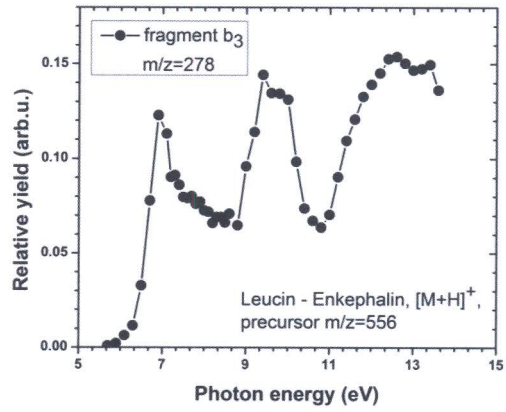

Figure 1. Relative ion yield of fragment b_3 from the photodissociation of precursor $[Leu\text{-}Enk+H]^+$.

We acknowledge the support by the ANR, France, under project ANR-08-BLAN-0065. A.R.M. and M.LJ.R. acknowledge support by the MESTD RS (Projects No. 171020). The SOLEIL synchrotron radiation facility is acknowledged for providing beamtime under project 20130388.

References

[1] S. Bari et al 2011, J. Chem. Phys. 18 **134**, 024314.
[2] L. Nahon et al 2012, J. Sync. Rad. **19**, 508 – 520.
[3] A. Milosavljević et al 2011, Phys. Chem. Chem. Phys. **13**, 15432–15436.
[4] A. Milosavljević et al 2012, J. Sync. Rad. **19**, 174.

* E-mail: mrankovic@ipb.ac.rs

TUESDAY

Photoinduced fragmentation of gas-phase protonated leucine- enkephalin peptide in the VUV range

2015 J. Phys.: Conf. Ser. 635 012034

(http://iopscience.iop.org/1742-6596/635/1/012034)

Journal of Physics: Conference Series **635** (2015) 012034 doi:10.1088/1742-6596/635/1/012034

Photoinduced fragmentation of gas-phase protonated leucine-enkephalin peptide in the VUV range

M Lj Ranković[1*], F Canon[2], L Nahon[3], A Giuliani[3,4] and A R Milosavljević[1,5]
[1] Institute of Physics Belgrade, University of Belgrade, Pregrevica 118, 11080 Belgrade, Serbia
[2] INRA, UMR1324 Centre des Sciences du Goût et de l'Alimentation, F-21000 Dijon, France
[3] SOLEIL, L'Orme des Merisiers, St Aubin, BP48, 91192 Gif sur Yvette Cedex, France
[4] INRA, UAR1008, CEPIA, Rue de la Géraudière, BP 71627, 44316 Nantes, France
[5] Radiation Laboratory, University of Notre Dame, Notre Dame, Indiana 46556, USA

E-mail: mrankovic@ipb.ac.rs

Abstract. In this article we report new results for action spectroscopy of protonated peptide Leucine enkephalin (YGGFL). By coupling a linear ion trap mass spectrometer with a vacuum ultraviolet (VUV) synchrotron radiation beamline, we investigate photofragmentation pattern of this peptide, through the analysis of tandem mass spectra recorded over a range of VUV photon energies, below and above the ionization energy. The obtained fragmentation patterns are discussed and compared to previous results.

1. Introduction

Development of electrospray ionization (ESI) [1], along with the advances in mass spectrometry techniques in recent years, has allowed manipulation of large bio-molecular ionic species in the gas phase. Therefore, fundamental properties of peptides, proteins, and nucleic acids such as ionization energies, bond energies and electronic energy levels could be investigated through action spectroscopy methods. In the present work ESI technique is used to produce intact biomolecular ionic species in the gas phase, from liquid solutions of these molecules. Tandem mass spectrometry by using VUV as an activation method was employed to investigate targets of interest.

Leucine enkephalin (Leu-enk) peptide is formed from five amino acids joined through peptide bonds, with the sequence tyrosine-glycine-glycine-phenylalanine-leucine (or YGGFL, in one letter coding). Leu-enk is an ideal candidate to study because it is small enough to be easily manageable with mass spectrometry techniques and to allow clear analysis of fragmentation products, while still being big enough to represent peptides. Usually the site of protonation is at N-terminus of the first amino acid - tyrosine, although other protonation sites were reported in the literature, as a consequence of proton mobility (see [2] and references therein). A standard nomenclature of the backbone fragments is based on where the positive charge (proton) stays upon bond scission and which particular bond is cleaved. If the proton stays at C-terminal, fragments a, b, c are formed, while fragments x, y, z originate from the N-terminal. Numbers in the subscripts of the fragment letters indicate the number of amino acid residues left in the particular fragment. Cleavage of the peptide C-N bonds is the origin of b and y fragment ions. Figure 1 displays a schematic structure of the Leu-enk peptide and denotation of some backbone fragments relevant for the present work.

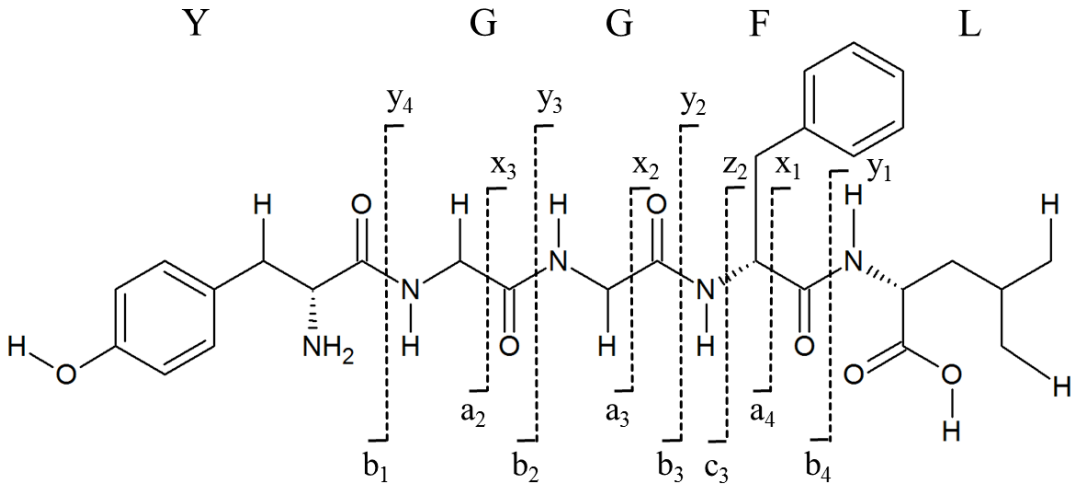

Figure 1. Schematic structure of Leucine enkephalin peptide with denoted fragments (dashed lines) and constituent amino acids (in one letter code).

Leu-enk has been probed with a vast number of different techniques, covering fragmentation pattern information and fragment yields. The reported results include collision induced dissociation (CID) [3], surface induced dissociation (SID) [4], blackbody infrared radiative dissociation (BIRD) [5] and laser-induced dissociation (LID) [6]. Each of these methods produces different conditions which favor certain decomposition pathways governed by certain fragmentation mechanisms. An extensive study of fragmentation schemes has been reported for protonated Leu-enk in the experiment involving multiple-resonance CID, by V. Rakov *et al*. in [3]. One of the reasons Leu-enk is used as a standard peptide is because it is very useful for testing and tuning new experimental setups, since it has been found that abundance ratios of some fragment ions can indicate an amount of internal energy deposited in the precursor ions [7]. Therefore, experimental parameters of a setup are adjusted in such a way that various ratios of Leu-enk's fragment intensities are kept constant. On the other hand, ratios of a_4/b_4 and b_3/y_2 can indicate at least qualitatively the degree of excitation of the precursor ions.

Amino acids and peptides strongly absorb VUV light [8]. Therefore an investigation of VUV interaction with peptides is of great interest. The only VUV light source with high enough brilliance and flexibility to continuously change the photon energy over a wide range is the synchrotron radiation source. A comprehensive study of VUV-induced fragmentation of protonated Leu-enk was reported by S. Bari *et al* in [9]. In the present work, we extend this investigation by means of mass resolution, the number of assigned ionic fragments and the photon energy range. The obtained results are also compared with existing data.

2. Experiment

Mass spectra in this article were obtained using the experimental setup located at the synchrotron SOLEIL near Paris, France. A commercial mass spectrometer Thermo Phiningan LTQ XL (LTQ) equipped with ESI was connected to the synchrotron VUV beamline DESIRS [10], with custom made turbo differential vacuum manifold [11-13]. Leu-enk ions produced by ESI were isolated in a linear quadrupole ion trap and subjected to VUV photons. After well-defined time of irradiation (500 ms in the present experiment) at particular photon energy, tandem mass spectra (MS^2) were recorded.

The LTQ mass spectrometer was connected to the synchrotron beamline from the back side of the LTQ. A dedicated vacuum manifold has been made to accommodate the pressure difference between

the LTQ and the beamline. One side of the vacuum manifold was fixed to the beamline where the pressure is in the order of 10^{-8} mbar, while the other side was connected via flexible bellow to the back plate window of the mass spectrometer. The pressure of the Helium buffer gas inside the ion trap of LTQ is of the order of 10^{-3} mbar while the pressure in the spectrometer is of the order of 10^{-5} mbar. During the operation and photon irradiation, the pressure inside the vacuum manifold was in the order of 10^{-6} mbar. A home-made rotating mechanical shutter driven by an electric motor was built and positioned in front of the photon beam inside the vacuum manifold. Cooling of the electric motor in the vacuum was established through heat conduction through a massive copper heat sink (holder) tightly surrounding the motor [14]. Alignment of the photon beam with respect to the ion trap's axis was achieved by using a custom supporting frame, mounted under the LTQ. It has several degrees of freedom, both translational and rotational, which allow for a fine alignment of the ion trap position with respect to the incident photon beam. An optimal alignment provides the highest overlap between cylindrical ion trapping region and the photon beam and is essential for the experiment.

Leu-enk was provided from Sigma-Aldrich as a powder and it was diluted with water/acetonitrile 75:25% v/v solution to the final concentration of 10 μM. The ESI source is positioned on the front side of LTQ. The ions formed by ESI source from the solution are guided by a system of ion lenses and stored in the ion trap. Parameters of ESI were optimized to obtain highest possible abundance of protonated Leu-enk cations $[YGGFL+H]^+$. A typically recorded mass spectrum (MS^1) produced by ESI is displayed in figure 2.

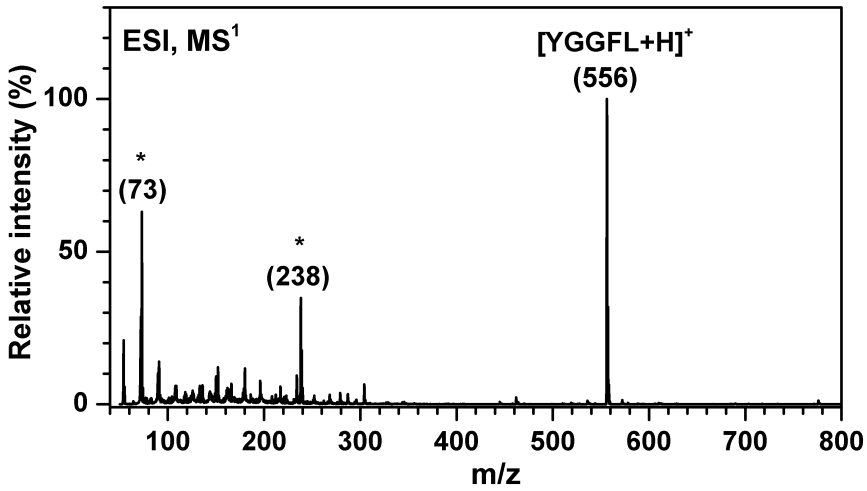

Figure 2. The mass spectrum of electro-sprayed Leu-enk ions from water/acetonitrile 75/25% solution with 10 μM concentration of peptide molecules. The peak in the spectrum at m/z 556 corresponds to the protonated Leu-enk cation $[YGGFL+H]^+$, while two peaks denoted with a star originate from pollutions.

The precursor ions of interest, in this case $[YGGFL+H]^+$, were selected and isolated in the ion trap, by means of ejecting all other ions. When enough precursor ions are accumulated in the ion trap or when a time limit for ion accumulation is reached, the mechanical shutter opens and the monochromatic VUV photon beam of defined energy irradiates the precursor ions. Synchrotron beamline DESIRS [10] is equipped with a gas filter cutting off higher order harmonics, which can create an additional signal originating from higher photon energies. If filled with Krypton, the gas filter cuts off all photon energies above 14 eV. Additionally, a MgF_2 glass filter is inserted as the part of the vacuum manifold assembly, to cut off the higher harmonics over 10.6 eV. The photon beam produced by the beamline undulator is monochromatized by using a normal incidence monochromator, resulting in final energy resolution of around 10 meV in the present case.

3. Results and discussion

J. Sztáray *et al*. in [15] performed a review of the studies about Leu-enk energetics and reaction pathways, so we will focus here only on the discussion of the most prominent fragments prevailing under our experimental conditions. Figure 3 displays the tandem mass spectra obtained for protonated Leu-enk precursor ions $[YGGFL+H]^+$ after activation with synchrotron VUV photons at three different energies. The mass spectra have been normalized to show the precursor ions $[YGGFL+H]^+$ at m/z 556 with 100 % relative intensity.

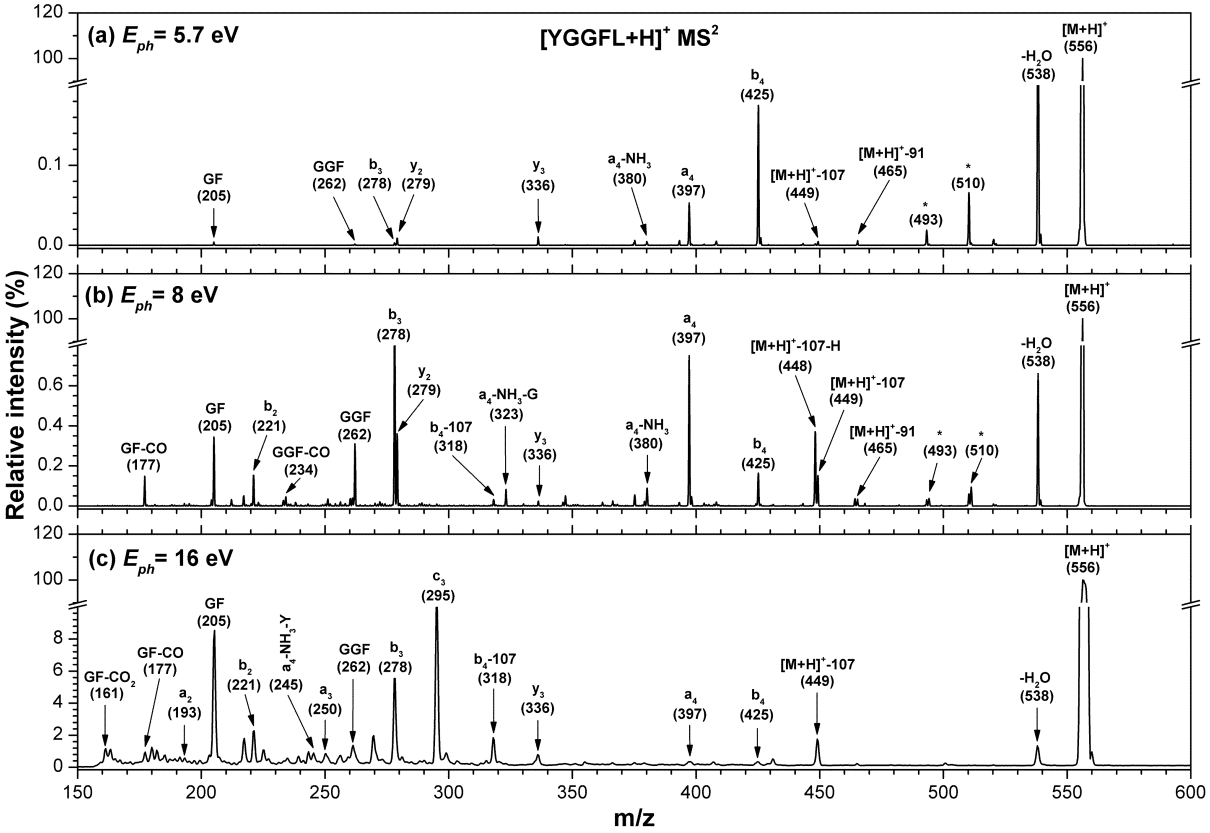

Figure 3. Tandem mass spectrum of protonated Leucine enkephalin precursor ions after irradiation with photons of a) 5.7 eV b) 8 eV and c) 16 eV.

Fragmentation patterns in our spectra are in good agreement with the ones reported in [9], which is expected considering the similar experimental conditions: VUV synchrotron photon activation of trapped ions. The lack of x and z and low abundant y-sequence ions in our spectra confirm that N-terminal ions are favoured. The ionization energy (IE) of protonated Leu-enk was determined by DFT calculations to be 8.87 eV [16]. The radical cation is not observed in our spectra and it is likely that it is not stable and fragments readily after its formation, as it has been proposed by Bari *et al*. [9]. For sub-ionisation energies absorption of photons by precursor ions leaves them in an excited electronic state. This energy may be redistributed internally via intramolecular vibrational processes, causing the weak peptide C-N bonds to break first, forming the backbone ions b and y. According to the fragmentation scheme proposed in [3], the major reaction pathway is following: YGFFL-b_4-a_4-b_3-b_2-a_2-Y. All these ions are present in our mass spectra, except Y (136), due to the mass cut off at m/z 150. Backbone ion b_4 (m/z 425) needs the lowest photon energy to form and it shows up as the strongest fragment at 5.7 eV in our mass spectrum. This ion is formed directly from dissociation of the precursor ions. The fragment at m/z 538 corresponds to the loss of a water molecule from the

precursor ions. Its intensity is highest among all fragments in the lowest energy region but falls quickly with the increase of the photon energy. Note that this fragment has not been discussed in the previous work by Bari et al. [9]. Following figure 1, after CO loss, b_4 forms into the fragment ion a_4 (m/z 397). Ion a_4 dissociates with the neutral loss of NH_3 into fragment at m/z 380. After Glycine residue loss (-57) near ionization energy, this ion is observed at a_4-NH_3-G (m/z 323). It is also reported and discussed in detail by a group of Glish, as a rearrangement fragment FYG (m/z 323) [17]. The intensity of the ion a_4 exceeds the b_4 intensity and peaks at around 7 eV, where it is the most prominent fragment in the mass spectrum. This energy corresponds to the peak of the absorption band coming from the π-π^* peptide transition. Fragment b_3 (m/z 278) is the next in line to show up as a dominant fragment with further increase of the photon energy. Ion b_3 is formed from a_4 ion while further dissociation of b_3 forms b_2 (m/z 221). C-terminal ion y_2 (m/z 279) has a higher intensity than b_3 (278) in the low energy region. With the increase of photon energy, the internal energy of the precursor ions rises, resulting in the drop of the intensity of y_2 ions compared to the intensity of b_3 ions, similarly as for b_4 and a_4 ions, respectively. The peak designated at m/z 449 corresponds to the tyrosine side chain loss of the precursor ions while the loss of the phenylalanine side chain is responsible for a small peak at m/z 465. H loss from 449 leads to a fragment designated at m/z 448. Loss of tyrosine side chain is also noticed from backbone fragment b_4, so fragment b_4-107 (318) is observed. As the photon activation energy goes over the IE of Leu-enk (8.87 eV) more reaction channels become open. New reaction channels above the IE lead to internal fragments GGF (m/z 262) and GF (m/z 205). These fragments are also present in the sub ionization energies, but with very small abundances. Suffering the CO loss, these ions form GGF-CO (m/z 234) and GF-CO (m/z 177). In the second channel with another CO_2 loss from GF, fragments at m/z 161 are created. Above the IE internal fragments dominate over the backbone by more than a factor of 10. At 16 eV, the most prominent fragments are c_3 (m/z 295) and GF (m/z 205). Mass-to-charge ratio of doubly ionized precursor ions $[Leu\text{-}enk+H]^{2+}$ is the same as for b_3 ion at m/z 278. According to [9], it is possible that small abundance of doubly ionized precursor ions contributes to the intensity of the m/z 278 peak. Internal C-terminal fragment a_3 (m/z 250) is formed upon CO loss from b_3 ion and along with ion a_2 (m/z 193) shows up at energies above 14 eV. Both backbone and internal fragment ions peak at around 20 eV with a very broad peak, which is also reported in [9]. At 24 eV being the final energy point in our scans, all fragments are in a decline with GF (205), b_2 (221), b_3 (278) and c_3 (295) dominating the spectra at around 1% of the precursor ion intensity.

4. Conclusions

A linear quadrupole ion trap mass spectrometer was coupled to a synchrotron beamline to study the VUV photo-induced dissociation of gas-phase protonated Leu-enk cations. The present experiment extends previous studies by means of high spectral purity of the photon beam, increased sensitivity and mass resolution (in the case of VUV/ion trap results) and increased energy range. Presented mass spectra are in good agreement with the existing fragmentation data in the literature. The fragmentation of the Leu-enk peptide shows a clear and interesting energy dependence that can be related to electronic excitation processes, which will be investigated in more details in future papers.

5. Acknowledgments

This work was supported by the French ANR (Project ANR-08-BLAN-0065), the “Pavle Savic” bilateral scientific project between Serbia and France (N27482TE) and the COST Action MP1002 (Nano-IBCT). Milosavljević A R and Ranković M Lj acknowledge support by the Ministry of education, science and technological development of Republic or Serbia under the Project 171020. We are grateful to the SOLEIL synchrotron general staff for providing the beamtime under the Projects 20110324 and 20130388.

6. References

[1] Yamashita M, Fenn J B 1984 *J Phys Chem* **88** (20) 4451-4459
[2] Polfer N C, Oomens J, Suhai S, Paizs B 2007 *J Am Chem Soc* **129** 5887-5897
[3] Rakov V S, Borisov O V, Whitehouse C M 2004 *J Am Soc Mass Spectrom* **15** 1794–1809
[4] Laskin J 2006 *J Phys Chem* A **110** 8554
[5] Schnier P, Price W, Strittmatter E and Williams E 1997 *J Am Soc Mass Spectrom* **8** 771
[6] Tabarin T, Antoine R, Broyer M and Dugourd P 2005 *Rapid Commun Mass Spectrom* **19** 2883
[7] Alexander A J, Boyd R K 1989 *Int J Mass Spectrom Ion Processes* **90** 211-240
[8] Kobayashi K, Kasamatsu T, Kaneko T, Koike J, Oshima T, Saito T, Yamamoto T and Yanagawa H 1995 *Adv Space Res* **16** 21
[9] Bari S, Gonzalez M O, Reitsma G, Werner J, Schippers S, Hoekstra R and Schlatholter T 2011 *J Chem Phys* **134** 024314
[10] Nahon L, Oliveira N, Garcia G, Gil J F, Pilette B, Marcouille O, Lagarde B and Polack F 2012 *J Synchrotron Radiat* **19** 508-520
[11] Milosavljević A R, Nicolas C, Lemaire J, Déhon C, Thissen R., Bizau J M, Réfrégiers M, Nahon L and Giuliani A 2011 *Phys Chem Chem Phys* **13** 15432
[12] Milosavljević A R, Canon F, Nicolas C, Miron C, Nahon L and Giuliani A 2012 *J Phys Chem Lett* **3** 119
[13] Milosavljević A R, Nicolas C, Gil J F, Canon F, Réfrégiers M, Nahon L and Giuliani A 2012 *J Synchrotron Radiat* **19** 174
[14] Milosavljević A R, Nicolas C, Gil J F, Réfrégiers M, Nahon L and Giuliani 2012 *Nucl Instrum Methods Phys Res B* **279** 34-36
[15] Sztáray J, Memboeuf A, Drahos L and Vékey K 2010 *Mass Spectrom Rev* **30** 298
[16] Frisch M J, Trucks G W and Schlegel H B 2004, Gaussian 03, Revision C.02 (Gaussian Inc. Wallingford CT)
[17] Vachet R W, Bishop B M, Erickson B W and Glish G L 1997 *J Am Chem Soc* **119** 5481-5488

Citation Report: 11

(from Web of Science Core Collection)

You searched for: **AUTHOR:** (Rankovic M*) **...More**

This report reflects citations to source items indexed within Web of Science Core Collection. Perform a Cited Reference Search to include citations to items not indexed within Web of Science Core Collection.

Published Items in Each Year

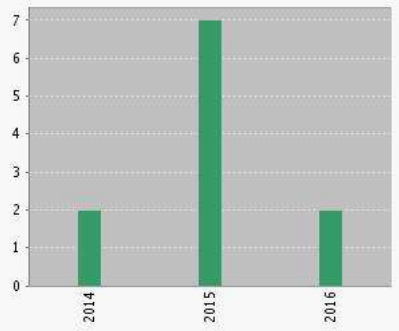

The latest 20 years are displayed.

Citations in Each Year

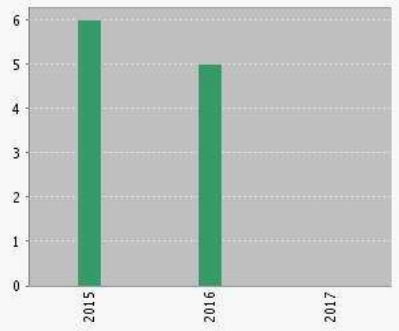

The latest 20 years are displayed.

Results found:	11
Sum of the Times Cited [?] :	11
Sum of Times Cited without self-citations [?] :	9
Citing Articles [?] :	11
Citing Articles without self-citations [?] :	9
Average Citations per Item [?] :	1.00
h-index [?] :	2

Sort by: **Times Cited -- highest to lowest**

Page 1 of 2

Use the checkboxes to remove individual items from this Citation Report

or restrict to items published between **1996** and **2017** Go

	2013	2014	2015	2016	2017	Total	Average Citations per Year
	0	**0**	**6**	**5**	**0**	**11**	**3.67**
1. **Energy-Dependent UV Photodissociation of Gas-Phase Adenosine Monophosphate Nucleotide Ions: The Role of a Single Solvent Molecule** By: Milosavljevic, Aleksandar R.; Cerovski, Viktor Z.; Canon, Francis; et al. JOURNAL OF PHYSICAL CHEMISTRY LETTERS Volume: 5 Issue: 11 Pages: 1994-1999 Published: JUN 5 2014	0	0	4	1	0	5	1.25
2. **K-Shell Excitation and Ionization of a Gas-Phase Protein: Interplay between Electronic Structure and Protein Folding** By: Milosavljevic, Aleksandar R.; Nicolas, Christophe; Rankovic, Milos L. J.; et al. JOURNAL OF PHYSICAL CHEMISTRY LETTERS Volume: 6 Issue: 16 Pages: 3132-3138 Published: AUG 20 2015	0	0	1	2	0	3	1.00
3. **Sensitizing DNA Towards Low-Energy Electrons with 2-Fluoroadenine** By: Rackwitz, Jenny; Kopyra, Janina; Dabkowska, Iwona; et al. ANGEWANDTE CHEMIE-INTERNATIONAL EDITION Volume: 55 Issue: 35 Pages: 10248-10252 Published: AUG 22 2016	0	0	0	1	0	1	0.50
4. **Study of electron transmission through a platinum tube** By: Milosavljevic, A. R.; Rankovic, M. Lj; Borka, D.; et al. NUCLEAR INSTRUMENTS & METHODS IN PHYSICS RESEARCH SECTION B-BEAM INTERACTIONS WITH MATERIALS AND ATOMS Volume: 354 Pages: 86-89 Published: JUL 1 2015	0	0	0	1	0	1	0.33
5. **VUV photofragmentation of protonated leucine-enkephalin peptide dimer below ionization energy** By: Milosavljevic, Aleksandar R.; Cerovski, Viktor Z.; Rankovic, Milos Lj.; et al. EUROPEAN PHYSICAL JOURNAL D Volume: 68 Issue: 3 Article Number: 68 Published: MAR 25 2014	0	0	1	0	0	1	0.25
6. **Electron impact action spectroscopy of mass/charge selected macromolecular ions: Inner-shell excitation of ubiquitin protein** By: Rankovic, Milos Lj; Giuliani, Alexandre; Milosavljevic, Aleksandar R. APPLIED PHYSICS LETTERS Volume: 108 Issue: 6 Article Number: 064101 Published: FEB 8 2016	0	0	0	0	0	0	0.00
7. **VUV action spectroscopy of protonated leucine-enkephalin peptide in the 6-14 eV range** By: Rankovic, M. Lj.; Canon, F.; Nahon, L.; et al.	0	0	0	0	0	0	0.00

JOURNAL OF CHEMICAL PHYSICS Volume: 143 Issue: 24 Article Number: 244311
Published: DEC 28 2015

8.	**Study of electron transmission through a metallic capillary** By: Milosavljevkic, A. R.; Rankovic, M. Lj.; Borka, D.; et al. Edited by: Diaz, C; Rabadan, I; Garcia, G; et al. Conference: 29th International Conference on Photonic, Electronic, and Atomic Collisions (ICPEAC) Location: Toledo, SPAIN Date: JUL 22-28, 2015 Sponsor(s): Univ Autonoma Madrid; Consejo Super Investigaciones Cient XXIX INTERNATIONAL CONFERENCE ON PHOTONIC, ELECTRONIC, AND ATOMIC COLLISIONS (ICPEAC2015), PTS 1-12 Book Series: Journal of Physics Conference Series Volume: 635 Article Number: 062011 Published: 2015	0	0	0	0	0	0	0.00
9.	**Novel approaches to study low-energy electron-induced damage to DNA oligonucleotides** By: Rackwitz, Jenny; Rankovic, Milos Lj; Milosavljevic, Aleksandar R.; et al. Edited by: Diaz, C; Rabadan, I; Garcia, G; et al. Conference: 29th International Conference on Photonic, Electronic, and Atomic Collisions (ICPEAC) Location: Toledo, SPAIN Date: JUL 22-28, 2015 Sponsor(s): Univ Autonoma Madrid; Consejo Super Investigaciones Cient XXIX INTERNATIONAL CONFERENCE ON PHOTONIC, ELECTRONIC, AND ATOMIC COLLISIONS (ICPEAC2015), PTS 1-12 Book Series: Journal of Physics Conference Series Volume: 635 Article Number: 062001 Published: 2015	0	0	0	0	0	0	0.00
10.	**Photoinduced fragmentation of gas-phase protonated leucine-enkephalin peptide in the VUV range** By: Rankovic, M. Lj; Canon, F.; Nahon, L.; et al. Edited by: Diaz, C; Rabadan, I; Garcia, G; et al. Conference: 29th International Conference on Photonic, Electronic, and Atomic Collisions (ICPEAC) Location: Toledo, SPAIN Date: JUL 22-28, 2015 Sponsor(s): Univ Autonoma Madrid; Consejo Super Investigaciones Cient XXIX INTERNATIONAL CONFERENCE ON PHOTONIC, ELECTRONIC, AND ATOMIC COLLISIONS (ICPEAC2015), PTS 1-12 Book Series: Journal of Physics Conference Series Volume: 635 Article Number: UNSP 012034 Published: 2015	0	0	0	0	0	0	0.00

Select Page | Save to Text File

Sort by: Times Cited -- highest to lowest

Page 1 of 2

11 records matched your query of the 36,843,663 in the data limits you selected.

Citation overview

Citation overview This is a overview of citations for the documents you selected

Export | Print

13 cited documents Back to document results | Add to list

Document h-index : 2 Scopus does not have complete citation information for articles published before 1996. View h-graph

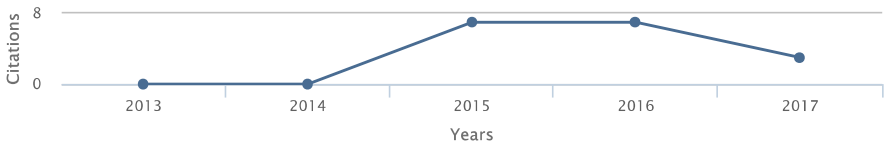

Date range: 2013 to 2017

Exclude self citations of all authors

Exclude Citations from books

Edit the data for this graph and the citation table below.

Update

Documents

Citations

Sort on: Date (newest) Citation count (descending)

	Documents		<2013	2013	2014	2015	2016	2017	Subtotal	>2017	Total
	Total		**0**	**0**	**0**	**7**	**7**	**3**	**17**	**0**	**17**
1	A novel setup for the determination of absolute cross sectio...	2017							0		0
2	Design and performance of an instrument for electron impact ...	2016					1		**1**		**1**
3	Electron impact action spectroscopy of mass/charge selected ...	2016					1		**1**		**1**
4	Sensitizing DNA Towards Low-Energy Electrons with 2-Fluoroad...	2016						2	**2**		**2**
5	VUV action spectroscopy of protonated leucine-enkephalin pep...	2015						1	**1**		**1**
6	Photoinduced fragmentation of gas-phase protonated leucine- ...	2015							0		0
7	K-Shell Excitation and Ionization of a Gas-Phase Protein: In...	2015				1	3		**4**		**4**
8	Study of electron transmission through a platinum tube	2015					1		**1**		**1**
9	Novel approaches to study low-energy electron-induced damage...	2015							0		0
10	Study of electron transmission through a metallic capillary	2015							0		0
11	Photodissociation of protonated Leucine-Enkephalin peptide i...	2015							0		0
12	Energy-dependent UV photodissociation of gas-phase adenosine...	2014				4	1		**5**		**5**
13	VUV photofragmentation of protonated leucine-enkephalin pept...	2014				2			**2**		**2**

Display 25 results

Page 1 / 1

UNIVERSITY OF BELGRADE
FACULTY OF PHYSICS

Miloš Lj. Ranković

Photon and electron action spectroscopy of trapped biomolecular ions - From isolated to nanosolvated species

Ph.D. Thesis

INSTITUTE OF PHYSICS BELGRADE
Belgrade, 2016.

UNIVERZITET U BEOGRADU
FIZIČKI FAKULTET

Miloš Lj. Ranković

Fotonska i elektronska akciona spektroskopija trapiranih biomolekularnih jona - od izolovanih do nanosolvatisanih čestica

Doktroska Disertacija

INSITUT ZA FIZIKU U BEOGRADU
Beograd, 2016.

Podaci o mentoru i članovima komisije

Mentor: dr Aleksandar Milosavljević, Naučni savetnik,

Institut za fiziku u Beogradu

Članovi komisije:

dr Bratislav Marinković

Naučni savetnik, Institut za fiziku u Beogradu

dr Alexandre Giuliani

Beamline scientist, synchrotron SOLEIL, France

Prof. dr Dragoljub Belić

Redovni profesor, Fizički fakultet, Univerzitet u Beogradu

Prof. dr Goran Poparić

Vanredni profesor, Fizički fakultet, Univerzitet u Beogradu

Prof. dr Nataša Nedeljković

Redovni profesor, Fizički fakultet, Univerzitet u Beogradu

Acknowledgements

The work presented in this Thesis was performed both in the Laboratory for Atomic Collision Processes, Institute of Physics Belgrade and at the beamlines DESIRS and PLEIADES of the SOLEIL synchrotron, France, during multiple beamtimes. All experiments were carried out under the supervision of my advisor Dr. Aleksandar Milosavljević, to whom I express my sincere gratitude. I would also like to thank Aleksandar for his help in writing this Thesis, his patience during the years, for answering all of my questions, for numerous advice and suggestions, for his trust and for always inspiring me to go forward.

During the past four years, we closely worked with Dr. Alexandre Giuliani from the SOLEIL, who always encouraged and supported me during my work as a Ph.D. student. I am very grateful for his suggestions, patience and help in both conducting the experiments and understanding the obtained results.

I would also like to thank Dr. Laurent Nahon, the DESIRS beamline manager, Dr. Cristophe Nicolas, the PLEIADES beamline scientist, Dr. Viktor Cerovski from Belgrade and Dr. Francis Canon from Dijon, for their help and interesting discussions during the beamtimes, as well as the SOLEIL general staff for running the beam smoothly.

I would like to thank Dr. Alexandre Giuliani, Dr. Bratislav Marinković, Prof. Dr. Dragoljub Belić, Prof. Dr. Goran Poparić and Prof. Dr. Nataša Nedeljković for accepting to be in the Commission Panel for the assessment of my Thesis, and for very useful suggestions and comments.

I am grateful to our technician Mr. Miroslav Maksimović for very useful suggestions and help in designing and assembling the experimental parts. Also, I would like to thank my father Mr. Ljubiša Ranković and Mr. Živko Sević for their help in designing and testing the custom electrical circuits.

I would like to thank my colleagues from the Institute of Physics in Belgrade, Dr. Jelena Maljković, Dr. Sanja Tošić, Dr. Predrag Kolraž, Dr. Dragutin Šević, Dr. Maja Rabasović, Dr. Jozo Jureta, Dr. Branko Tomčik, Mr. Andrej Bunjac, Dr. Nenad Simonović, Dr. Duška Popović and Dr. Tasko Grozdanov for their support and useful suggestions. I would like to thank Ph.D. students Mr. Ilija Simonović, Mrs. Tatjana Agatonović-Jovin and Ms. Nataša Tomić for their support during the hard times.

Finally, I am very grateful to my family, friends and Ms. Aleksandra Terzić for their understanding, help and support.

Belgrade, 15.04.2016.

Photon and electron action spectroscopy of trapped biomolecular ions – From isolated to nanosolvated species

In an effort to understand the vast complexity of the underlying processes within a cell at a molecular level, the first step lies in revealing the fundamental physical and chemical properties, as well as the structure, of biopolymers (proteins and DNA). With the development of modern experimental techniques it has become possible to study these large molecules under well-defined conditions in the gas phase, by closely inspecting their interactions with energetic photons and electrons.

In this Thesis, we present the experimental setups for the action spectroscopy of peptides, proteins and nucleotides, as well as the hydrated complexes (hydrated nucleotides), in the gas phase. We present the details and the operation of the two experimental setups based on coupling the linear quadrupole ion trap with: (1) a VUV or a soft X-ray synchrotron beamline and (2) a focusing electron gun.

In the case (1), the existing experimental setup consisting of a commercial quadrupole ion trap mass spectrometer (LTQ XL from Thermo Scientific), equipped with an electrospray ion source, was coupled to the VUV beamline DESIRS and the soft X-ray beamline PLEIADES at the synchrotron SOLEIL (France). The setups were used to study the photo-induced ionization/fragmentation of trapped biopolymers and nanosolvated species. The results obtained with this setups include VUV action spectroscopy of protonated Leucine-Enkephalin peptide (both a monomer and a dimer) and a nanosolvated nucleotide Adenosine monophosphate (AMP), in (5-15) eV photon energy range. The inner-shell action spectroscopy in the soft X-ray energy range (around C and N K-edge), was performed for multiply charged precursor of Ubiquitin protein. The photo-dissociation and photo-fragmentation ion yields for several fragment ions from all above mentioned macromolecules were extracted and the obtained spectral features were discussed considering relevant photon-induced processes.

In the case (2), new experimental setup was developed by coupling the same LTQ XL ion trap with a focusing electron gun, in order to perform an electron activation tandem mass spectrometry, as well as an electron-impact action spectroscopy of trapped biopolymer ions. The ion optic simulations using SIMION program were performed in order to investigate the propagation of the electron beam in the RF+DC ion trap. Tests measurements for electron-induced fragmentation of Substance P, Melittin and Ubiquitin are presented for the impact energy of 300 eV. Finally, we present the electron-impact inner-shell action spectroscopy of the multiply charged Ubiquitin protein, in the vicinity of C K-edge energies of (280-300) eV. The electron-impact results are compared with the soft X-ray photon-impact action spectroscopy results obtained for the same target.

Keywords: Mass spectrometry, Action spectroscopy, Photo-dissociation, Electron-induced dissociation, Synchrotron radiation, Electrospray ionization, Linear quadrupole ion trap, SIMION, Peptides, Proteins, Hydrated nucleotides.

Scientific field: Physics
Field of academic expertise: Atomic and molecular physics
UDC number: 539.2

Fotonska i elektronska akciona spektroskopija trapiranih biomolekularnih jona - od izolovanih do nanosolvatisanih čestica

U nastojanju da se razume ogromna složenost procesa u okviru ćelije na molekulskom nivou, prvi korak je otkrivanje fundamentalnih fizičko-hemijskih osobina, kao i strukture biopolimera (proteina i DNK). Razvojem savremenih eksperimentalnih tehnika omogućeno je proučavanje velikih biološki relevantnih molekula pod jasno definisanim uslovima u gasnoj fazi, izučavanjem njihovih interakcija sa fotonima i elektronima velikih energija.

U ovom radu su predstavljene eksperimentalne postavke za akcionu spektroskopiju peptida, proteina, nukleotida, kao i nanosolvatisanih kompleksa (hidratisani nukleotidi) u gasnoj fazi. Prikazani su detalji i princip rada dve eksperimentalne postavke zasnovane na povezivanju linearne kvadrupolne jonske zamke sa: (1) sinhrotronskim fotonskim mlazom (VUV i meki X-zraci) i (2) fokusirajućim elektronskim topom.

U slucaju (1), postojeća eksperimentalna aparatura koja sadrži linearnu kvadrupolnu jonsku zamku u okviru komercijalnog masenog spektrometra (LTQ XL od firme Thermo Scientific) povezana je sa VUV mlaznom linijom DESIRS i mlaznom linijom za meke X-zrake PLEIADES na sinhrotronu SOLEIL (Francuska). Aparatura je upotrebljena za izučavanje foto-indukovanih procesa jonizacije i fragmentacije zarobljenih jona biopolimera i nanosolvatisanih čestica. Rezultati dobijeni na ovoj aparaturi uključuju VUV akcionu spektroskopiju protonisanog leucin-enkefalin peptida (monomer i dimer), kao i nanosolvatisanog nukleotida adenosin monofosfata (AMP), u opsegu energija fotona od (5-15) eV. Akciona spektroskopija unutrašnje ljuske koristeći meke X-zrake (u oblasti C i N K-ljuske), urađena je za višestruko naelektrisani prekursor proteina ubikuitin. Za sve gore pomenute makromolekule, izučavani su absorpcioni spektri za neke od dobijenih jonskih produkata, pri čemu su analizirane uočene spektralne karakteristike dobijene u pomenutim fotonski indukovanim procesima.

U slucaju (2) razvijen je novi eksperimentalni sistem zasnovan na povezivanju iste LTQ XL jonske zamke sa elektronskim topim sa mlazom elektrona srednjih energija, koja omogućava tandem masenu spektrometriju i elektronski indukovanu akcionu spektroskopiju zarobljenih jona biopolimera. Korišćenjem programa SIMION, urađene su simulacije sa ciljem ispitivanja transmisije elektrona kroz jonsku zamku sa RF+DC potencijalima. Inicijalni testovi aparature uradjeni su fragmentacijom peptida supstance P i melitin, kao i ubikuitin proteina pri energijama elektrona u oblasti oko 300 eV. Na kraju, prikazani su rezultati elektronski-indukovane akcione spektroskopije višestruko naelektrisaniog jona ubikuitin proteina, u oblasti energija oko C K-ljuske (280-300) eV. Ovi rezultati su upoređeni sa rezultatima dobijenim za istu metu pri fotonski-indukovanim (X-zraci) procesima iz iste oblasti energija.

Ključne reči: Masena spektrometrija, Akciona spektroskopija, Foto-disocijacija, Elektronski indukovana disocijacija, Sinhrotronsko zračenje, Linearna kvadrupolna jonska zamka, Peptidi, Proteini, Hidratisani nukleotidi.

Naučna oblast: Fizika
Uža naučna oblast: Fizika atoma i molekula
UDK broj: 539.2

Contents

1 Introduction

The possibility to experimentally investigate the interactions of photons and electrons with large biopolymers such as peptides, proteins, nucleotides or complex weakly bound biological systems (for example hydrated biopolymers), in the gas phase under well-defined conditions, is of a great scientific importance. Such investigations provide more insights into fundamental physical and chemical properties, which lead to a better understanding of both their biological functions in the living organisms and the radiation damage on the molecular level.

A vast number of experimental studies performed on biopolymers are focused on revealing their electronic structures, ionization energies, bond energies, primary structures (amino acid sequences) and secondary structures (three-dimensional arrangements). It is also important to explore correlations between the electronic structure of large biopolymers, which is defined by their atomistic representation (governed by the laws of quantum mechanics) and the spatial arrangement of these macromolecules (which defines their active biological function). Understanding these relations could help developing a method for modeling the functions of biopolymers - a subject of much interest in the wide field of science.

Moreover, the study of the interaction of photons and electrons with isolated biological macromolecules helps to understand the radiation damage processes, which is important for the development of new and more efficient methods in medicine, for example in the therapy of cancers [1]. The interaction of UV radiation with DNA molecule was for many years a subject of an intensive theoretical and experimental research. It is known that DNA molecule very efficiently absorbs electromagnetic radiation in the ultraviolet (UV) region, but on the other hand, it is rather stable against the UV-induced destruction.

Out of all secondary products generated by the primary radiation, electrons are the most abundant. They can effectively interact with the constituents of DNA and induce braking of single and double chains of DNA (single and double strand brakes). Therefore, a huge number of studies of the interactions of electrons and isolated molecules, which are parts of the large macromolecules [2, 3] have been performed. However, the majority of the experimental research, both for the photons and electrons, has been conducted either with solvents or with relatively small molecules, which are isolated parts of the biopolymers.

1.1 Ion spectroscopy

In order to study the interaction of electrons and photons with large isolated biopolymers, it is necessary to somehow transfer these molecules in the gas phase. At the end of the last century, modern ionization techniques were developed, which enabled the isolation and the study of large molecular ions, in the gas phase. For example, electrospray ionization (ESI) [4] is a method which allows for very large (kDa) and fragile

biomolecules to be introduced from a solution, without degradation, into the gas phase. Furthermore, these ions can be isolated in a variety of high charge states (which is determined by the number of added or removed protons). The development of modern ionization techniques enabled the use of the mass spectrometry (MS) method for investigating the structure of macromolecules. Particularly, the ability of MS to selectively manipulate with ions according to their mass to charge ratio - m/z [5], coupled with spectroscopic techniques, lead to a new field called ion spectroscopy.

However, photon or electron spectroscopy of large macromolecular ions in the gas phase remains experimentally very challenging. First of all, due to the space charge, it is impossible to obtain a high concentration of target particles in the interaction volume. On the other hand, the classical sources of high-energy photons cannot provide sufficient beam intensities that would allow obtaining measurable and statistically reliable results in classical crossed beam experiments. Therefore, vacuum UV (VUV) and X-ray spectroscopy of macromolecular ions in the gas phase, were practically inaccessible until recently. Nevertheless, the experimental techniques based on isolation (trapping) of size-selected clusters [6] and Xenon ions [7], have demonstrated the possibilities to apply this method on biological macromolecules.

The first coupling of a linear ion trap integrated within the commercial mass spectrometer (Thermo Scientific LTQ XL) to the VUV beamline DESIRS [8] at the synchrotron SOLEIL facility in France, has been done by A. Milosavljević et al [9–12]. A similar project with coupling an ion trap to the VUV beamline at the synchrotron BESSY II in Germany was carried out by S. Bari et al [13] and O. Gonzalez et al [14]. These experimental setups offer a unique opportunity to study photo-induced dynamics and electronic properties of macromolecules (for example proteins), using action spectroscopy of trapped ions in a high vacuum. Moreover, these experiments demonstrated that high-energy photons can be used as a new activation method intended for protein sequencing, which allows fast and intensive fragmentation, as well as the mapping of weakly bound complexes [15].

The protein damage also needs to be taken into account in order to perform realistic modeling of the radiation damage. So far, the majority of the reported experimental results were focused on VUV photon interaction with their building blocks - amino acids (for example [16, 17]). However, proteins do not necessarily have to inherit the VUV/X-ray susceptibility of their constituent amino acids. Recently, A. Milosavljević et al [18] demonstrated that an isolated protein was very resistant to soft X-ray fragmentation in comparison with isolated amino acids. Therefore, the studies of energetic photon interactions with the isolated polymers of amino acids (peptides) are also very important.

The structure and function of biomolecules are closely linked with their aqueous environment. For this reason, there has been a long standing effort to understand the influence of solvent molecules in the immediate surroundings on the three-dimensional structure of biopolymers (such as proteins and DNA) [19]. It is believed that the weak molecular interactions play an important role in the folding of the protein and formation of macromolecular complexes. The solvation may play a key role in this process. Hence,

studies of nanosolvated systems under well-defined conditions could help bridging the gap between the results obtained for biomolecules isolated in the gas phase and their applications in real biological systems.

Finally, the experimental research of interaction of electrons with trapped molecular ions represents an additional level of challenge. Unlike photons, electrons are charged particles and therefore are susceptible to electric fields that are used to capture ions, as well as by the space charge effects induced by the tightly packed ions. On the other hand, the electron beam itself can disturb the electric fields inside the ion trap, which are necessary for an efficient ion trapping. The first experiments of this type that are focused on the interaction of electrons with large isolated biopolymers were made with very low-energy electrons in the experiments involving Furrier transform ion cyclotron resonance (FT-ICR) ion traps. The first experiments of this type were carried out in the group of Zubarev [20, 21]. However, the work of this and other groups was primarily focused on the development of a new activation method for the protein sequencing, but not for the electron spectroscopy of large biopolymers over a wide range of energies.

2 Biomolecules

2.1 Amino acids

Amino acids are organic molecules, which contain an amino group (-NH_2) and a carboxylic acid group (-COOH), as depicted in Figure 2.1. Taking all combinations into account there is an infinite number of amino acids which could be formed, but only around 22 can be found in nature [22, 23]. Each standard amino acid is characterized by a different functional side chain, which is attached to the alpha Carbon C_α (see Figure 2.1). The standard amino acids are joined with one and three letter code [24].

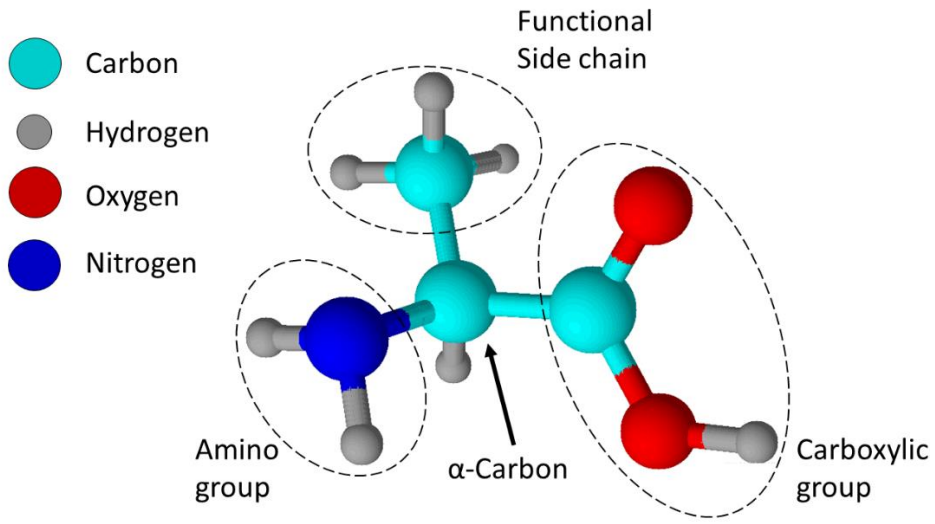

Figure 2.1 - Representation of Alanine amino acid. Alpha Carbon - C_α is the so-called backbone Carbon atom which binds all three functional groups.

2.2 Peptides

Peptides are organic molecules consisted of two or more amino acids linked together through the so-called peptide bonds. This bond is formed when the amino group of one amino acid reacts with the carboxyl group of another amino acid resulting in a covalent bond between the Nitrogen (N) and the Carbon (C). During this process, a water molecule is released, as depicted in Figure 2.2. The peptide C-N bond has partially double bond properties because it is influenced by two strong resonance electron structures. One such structure is a double bond between C and Oxygen (O) atoms and the other one is a double bond between C and N atoms. Atoms O, C, N and Hydrogen (H) involved in this bond belong to a peptide group. The coulomb interaction between atoms from a peptide group creates such electron density distribution that the involved atoms are approximately arranged in a plane. Because of this, the peptide bond is prone to rotation along the axis

defined by the peptide bond. This gives peptides the possibility to change their three-dimensional structure by folding.

Peptides are named by the sequence of appearance of their amino acids starting from the N-terminal part of the peptide. This amino acid sequence is also termed the primary structure of the peptide. The spatial arrangement is termed the secondary structure.

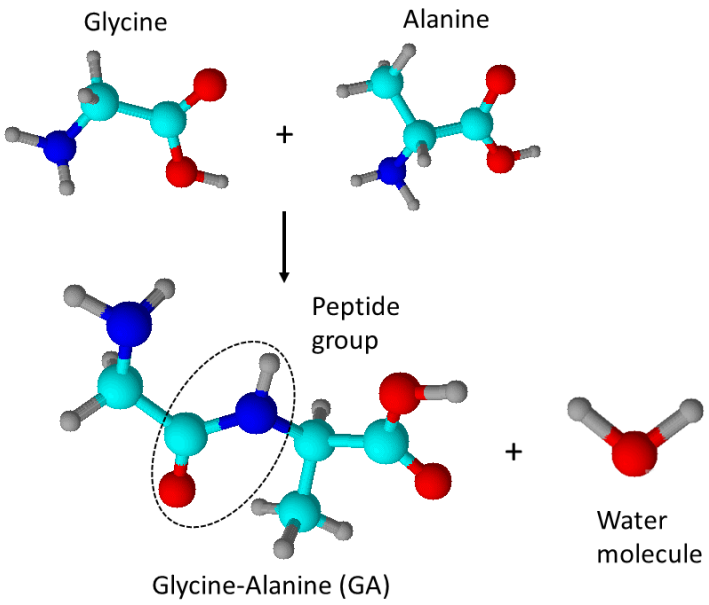

Figure 2.2 - Schematic representation of a formation of a dipeptide composed of amino acids Glycine and Alanine. In this process, a water molecule is released.

The side of the peptide bearing the NH_2 group is termed the N-terminal part. Likewise, the other side of the peptide bearing the acidic function is termed the C-terminal part. A standard nomenclature of the fragments is proposed in [24]. The fragments containing the N-terminal are termed a_n-, b_n-, and c_n- fragments, while the ones containing the C-terminal are termed x_n, y_n, and z_n- fragments (Figure 2.3). The number n in the subscript indicate the number of amino acid residues.

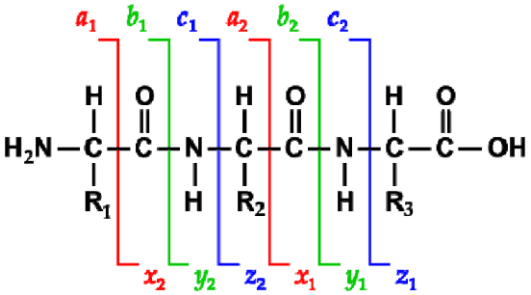

Figure 2.3 - Nomenclature for peptide fragmentation. Image adopted from [25].

Peptides can be linked together to form a large polymer chain called proteins, which can consist up to thousands of amino acid residues [23]. Finding a protein sequence is called protein sequencing. It is found that the three-dimensional structure of a protein is closely related to its biological activity in a living cell [26]. Therefore, a very important goal of mass spectrometry (Section 4.2) is to obtain the primary structure of a protein.

3 Density functional theory (DFT)

Description and evolution of any system in the molecular physics or quantum chemistry is given by the time-dependent non-relativistic Schrödinger equation:

$$\hat{H}\Psi_i = E_i \Psi_i \tag{3.1}$$

Hamiltonian $\hat{H}$ of the system that consists of M nuclei and N electrons can be written as:

$$\hat{H} = -\frac{1}{2}\sum_{i=1}^{N}\nabla_i^2 - \frac{1}{2}\sum_{A=1}^{M}\frac{1}{M_A}\nabla_A^2 - \sum_{i=1}^{N}\sum_{A=1}^{M}\frac{Z_A}{r_{iA}} + \sum_{i=1}^{N}\sum_{j>i}^{M}\frac{1}{r_{ij}} + \sum_{A=1}^{N}\sum_{B>A}^{M}\frac{Z_A Z_B}{R_{AB}} \tag{3.2}$$

Numerators A, B run over all nuclei and i, j run over all electron coordinates. The first two terms are the kinetic energy of electrons and nuclei respectively. The remaining three terms are the electrostatic interaction between nuclei and electrons, the repulsive electron-electron interaction and the repulsive nucleus-nucleus interaction, respectively.

In the Born-Oppenheimer approximation (BOA), due to the large mass difference, the electrons can be considered to move in the fields of the much slower nuclei, while the kinetic energy of the nuclei is a constant (set to zero). Therefore, in BOA the electronic Hamiltonian is given by the following equation:

$$\hat{H}_{elec} = -\frac{1}{2}\sum_{i=1}^{N}\nabla_i^2 - \sum_{i=1}^{N}\sum_{A=1}^{M}\frac{Z_A}{r_{iA}} + \sum_{i=1}^{N}\sum_{j>i}^{M}\frac{1}{r_{ij}} = \hat{T} + \hat{V}_{Ne} + \hat{V}_{ee} \tag{3.3}$$

$$\hat{H}_{elec}\psi_{elec} = E_{elec}\psi_{elec} \tag{3.4}$$

$$E_{tot} = E_{elec} + E_{nucl} \text{ where } E_{nucl} = \sum_{A=1}^{N}\sum_{B>A}^{M}\frac{Z_A Z_B}{R_{AB}} \tag{3.5}$$

The electronic Hamiltonian $\hat{H}_{elec}$ is rewritten as the sum of electron kinetic energy $\hat{T}$, external (nuclear) potential $\hat{V}_{Ne}$, and electron-electron interaction $\hat{V}_{ee}$. Schrödinger equation (3.4) can now be solved for electronic energies E_{elec} and wave functions ψ_{elec} depending on static nuclear coordinates.

The Hartree-Fock (HF) method states that N-body wave function for a fermionic system in the ground state Ψ_0, can be approximated with the Slater determinant, composed from one body wave functions:

$$\Psi_0 \approx \Psi_{HF} = \frac{1}{\sqrt{N}} \begin{vmatrix} \psi_1(\vec{x}_1) & \psi_2(\vec{x}_1) & \cdots & \psi_N(\vec{x}_1) \\ \psi_1(\vec{x}_2) & \psi_2(\vec{x}_2) & \cdots & \psi_N(\vec{x}_2) \\ \vdots & \vdots & \ddots & \vdots \\ \psi_1(\vec{x}_N) & \psi_2(\vec{x}_N) & \cdots & \psi_N(\vec{x}_N) \end{vmatrix} \tag{3.6}$$

First Hohenberg-Kohn theorem [27] demonstrates that the electron density of the ground state ρ_0 for any electronic system uniquely determines the Hamiltonian operator, which describes all properties of the given system. The energy of the ground state is a functional[1] of this density and is given by the relation:

$$E_0(\rho_0) = T(\rho_0) + E_{Ne}(\rho_0) + E_{ee}(\rho_0) \tag{3.7}$$

Second Hohenberg-Kohn theorem states that functional for which the true ground state is obtained, is the one which yields the lowest energy:

$$E_0(\rho_0) \le E(\rho) = T(\rho) + E_{Ne}(\rho) + E_{ee}(\rho) \tag{3.8}$$

The difficulty arises with this method, because $T(\rho)$ and $E_{ee}(\rho)$ cannot be calculated exactly. One electron Kohn-Sham equations [28] were introduced to utilize the HF orbital method with the modified Slater determinant. In that case, non-interacting particles can be described with:

$$f_{KS}\phi_i = \varepsilon_i \phi_i , \tag{3.9}$$

$$\text{where, } f_{KS} = -\frac{1}{2}\Delta + V_S(\vec{r}) \tag{3.10}$$

is the one-electron operator, ϕ_i are one-electron (atomic) orbitals and ε_i is the energy of the state defined by the orbital ϕ_i. Since the orbitals define the state, the electron density can be calculated from $\rho = \sum_{i=1}^{N} \phi_i^* \phi_i$. The kinetic energy of non-interacting electrons is:

$$T_S[\rho] = -\frac{1}{2}\sum_{i=1}^{N} \langle \phi_i | \Delta | \phi_i \rangle \tag{3.11}$$

Therefore, total electron energy functional in Kohn-Scham interpretation can be separated to a non-interacting kinetic energy T_S, an electron Coulomb repulsion term J, electron-nucleus interaction E_{Ne} and the remaining electron-electron exchange term E_{XC}:

$$E_{elec}[\rho] = T_S[\rho] + J[\rho] + E_{Ne}[\rho] + E_{XC}[\rho] \tag{3.12}$$

The correlation exchange term E_{XC} contains corrections for the anti-symmetry which were not included in modified Slater determinant (electrons with antiparallel spins), as

[1] A functional is a function of a function. The energy functional outputs the energy from an electron density function $\rho(\vec{r})$.

well as corrections coming from the fact that electrons indeed are interacting. Therefore, the DFT problem lies in finding the exact form of the exchange functional:

$$E_{XC}[\rho] \equiv (T - T_S) + (E_{ee} - J) \tag{3.13}$$

The potential energy can then be calculated by:

$$V_S = \int \frac{\rho_{r_2}}{|\vec{r}_1 - \vec{r}_2|} d\vec{r}_2 - \sum_{A=1}^{M} \frac{Z_i}{|\vec{r}_1 - \vec{R}_2|} + V_{XC} \tag{3.14}$$

$$\text{where } V_{XC} = \frac{\delta E_{XC}}{\delta \rho} \tag{3.15}$$

A large variety of functionals has been developed in order to approximate the correlation exchange term E_{XC}. The most simple one which treats electron density as the homogenous electrons gas is called the local density approximation (LDA). The more advanced one is the generalized gradient approximation (GDA).

4 Experimental methods

4.1 Electrospray ionization

Electrospray ionization (ESI) is a soft ionization technique that allows one to introduce large bio-molecular targets, intact into the gas phase. The first production of the gas-phase ions from liquid solutions was demonstrated by M. Dole in 1968 [29]. Later on, with further developments of the technique by M. Yamashita and J. B. Fenn in 1980's [4, 30] ESI was widely accepted. In the year of 2002, J. Fenn received the Nobel prize in chemistry, for the development of the technique that allowed new insights into the structural analysis of the macromolecules.

The ESI technique is soft in a sense, that a very low amount of energy is deposited in the analyte after the ionization process. When working under normal operating conditions, the residual energy is not enough to induce fragmentation of the analyte [31]. The process of ionization of the analyte by ESI is essentially different in comparison with conventional ionization techniques. For example, in the process of the electron (or photon) impact ionization of atoms or molecules, an electron is removed, creating a positively charged radical ion. In the ESI technique, multiple charging of the analyte is achieved through attachment or detachment, of one or more Hydrogen nuclei - protons. Protonated species are obtained if a proton is attached to the analyte, forming a positive ion - cation. Removal of the proton from the analyte is called deprotonation, yielding a negative ion - anion. ESI allows multiple (de)protonation, as opposite to Matrix assisted laser desorption ionization (MALDI) [32]). Therefore, using the ESI to produce highly charged states of the analytes with large molar weight (> 100 kDa), provides a very important possibility to reduce the mass-to-charge ratio of the target molecule. Mass spectrometers with a modest m/z range,

are then able to manipulate with such species. For example, precursor ion of a 7+ charge state of the Ubiquitin protein studied in this Thesis, with a molar weight of 8.5 kDa, has a mass-to-charge ratio of 1225. The general principle of the ESI source is presented in Figure 4.1. An ESI source is usually coupled to the mass spectrometer within one instrument, abbreviated as an ESI-MS device.

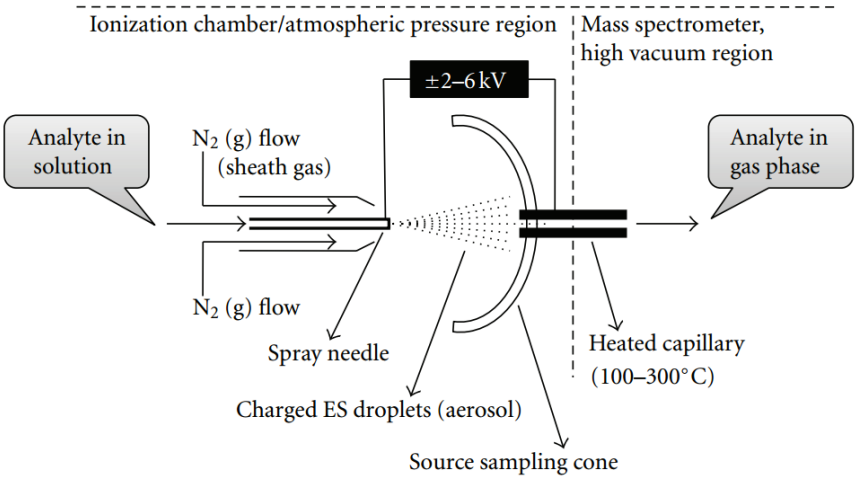

Figure 4.1 - Schematic representation of an electrospray ion source. Adopted from [33].

A mechanical syringe pump forces the solution with the analyte through a stainless steel capillary (spray needle), with an inner diameter of typically 0.1 mm, at a low flow rate in the range of (1-100) μL/min. The capillary tip is polarized to a high voltage of up to ±6 kV, relative to the surrounding counter electrode, positioned 1 to 3 cm from the tip. In order to help the formation of a fine mist and define the direction of the spray, Nitrogen sheath gas is pumped around the capillary to assist the formation of a spray. The counter electrode can either be an ion sweep cone extended into another heated capillary, or just a capillary heated up to the temperatures of 300 °C. Another end of the heated capillary is held at a high vacuum, obtained with a turbo molecular pumps of the mass spectrometer. A very important aspect of the electrospray ion source is that the solution is pumped at an atmospheric pressure into the mass spectrometer, without the need of additional differential pumping. This is because the heated capillary inner diameter (usually 0.2 mm), is small enough to impose a high flow resistance. The length of the capillary which is typically somewhere between 5-10 cm, also contributes to a small flow resistance.

The electrospray ionization process is presented in Figure 4.2. Influenced by the strong gradient of the electric field, the charges in the solution are electrophoretically separated inside the spray capillary. In the positive ion mode, a positive potential is applied, causing the positively charged ions to accumulate at the surface of the solution, near the tip of the spraying capillary. Taylor cone [34] is formed at a critical value of the electric field and a solution is dispersed into aerosol droplets. Droplets are surrounded by positive charges

and contain well-preserved analyte molecules. Reversing the polarity of the voltage supply yields a negative ion mode, where negatively charged droplets are obtained. The charges on the surface of the droplet are uniformly distributed since it is a configuration with a minimal potential energy. Two opposing forces act on the droplet. One is Coulomb force, trying to repel the charges and the other one is the surface tension, acting between molecules of the liquid. As the droplets travel towards the counter electrode, the solvent is evaporating with the assistance of a sheath gas, resulting in a droplet size decrease. A Rayleigh limit [35] is reached when the size of the droplet is small enough, that the Coulomb repulsion overcomes the surface tension of the droplet. So-called Coulomb explosion (fission) occurs, breaking the droplet into smaller ones, which contain fewer analyte molecules. At the end, multiply charged molecules are obtained.

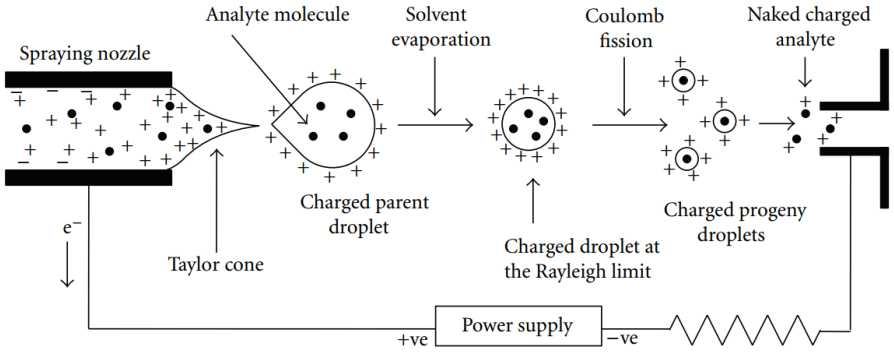

Figure 4.2 - Schematic representation of the electrospray ionization process. Adopted from [33].

Currently, there are two strongly debated theoretical models, which describe the final formation of charged analytes [36]: 1) Ion evaporation model (IEM) and 2) Charge residue model (CRM).

IEM [37] suggests that at a critical radius of the droplet above the Rayleigh limit, at ≥10 nm, the electric field is strong enough to directly evaporate the droplets and form the charged analyte ions. This approach is experimentally well supported for the formation of small organic and inorganic ions like salts.

CRM [29, 38, 39] assumes cascade series of the Coulomb fission events, which leads to a formation of a droplet containing a single analyte molecule. Then by evaporating or complete desolvation, the charged analyte ion is obtained. For larger analytes like proteins, CRM seems more suitable.

Among many variations of the ESI, a nano-electrospray ion source (nano-ESI), developed by Wilm and Mann [40, 41] is widely used. As the name suggests, the main difference between the standard ESI and nano-ESI is in the much smaller size of the capillary allowing lower flow rate. Nano-ESI typically operates with flow rates in the range of (20-50) nL/min. This imposes a big advantage over the standard ESI, where the most of the

solution volume is wasted. Moreover, the required amount of the solution in the experiment using nano-ESI is in the order of a few μL, compared to around 1 mL, typically used for standard ESI. The small flow rate is achieved with the use of borosilicate glass spray capillary, with the tip inner diameter of (1-4) μm. Glass capillary is sputtered on the outside with a gold film, in order to enable electrical conductivity. The applied potential is typically in the range of (0.7-1.5) kV. The distance from the tip of the capillary to the ion sweep cone can be much shorter, compared with standard ESI. The presence of the strong electric field initiates the solution flow, which is further propelled by the capillary forces only, as the droplets leave the tip. The Size of the produced droplets by nano-ESI are in the order of 200 nm, whereas 1.5 μm droplets are usually produced by standard ESI. The most attractive feature of the nano-ESI is the favoring of the highly aqueous species. This opens the important possibility to produce a hydrated and charged adducts of the analytes, which were studied in this Thesis.

4.1.1 Sample preparation

The biomolecule samples used in this Thesis, are provided from Sigma Aldrich. They are received in a powder form and require to be prepared in the form of a liquid solution. The obtained solution without further purification was then directly injected into ESI or nano-ESI.

Table 4.1 - Concentrations and solvents of the daughter solutions of the analytes studied in this Thesis.

Analyte	Concentration [μM]	Solvent [vol/vol %]
Leucin Enkephalin	10	water/ACN - 75/25
Adenosine monophospate	100	pure water only
Ubiquitin	10	water/ACN - 70/30
Substance P	10	water/ACN/acetic acid - 49.5/49.5/1
Melittin	100	water/methanol/ - 50/50

In this section, a brief description of the procedure for obtaining such solutions is presented. First, the mother solution is prepared, at a higher concentration of the given analyte, using an appropriate solvent. The mother solution is then diluted to a desired final concentration, obtaining a daughter solution. Solvents used for the daughter solutions were mainly deionized water (max. resistance of 18.6 MΩ) and acetonitrile (ACN) or methanol. Depending on requirements of a particular study a small percentage of the acid could be added to the solvent for the daughter solution. For example, if highly charged positive precursor ions are to be obtained, the acetic acid is added (typically 1%). Basic properties of the daughter solutions of the analyte molecules studied in this Thesis are presented in Table 4.1.

4.2 Mass spectrometry (MS)

Mass spectrometry (MS) has become a very powerful tool for the analysis of the charged particles (ions) [5]. Once the ions are produced in the gas phase by means of the ionization techniques (for example ESI), they need to be separated in some way. The instruments which perform the actual ion separation are called mass analyzers. Rather than separating the ions according to their masses, mass analyzers are designed to select the ions based on their mass-to-charge (m/z) ratios.

In order to achieve the ion selection according to the m/z ratio, mass analyzers are designed to utilize the static or dynamic electric or magnetic fields, either individually or a combination of both. Specific differences between various types of mass analyzers are expressed through the actual applications of magnetic and electric fields. With this respect, different types of mass analyzer used in mass spectrometry are summarized in Table 4.2.

Table 4.2 - Types of mass analyzers. Adopted from [5].

Analyzer type	Symbol	Principle of separation
Electric sector	E or ESA	kinetic energy
Magnetic sector	B	momentum
Quadrupole	Q	m/z (trajectory stability)
Ion trap	IT	m/z (resonance frequency)
Time-of-flight	TOF	velocity (time of flight)
Fourier transform ion cyclotron resonance	FTICR	m/z (resonance frequency)
Fourier transform orbitrap	FT-OT	m/z (resonance frequency)

Each of the presented types of mass analyzers has its own advantages and disadvantages, which makes it suitable for a certain application. In this Thesis, linear quadrupole ion trap as a part of a commercial mass spectrometer (Thermo Scientific LTQ XL) was used to select and isolate target ions. For this reason, the principle of operation of a quadrupole mass analyzer (filter) is presented in the following section.

4.2.1 Quadrupole analyzer (Mathieu equations)

The principles of guiding and trapping ions are based on generating electric field which imposes a binding force that increases linearly with the particle distance from the axis [42]:

$$\vec{F} = -c\vec{r} \tag{4.1}$$

This force generates the parabolic potential Φ, given by relation:

$$\Phi \sim (\alpha x^2 + \beta y^2 + \gamma z^2) \tag{4.2}$$

Appropriate tools which can generate such potentials and restrict the motion of ions are electric or magnetic multipole fields. If the number of "poles" is labeled with m, then in general case multipole potential is given with the relation:

$$\Phi \sim r^{\frac{m}{2}} \cos(\frac{m}{2}\varphi) \tag{4.3}$$

If a number of multipoles m=4 then quadrupole potential is obtained, where the quadratic potential is $\Phi \sim r^2 \cos 2\varphi$. For electric quadrupole field, the potential in the Cartesian coordinates has the form:

$$\Phi = \frac{\Phi_0}{2r_0^2}(\alpha x^2 + \beta y^2 + \gamma z^2) \tag{4.4}$$

In order to satisfy the Laplace equation $\Delta\phi = 0$, the condition $\alpha + \beta + \gamma = 0$ has to be valid. The imposed condition is valid for two simple cases:

(i) $\alpha = -\gamma = 1,\ \beta = 0$ (2D field) $\rightarrow$ $\Phi = \frac{\Phi_0}{2r_0^2}(x^2 - z^2)$ (4.5)

(ii) $\alpha = \beta = 1,\ \gamma = -2$ (3D field) $\rightarrow$ $\Phi = \frac{\Phi_0(r^2 - 2z^2)}{r_0^2 + 2z_0^2},\ 2z_0^2 = r_0^2$ (4.6)

Quadrupole mass filter

Potential obtained in case (i) can be generated by four parallel hyperbolic electrodes extended in Y-axis direction, as depicted in Figure 4.3b.

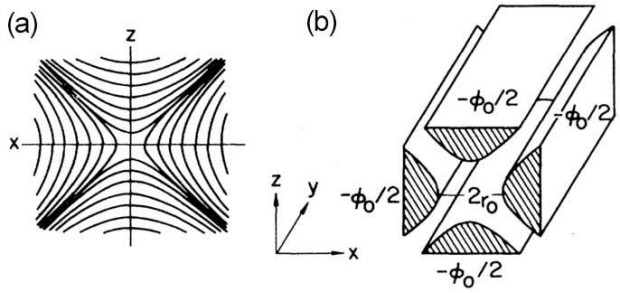

Figure 4.3 - (a) Equipotential lines for a quadrupole field in a plane and (b) Electrode configuration of quadrupole mass filter. Adopted from [42].

Time-dependent potential difference (voltage) applied to electrode pairs of the quadruple mass filter, that results in a restricted ion motion in XZ plane, is given by the following relation:

$$\Phi_0(t) = U + V\cos\omega t\,, \tag{4.7}$$

where U is direct current (DC) voltage and V is the amplitude of the RF voltage with a circular frequency ω. Equations of motion are given by the second Newton law:

$$m\frac{d^2\vec{r}}{dt^2} = -e\nabla\Phi \tag{4.8}$$

$$\ddot{x} + \frac{e}{mr_0^2}(U + V\cos\omega t)x = 0 \tag{4.9}$$

$$\ddot{z} - \frac{e}{mr_0^2}(U + V\cos\omega t)z = 0 \tag{4.10}$$

Equations (4.9) and (4.10) can be simplified by introducing the following parameters:

$$a = \frac{4eU}{mr_0^2\omega^2},\ q = \frac{2eV}{mr_0^2\omega^2},\ \tau = \frac{\omega t}{2} \tag{4.11}$$

$$\begin{aligned}\frac{d^2x}{d\tau^2} + (a + 2q\cos 2\tau)x = 0\\ \frac{d^2z}{d\tau^2} - (a + 2q\cos 2\tau)z = 0\end{aligned} \tag{4.12}$$

Equations (4.12) are the canonical form of the second-order differential Mathieu equations. There are two types of solution for Mathieu equations: (1) stable motion, where ions oscillate in the XZ plane and are free to move along the Y-axis direction passing through the quadrupole filter; (2) unstable motion, in which their coordinates grow exponentially along X- or Z-axis, or both. For any given ion with mass m and charge e,

the stability of its trajectory depends only on parameters a and q, defined by the voltages U and V applied on the quadrupole electrodes. If the relation between parameters a and q is plotted on a graph (see Figure 4.4), the stability diagram is obtained. The stability diagram shows the areas, for which the ion motion is stable in Z- and in the X-axis direction. In a small region near the origin of the diagram, ion motion is stable in both X- and Z-axis directions. A zoom of this region is presented in Figure 4.5.

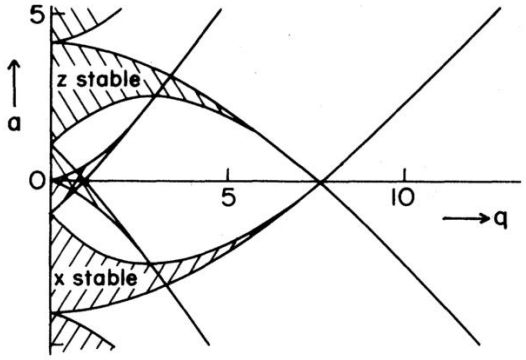

Figure 4.4 - Stability diagram for 2D quadrupole field. Adopted from [42].

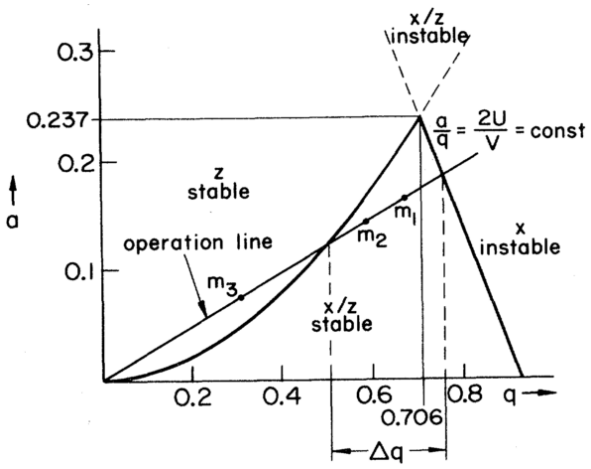

Figure 4.5 - The lowest region of simultaneous stability of ion motion in X- and Z-axis directions. Operation line is defined with the ratio $a/q = \text{const}$, all ion masses are located on this line ($m_3 > m_2 > m_1$). Adopted from [42].

If the values r_0, ω, U and V are fixed, all ions with the same mass will have the same operating line in the stability diagram. Because the ratio a/q=2U/V does not depend on ion masses, all ion masses lie on the operating line a/q =const. For the stability line on the q axis (a=0, RF only filter), the possible values of parameter q are in the range [0, q_{max}], where q_{max}=0.92. If we put q_{max} in the equation (4.11) for q parameter, we can see that all ions with masses in the range from m_{min} to infinity have stabile trajectories. For such quadrupole field conditions, the quadrupole works as a high-pass mass filter. By

increasing the DC voltage U operating line is rising, which decreases the range Δm. At some point, it touches the tip of the stability region, where Δm=0, meaning that in theory ions with only one exact mass will have the stable trajectories. In practice, this is never the case and the mass bandwidth is defined by voltage fluctuations. If voltages U and V are simultaneously changed in a way that their ratio keeps constant, then ions with successive masses will have the stabile trajectories and all other ions will be splatted on electrodes. This operation gives the possibility to scan the mass spectrum, therefore, the quadrupole will work as a mass spectrometer. By adding two more sections (with the same electrode profile) axially before and after the quadrupole mass filter, axial ion trapping can be achieved and thus the linear quadrupole ion trap is obtained.

4.2.2 Tandem mass spectrometry (MS^n)

The principle of tandem mass spectrometry is depicted in Figure 4.6. Once ions are produced in the gas phase, a certain small m/z range is defined by setting the operating line close the tip of the stability diagram, which results in an isolation of precursors with a defined m/z ratio. The selected precursor ions are then activated, which means that their internal energy is increased, and eventually it will lead to the fragmentation. If the activation process is carried out through inelastic collisions with neutral gas atoms (Helium or Nitrogen), the process is called the collision induced dissociation (CID) [43]. Product ions are then analyzed according to their m/z ratio which yields a tandem mass spectrum (MS^2). It should be noted that the process of ion isolation and activation can be repeated further up to the n-th level in ion traps, yielding MS^n. Other activation methods may be also applied, in order to increase the intensity and selectivity of the fragmentation. For example, photons from synchrotron radiation [9, 44], or low energy electrons [45].

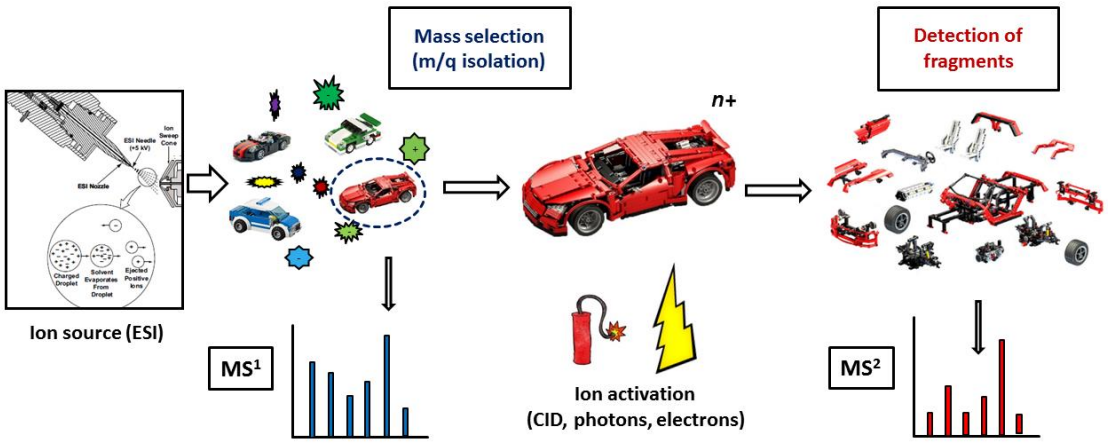

Figure 4.6 - Schematic representation of tandem mass spectrometry (MS^2).

The primary goal of mass spectrometry is to provide the information about the structure of the target precursor ion by analysis of the fragmentation patterns. MS^2 has demonstrated a huge potential to investigate the primary structure of large biopolymers [46].

By repeating photons or electrons activation tandem MS for many activation energies in small energy steps, one obtains the experimental technique called action spectroscopy. Experimental setups presented in this Thesis are based on this technique and were used for investigating the electronic structure of peptides, proteins and nucleotides.

4.3 LTQ XL - details and operation

In this section, details of operation of a commercial mass spectrometer Thermo Scientific LTQ XL (LTQ) are given. LTQ is the main instrument of the experimental setups, presented in this Thesis. Figure 4.7 depicts a functional block diagram of the spectrometer. LTQ comprises three major hardware systems: 1) ion source, 2) MS detector system and 3) data system.

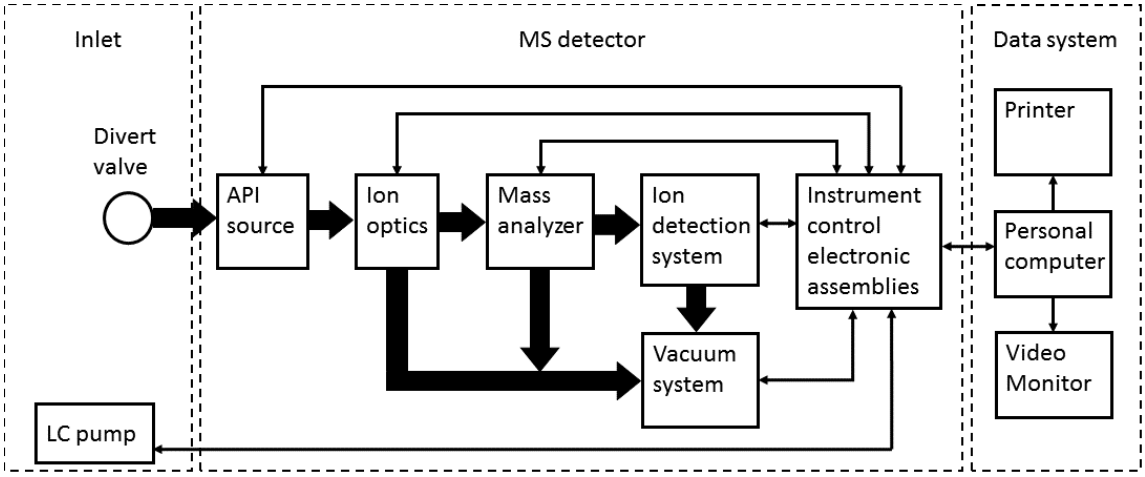

Figure 4.7 - Functional block diagram of LTQ XL mass spectrometer. Adapted from [47].

(1) The atmospheric pressure ionization (API) source is composed of two components. The first component is permanently mounted on the front side of the spectrometer chassis. It consists of an ion sweep cone, a transfer tube (heated capillary), a tube lens and a skimmer (see Figure 4.8). The second component is completely removable and is essentially a spraying needle of an ESI source, in enclosed assembly. Depending on requirements of the experiment, assembly with the standard ESI or a nano-ESI needle is mounted. Analyte solution is automatically injected into a spray needle through flexible capillaries (at a user defined flow rate), with the assistance of a mechanical syringe pump located on the front side of the mass spectrometer.

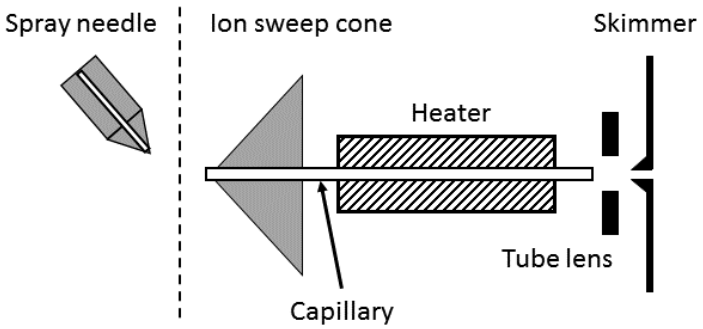

Figure 4.8 - Schematic representation of an API source of the LTQ XL mass spectrometer. Spray needle is a part of an independently detachable assembly - of the standard ESI or a nano-ESI source.

A Standard ESI source is used in this Thesis for producing non-hydrated (bare) charged precursor ions. In general, when using the standard ESI source in the positive mode, precursor ion $[M+nH]^{n+}$ can be produced, where n indicates the ion charge state. Letter M indicates the molar weight of the target molecule, while H denotes the Hydrogen nucleus - proton. Typically, a wide range of precursor charge states are produced simultaneously, with a certain intensity distribution, which depends on solution and ESI parameters. Mass-to-charge ratio (m/z) of such precursor in arbitrary mass units (amu) is given by Equation (4.13).

$$\frac{m}{z} = \frac{M + n}{n} \tag{4.13}$$

Both ESI and Nano ESI are able to produce bare and hydrated precursor ions. In the case of nanosolvated molecules, the general formula for the obtained precursor ions is $[M+kH_2O+nH]^{n+}$, where k is the number of the attached water molecules. In general, Equation (4.14) gives the m/z ratio for the obtained hydrated precursor.

$$\frac{m}{z} = \frac{M + n + 18k}{n} \tag{4.14}$$

Since LTQ is designed to efficiently remove remaining water molecules, non-standard ESI parameters had to be used in order to produce hydrated precursors. In the present study, we favorably used nano-ESI in order to produce nanosolvated molecules. Since automatic tuning of nano-ESI parameters was not possible, in order to produce hydrated precursors we reduced capillary temperature well below optimal values, to around 40 °C. The capillary voltage, the sheath gas flow rate and the tube lens voltage also had to be manually retuned accordingly.

(2) The mass spectrum (MS) detector system comprises the ion optics (quadrupole and octupole ion filters), the mass analyzer (a linear quadrupole ion trap), the ion detection

system (electron multiplier detectors) and an electronic control system, as depicted in Figure 4.9.

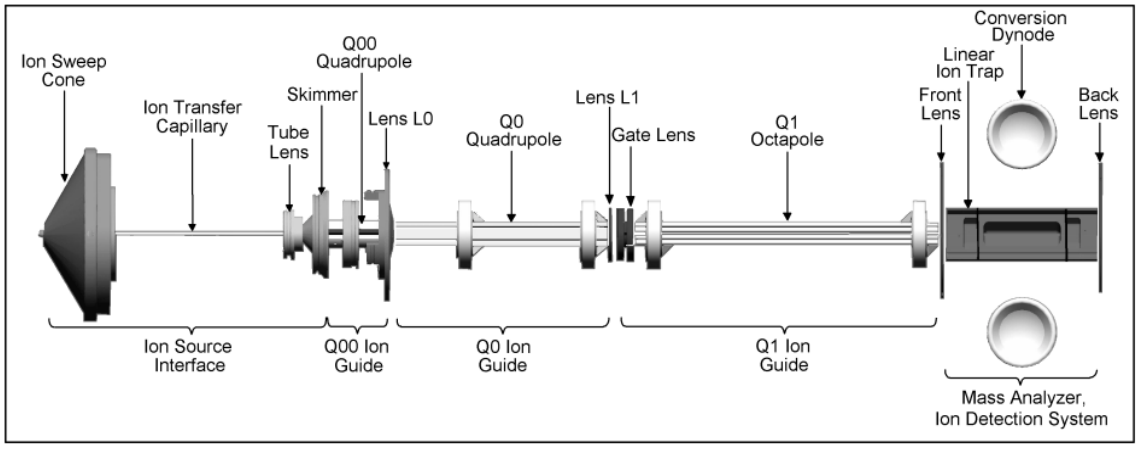

Figure 4.9 - Schematic representation of the LTQ XL mass spectrometer. Adopted from [47].

LTQ allows for sending TTL[2] signals at specific sequence events. These trigger signals can be initiated at the start or at the end of particular processes, during the operation of the device. One such process is the ion activation. In the Xcalibur™ software [47] which runs the LTQ, the option to enable triggers on the activation has to be selected. IF it is enabled, during the activation time TTL signal state is always high (5 V), whereas during all other times TTL signal is kept in the low state (0 V). The activation process in the LTQ is initiated each time when enough ions are stored in the ion trap. In the LTQ software there are two ways to define the ion storage procedure, which then triggers the TTL signal. The first one is by defining the ion storage time limit. This was often used when desired precursor ion abundance was very low, in order to avoid excessively long data acquisition. This means that we prevent LTQ from waiting for optimal ion density in the trap, which lowers the signal to noise ratio. Typically the ion storage time was set to 100 ms. In the case when high ion abundance is obtained, the ion trap capacity can be quickly reached in around (10-30) ms. Therefore, the second way of defining ion storage process is based on measuring the ion density in the ion trap. This process is automatically controlled by internal LTQ electronics and as soon as the optimal capacity is reached TTL signal is triggered to a high 5 V state, signaling the start of activation time (ion irradiation time). The use of mentioned TTL signals is explained in Sections 4.5.2 and 4.5.3.

The ion detection in LTQ is performed by electron multipliers. Schematic representation of the LTQ detection system is presented in Figure 4.10. It comprises a conversion dynode, a series of cathodes and the anode.

[2] TTL stands for transistor-transistor logic, representing the binary logic states 0 and 1, with the voltages 0 V and 5 V respectively. TTL signals are used in the digital electronic circuits.

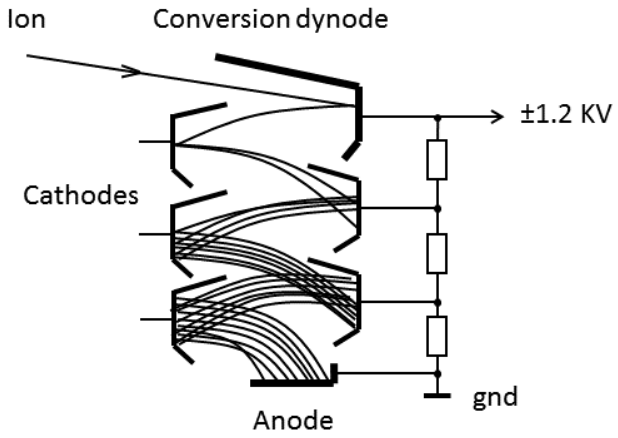

Figure 4.10 - Schematic representation of the electron multiplier detector with conversion dynodes in the LTQ XL mass spectrometer. Two such detectors are located at each side of the ion trap.

Conversion diode is a concave metal surface with a high secondary particle emission coefficient and is positioned at an almost right angle in relation to the incident ion trajectory. If positive ions are to be detected negative voltage is applied, whereas for detection of negative ions a positive voltage is applied to the conversion dynode in relation to the anode potential (ground). The cathodes in between the conversion dynode and the anode are connected to progressively higher voltages through the resistor network. When an ion strikes the conversion dynode one or more secondary electrons are produced. Due to the concave shape and a voltage gradient, secondary electrons are focused and accelerated on the next cathode. Electron striking the inner surface of the cathode ejects more secondary electrons and the process creates the electron avalanche that finally strikes the anode where electrons are collected. Current on the anode is proportional to the number of the ions striking the conversion dynode. This current is additionally amplified in the electronic system of LTQ, converted and stored in a digital form by the data system. Since the electron multipliers are positioned slightly off-axis, background noise from neutral particles is significantly reduced. The electron multipliers are electrostatically shielded which decreases the noise even further.

Linear quadrupole ion trap in the LTQ comprises three axial sections (the same electrode profiles) with three different DC potentials in order to obtain axial ion trapping (see Figure 4.11). In order to create an electric potential well for the trapped ions in the axial direction, the center section DC2 has a different potential in relation to the sections DC1 and DC3. For trapping the positive ions, potential on DC2 is lower, while in order to trap the negative ions the potential on DC2 has to be higher in relation to potentials applied two other sections. The voltage difference is usually not more than 10 V.

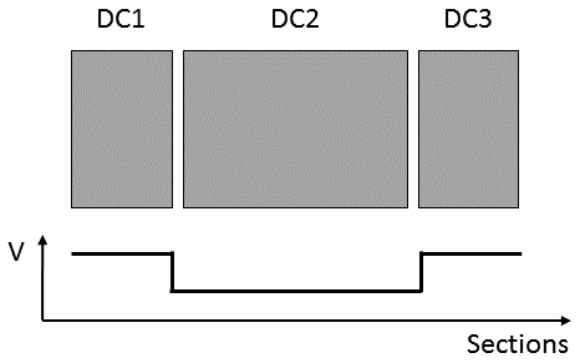

Figure 4.11 - DC voltages on the LTQ ion trap required for axial ion trapping.

Maximal DC voltages are ±100 V, the maximal RF voltage amplitude is 400 V with the frequency of 1 MHz. The ion trap is 68 mm long, with the minimal radial distance between the hyperbolic electrodes of 4 mm.

For the process of ion selection (trapping of desired precursor ions) specific high-frequency pulse is generated by the LTQ electronics. This pulse ejects all ions except the ones corresponding to a small m/z range (isolation width) defined by the user. Typically, we used isolation widths of up to $\Delta m/z = 10$ (±5 from the precursor ion m/z).

After the activation (irradiation) of trapped ions, the ion products are successively ejected by applying different high-frequency detection pulse which ejects all ions with the same m/z. This pulse is quickly ramped so that ions of all m/z are ejected, but in a sorted way from the lowest the highest m/z ratios. After calibration, this procedure yields the action MS^2.

4.4 Synchrotron radiation

Synchrotron radiation (SR) refers to an electromagnetic radiation generated by charged particles when accelerated to the relativistic velocities. SR is first observed in the particle accelerators, used in high energy physics in middle 1940's. At the time, SR was considered as a byproduct, imposing not yet explained energy loss to the accelerated charged particles. Shortly after, it was realized that the missing energy is due to photon emission. The theory describing SR in circular accelerators is reported by Ivanenko and Pommeranchuck in 1944 [48] and also by Schwinger in 1946 [49, 50] independently. Only later in the 1960's, the possibility to use the SR in spectroscopic studies was demonstrated [51–54]. A good overview of the development of the SR is reported by Kuntz et al [55].

A storage ring is the most commonly used type of the particle accelerator, designed specifically for the production of the SR and represent the first generation of synchrotron radiation sources. It is constructed of many straight sections arranged in a polygon, with

a dipole bending magnets residing in between. In modern synchrotrons, electrons are first accelerated in a smaller ring to the relativistic energies of up to a few GeV and then injected in the storage ring. In a storage ring electrons follow a straight path until reaching the dipole magnets, where their trajectory is bent, experiencing an angular acceleration. At these points, photons are emitted in the tangent direction in the form of SR. Due to the photon emission, electrons in a storage ring lose energy. This energy is recovered by radiofrequency cavities, hence the term synchrotrons. The radiation from a bending magnet is characterized by the linear polarization in the plane of the electron orbit. Synchrotrons that produce SR with bending magnets belong to the second generation of synchrotrons, dedicated to study specifically the SR. Third generation synchrotrons utilize insertion devices installed on the straight sections of the storage ring. Also, in this type of synchrotrons, electrons are repeatedly injected in the storage ring in order to maintain the electron current. In the year of 1986, Klaus Halbach invented insertion devices called undulator, which comprises periodic series of dipole magnets arranged linearly (see Figure 4.12). The electron beam passes longitudinally through the alternating dipole array resulting in a radial acceleration many times, which leads to an electron oscillatory trajectory in the horizontal plane. Due to the relatively weak magnetic field, the radiation cones emitted at each bend overlap with each other which results in a constructive interference and formation of spectrally very narrow peaks. Therefore, SR obtained from an undulator is composed of harmonics and its Brilliance [equation (4.15)] is many orders of magnitude higher compared to the SR generated by the bending magnet. Furthermore, radiation obtained from an undulator is in general elliptically polarized. For this reason, in modern synchrotrons, the polarization can be tuned to linear, horizontal or circular (or any other). Tuning the wavelength of SR produced by an undulator is performed by means of mechanical adjusting of the vertical distance (gap) between the pole tips.

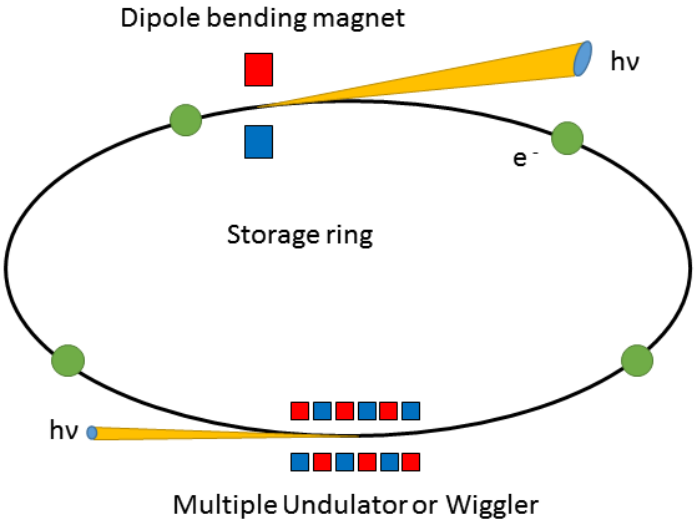

Figure 4.12 - Schematic representation of the synchrotron radiation source. The electron storage ring is composed of many straight sections, connected by the dipole bending magnets. An undulator or wiggler is installed along the straight portions of the storage ring.

In order to compare SR sources of different kinds, a measure of the quality of the source called Brilliance is introduced. It is defined by the following relation:

$$\text{Brilliance} = \frac{N}{t \cdot d\theta \cdot A \cdot 0.1\%BW} (=) \left[\frac{\text{photons}}{s \cdot \text{mrad}^2 \cdot \text{mm}^2 \cdot 0.1\%BW} \right] \quad (4.15)$$

where N - the number of photons, t - time, dθ - angle divergence, A - cross section of the photon beam and 0.1%BW - denotes a bandwidth $10^{-3}\omega$ centered around frequency ω.

The key features of the SR are:

- Wide energy range covering THz to hard X-rays
- High brilliance
- High collimation (small dθ)
- Time-resolved pulsed light (in nanoseconds)
- High level of polarization (linear, circular or elliptical)

Synchrotron SOLEIL

Experimental results presented in this Thesis are obtained at the synchrotron SOLEIL radiation facility near Paris, France. Specifically, the experiments were performed at the beamlines DESIRS [8] and PLEIADES. In the following paragraphs, a brief description of the most important aspects of the synchrotron SOLEIL and the mentioned beamlines are presented. Figure 4.13 presents the simplified schematic of the SOLEIL synchrotron. It is a third generation synchrotron, with a total of 29 beamlines, covering a very wide range of photon energies in the range (10^{-4}-10^{5}) eV.

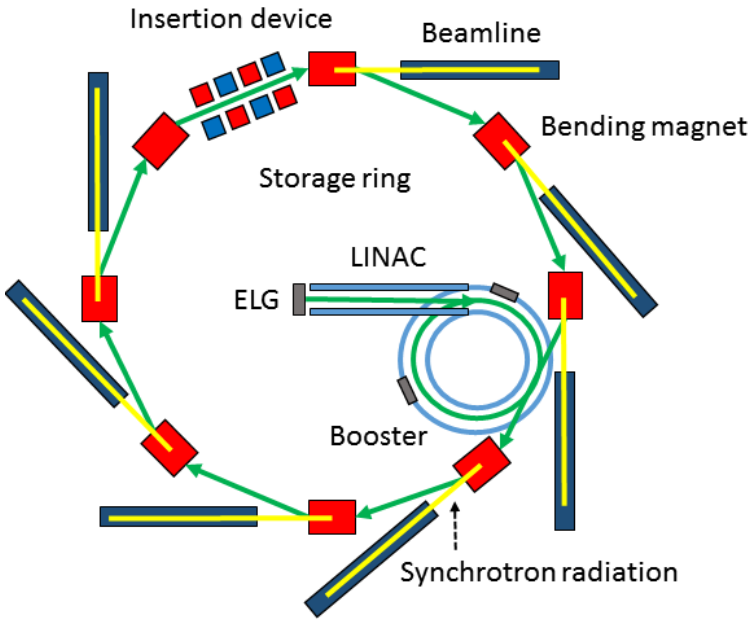

Figure 4.13 - Simplified schematic representation of the SOLEIL synchrotron.

Briefly, the electron gun produces bunches of electrons accelerated in a linear accelerator (LINAC) to 100 MeV. Electrons are then additionally accelerated in a smaller ring (booster), up to the nominal relativistic energy of 2.75 GeV and injected into a storage ring. The bending magnets, undulators and wigglers are positioned around the 345 m circumference of the storage ring, where SR is generated. At these points the photon energy range is from far IR (~1 mm) to hard X-rays (0.012 nm).

4.4.1 DESIRS beamline

The DESIRS [8] beamline is a vacuum ultra-violet (VUV) beamline, with a photon energy range of (5-40) eV. It uses an undulator to produce VUV light, with fully adjustable polarization. Equipped with a gas filter, which effectively cuts off the higher orders of the radiation, this beamline opens up the possibility to perform experiments with a high spectral purity in the low VUV region. The beamline (see Figure 4.14) has three different branches (A, B and C), with the one end station (on branches B) available for user particular experimental setups. Branch C is a permanent experimental setup for Furrier transform absorption spectroscopy (FTS), with an ultra-high resolving power of 10^6 at 10 eV. After passing through the gas filter the light produced by undulator can be split in two directions: to the branch C or to the normal incidence monochromator (NIM). After the NIM, the monochromatized beam can be split and directed to the brunches A or B. The branch A comprises multipurpose molecular beam chamber, SAPHIRS, consisting of a source chamber and an ionization chamber separated by a skimmer. With maximum resolving power of $2x10^5$, the B brunch is open for user's setups. At this branch we have coupled our experimental setup, consisting of a dedicated vacuum stage and a mass spectrometer, equipped with an ESI source.

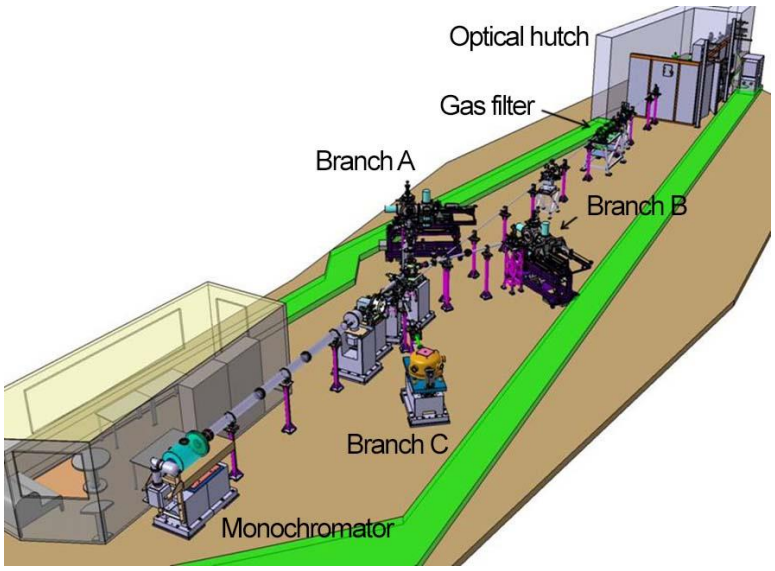

Figure 4.14 - Schematic representation of DESIRS beamline. Adopted from [8].

4.4.2 PLEIADES beamline

PLEIADES beamline is a soft X-ray beamline, capable of producing photons with an energy range of (10-1000) eV, with very high resolving power (10^5 is obtained at the energy of 50 eV). The beamline comprises two undulators with either permanent magnets or electromagnets. It can produce horizontal and vertical linearly polarized light down to energies of 10 eV. Above energies of 55 eV, fully adjustable polarized light is available. This beamline is characterized by a very high energy resolution and brilliance in a wide energy range of the soft X-ray photon beam due to the quasi-periodic design of undulators and varied groove depth of the plane grating. It is also equipped with a high resolution electron spectrometer, Auger electron-ion coincidence setup and a dedicated station for positive and negative ion photoionization studies. It consists of three optical branches with different beam focusing properties.

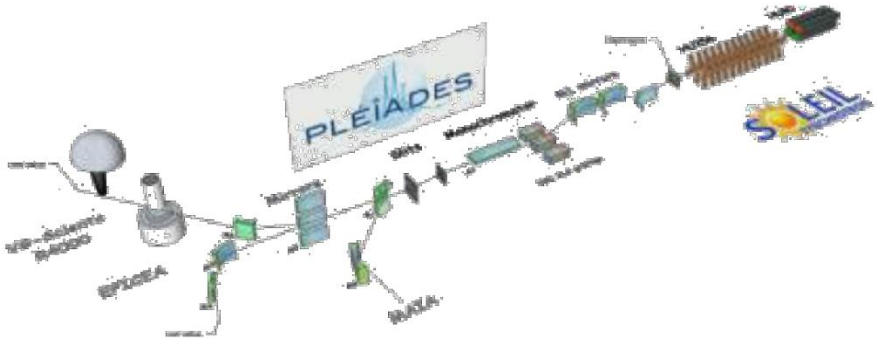

Figure 4.15 - Schematic representation of the PLEIADES beamline. Adopted from [56].

4.5 Photon experimental setup - SRMS2

4.5.1 Vacuum stage, coupling and alignment test

Vacuum stage

For the activation of the trapped ions with the photons from synchrotron radiation, a commercial mass spectrometer Thermo Scientific LTQ XL is coupled to one of the beamlines of the SOLEIL synchrotron facility. In order to couple the LTQ mass spectrometer with the appropriate beamlines a turbo pumping differential vacuum stage was designed by A. Milosavljević et al [9]. 3D model of the vacuum stage assembly is presented in Figure 4.16.

The vacuum stage is based on a six-way cross, with two CF100 and four CF40 flange connections (see Figure 4.16). The main function of the vacuum stage is to maintain the pressure difference between the surroundings of the operating ion trap, which can go

down to 10^{-5} mbar and ultrahigh vacuum of the beamline, in the order of 10^{-8} mbar. The actual pressure inside the ion trap is 10^{-3} mbar, because of the Helium buffer gas. For this reason, the vacuum stage is equipped with a 300 L/s turbo pump, installed on the CF100 flange. The beamline is attached to the left side of the vacuum assembly from Figure 4.16, via a short flexible CF40 bellows and a high vacuum valve with a MgF_2 window.

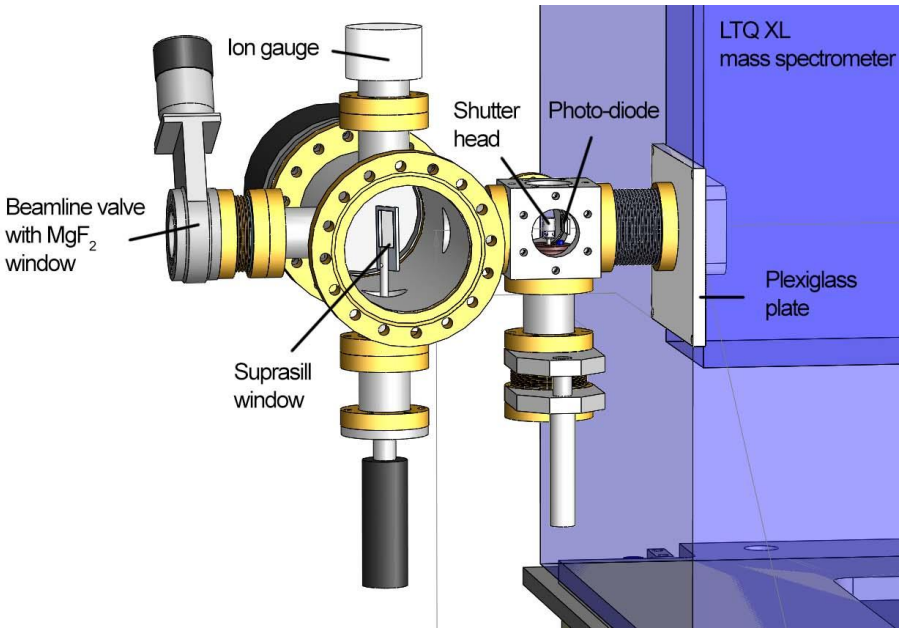

Figure 4.16 - 3D model of the differential turbo pumping assembly fitted with a mechanical shutter, ion gauge, a photodiode and a turbo pump. Designed by A. Milosavljević et al [9].

An ion gauge and Z-axis mechanical manipulator are installed vertically on CF40 flanges. The manipulator is used to optionally insert the Suprasill glass window, in order to cutoff the higher order harmonics of the VUV photon beam above 10 eV (for the lowest incident photon energies used) for improved spectral purity. A photodiode (AXUV100, International Radiation Detectors) and the shutter assembly[3] are coupled to the vacuum stage via a custom made stainless steel box with CF40 coupling. Both the mechanical shutter and the photodiode are installed on the one axis precision manipulators. This enables the fine tuning of the position of the shutter head[4] with respect to photon beam. Moreover, the photodiode can be inserted optionally, in order to measure the photon flux just before the ion trap. The vacuum assembly is rested on a rigid support and positioned behind the LTQ mass spectrometer (at the ion trap side).

In order to precisely align the axis of the ion trap with respect to the photon beam, an adjustable supporting frame was constructed by A. Milosavljević et al [9]. The adjustable

[3] Details and operation of the mechanical shutter are presented in Section 4.5.2.
[4] For reference, see Figure 4.22.

frame is positioned on a rigid table and LTQ mass spectrometer is mounted on top of it. Figure 4.17 presents the 3D model of the adjustable supporting frame.

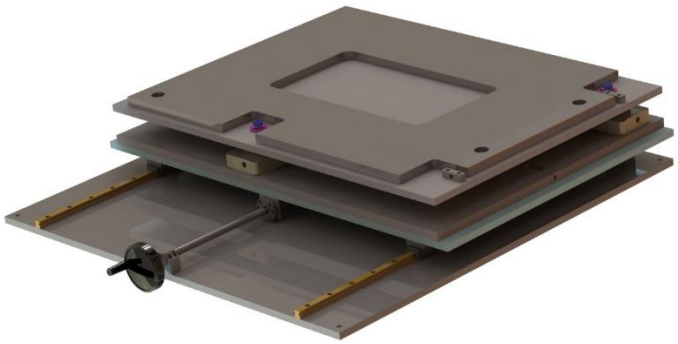

Figure 4.17 - 3D model of the adjustable supporting frame for LTQ mass spectrometer used to precisely align the ion trap axis with respect to the photon beam. Designed by A. Milosavljević et al [9].

The supporting frame is designed to enable fine tuning of the position in 3 translational axes, and 3 rotational axes, covering all degrees of freedom. Adjustments for each axis are realized with the hex key screws. The alignment process is rather tedious and crucially important for obtaining the best overlap of the trapping volume with the photon beam, ensuring the high signal to noise ratio. Figure 4.18 presents a 3D model of final assembly with the vacuum stage, LTQ mass spectrometer, the supporting frame and the carrier table.

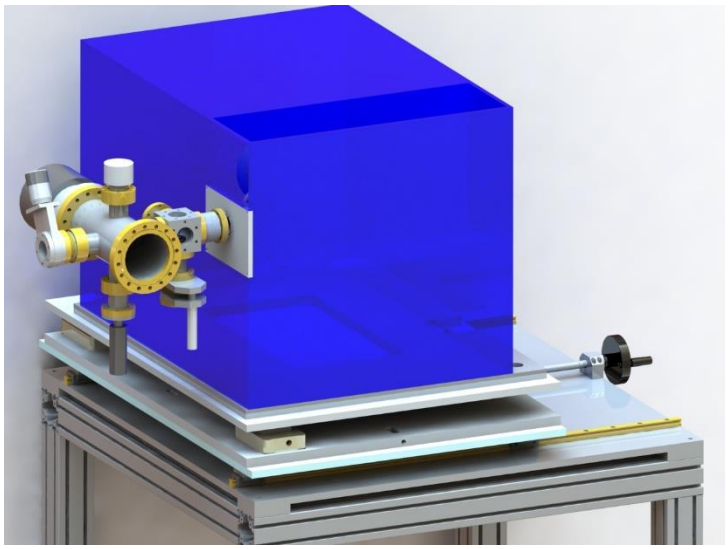

Figure 4.18 - 3D model of the vacuum stage coupled to the LTQ mass spectrometer, installed on an adjustable supporting frame, which is rested on a rigid table. The entire system is mobile. Designed by A. Milosavljević et al [9].

Coupling

The vacuum stage is coupled to the back side of the LTQ mass spectrometer via CF40 flexible bellows. In order to obtain a coupling of the vacuum stage through CF40 bellows to the chassis of the LTQ mass spectrometer, a custom Plexiglas window plate is designed. The back side of the LTQ mass spectrometer was originally sealed with a metal plate. 3D model of the Plexiglass window is presented in Figure 4.19.

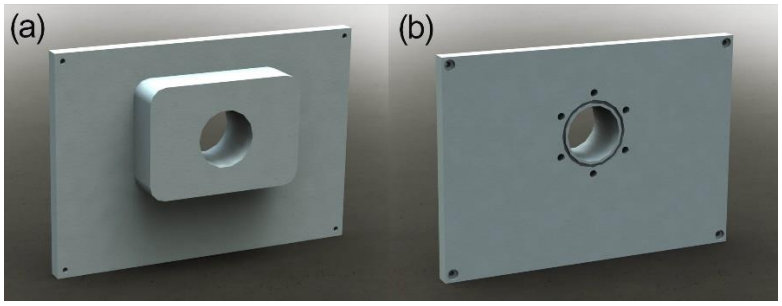

Figure 4.19 - 3D model of the Plexiglass back plate window, designed to couple the vacuum stage to the LTQ XL mass spectrometer: a) back side, positioned towards LTQ and b) front side, with CF40 rubber seal groove and threaded holes. Designed by A. Milosavljević et al [9].

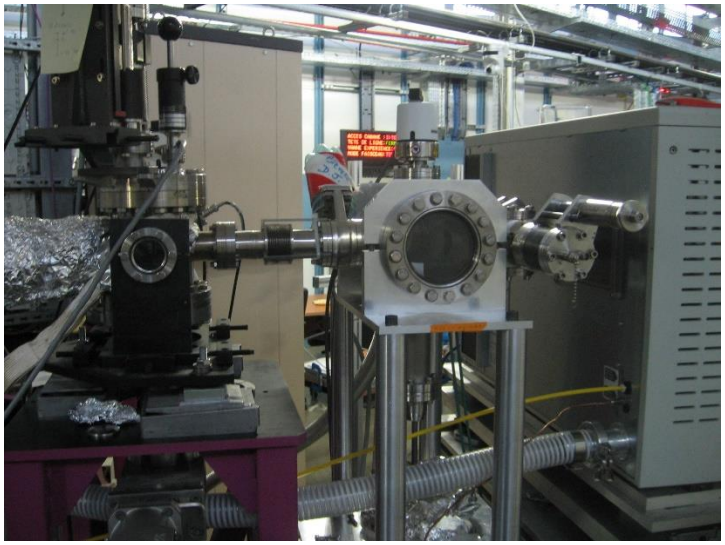

Figure 4.20 - Picture of the experiment with LTQ mass spectrometer coupled to the DESIRS beamline of the SOLEIL synchrotron.

Entire assembly with the LTQ mass spectrometer presented in Figure 4.18, is portable. The carrier table is equipped with small subtractable wheels. This allows for a quick transport of the whole system to another beamline of the synchrotron SOLEIL. With this system, trapped target molecules can be subjected to a wide range of the photon energies, covered by the several beamlines. The system has been so far effectively coupled to the

DESIRS, PLEIADES and DISCO beamlines of the SOLEIL facility, as well as to the keV ion beamline GANIL. The results presented in this Thesis were obtained from the experiments involving the first two mentioned beamlines. A photograph of the coupling the system to the DESIRS beamline is presented in Figure 4.20.

Alignment process

The alignment of the ion trap axis with respect to the photon beam is done in 3 steps. In the first step, before the beamtime and the pumping, the table with the supporting frame and LTQ is positioned roughly into place with respect to the beamline theoretical optical line. If coupled to the DESIRS beamline, the advantage is a still visible part of the zero-th order of the VUV photon beam, which can be detected by eye when reflected from a sheet of white paper. In that case the second step is performed. ESI source is removed from the LTQ mass spectrometer, enabling the clear path of the VUV photon beam, after passing through the ion trap and ion optics. In order for this step of the alignment process to work, both LTQ and vacuum stage have to be brought back to the atmospheric pressure. The beamline coupling valve is closed. Since the moving part of the valve is constructed out of MgF_2 glass window, it is still transparent UV light. The beamline is then set to the lowest possible energy of 4 eV. The UV photon beam can then pass all the way through the ion trap and the ion optics system. Small adjustments are made on the supporting frame, until the bright violet spot is seen on the UV reflective paper positioned just after the ion optics, at the front side of the LTQ mass spectrometer.

In the final third step of the alignment process vacuum stage and LTQ mass spectrometer are pumped to the ultimate pressures of 10^{-6} mbar and 10^{-5} mbar, respectively. Cytochrome C or Insulin precursor ions are electrosprayed and selected in the ion trap[5]. The trapped ions are subjected to the beam of VUV photons, with an energy of 15.4 eV. Figure 4.21 presents the obtained action MS^2 after optimal alignment, obtained for Cytochrome C, 8+ precursor ions.

The MS^2 was normalized to the precursor ion $[M+8H]^{8+}$, designated at m/z 1542. Relaxation channels corresponding to the ionization of the precursor ions with VUV photons appear in the spectrum. Peaks at mass-to-charge ratios of 1370, 1233 and 1121 correspond to radical cations $[M+8H]^{\bullet 9+}$, $[M+8H]^{\bullet 10+}$ and $[M+8H]^{\bullet 11+}$ originating from single, double and triple ionization of the precursor ion, respectively. Optimal alignment was obtained by maximizing the relative intensities of these ion fragments by fine tuning the position of LTQ with the supporting frame.

[5] More details about the experimental procedure are presented in Section 4.5.4.

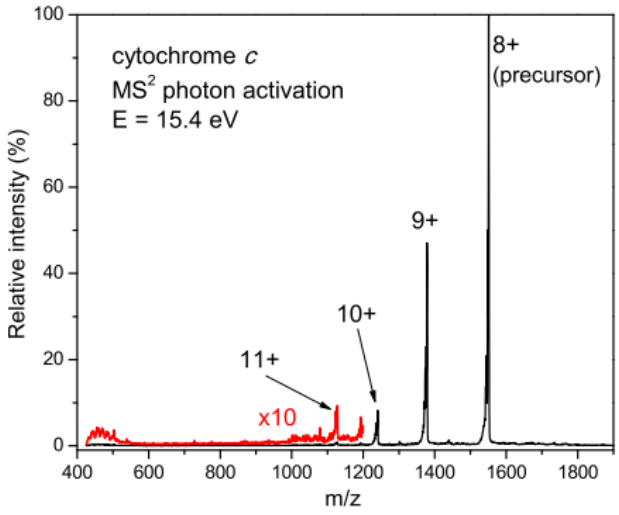

Figure 4.21 - Tandem mass spectrum, recorded for Cytochrome C precursor ions of 8+ charge state, after activation with VUV photons at 15.4 eV energy. Adopted from [57].

4.5.2 Mechanical shutter - design and operation

Photon beam chopping was achieved by positioning the rotating mechanical shutter at its path, just before the entrance to the ion trap. The shutter is designed by A. Milosavljević et al [57] and installed in the turbo vacuum stage. The assembly with the mechanical shutter is presented in Figure 4.22. The mechanical part called shutter head is attached to the shaft of the rotational electric motor *Khunke*, in order to physically block the photon beam. The shutter head is made from Aluminum, with a cylindrical shape and a hole perpendicular to the cylinder axis. The motor is powered by the shutter circuit[6] consisting of a solid state relay connected to the power supply. The motor actuation is initiated by the TTL signal from the LTQ mass spectrometer, whose length is defined by the activation (irradiation) time of the selected ions.

TTL signal line was traced in the electronic board of the LTQ and taken out of the casing. The line of the signal is connected to the input of the shutter circuit and acts as a trigger. Activated by the high state (5 V) of the TTL signal, the shutter circuit drives the electric motor which rotates the shutter head. Optionally, a delay generator is inserted in front of the shutter circuit in order to close the shutter typically 50 ms before the end of the actual activation time. If so, the activation time then has to be set to 50 ms longer. The delay generator is set to activate at the rising edge of the TTL signal sent by the LTQ and to generate a new TTL signal in the phase with the original one (see Figure 4.23). In this way, the interaction of photons with ions is stopped before the detection of the ion fragments. When the activation time runs out and TTL signal goes to 0 V, the mass

[6] In the following text term "shutter circuit", will be used to refer to the electrical part of the mechanical shutter in the experiment with photons. In the second part of the Thesis, the same term will be used for different circuit, required in the experiment with electrons.

spectrum is recorded. As a result, the recorded mass spectra showed fairly reduced background signal noise peaks.

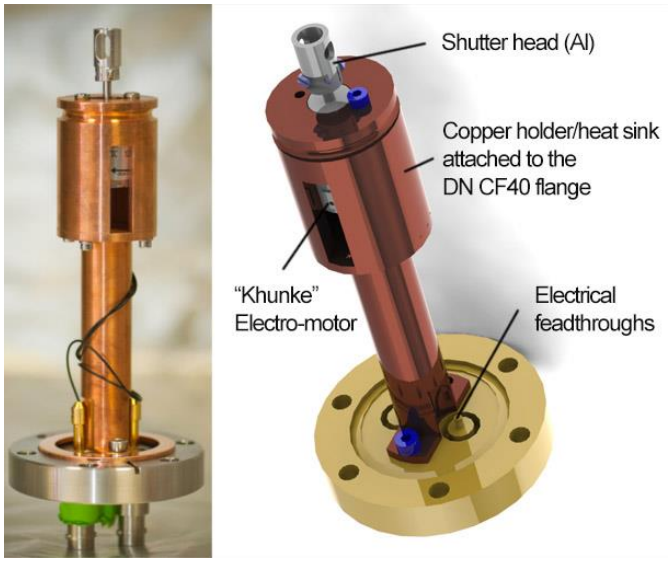

Figure 4.22 - Mechanical shutter for the chopping of the photon beam. Picture of the shutter assembly mounted on a CF40 flange is on the left. 3D model of the shutter assembly is on the right. Adapted from [57].

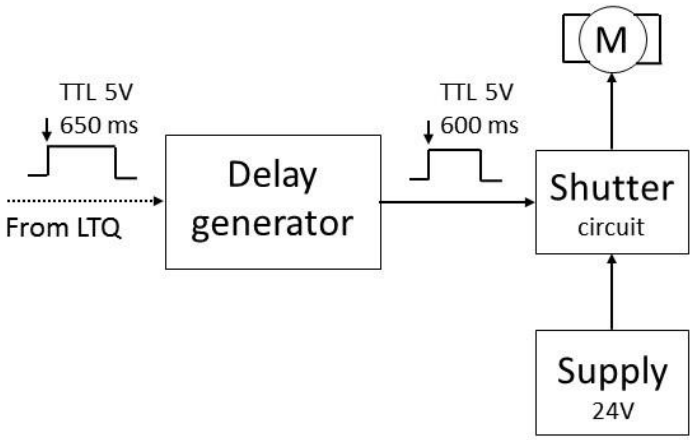

Figure 4.23 - Block diagram with delay generator in front of the shutter circuit, for better signal to noise ratio. TTL signal length of 600 ms is used as an example.

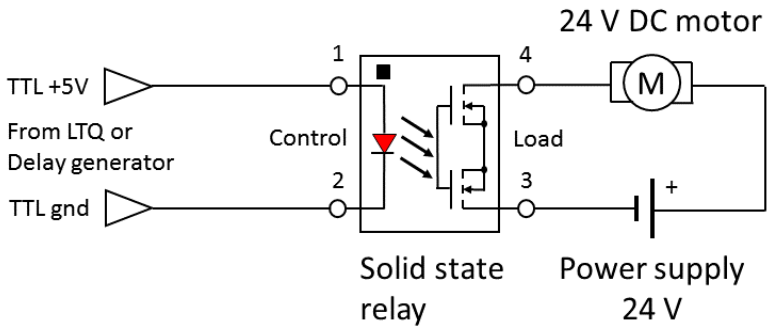

Figure 4.24 - Electrical circuit for the mechanical shutter. Solid state relay (SSR) switch consist of an IR photo-diode and two field effect transistors (FETs) with a photosensitive gate. The high state of TTL signal turns on the photo-diode which results in a closing of the two transistors, closes the circuit on the right side by applying 24 V to the electric motor. The absence of TTL signal (or low state - 0 V) leads to the open circuit and electric motor is not powered.

The electronic circuit for the mechanical shutter is represented by "Shutter circuit" box in Figure 4.23. Actual schematic of the circuit is presented in Figure 4.24. It consists of a solid state relay switch, which connects a power supply of 24 V directly to the electric motor, as long as 5 V TTL signal is present at its input. Applying the 24 V on the motor quickly rotates the shutter head. Mechanical constraints allow the shutter head to rotate only for 90°, locking it in a position such that the hole is parallel with the direction of the photon beam. The shutter head is spring loaded, thus as soon as the motor power is cut, the shutter head is rotated back for 90°, to the position such that the photon beam is blocked.

In order to estimate the shutting speed of the entire shutter system, test measurements are conducted under high vacuum, at the pressure of 10^{-7} mbar. The performance of the mechanical shutter is evaluated by measuring the current from the photodiode (AXUV100, International Radiation Detectors), positioned just after the shutter head in the vacuum assembly. The photodiode current measured with the digital oscilloscope (DG645, Stanford 150 Research Systems, Sunnyvale, CA, USA), was generated by the zero-th order of the VUV light from DESIRS [8] beamline. The signal obtained from the photodiode after applying the power to the shutter motor is presented in Figure 4.25.

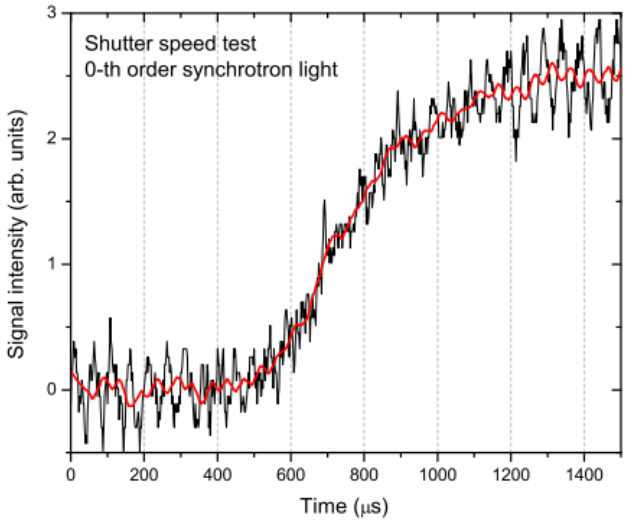

Figure 4.25 - Photodiode current generated by the zero-th order of synchrotron radiation light, measured after opening the mechanical shutter under high vacuum. The red line is generated by 50 point Savitzky Golay smoothing of the obtained signal, in order to reduce the noise. Adopted from [57].

The results of the performance test [57], reveal that the shutter has a systematical delay of about 20 ms, because of the mechanical inertia of the moving parts, although this does not influence the irradiation of trapped ions. The shutting speed was estimated from Figure 4.25, to be around 1 ms.

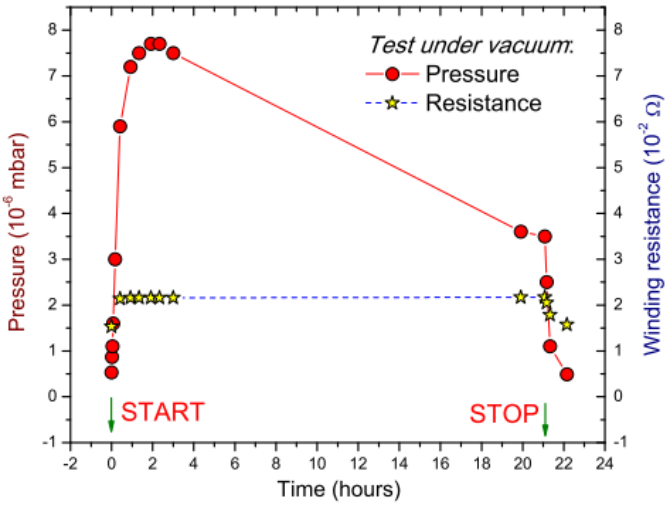

Figure 4.26 - Durability test of the shutter, during 24 hours in vacuum conditions. Shutter motor winding resistance is represented with stars, while circles show the pressure in the vacuum assembly. Adopted from [57].

The resistance of the motor windings was checked under high vacuum conditions, through 24 hour period with a 70 % of the duty cycle. The results of the test [57] are presented in

Figure 4.26. Durability test showed only slightly elevated resistance of the motor windings, proving that large copper holder/heat sink is absorbing most of the generated heat, even under vacuum. The heat from the copper holder is conducted to the vacuum parts of the vacuum stage assembly. The latter is then quickly cooled by the surrounding air at room temperature of 21 °C. The pressure in the vacuum assembly is increased during the first hours of the test due to the degassing of the motor windings. The pressure decrease was observed after 3 hours from starting the test. The resistance of the windings only slightly increased and remained practically constant during the entire test, meaning that the temperature of windings was well below the alarming limits. Both the vacuum stage pressure and motor winding resistance drop to starting values, within an hour after the motor was turned off.

4.5.3 Synchronization with the beamlines

The action spectroscopy of the macromolecular targets presented in this Thesis is achieved through automated acquisition system made by A. Milosavljević and A. Giuliani. The acquisition system is based on the home-made software, which couples two independent hardware components - the LTQ XL mass spectrometer and a synchrotron beamline into one instrument. TTL electric signals are utilized in order to synchronize the operation of these two devices. The control logic for the electric signals is governed by a home-made computer program, written in Igor Pro. The basic principle of the instrument lies in repeating three processes: 1) the ion production and selection, 2) the ion activation at defined energy and 3) the detection of fragments. Each cycle is performed at different activation energy, obtaining activation tandem mass spectra (MS^2) for the desired molecular target. The procedure for the acquisition of many MS^2, for a range of different energies, is defined as an "*energy scan*".

One energy scan consists of a number of energy points, ranging from 10 to 100. A custom temporal sequence is defined and ran for every energy point. One temporal sequence comprises sequential isolation of one or multiple precursors. Individual acquisition (ion irradiation) time length for each precursor is set, which defines the total time length of the sequence. All precursors in the sequence are first subjected to one photon energy and recorded in a "raw file"[7], which contains one mass spectrum for every precursor. The sequence is then repeated until all energy points are scanned. At the end of an energy scan, depending on the number of energy points, the same number of raw files containing all precursor mass spectra is generated. The total time required for one energy scan is determined by the number of energy points multiplied by the time length of the sequence. Typically, for practical reasons, the energy scans were created to last not more than 10 hours.

[7] Raw file is the digital computer file format (example scan1.raw) generated by the mass spectrometer software, which contains all data stored during one sequence. This data contains tandem mass spectra and a range of instrumental parameters.

The energy scan process is practically realized by the usage of peripheral controls - *start in* and *ready out*, as an inbuilt hardware option of the LTQ XL mass spectrometer. As their names suggest, *start in* is an input type of connection, while *ready out* serves as an output. Operating principle of these controls is the two state digital logic - TTL. Each control has two contacts, which can be either open (not connected, 5 V) or closed (shorted to the ground, 0 V). LTQ peripheral controls are connected to the PC computer via external USB National Instruments (NI USB-6501) analog-to-digital (AD) card. The computer program was written in Igor Pro software in order to control and automate the entire energy scan process. For the purpose of synchronization, one input and two output connections are utilized from the AD card. A schematic diagram for the digital communication of LTQ mass spectrometer with the DESIRS beamline is presented in the Figure 4.27.

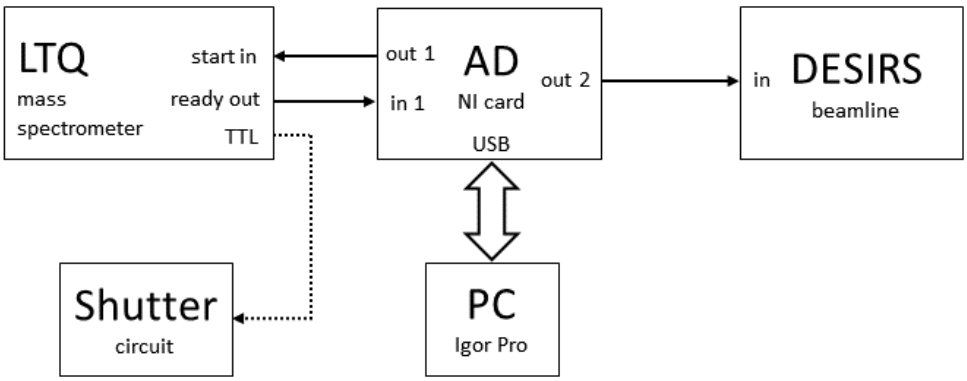

Figure 4.27 - Block diagram for connection of LTQ mass spectrometer with DESIRS beamline.

The LTQ mass spectrometer is set to send 5 V TTL signals in the duration of ion activation time (600 ms in the present case). These signals were traced on the internal board of LTQ, hard wired and taken out of its case, for the synchronization of the shutter circuit. In Figure 4.27 dashed line symbolizes the wire that carries the TTL signal out of the LTQ to the shutter circuit[8].

At the end of each sequence (scan for one energy point has finished) a long contact closure signal (1000 ms) is sent by the LTQ at *ready out.* The long signal is detected by the computer program in Igor Pro, which then sends a TTL signal of 5 V through AD card to the beamline in order to change the photon energy to the next one. Regarding the communication there are two types of beamlines utilized to conduct experiments, whose results are presented in this Thesis. For them, the communication can be one-way (DESIRS beamline), or two ways (PLEIADES beamline).

[8] TTL signal can either be connected to the inputs of the circuit for the mechanical shutter Figure 4.24, or the electrical shutter circuit presented in Figure 4.42 in Section 4.6.4.

The one way communication beamline like DESIRS, has the option to only receive signals. It is the reason why the intermediate stage with an AD card and a computer program have to be used. When a sequence is finished, the contact closure at *ready out* is detected by the program. This initiates a TTL signal through the AD card, which is sent to the control input of the DESIRS beamline. The program then waits for a custom defined 5 seconds for the beamline to change the photon energy (wavelength). Waiting period of 5 seconds is determined experimentally as the optimal time window length, during which the DESIRS beamline will certainly finish the wavelength changing process. After this time passes, the program generates a TTL signal and sends it through the out 1 of the AD card to the LTQ *start in* input, as a signal to start the new sequence. The program algorithm is depicted in the Figure 4.28, while the control window of the program is presented in Figure 4.29.

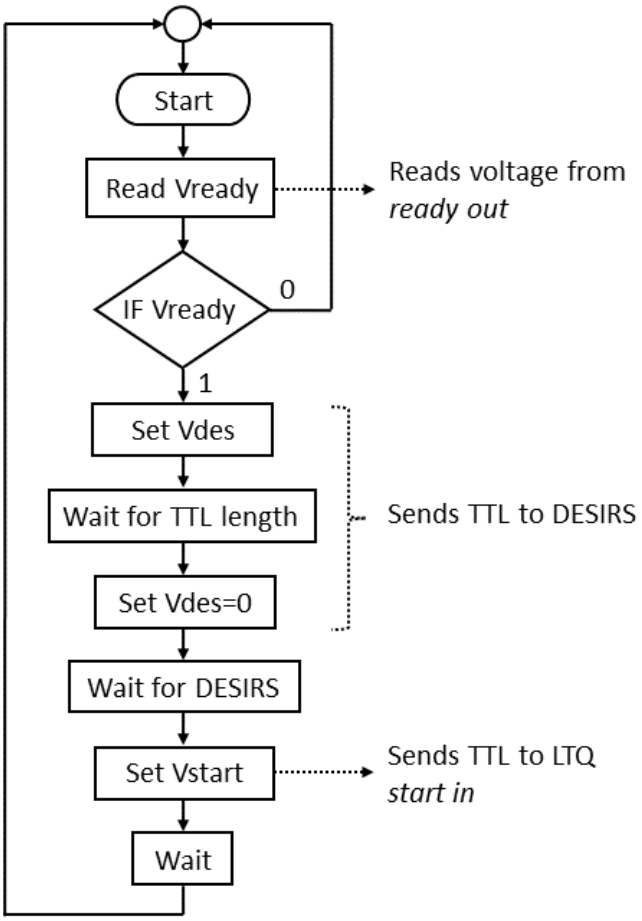

Figure 4.28 - Algorithm for Igor Pro program, used for energy scan process automation. Designed by A. Milosavljević and A. Giuliani.

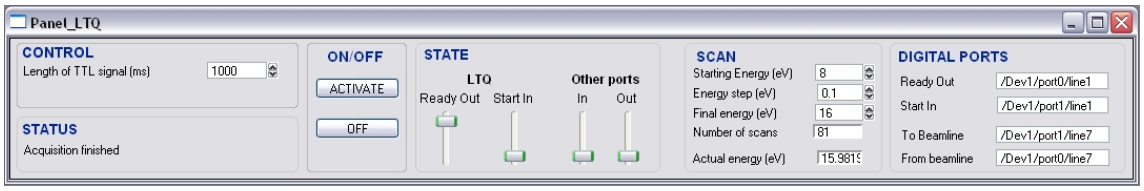

Figure 4.29 - Custom made Igor Pro control window running on mass spectrometer's PC, used for energy scan process automation. Designed by A. Milosavljević and A. Giuliani.

On the other hand, the beamline PLEIADES is capable of changing the photon energy initiated by the external signal. Upon receiving a signal from LTQ, indicating that one energy point is finished, the beamline automatically prepares the necessary readjustments for the next photon energy. After the change to a new photon energy is done, the beamline sends the signal to its control output. The block diagram for the connection with PLEIADES beamline is depicted in Figure 4.30.

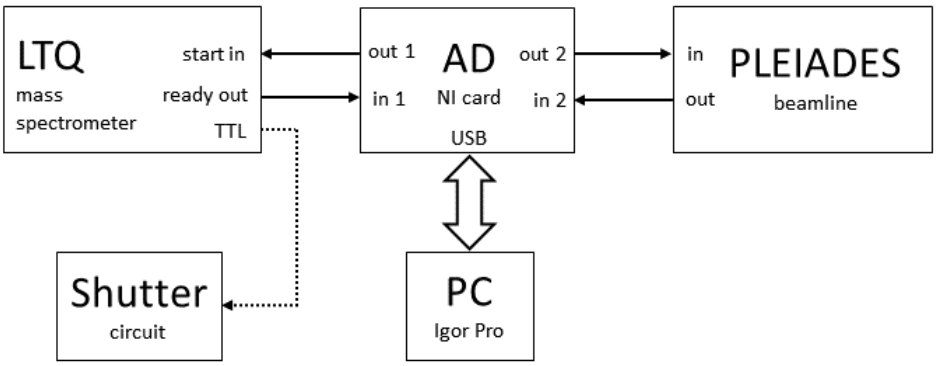

Figure 4.30 - Block diagram for connection of LTQ mass spectrometer with PLEIADES beamline.

4.5.4 Experimental procedure

This section is dedicated to the experimental procedure used in order to activate the trapped ions with photons from synchrotron radiation. As previously mentioned, the system is mobile and can be coupled to one of the three appropriate beamlines of the synchrotron SOLEIL. Figure 4.31 presents the part of the experimental setup involving the VUV photons from DESIRS beamline at the brunch B. The schematic representation of our experimental setup coupled the end station of brunch B at DESIRS beamline, is presented in Figure 4.32. The experimental procedure for coupling and synchronizing the system with the PLEIADES beamline is similar in principle, thus it is not presented in the Thesis. The timeline of the experiment is presented in Figure 4.33.

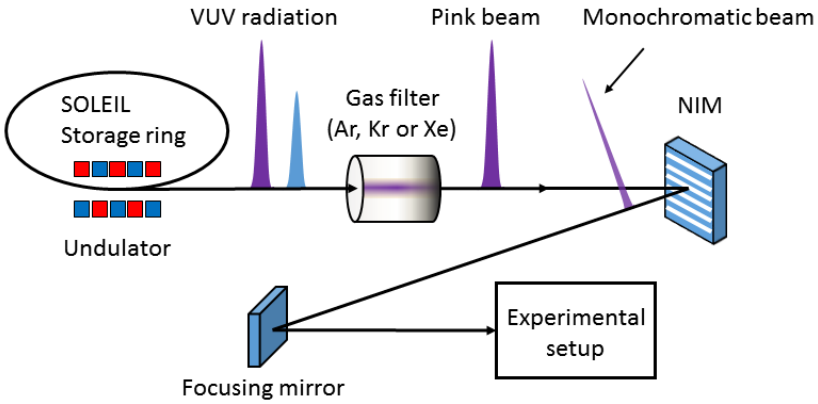

Figure 4.31 - Schematic representation of the VUV photon path in brunch B at the DESIRS beamline, starting from an undulator to the point where the experimental setup is coupled. Adapted with permission from [9].

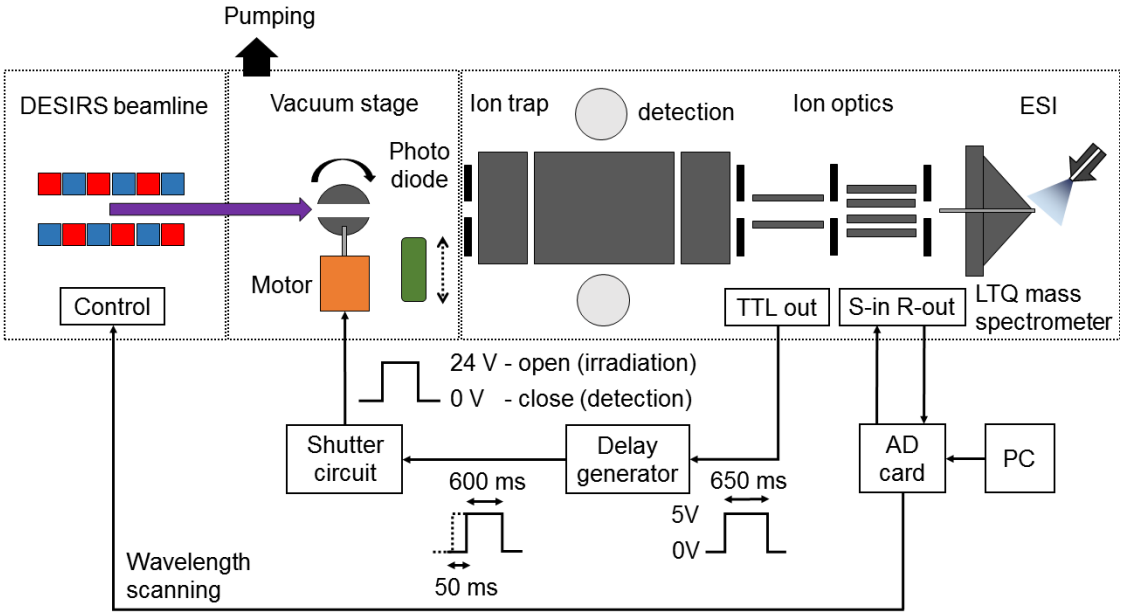

Figure 4.32 - Experimental method and schematic for synchronization of the LTQ mass spectrometer with the DESIRS beamline.

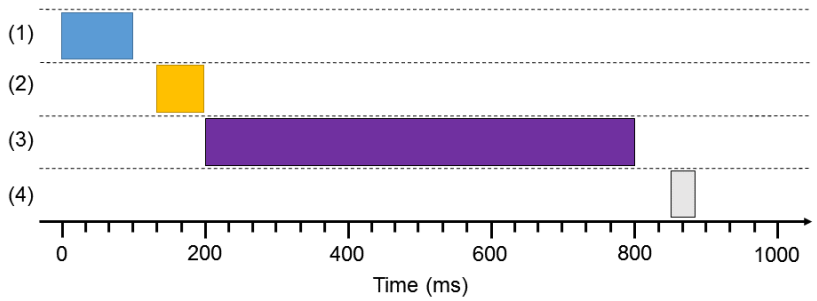

Figure 4.33 - Timeline of the experiment for the activation of trapped ions with VUV photons from DESIRS beamline: 1) ion injection, 2) ion selection, 3) ion irradiation and 4) fragment ion detection.

The experimental procedure is performed through four sequences: 1) ion production, 2) ion selection, 3) ion activation and 4) detection. More details are given below:

(1) Analyte solution was injected into a syringe and forced with the assistance of the mechanical pump through small capillaries into the ESI at the desired flow rate. Depending on a desired state of the target molecules, LTQ mass spectrometer can be equipped with two types of the ESI sources - standard ESI or nano-ESI. In this Thesis both hydrated and bare peptide precursor ions were probed with VUV photons. The production of hydrated precursor ions is more difficult and requires adjustments of the spray parameters. In both cases, all electrosprayed ions are guided by the ion optics and stored into the ion trap.

(2) A vast number of different charge state precursors can be produced simultaneously by a standard ESI (or nano-ESI) source. Only one precursor of the interest is selected, by defining the mass-to-charge ratio in the LTQ mass spectrometer software. The selected precursor was isolated in the ion trap by ejecting all other ions.

(3) After reaching the storing capacity of the ion trap, a 5 V TTL pulse is initiated by the LTQ electronics. The presence of the 5 V TTL signal on the shutter circuit closes the relay contacts and applies a 24 V on the electric motor inside the vacuum stage. The shutter head is rotated, allowing the VUV photon beam to irradiate the trapped ions. TTL 5 V signal is present during the activation time, defined previously (for example to 650 ms) in the LTQ software. In addition, a delay generator was installed on the path of the TTL signal, in order to introduce an acquisition delay (of usually 50 ms). As a result, the trapped ions are irradiated during a shorter time. After the activation time passes, LTQ sets TTL signal to the low state (0 V), the motor power is cut and the spring quickly rotates back the shutter head closing the photon beam.

(4) The detection takes place as soon as the TTL signal goes back to the low state (0 V). All ion fragments are ejected from the ion trap and an action tandem mass spectrum is recorded at the given photon energy and for the currently trapped precursor ion.

The LTQ software gives the possibility to program the selection method, containing a procedure with multiple precursors, with user defined duration for each precursor. In that case, each precursor is successively isolated in the ion trap during a specified time, ranging from (1-30) minutes. Steps (3) and (4) are then repeated for one photon energy until all precursors contained in the selection method are irradiated.

Each time the selection method is completed, or after the irradiation of all defined precursors at one photon energy, the LTQ initiates a long contact closure at *ready out*. This signal is detected by the program in Igor Pro and the TTL signal is sent to the DESIRS beamline in order to change the photon energy. The entire process is repeated until all predefined energy points are scanned. At the end of the energy scan, an action MS^2 for every precursor of the analyte macromolecule is acquired, at each photon energy defined in that particular energy scan.

4.6 Electron experimental setup

4.6.1 Electron gun

Double focusing electron gun was used as a source of electrons, for the purpose of activating trapped ions. It was developed at the Institute of Physics in Belgrade by S. Madžunkov and it is a constituent part of the experimental setup UGRA [58]. It is capable of producing relatively high primary electron current in the order of few μA in the electron energy range of (40-350) eV. A cross section view of the electron gun is depicted in Figure 4.34.

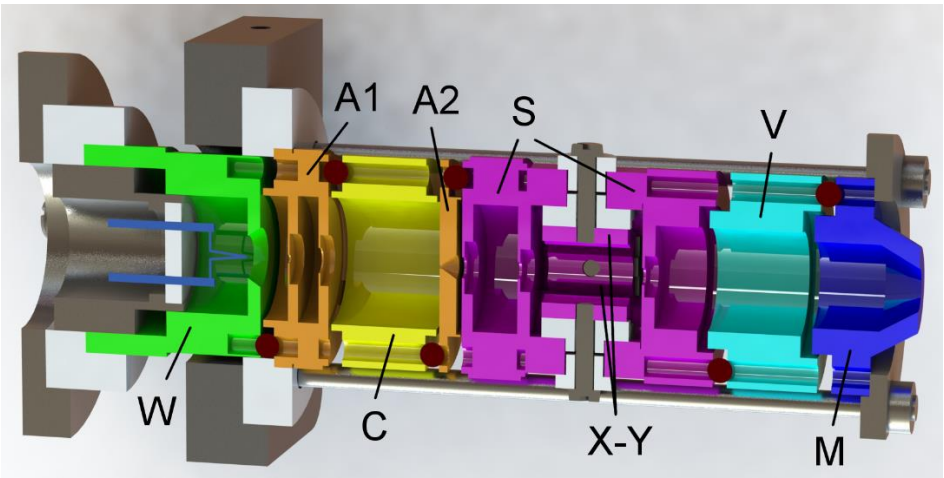

Figure 4.34 - 3D model of the electron gun, electrode cross section view.

The electron gun consists of seven concentric cylindrical electrodes. The electrodes are separated using the rubidium balls of 3 mm in diameter. The last electrode (M) is grounded, as well as the interaction region. The electrons are produced in the thermo-electron emission from the tip of the hairpin cathode, directly heated with currents of 2 A to 2.5 A. The cathode is made of thoriated tungsten wire 0.2 mm in diameter and spot welded to suitable pins cast in a ceramic disc. The electrodes of the electron gun can be divided into two parts: 1) the extraction and the focusing part. The extraction part of the electron gun comprises a hairpin cathode, electrodes W (Wehnelt), A1 (Anode) and C, whereas the focusing part is composed of electrodes A2, S, V and M. Two axis deflector unit have been installed inside the electrode S in order to enable the fine adjustment of the electron beam in the plane normal to the axis of the electron gun. In order to produce electrons with a defined energy, the cathode is supplied with a negative voltage in relation to electrode M, which is grounded along with the rest of the vacuum chamber. All other electrode voltages are floating on the negative cathode potential, such that focusing properties of the electron gun can be preserved with the change of the electron energy (cathode voltage). Since the electrodes W and C have a negative voltage applied in

relation to the cathode, while A is positive, the extraction part of the gun formed from these three electrodes, has double focusing properties. First focusing of the electron beam happens by the lens formed with electrodes W and electrode A1. Second focusing happens between electrodes C and A2, which has a 0.5 mm diameter hole extending into a cone. After the extraction part, an image of the cathode with a defined circular shape is formed. The electrodes S, V and M, form a three-electrode lens with the purpose of defining the final geometry of the electron beam and focusing it on a given distance from the gun. Tuning the voltage on the electrode V is used to regulate the focusing properties of the electron beam for a given distance and electron energy. Present electron gun has been designed to generate a continuous electron current. This means that the cathode is constantly heated and that a steady stream of electrons with a defined energy and a beam geometry is produced continuously.[9]

4.6.2 Electron beam cut off principle and current measurements

For the purpose of activating trapped ions in the collisions with electrons, a continuous mode of the electron gun current cannot be used. Because of the temporal nature of tandem mass spectrometry experiments, the ion activation has to be engaged only during the short period of times - typically several hundreds of milliseconds. Therefore, in order to perform the action spectroscopy experiment with electrons as projectiles, a pulsed electron beam is required.

To cut off the photon UV (or X-ray) beam, a simple mechanical blocking was enough, as described in the previous chapters. For electrons this type of beam cut off is not desirable. The electrons are charged particles and can be easily splatted or reflected from conductive surfaces. On the other hand, they can charge nonconductive materials. As a consequence, the presence of an additional charging perturbs the optimal electric field generated by the electron optics. The final outcome is either a significant distortion or scattering of the electron beam.

In the present experiment, we chose to block the electron beam by means of preventing the emission of electrons from its source – the cathode. This can also be achieved by lowering the cathode temperature (for example, by decreasing the cathode current), but it is a very inefficient, unstable and slow process. An efficient electron beam cut-off can be achieved through a controlled change in the geometry of the electric field. For example, by applying the convenient pulsed voltage on one of the electron gun's electrodes. In the process of thermo-electron emission, a direct heating of the metal cathode increases the energy of the free electron gas inside it. At an appropriate cathode temperature, electrons have enough energy to escape the surface of the metal. The amount of this energy is defined by the metal work function, specific to every material. Therefore, by applying convenient voltages on the W electrode, placed just between the cathode and the anode, the metal work function of the cathode can be additionally altered in a controlled way -

[9] In the following text, this way of operation will be referred as a continuous mode of the electron gun.

to enable or prevent the electron emission from the tip of the hot hairpin cathode. The voltage applied to the W electrode required to fully suppress the electron emission was determined experimentally. It was done by measuring the electron current at a fixed distance from the electron gun, as a function of W electrode voltage.

Schematic for measuring the electron current in a Faraday cup is presented in Figure 4.35. The Faraday cup assembly is made from stainless steel. The electron collector is made from stainless steel bar, cut at 45° relative to its axis. It is installed in an isolated shielding tube, with 2 mm diameter hole at the front end. The entire Faraday cup assembly is positioned at a distance of 72 mm from the last electrode (M) of the electron gun. The electrode voltages are optimally adjusted to focus the electron beam on the Faraday cup, indicated by the maximal current readout, for a given cathode heating current and the electron energy.

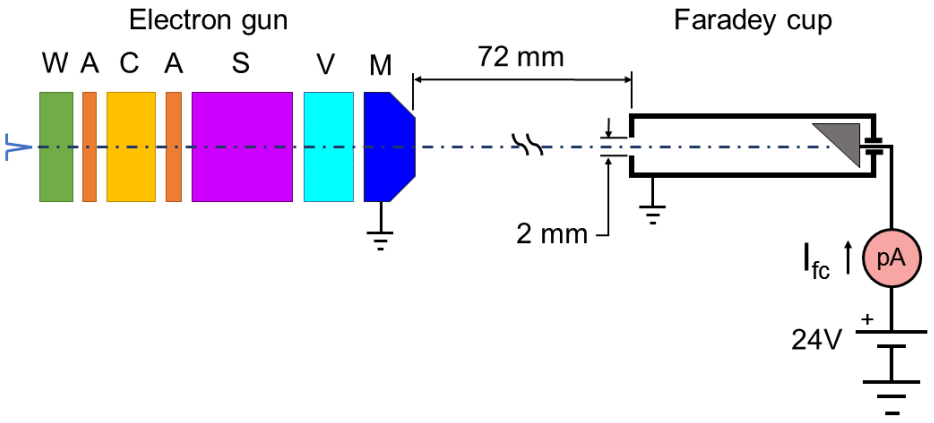

Figure 4.35 - Schematic diagram for electron current measurement using a Faraday cup.

Schematic for the electron emission current measurement is presented in Figure 4.36. An external power supply provides the relatively high current of 2.3 A for direct heating of the cathode. Another external supply provides a tunable negative voltage of up to 350 V which defines the electron energy since the interaction region is grounded. It is connected to the cathode through two equal high power resistors of 220 Ω, labeled with letter R in the Figure 4.36. This connection creates such voltage drop across the cathode, that potential on its tip is exactly -150 V. The cathode tip is a rather small surface and the energy distribution of all ejected electrons is dictated by the cathode tip temperature only. For this configuration, the influence of the geometry of the ejecting surface on the energy spread of ejected electrons is minimal. Thermo-electron emission process yields a typical energy bandwidth of 0.5 eV, for the tungsten hairpin cathode. Another important

advantage of applying the voltage to the cathode through resistors, as depicted in Figure 4.36, is that the electron emission current from the cathode can be directly measured[10].

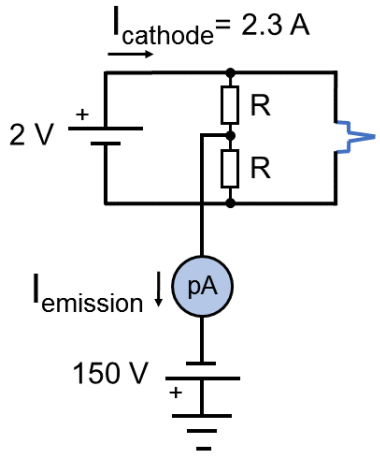

Figure 4.36 - Schematic diagram for electron emission current measurement.

Figure 4.37 presents the measured electron emission current from the cathode for different W voltages, as well as the Faraday cup current. For W voltages up to -20 V, we can see that both the emission current and the Faraday cup current are zero. Therefore for this given configuration of all other electrode voltages, both currents start increasing from about W=-20 V until they reach saturation at around W=-14 V.

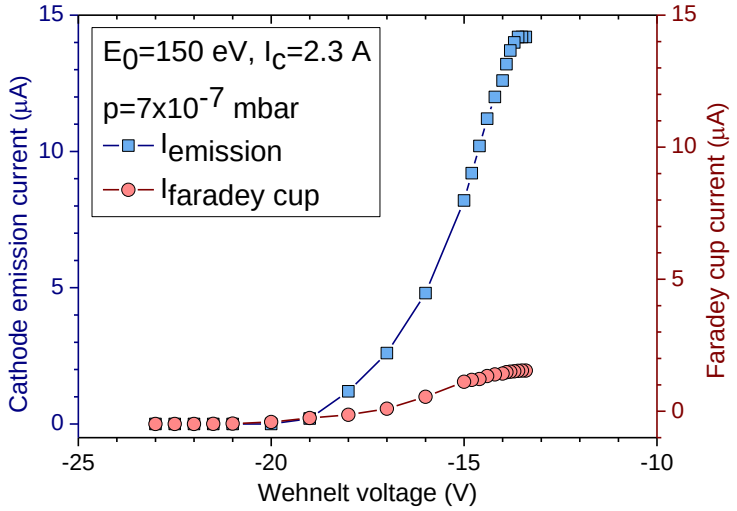

Figure 4.37 - Electron emission current from electron gun cathode and current measured in the faraday cup, as a function of W (Wehnelt) electrode voltage, for 2.3 A cathode current and 150 eV electron energy, for the pressure of $7x10^{-7}$ mbar.

[10] In this method of electron emission current measurement, only approximate value can be obtained. Measured current is linearly proportional to the real emission current, in the limited range only.

In order to make sure that there are no electrons emitted from the cathode, we used -50 V for the *beam cut off* W voltage. On the other hand, the working W voltage which enables a good focusing, called *beam on* voltage, is set to -14 V. It should be noted that only a small part from 15 μA current emitted from the cathode, actually exits the electron gun because the majority of electrons are lost inside the electron gun, as seen in Figure 4.37. For this particular electrode voltage preset current measured in the Faraday cup was around 2 μA.

Figure 4.38 compares the electric field distribution and the electron beam trace simulation from program SIMION [59] for different W voltages. The angular distribution of electrons emitted from the hairpin cathode is wide, thus a negative voltage has to be applied to the W electrode relative to the cathode potential, in order to narrow the beam. The influence of a negative W voltage can be seen by comparing Figure 4.38 (a) and (b). The electrons are scattered over the small aperture of electrode A if the W potential is kept at the cathode potential (W voltage of 0 V) Figure 4.38a. Optimal W voltage provides a good focusing and minimizes the loss of electrons that would otherwise scatter on the anode (Figure 4.38b). However, further lowering of the W voltage relative to the cathode to a critical value, creates a potential barrier which prevents the electron emission (Figure 4.38c). In this case, the metal work function of the cathode is effectively increased and the energy of the electrons is lower than the depth of the potential barrier, for the same temperature (the current) of the cathode.

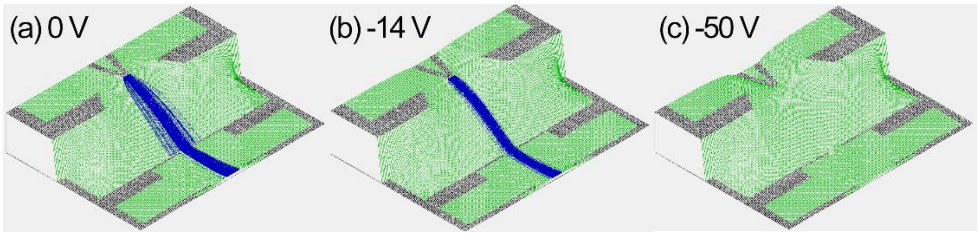

Figure 4.38 - Electric field and electron beam trace simulation from program SIMION. Voltages applied on Wehnelt electrode are relative to the cathode voltage: a) 0 V, b) -14 V and c) -50 V. High enough negative voltage completely blocks the electron emission.

4.6.3 Pulsing the electron gun

An electrical schematic of the electron gun with electronic shutter circuit[11] is presented in the Figure 4.39. The cathode and all electrodes are connected to the external power supplies. Each electrode has its own dedicated voltage divider constructed of variable resistors (helipots[12]) and a few fixed precision resistors. Two power supplies (one positive

[11] In the following text, term "shutter circuit" will be used to refer to the electronic shutter circuit, which supplies pulsed voltages on electrode W, in order to pulse the electron beam.
[12] Helipot is a multi-turn (up to 20 turns) variable resistor and is commonly used in electric circuits which require precise resistance adjustment along with high stability of voltages.

150 V and one negative -50 V) supply electrode voltages required for the operation of the electron gun. The electrode W is connected to its power supply through the shutter circuit. It was specially designed for the purpose of this experiment, in order to chop the electron beam. Details about the shutter circuit and its operation are given in the following paragraphs. In Figure 4.39, the shutter circuit is represented by a box, as the rest of the power supplies. The voltage input of the shutter circuit is the same negative power supply (of -50 V) as the one used for the electrode C. The output of the shutter circuit is triggered by the external TTL signal, generated by the LTQ mass spectrometer. The shutter circuit output has two states, depending on the state of the TTL signal. Each state is defined by one voltage, tuned to either enable or prevent the electron emission, thus allowing for the pulsed mode of operation.

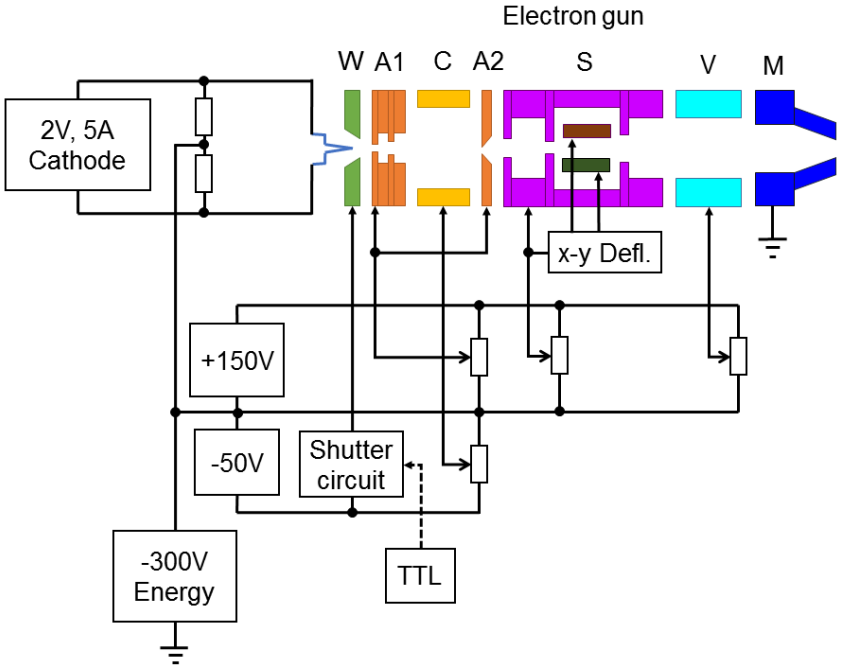

Figure 4.39 - Electron gun schematic with shutter circuit driven by TTL signal. All electrode voltages are floating on the potential of the cathode, which defines the electron energy.

4.6.4 Electron gun shutter circuit

A custom electric circuit was designed in order to supply two different voltages on the W electrode, triggered by the TTL signal sent from LTQ mass spectrometer. The circuit operates as a simple switch, connecting either the fixed -50 V to cut off the beam, or the tunable -14 V voltage, which allows optimal focusing of the electron beam. The basic principle of operation of the electron shutter circuit is presented in Figure 4.40.

In order to obtain fast and stabile voltage changes, we decided not to use mechanical relays. The reason is because of their multiple contact closures before the final contact closure, which would create noise in the highly stable voltages required for electron gun

electrodes. On the other hand, the solid state relay used in the photon shutter circuit to drive the DC motor was the barely sufficient speed and stability for this purpose. Moreover, its power handling is well above nano-ampere currents that are typically required for electrodes of the electron gun. Also, it would require two of these relays to assemble the switch from the Figure 4.40. Instead, we designed a switching circuit that works on a similar principle as the solid state relay – using two optocouplers.

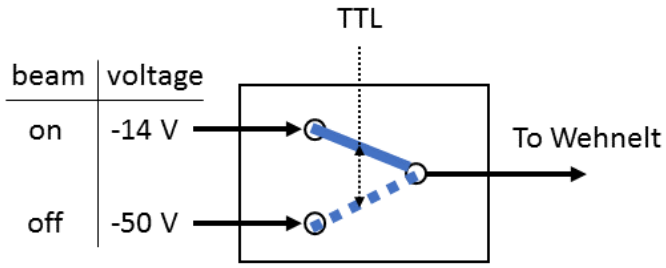

Figure 4.40 - The basic principle of operation of the electronic shutter circuit. In the upper position a switch connects -14 V to the W electrode, enabling the electron emission. Electron emission is completely blocked if the switch is in the lower position, where -50 V is applied to the W electrode.

An optocoupler is a passive electronic component, used to transfer the electric signal from one stage to another, using an infrared photodiode and a phototransistor. When the photodiode is turned on, infrared light opens the bipolar phototransistor. Because the resistance between the emitter and collector is very small when the transistor is open and vice versa, it is suitable for switching. If there is no infrared light, the transistor stays closed and the collector to emitter resistance is in the order of giga ohms. The basic principle of operation of an optocoupler is presented in Figure 4.41. The advantage is that the two optocoupler stages are galvanically isolated from each other and the reaction speed of the output phototransistor in relation to the input of the photodiode is in the order of microseconds. The shutting speed used for photons was in the order of 500 ms, but in the present case with electrons, the shutter circuit was designed to achieve the activation time of at least 1 ms.

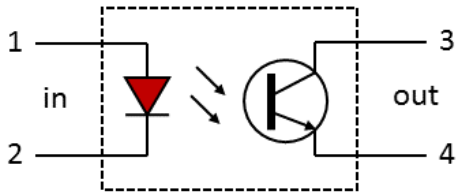

Figure 4.41 - Optocoupler – semiconductor electronic element. Infrared (IR) photodiode and an IR phototransistor are enclosed in a sealed package. Input terminals of the photodiode are (1) – anode, (2) – cathode, while output terminals of the phototransistor are (3) - collector and (4) – emitter.

Schematic of the shutter circuit for W electrode is presented in the Figure 4.42. A detailed description of the circuit follows. The circuit is designed in two stages, the driver (optocoupler) and the switching (transistor) stage. The function of the driver stage is to galvanically insulate the input - the LTQ mass spectrometer, from the high voltage output – required for the electron gun electrodes. Driven by the first stage, switching stage is composed of the voltage divider along with two transistors, which applies the high voltages to the W electrode.

The driver stage consists of two optocouplers O1, O2, the voltage supply for the optocouplers V1, the current limiter resistors R1, R2 for protection and two digital logic inverters enclosed in an SN7404 integrated chip. It should be noted that a signal generator (labeled TTL) in Figure 4.42 is not a part of the shutter circuit and is used for the simulation purpose only. The anodes of the photodiodes (their left sides in Figure 4.42) in both optocouplers are connected to the 5 V supply, through the resistors R1 and R2. The photodiode lights up only if there is enough voltage applied across its terminals[13]. In order for optocouplers to be in the conducting state, the cathode (right sides of the photodiodes in Figure 4.42) has to be polarized at 0 V (grounded). In order to design a switch which connects only one of the two input voltages to the output (W electrode), two optocouplers must always work in the opposite states – the first one on, the second one off and vice versa. The alternating operation is achieved with two digital inverters labeled N1 and N2 in the Figure 4.42. TTL signal from the LTQ mass spectrometer is simulated by the signal generator, setup to output a square wave pulse signal, with an amplitude of 5 V and 500 Hz frequency. This signal corresponds to the TTL output of the LTQ mass spectrometer for the activation time of 1 ms. The signal from the function generator is connected to the inverter N1, whose output is in series with the second inverter N2. The outputs of the first N1 and the second N2 inverters are connected to the cathodes of the photodiodes in the first O1 and second O2 optocoupler respectively. Since both anodes of the optocouplers are fixed at 5 V, this connection will ensure that the cathodes of the photodiodes are always connected to different voltages (0 V or 5 V). As a result, only one optocoupler can be in the conducting state while the other one is turned off. For example, if the input signal (from the signal generator) is at 5 V, the optocoupler O1 will be turned on, since its cathode will be at 0 V. Inverting the 5 V twice, after passing through both inverters, the cathode of the photodiode in the optocoupler O2 will, in that case, be at the same 5 V as its anode - meaning that it is turned off.

[13] For silicon PN junctions (diodes) this usually means at least 0.6 V, since it is the value of voltage drop generated across its terminals in the forward (conducting) direction.

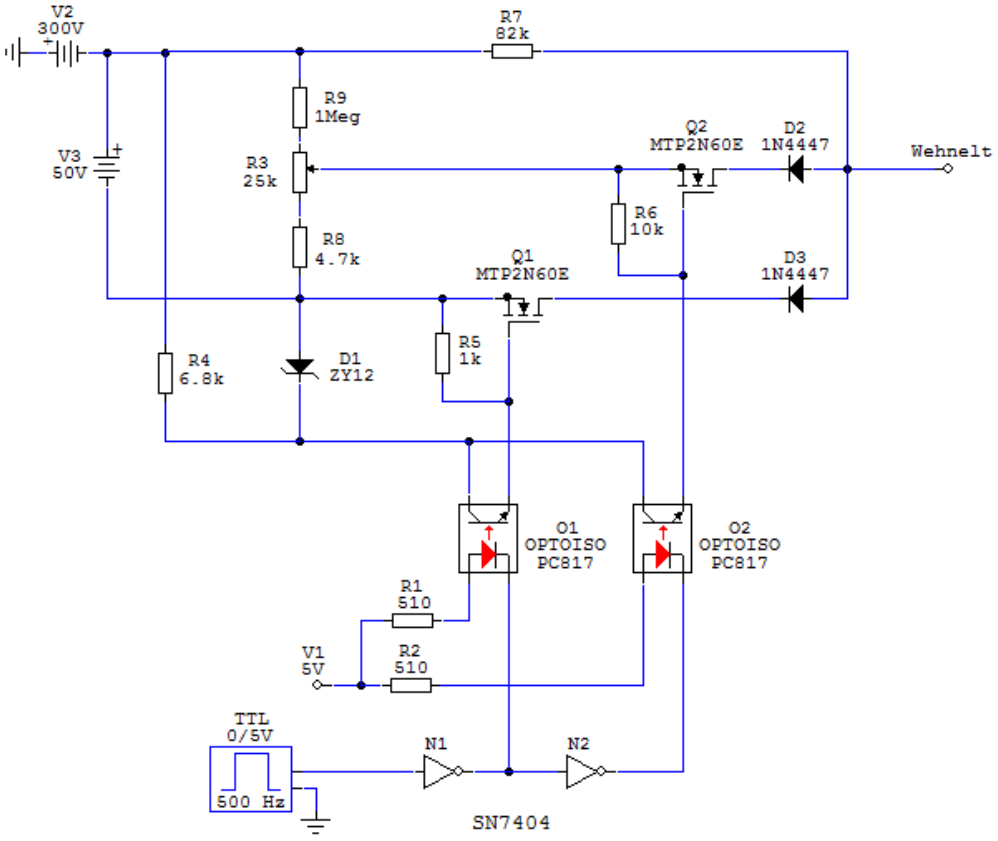

Figure 4.42 - Electric schematic for shutter circuit used to simulate and record the circuit response.

The driver stage of the shutter circuit has the function to drive the FETs (field effect transistors) that work as switches. An optocoupler driver stage alone cannot handle the high voltages floating voltages, therefore, the transistor switch stage had to be added. Both stages combined have a microsecond switching speed, determined by the slower driver stage, even though the transistor (FET) stage may work in the sub-microsecond regime. The collectors of the optocoupler output transistors are polarized to 12 V, through the Zener diode D1. This is not entirely true for the Q2 because it is floating on a variable part of the voltage divider created by R3 and R8 in addition to 12 V from the D1. For the transistor Q2, the resistor R6 value had to be increased enough so that it does not always stay closed. The increasing of the R6 has a downside of lowering the response time of the rising edge, which is clearly visible in Figure 4.44. The resistor R4 has the protection function, by limiting the maximal current passing through the bipolar output transistors of the optocouplers. The transistors Q1 and Q2 are N-channel enhancement mode field effect transistors and their gates are connected to the emitters of the optocoupler output transistors. The resistors R5 and R6 are connected in parallel with the drain and the gate of the FETs, to turn them off when optocouplers are in the off state. FETs have small capacitance between gate and drain, which can charge up and leave them open for a while. Resistors R5 and R6 are placed in order to dissipate this charge and close the FETs as soon as optocouplers are in the off state. Values of these resistors are critical for the

performance of the circuit and they have been carefully chosen and tested to obtain the fastest reaction possible. When open, the transistor Q1 shorts its drain and source, thus -50 V from the external voltage supply V3 goes directly to the W electrode. If the transistor Q2 is open, then the adjustable voltage from voltage divider formed by helipot R3, resistors R8 and R9 is connected to the W electrode. In this case, only part of the negative voltage from V3 is taken, equal to -14 V, required for good focusing in the electron beam on state. The diodes D2 and D3 ensure that current flow is always in the appropriate direction, during the transition period between two states. Since all voltages are negative, the technical direction of the current flow is from W electrode to the voltage supplies V2 and V3. The resistor R7 has the function to polarize the drains of the FETs. The resistance of R7 also have a significant influence on the shutter circuit performance, thus its optimal value is experimentally determined.

The performance of the shutter circuit was evaluated in the PC program Circuit Maker, as well as by measuring the response on a digital oscilloscope. The results of the simulation are presented in Figure 4.43, while a real performance test is presented in Figure 4.44. Tests with the electron gun connected to the circuit showed minimal difference opposed to the unloaded circuit, although there is a visible difference between the simulation and the real circuit operation. The explanation of such difference lies in the simple resistive load used for the simulation, compared to a dynamic capacitive load of the operating electron gun in the real test. The rise time of the circuit was estimated from Figure 4.44 to around 100 μs, an input delay is in the order of 40 μs, while a fall time is ≈0.5 μs. A big difference between the rise and the fall time of the circuit is a consequence of discharging the parasitic capacitance of the FETs in the switching (FET) stage. Future developments of the circuit should be addressed at minimizing this delay by improving the circuit design with higher performance switching transistors, or even an optocoupler and a FET integrated into one package. Nonetheless, the results were more than enough for what was expected from the design and as required for the present experiment, given that optimal electron activation time was in the order of 500 ms. Figure 4.45 presents the home-made power supply box used in the electron experiments.

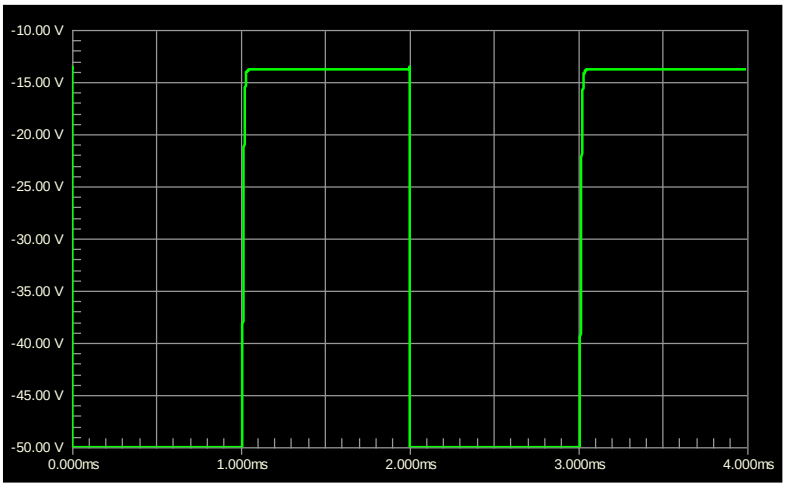

Figure 4.43 - Simulation of the shutter circuit in the program Circuit Maker, for 500 Hz square wave input signal, corresponding to 1 ms activation time.

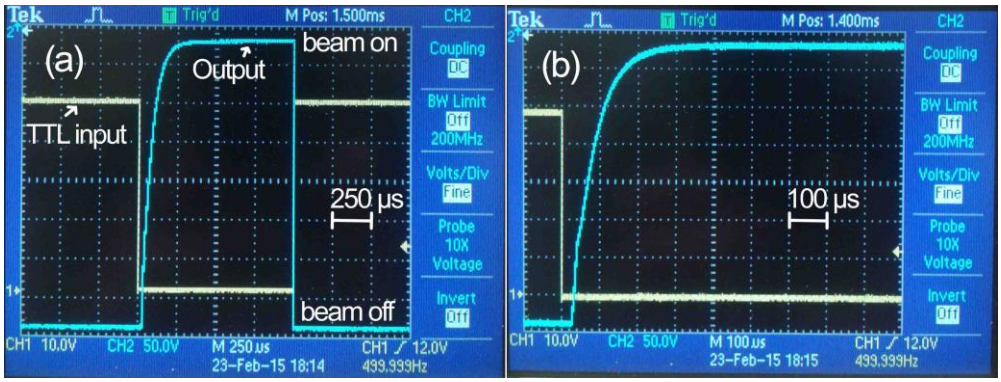

Figure 4.44 - Digital oscilloscope measurement of the shutter circuit response (Output) for 500 Hz square wave input signal (TTL input), corresponding to 1 ms activation time: (a) 250 µs per (horizontal) grid unit and (b) zoom in, at 100 µs per grid unit.

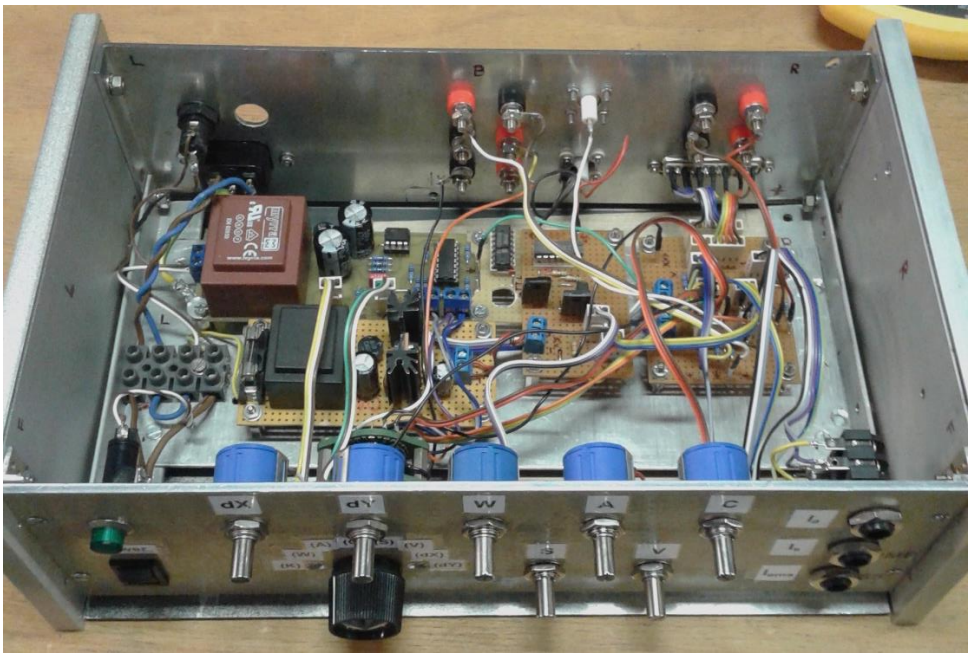

Figure 4.45 - Photograph of the electron gun power supply assembled for the present experiment. Electronic shutter circuit is integrated into the box. External high power supply for the cathode and high voltage supply which defines the electron energy are connected at the back side.

4.6.5 Coupling the electron gun with LTQ XL mass spectrometer

The differential turbo pumping vacuum stage was designed to couple the electron gun (described in Section 4.6.1) with the LTQ mass spectrometer. A 3D model of the vacuum stage with the electron gun is presented in Figure 4.46. It is based on a standard six-way CF100 cross, with a length of 220 mm. The electron gun is firmly fixed on an L-shaped Aluminum frame, mounted on a custom CF100 flange. The flange was modified to

accommodate two CF16 electrical feedthrough flanges mounted on its back side, for the electron gun connections. A reducer flange CF100-40 and CF40 flexible bellows, provide the final coupling and allow for a precise alignment of the electron gun with respect to the ion trap axis.

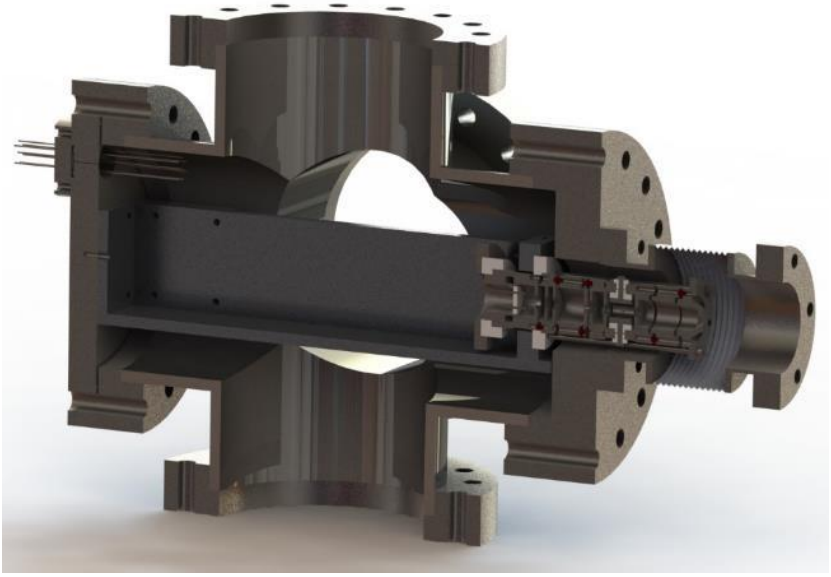

Figure 4.46 - Cross section view of 3D model of differential turbo pumping vacuum stage assembly with the electron gun, based on a six-way CF100 cross.

The remaining connections from the CF100 cross are used to fit a turbo pump, an ion pressure gauge and a glass window. The vacuum gauge is attached to the long flexible bellows and positioned approximately 1 m away from the vacuum assembly, in order to reduce the magnetic stray fields as much as possible. The present experimental setup is only equipped with the electrostatic shielding, while the magnetic shielding was not installed[14]. The vacuum stage design was focused on the alignment precision, as experience from the experiment with photons showed that it was important. Optimal alignment is crucial in order to obtain an efficient activation of trapped ions, which results in a high signal to noise ratio of the instrument. The practical realization of the vacuum assembly with the electron gun is presented in Figure 4.47.

The entire vacuum assembly is mounted on a rigid support frame and coupled to the back Plexiglass window of the LTQ mass spectrometer. Figure 4.48 presents the 3D model of the experimental setup. The initial rough alignment of the electron gun was done by moving the vacuum stage relative to a fixed position of the LTQ mass spectrometer. The verification of the rough alignment was done with the laser pointer directed through the ion trap from the front side (right side of the ion trap in Figure 4.48). The LTQ mass spectrometer is installed on an adjustable supporting frame [9], with translational and rotational degrees of freedom. The precise final alignment of the electron gun axis with

[14] Due to the space limitations and mechanical complexity, magnetic shielding with Mu-metal sheet foil was not possible to implement efficiently in the present flexible coupling design.

respect to the ion trap axis is achieved by fine tuning the position of the LTQ mass spectrometer frame, during ion activation measurements.

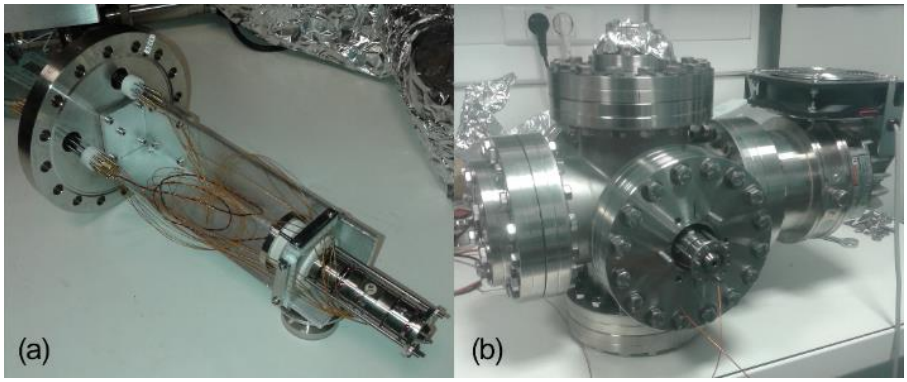

Figure 4.47 - Differential turbo pumping vacuum stage assembly with the electron gun: (a) electron gun is mounted on a CF100 flange via L-shaped frame and (b) CF100 cross, fitted with the electron gun, a turbo pump and a glass window (a pressure gauge is attached via a flexible extension to the upper flange - not shown here).

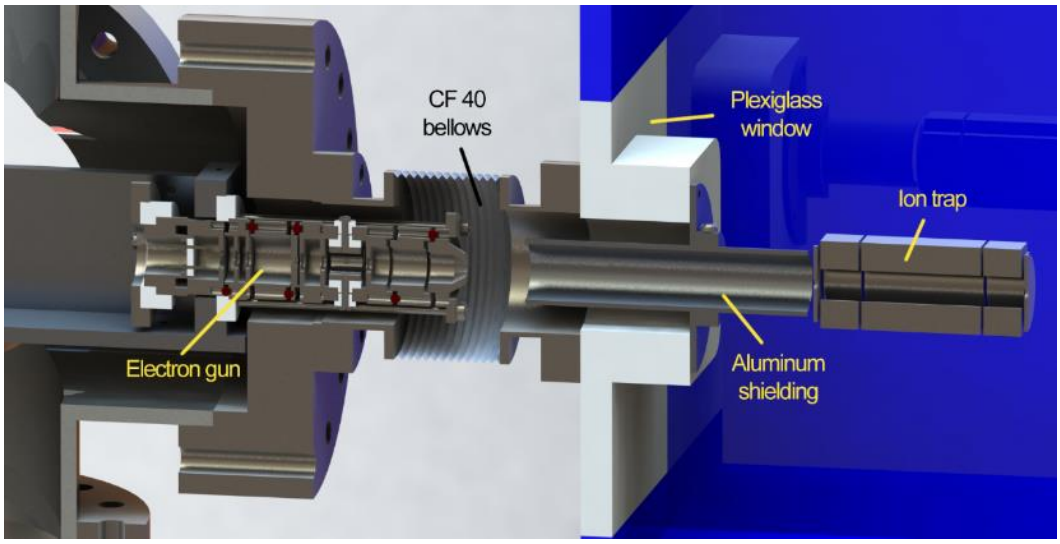

Figure 4.48 - 3D model of the coupling of the electron gun with LTQ XL mass spectrometer.

The electrostatic shielding of the electron gun is achieved with an Aluminum tube shield, installed along the axis between the electron gun and the ion trap. The Aluminum shield also prevents charging of Teflon insulated wires installed temporarily for the purpose of testing the electron gun, as well as all other insulated parts in the ion trap vacuum chamber inside the LTQ. Details of the electron gun test measurements are given in the Section 6.2.1.

4.6.6 Experimental procedure

In this section, a description of the experimental procedure for the activation of trapped ions in the collisions with electrons is presented. Figure 4.49 displays the schematic of the experiment. The main instrument of the experimental setup is the LTQ mass spectrometer, equipped with an ESI source on the front side. The vacuum stage with the electron gun is coupled to the back side, allowing a direct injection of electrons into to the ion trap.

The experiment is conducted in four steps: 1) ion production, 2) ion selection, 3) ion activation and 4) detection of fragments. The timeline of the experiment is presented in Figure 4.50.

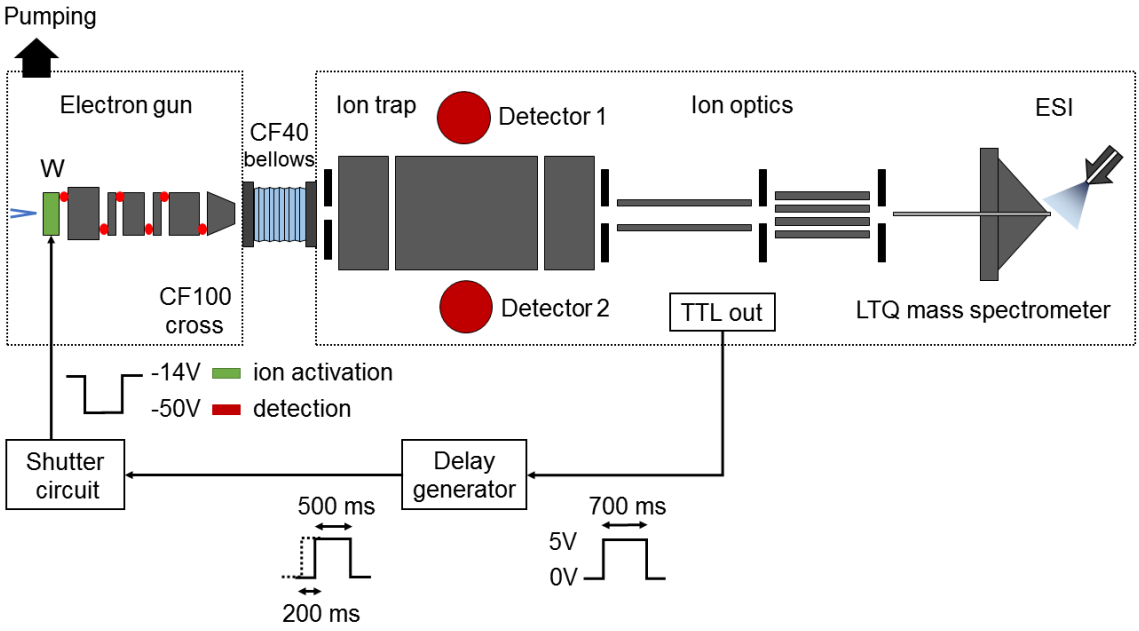

Figure 4.49 - Experimental method and schematic for synchronization of the LTQ mass spectrometer with the electron gun.

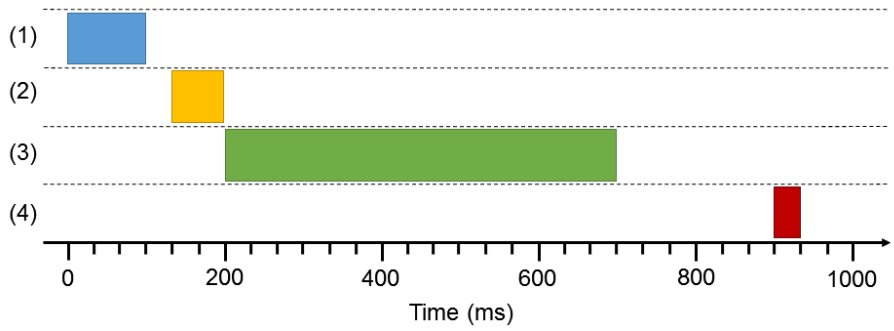

Figure 4.50 - Timeline of the experiment: 1) ion production, 2) ion selection, 3) activation and 4) detection.

(1) Solutions with biomolecular targets were prepared at desired concentration and injected into the ESI. By fine tuning of ESI parameters as well as solution properties, a wide range of precursor charge states of molecular ionic species can be produced. The generated ions pass through a long capillary that ensures pressure difference. The capillary is heated in order to remove excess water molecules. Guided by ion optics, comprised of octupole and quadrupole mass filters the electrosprayed ions are introduced into the ion trap from the front side (right side of the ion trap in Figure 4.49).

(2) Desired precursor ions, with user specified mass-to-charge ratios, are selected and isolated in the ion trap. In the LTQ, the efficiency of the trapping is further increased by the presence of the buffer gas. In order to stabilize the trajectories of ions selected in the trap, Helium buffer gas at the pressure of 10^{-3} mbar was used.

(3) Each time the number of trapped ions reach the storing capacity of the ion trap, a TTL pulse is triggered by the electronics of the LTQ mass spectrometer. In Figure 4.49, the output of this signal is symbolized with a "TTL out" box. The amplitude of the pulse is 5 V, while its duration is defined by the activation time, specified by the user. TTL signal is directed to the shutter circuit, which switches its output state to -14 V and enables the electron emission. Consequently, a focused electron beam of defined energy is formed, which activates the trapped ions. As soon as TTL signal goes back to low state (0 V), shutter circuit applies -50 V to W electrode, which in turn stops the electron beam.

A delay generator (DG645, Stanford 150 Research Systems, Sunnyvale, CA, USA) is inserted between the TTL out and the shutter circuit. Its function is to introduce an acquisition delay between the end of ion activation and the start of the fragment detection. In that case, the activation time as defined in LTQ software has to be increased by the amount of the desired acquisition delay. The delay generator is set to output a new TTL signal on the rising edge of the first one. As a result, a background noise can be fairly reduced.

(4) The low state of the TTL signal also initiates the start of the ion fragment detection. In the LTQ, a high-frequency pulse is applied to the ion trap ring electrodes, which ejects all ion fragments and action MS^2 is recorded. Optionally, several successively obtained action MS^2 for a single electron energy are averaged in order to increase statistics.

The entire process can be repeated for a number of different electron energies, in small energy steps (typically 0.2 eV), obtaining many MS^2 as a function of the electron energy.

5 Ion optic basics and simulations

In the electron optics, the electric fields can be generated by applying electric potentials on specially designed electrodes. The electric potentials are applied to two adjacent electrodes, in order to form the electrostatic lenses. Depending on an application, the electrodes are created in a wide range of shapes. The electrodes with planar, cylindrical or spherical symmetry are the most common. The cylindrical electrodes are typically used to generate two-dimensional radial electric fields. Other shapes can also be manufactured, if the requirements for the electric field geometry are more complex, for example, for a three-dimensional ion trap. The electron lenses work by creating the electric field gradient that changes the trace of the charged particles. The charged particles can be accelerated, decelerated, or collimated in a focused ion beam. In the present work, the commercial program for simulation of ion optics SIMION [59] was used.

5.1 SIMION

First step in the simulation is to define a desired electron optics geometry and its electric potentials via a special programming code by creating a geometry file. The potentials on each electrode are defined by the user. In a process called "*refining"*, the program then solves the Laplace equation for the electric potential and calculates the electric field defined by the gradient of that potential using a method of finite differences. This process gives the solution for the electric field in an empty space between electrodes. After obtaining the electric field, desired charged particle initial conditions can be set and the program solves differential equations of motion. In the final step, the program displays particle trajectories. Additionally, a special LUA programming code can be used for recording the particle statistics and the definition of time-dependent potentials on the electrodes.

5.2 Ion trap modeling

The linear quadrupole ion trap from LTQ mass spectrometer was modeled in order to investigate the influences of RF electric fields on the transmission of electrons. A total length of the ion trap is 68 mm and it is composed of three axial sections. In order to save the computer resources, each section (see Figure 5.1b) is modeled separately. The front (1) and the back (3) sections are created in 3D, without the use of symmetry. The center section (2) is defined by extending a two-dimensional profile in the axial direction. All sections are composed of four hyperbolic electrodes with a minimal radius of 4 mm (see Figure 5.1a). Two disk-shaped electrodes (the front and the back plate) with 2 mm apertures are also modeled in order to accurately simulate the ion trap. Figure 5.1c presents the isometric view of the modeled ion trap.

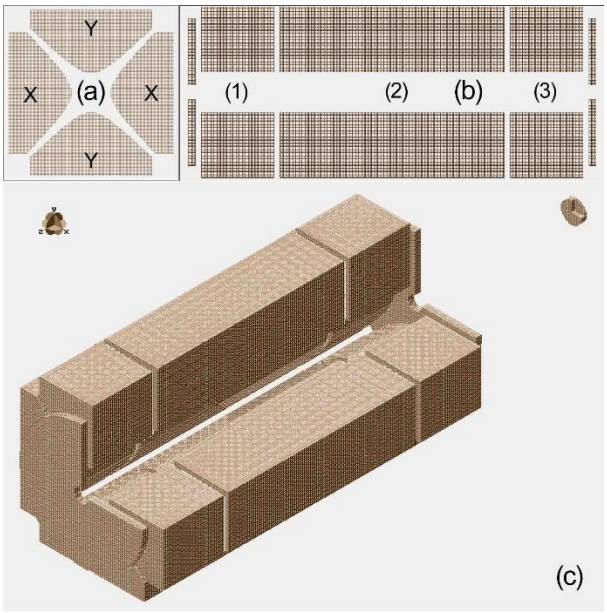

Figure 5.1 - 3D model of the ion trap from LTQ mass spectrometer from SIMION.

Regarding the applied potentials, the ion trap electrodes are arranged in two pairs, one located on the vertical (Y pair) and the other located on the horizontal axis (X pair), as depicted in Figure 5.1a. Amplitude of the RF potential is A=400 V, with the frequency of 1 MHz ($\omega/2\pi$), while the amplitude of DC potential is B=100 V. The polarity of the applied potentials on the each pair of electrodes is given by the following relation:

$$\begin{aligned} Y &: A\sin\omega t + B \\ X &: A\sin(\omega + \pi)t - B \end{aligned} \tag{5.1}$$

Above described configuration of the applied potentials enables only radial trapping of the charged particles, meaning that they can move freely in the axial direction and eventually exit the ion trap. In order to restrict the motion of the charged particles in the axial direction as well, DC potentials in the center section are lowered by 10 V, in relation to the DC potentials applied to the front and back section. It should be noted that the amplitudes of the RF and DC voltages in the actual ion trap depend on the m/z ratio of the selected ions. The amplitudes used in the simulation are the maximal values of these voltages, which are selected in order to estimate the highest perturbation of the electron beam. The main program (LUA code) through which the RF and DC fields are applied as well as the definitions of the electrode geometries (GEM files) are given in Appendix 8.2.

5.3 Pulsed electron beam transmission

The influence of the RF and DC electric fields on the electron beam in the simulation are quantified by measuring the geometrical properties of the electron beam at the center of the ion trap (at 34 mm in the axial position). More specifically, for each electron crossing the plane perpendicular to the trap axis at the axial position of 34 mm, three variables were measured: x-coordinate, y-coordinate and the energy.

The initial electron beam has a radius of 0.5 mm with a uniform spatial distribution of a total of 1.21×10^5 electrons per pulse, with initial velocities parallel to the ion trap axis. All electrons have the same initial energy of 300 eV. The electrons are generated with a Gaussian time distribution, where a standard deviation defines the electron beam pulse width. In relation to the phase of the RF field, the center of the Gaussian distribution for each pulse width was always set to an optimal value, for which the highest transmission is obtained. Since the full period of the RF field is 1 μs, any pulse width above this value can practically be considered as the continuous beam.

The space charge effects were not included in this part of the simulation. The electron-He collision cross section decreases significantly above the energies of about 60 eV, as reported by J. Nickel et al [60]. Nevertheless, we investigated the influence of the He buffer gas to the propagation of 300 eV electron beam in the ion trap.

We present the simulation results obtained after including the interaction between the electrons and the He atoms. The inclusion of the He buffer gas was done using the collision model (HS1) within the SIMION8.1 example programs, made by D. Manura [61]. The temperature of the He buffer gas was set to 300 K, at the pressure of 5.3×10^{-3} mbar, whereas the total cross section for electron-He scattering was $\sigma = 5.56 \times 10^{-21}$ m^2 [60].

The obtained results were recorded for three electron beam pulse widths of: (i) 1μs, (ii) 100 ns and (iii) 10 ns, as well as the case (iv) 1μs where the He buffer gas was included. Table 5.1 presents the recorded electron beam properties at the center of the trap.

Table 5.1 - Electron transmission results in the ion trap. Tob is the time of the electron birth with respect to the phase of the RF field phase, while T_{end} is the transmission recorded at the end of the ion trap.

Pulse width [ns]	Tob [ns]	T_{end} [%]
1000	0.5	65
1000 (He buffer)	0.5	62
100	0.6	80
10	0.65(5)	100

The electron beam propagation through the ion trap at three different pulse widths is presented in Figure 5.3. The electron beam spatial and energy distributions recorded at the center of the ion trap are presented in Figure 5.3.

The case (i) with a pulse width of 1 μs practically represents the continuous electron beam. We can see that the electrons are highly scattered just at the entrance of the ion trap. However, a significant number of electrons of about 65% are able to pass through the entire length of the ion trap. The electron energy distribution presented in the right side of Figure 5.3(i) show that majority of electrons at the center of the ion trap still have the same initial energy of about 300 eV, although there is a visible broadening of the energy distribution of about ±2 eV. The spatial distribution of the electrons presented in the left side of Figure 5.3(i) show that majority of electrons are still within the initial radius of 0.5 mm, whereas the rest is scattered on the electrodes.

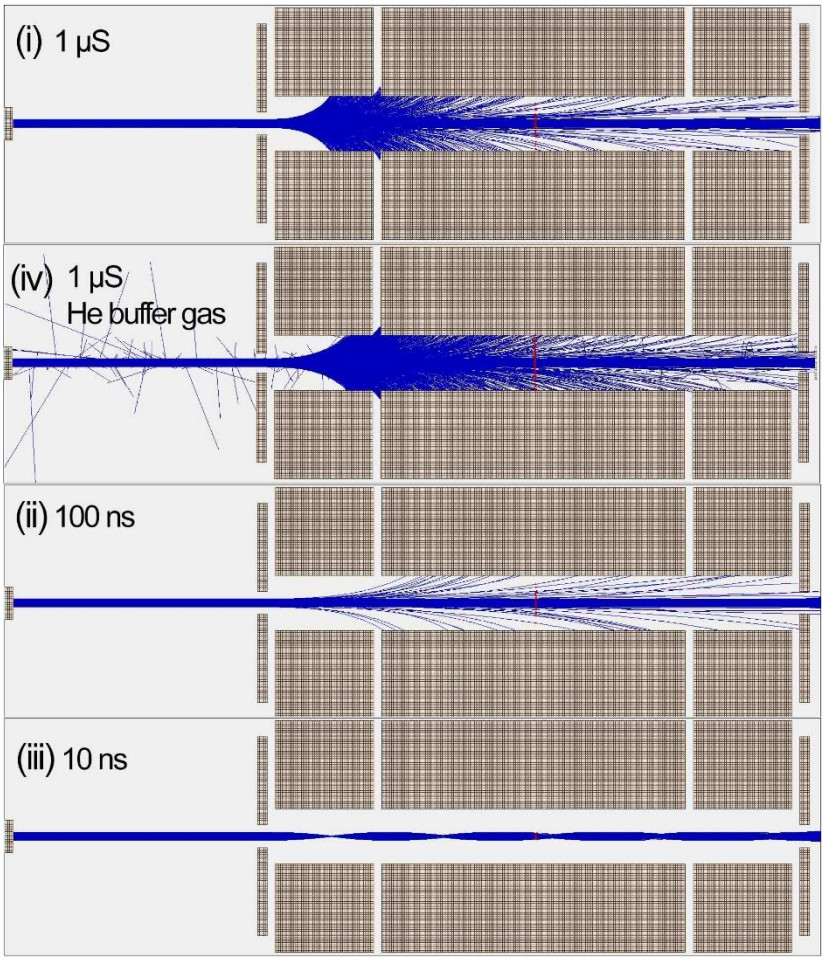

Figure 5.2 - Electron beam transmission in the ion trap: (i) 1 μs, (ii) 100 ns (iii) 10 ns and (iv) 1 μs with included He buffer gas at the pressure of $5x10^{-3}$ mbar and temperature 300 K. The total electron-He cross section used for simulation was $\sigma=5.56x10^{-21}$ [60].

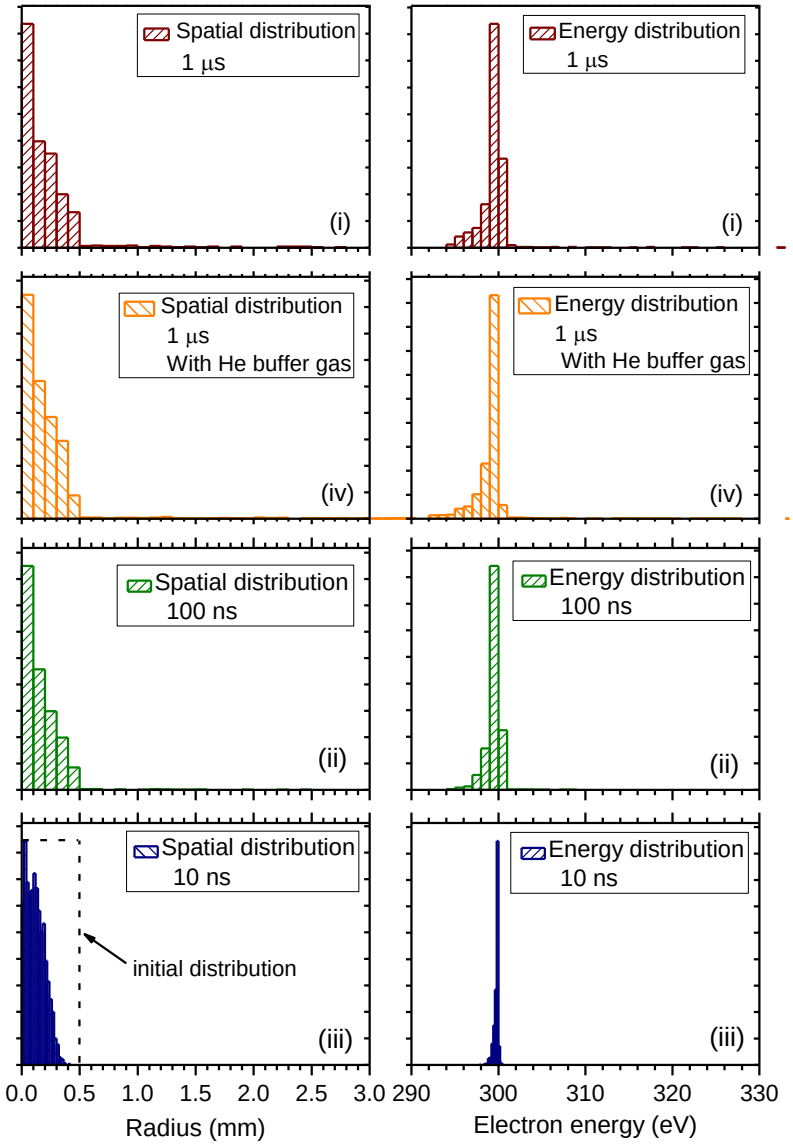

Figure 5.3 - Simulation of 300 eV pulsed electron beam in a linear quadrupole ion trap**,** for 400 V RF and 100 V DC, for three different pulse widths of: (i) 1 μs, (ii) 100 ns (iii) 10 ns and (iv) 1 μs with included He buffer gas at the pressure of $5x10^{-3}$ mbar and temperature 300 K. The total electron-He cross section used for simulation was $\sigma=5.56x10^{-21}$ [60].

Decreasing the electron beam pulse widths to (ii) 100 ns and (iii) 10 ns leads to a significant transmission increase [see Figure 5.3(ii), (iii) and Table 5.1]. The electron transmission is increased to 80% and even up to 100% (for 10 ns). The influence of the RF electric fields on the spatial and energy distributions is almost negligible. The broadening of the electron energy distribution is about ±0.5 eV. In comparison with the real experiment, this broadening is practically in the order of initial energy distribution of the electrons produced in the thermo-electron emission from the heated cathode. However, it should be noted that for a very narrow pulse widths (10 ns) the synchronization with the RF fields is crucial. According to the simulation, deviation of

about ±25 ns from the optimal synchronization point with respect to the RF field phase can cause a total suppression of the electron beam (a transmission of 0 %).

The electron beam transmission results obtained for the included He buffer gas at 1 μs pulse width (continuous beam) can be seen in Figure 5.2(iv) and Figure 5.3(iv). Spatial and energy distributions, as well as the transmission recorded at the end of the ion trap are very similar with the obtained simulation results without the He buffer gas. Although, we can see that a very small percentage of the electrons is randomly scattered. This is clearly visible in Figure 5.2(iv) in the region just in front of the ion trap, however, the scattering is also present in the space between the electrodes inside the ion trap. Qualitatively, we can say that 300 eV electron beam is not affected significantly by the presence of the buffer gas. The transmission at the end of the ion trap is slightly reduced - from 65 % to about 62 % due to the additional scattering on the He atoms.

Present simulation findings clearly show the benefits of the lower pulse widths, although in the case of a pulse width of 1 μs (continuous beam), satisfactory results were also obtained, even with the He buffer gas. It should be noted that in the present experimental setup for electron activation of trapped ions (Section 4.6), due to the limitations imposed by the response of the shutter circuit, the absolute minimum of the obtainable pulse width is around 250 μs (see Figure 4.44). This is still over 100 times more of what is required in order to effectively achieve the pulsed electron beam, with respect to the ion trap RF period. Therefore, according to the simulation, we were not able to experimentally obtain the optimal electron transmission through the ion trap, since we practically used the continuous electron beam. The obtained experimental results for the electron-impact dissociation of biopolymers are presented in Section 6.2.

6 Results and discussion

6.1 Photon experiments

6.1.1 VUV photo-dissociation of peptides and hydrated nucleotides

Leucine-Enkephalin (Leu-enk) monomer

Peptides are polymeric chains composed of amino acids. They are very important for living organisms since they play an important roles in performing biological functions [62]. Their function is linked with their primary structure - amino acid sequence [63]. Any modifications or degradations of the primary structure of biopolymers by energetic photons (UV, VUV or X-rays) could potentially lead to a cellular death. These processes are called radiation damage. The investigation of the photo-induced processes in peptides, mainly with UV and VUV light are important for the understanding of both the radiation damage at the molecular level and the electronic structure of these species. With developments of synchrotron radiation sources, the action spectroscopy of building blocks of biomolecules has become a powerful experimental method capable of giving more insights into fundamental physicochemical properties of these species. This could hopefully help understanding the biological functions of large macromolecules that they form.

In this section, our results of VUV action spectroscopy of protonated Leucine-Enkephalin (Leu-enk) peptide [64] are presented. Figure 6.1 shows a schematic structure of the Leu-enk peptide, with the nomenclature of the most prominent ionic fragments. Leu-enk is a small peptide, consisted of five amino acids with the sequence: YGGFL (tyrosine-glycine-glycine-phenylalanine-leucine).

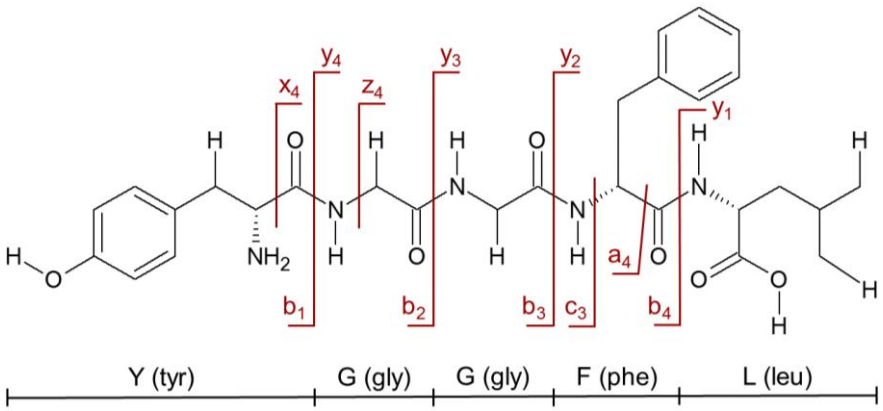

Figure 6.1 - The structure of the Leucine-Enkephaline peptide with its five amino acid constituents and imonium ions with mass-to-charge ratios of Y(136), F(120) and L(86).

Leu-Enk has been frequently investigated in the past using a vast number of mass spectrometry techniques. For example, by collision induced dissociation (CID) [65, 66], surface induced dissociation [67] (SID), black body infrared dissociation (BIRD) [68] and laser induced dissociation (LID) [69]. The experimental conditions and activation methods favor certain dissociation pathways dictated by particular fragmentation mechanisms. The fragmentation scheme of the protonated Leu-Enk was investigated by V. Rakov et al [66] in the experiment involving multiple resonance CID. The protonation site is usually located at Nitrogen in the tyrosine amino acid, although other protonation sites are reported due to the ion mobility ([70] and references therein). Recently, S. Bari et al [44] reported the VUV photo-induced dissociation of the protonated Leu-Enk by coupling SR photons with a 3D ion trap, where the ionization energy (IE) was estimated with DFT calculations to 8.87 eV. Their findings suggest that below IE the absorption of photons primarily lead to the cleavage of the peptide bonds, while above IE they could find a new dissociation pathways leading to a fast loss of a tyrosine side chain.

In the present work, protonated Leu-Enk cations $[M+H]^+$ (m/z 556) were isolated in the ion trap and subjected to VUV photons, with the energies in the range from 5.5 eV to 14 eV, with a small energy step of 0.2 eV. Figure 6.2 presents the obtained action MS^2 after photon impact at a few selected energies, below and above the IE.

The absorption of VUV photons leads to electronic excitation of the precursor ions, followed by the dissociation (below IE) or dissociative ionization (above IE), resulting in the formation of different fragment ions. In the case of backbone fragments (cleavage of C_α-C or C-N bonds), depending on where the remaining charge (proton) stays upon bond scission, a standard nomenclature was proposed by K. Biemann [71]. If the charge stays at N-terminal fragments a_n, b_n and c_n, are formed. The fragments x_n, y_n and z_n are formed if the charge stays at C-terminal. The number in the subscript indicates the remaining amino acid residues in the particular fragment ion. The absorption of photons can also lead to detachment of neutral groups (for example amino acid residues) or scission of several bonds.

Below the IE, in the action MS^2 obtained for 6.7 eV (Figure 6.2a), the most prominent fragments correspond to the cleavage of the peptide backbone. Namely, ion fragments b and y originate from scission of C-N bond, while the cleavage of C_α-C bond results in the formation of ion fragments a. The backbone fragments are designated at mass-to-charge ratios b_4 (m/z 425), a_4 (m/z 397), b_3 (m/z 278) and y_2 (m/z 279). This fragmentation pattern is in a good agreement with the CID experiments [65], where backbone fragments are also dominant. Moreover, we could observe peaks corresponding to precursor loss of water molecule $[M+H]^+$-H_2O (m/z 538), the tyrosine side chain [M+H]+-107 (m/z 449) as well as loss of phenylalanine side chain $[M+H]^+$-91 (m/z 465). Even though the fragments b_3 and y_2 have close m/z values, mass resolution in the present experiment was sufficient to resolve these peaks (see inset in Figure 6.2a). An internal fragmentation of the ion a_4 leads to the formation of fragments a4-NH_3 (m/z 380) and another loss of glycine a4-NH_3-57 (m/z 323). With a loss of the tyrosine side chain, fragment b_4 forms into b_4-107 (m/z 318). Less abundant peaks correspond to internal fragments GGF (m/z

262) and GF (m/z 205), while neutral (carbon monoxide) loss from this fragment is the origin of ion assigned to GF-CO (m/z 177).

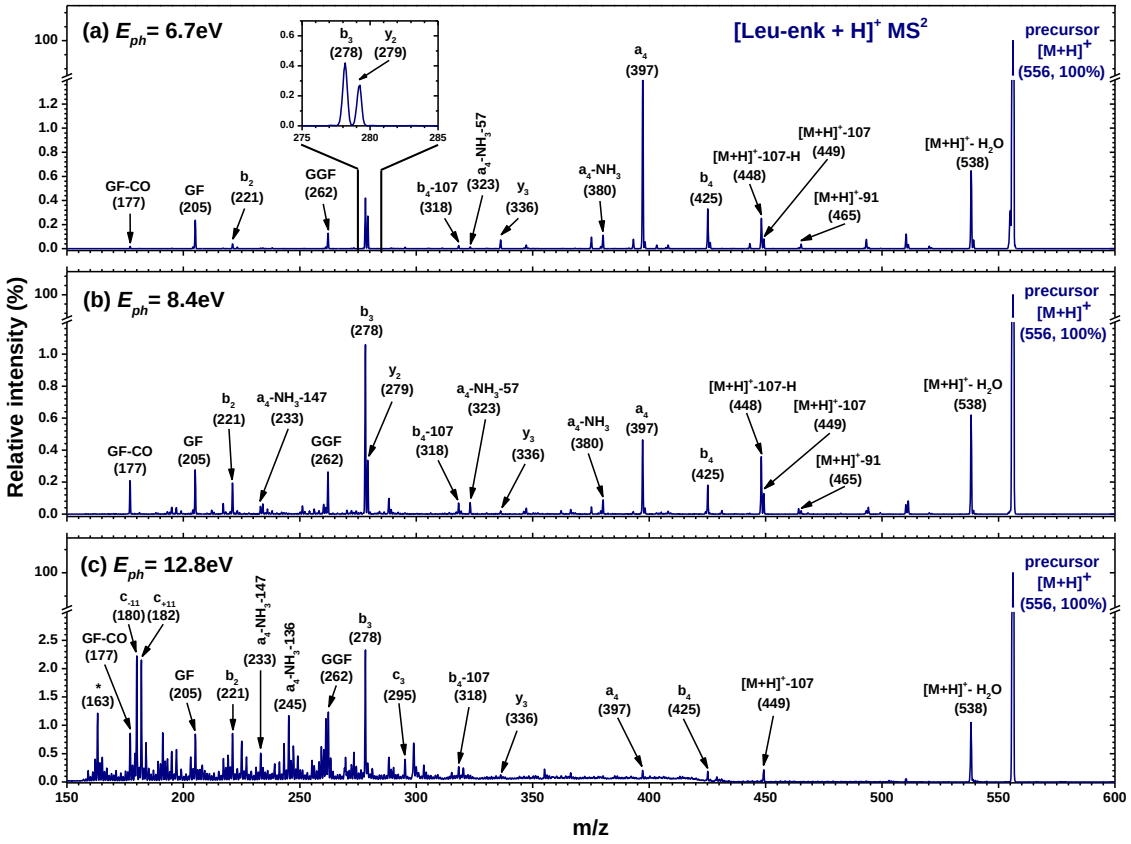

Figure 6.2 - Photo-activation tandem mass spectra of leucine-enkephalin, after 500 ms irradiation of [Leu-Enk+H]$^+$ precursor at: (a) 6.7 eV, (b) 8.4 eV and (c) 12.8 eV photon energies. The proposed assignments of the most important fragments are given in the figure while "M" denotes the pseudomolecular ion.

As the photon energy increases towards the IE, in the MS^2 obtained at 8.4 eV (Figure 6.2b), we can observe quantitative changes the fragmentation pattern. More specifically, fragment b_3 (m/z 278) becomes the most prominent, followed by b_2 (221) and GF-CO (m/z 177), whereas the ions a_4 (m/z 397) and b_4 (m/z 425) are fairly decreased.

Similar fragmentation patterns below the IE as in the CID experiments [65] suggests that the absorption of photon proceeds with the electronic excitations of protonated Leu-Enk precursor ions, followed by a fast internal conversion and/or intramolecular vibrational energy redistribution (IVR) to the vibrationally hot electronic ground state. The relaxation from these vibrationally excited states results in the dissociation of the Leu-enk precursor ions dominantly through backbone cleavage.

Above the IE, in MS^2 recorded for 12.8 eV (Figure 6.2c) we observe a rich fragmentation pattern in the low m/z region of 150-350. This is due to the opening of more relaxation channels which become available above IE. It should be noted that the photoionization of

the residual contaminants in the ion trap is the origin of many unassigned fragments. The peak at m/z 538 corresponding to water loss is increased by two-fold, as well as the ion fragment b_3 (m/z 278). Mass-to-charge ratio of doubly ionized precursor ion $[M+H]^{2+}$ is also 278, but the question remains if these ions indeed contribute to the mentioned peak. Indeed, the doubly ionized precursor ion is probably unstable and thus, its contribution to the peak at m/z 278 is very low, although further studies are required for a definite answer.

Due to a high photon energy resolution, a high mass resolution, as well as a high signal to noise ratio, the present experimental setup gives the possibility to record the spectroscopic features and investigate the electronic structure of the protonated Leu-enk cations. The ion yields for several backbone and internal fragments are extracted from MS^2, by integrating the area under the particular peaks and plotting it against the photon energy. The ion yields were normalized to both the photon flux and the total ion current, in order to compensate for their changes throughout the energy scan.

Figure 6.3 presents the ion yields in the photon energy range of (5.7-13.8) eV, obtained for Leu-enk fragments corresponding to the backbone dissociation. The ion yields are characterized by a rich spectroscopic structure.

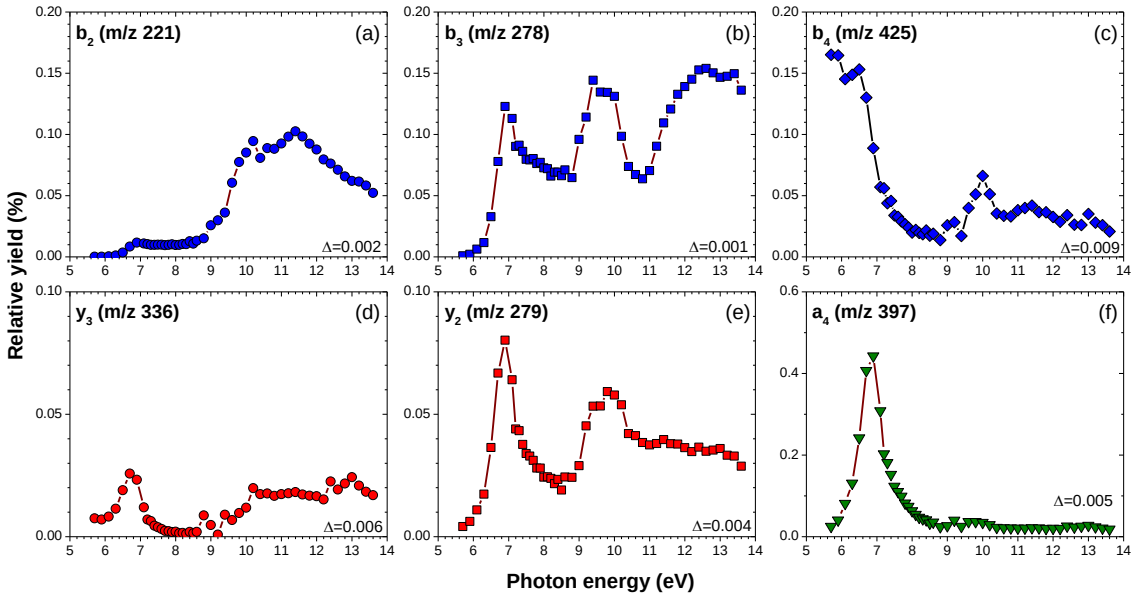

Figure 6.3 - Normalized relative ion yields from the photodissociation of precursor $[Leu\text{-}Enk+H]^+$ in the range from 5.7 to 14 eV. Integrated mass ranges are: (a) b_2 (m/z = 220.5-221.5), (b) b_3 (m/z = 277.5-278.5), (c) b_4 (m/z = 424.5-425.5), (d) y_3 (m/z = 335.5-336.5), (e) y_2 (m/z = 278.5-279.5) and (f) a_4 (m/z = 396.5-397.5). The absolute uncertainties of the experimental points are shown on the right bottom corner of each panel as Δ values.

According to the previous studies [15], [72–75], the electronic structure of the peptide bond in small peptides (di- and tripeptides) can be approximated by a four energy level system: two occupied π orbitals (π_1 and π_2), the oxygen lone pair n_o and the virtual π_3^*

orbital. Orbitals π_1, π_2 and π_3^* originate from the peptide bond and are bonding, non-bonding and anti-bonding respectively. A comprehensive fragmentation study of Substance P peptide with VUV photons was reported by F. Canon et al [15]. Figure 6.4 presents a schematic representation of the electronic structure of Substance P peptide [15].

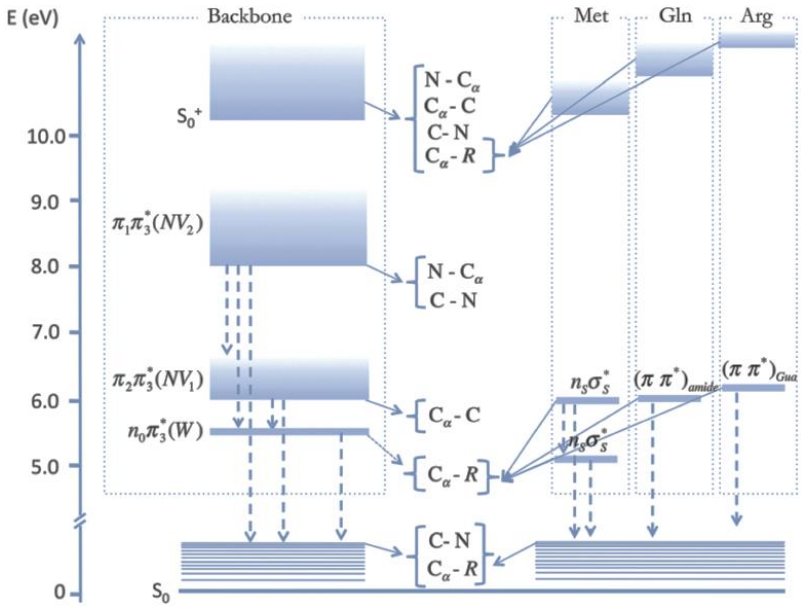

Figure 6.4 - Energy diagram for Substance P peptide. Adopted from [15].

The ion yields presented in Figure 6.3 (a) to (e), correspond to the fragments b_2, b_3, b_4, y_3 and y_2 respectively, which originate from the cleavage of the peptide C-N bond (peptide backbone fragments). All ion yields obtained for peptide backbone fragments show a distinctive spectroscopic band centered at about 6.9 eV. This spectroscopic band is associated with $\pi_2\pi_3^*$ (NV_1) transition, followed by a fast non-radiative deexcitation to the vibrationally hot electronic ground state. Most probably, C-N bond cleavage could then proceed from this hot ground state. A distinctive spectroscopic band centered at around 7 eV in the ion yield for fragment a_4 (Figure 6.3e) can be associated with the same transition, but with different fragmentation channel corresponding to the scission of C_α-C bond. The ion yields for fragments b_3 and y_2 show the second band centered at about 9.6 eV, which can be associated with transition $\pi_1\pi_3^*$ (NV_2). The scission C-N peptide bond can, in this case, proceed directly from the excited state π_3^* [15].

The photo-dissociation yields for b ions (N-terminal fragments), presented in the first row of Figure 6.3, originate from the scission of the same C-N bond, but at different locations along the peptide chain. Therefore by comparing their ion yields we can investigate the differences in the VUV absorption efficiency along the peptide chain. Going from ion b_2 towards b_4 (i.e. approaching to the C-terminus) the fragment mass increases. According to the present results, the low energy part of the photo-dissociation yields becomes more important. Particularly for ion b_4 (Figure 6.3c), we can see that with lowering of the photon

energy, the ion yield increases, suggesting that the formation of b_4 ion can also be associated with $n_0\pi_3^*$ (*W*) transition, previously estimated at about 5.5 eV [15].

Since both b and y ion fragments are formed by the cleavage of the same C-N bond, ion pairs b_2/y_3 and b_3/y_2 should have similar photo-dissociation yields. This can be seen in Figure 6.3 by comparing the ion yields from the first and the second column. These pairs of fragments indeed have similar absorption efficiencies, although the lower energy part of the yield for y ions is actually more pronounced. The ion yield of the fragment b_3 shows a strong increase above 11 eV, whereas the ion yield of the fragment y_2 slowly decreases. It was already noted that b_3 ion has the same m/z 278 as the doubly ionized precursor ion $[M+H]^{2+}$, which should strongly increase above the IE. On the other hand, the doubly charged precursor is very unstable and might decay before the detection. Furthermore, the ion yield of b_2 and b_3 (N-terminal) fragments is higher in the whole photon energy range relative to the ion yields of y_3 and y_2 (C-terminal) fragments. This is in a good agreement with the finding that the preferential protonation site for the gas phase Leu-enk is at the N-terminus [76].

The both b_4 and a_4 ions shown in the last column of Figure 6.3, are formed by the cleavage of the neighboring bonds C-N and C_α-C, respectively, with the charge left at N-terminus. Therefore, we can compare their photo-dissociation yields. In the low energy region both ion yields show distinctive spectroscopic band, suggesting that they are dominantly formed in dissociation process involved with the $\pi_2\pi_3^*$ (*NV1*) transition.

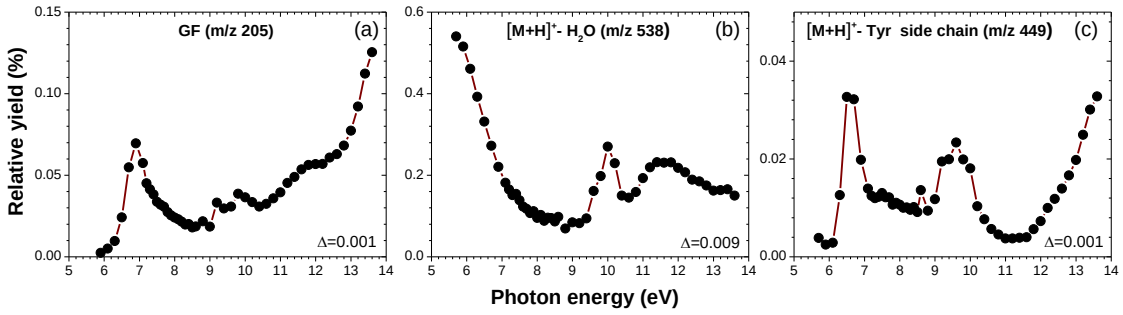

Figure 6.5 - Normalized relative ion yields from the photodissociation of precursor $[Leu\text{-}Enk+H]^+$ in the range from 5.9 to 14 eV. Integrated mass ranges are: (a) GF (m/z = 203.5-204.5), (b) $[M+H]^+$-H_2O (m/z = 537.5-538.5) and (c) $[M+H]^+$-tyrosine side chain (m/z = 448.5-449.5).

Figure 6.5 presents the photodissociation yields for fragments originating from cleavage of multiple bonds (GF m/z 205), as well as by a neutral loss (water and tyrosine side chain) from precursor ions. The fragment GF is formed mainly from y_3 and a_4 according to [67], suggesting that its photo-dissociation yield should be similar to yields of these fragments. It is indeed similar, although only in the lower energy region with the spectral band centered at around 7 eV (associated with transition *NV1*). Unlike for fragments y_3 and a_4, which show a few spectroscopic features but mainly remain flat with the increase

of energy, ion yield of the fragment GF shows a strong increase as the photon energy passes the IE. The peak at m/z 538, corresponding to the water loss shows a similar increase of the photo-dissociation yield as the fragment b_4 with the lowering of the photon energy, suggesting that its formation may also proceed from $n_0\pi_3^*$ (*W*) transition. Formed by the cleavage of the C-N bond, the C-terminal fragment b_4 is in close proximity to the carboxyl group. Therefore, based on the similarity in their photo-dissociation yields, it is possible that water molecule extraction site is also close to the carboxyl group [64]. In CID [65] and SID [67] experiments with protonated Leu-Enk, the peak corresponding to water loss was also observed as the strong relaxation channel. On the other hand fragment at m/z 449 corresponding to tyrosine side chain loss, show the spectroscopic bands centered at 6.9 eV and 9.8 eV. These two bands are in a good agreement with the observed spectroscopic bands obtained for the backbone fragments, associated with electronic transitions NV_1 and NV_2 respectively. The photo-dissociation yield of the fragment at m/z 449 is similar to the obtained ion yields for b and y fragments, suggesting that its origin might also be from the peptide backbone cleavage.

Leucine-Enkephalin (Leu-enk) dimer

Leu-enk dimmer is composed of two non-covalently bound monomer units of the Leu-enk peptide. In the present experiment, dimer precursor ions are produced by ESI from the same solution used to obtain Leu-enk monomer precursor ions. In this section, our results from the action spectroscopy of protonated Leucine-Enkephalin (Leu-enk) peptide dimer below the IE [77] are presented.

The same consideration for fragment nomenclature given in the previous section also applies here (for a reference see Figure 6.1). Singly charged precursor ions $[2\text{Leu-Enk} + H]^+$ are selected in the ion trap and subjected to VUV photons in the range of (5.7-8) eV with 0.2 eV steps. Figure 6.6 presents the action MS^2 obtained for 6.7 eV photon energy.

Besides the precursor ions $[2M+H]^+$ designated at m/z 1111, we can clearly see that the most prominent dissociation channel corresponds to the cleavage of the weak non-covalent bond between monomers, resulting in the formation of the protonated monomer unit $[M+H]^+$ at m/z 556. If we take a closer look in the m/z regions below the monomer precursor Figure 6.6b, as well as in the region between the dimer and monomer precursors Figure 6.6c, we can observe a rich fragmentation pattern.

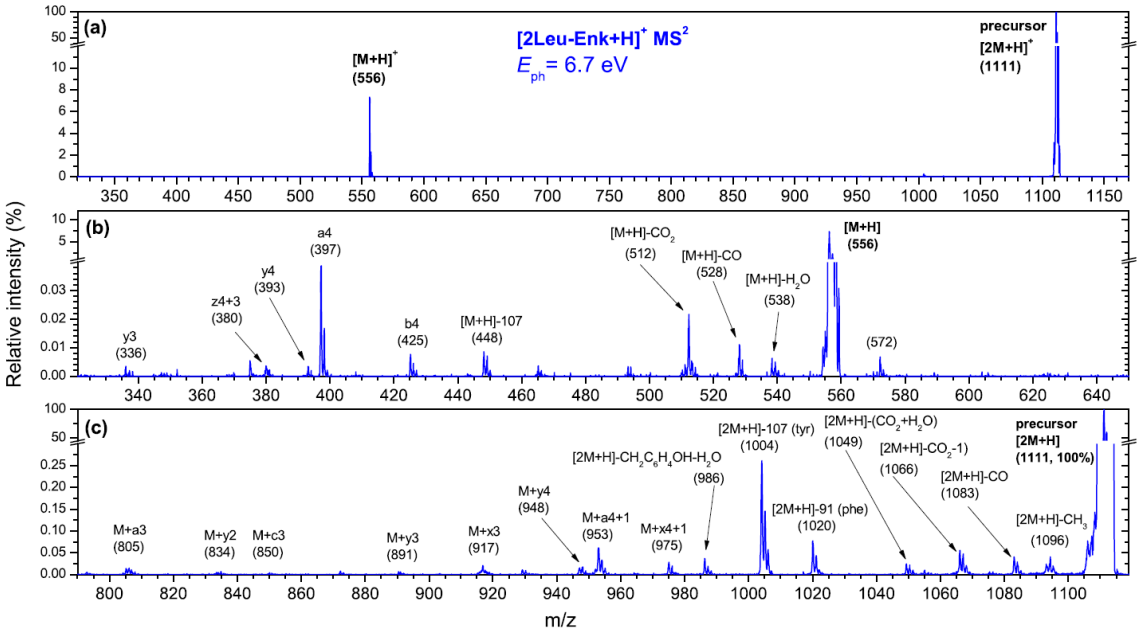

Figure 6.6 - Photo-activation tandem mass spectrum of leucine-enkephalin (Leu-Enk) peptide dimer recorded after irradiation of $[2Leu\text{-}Enk+H]^+$ precursors at 6.7 eV photon energy. The lower panels (b), (c) show close up of the mass regions up to (m/z 650) (b) and down to (m/z 800) (c), respectively. The proposed assignments of the fragments are given in the figure, where notation "M" corresponds to monomer unit "Leu-Enk".

The action MS^2 from Figure 6.6b show strong peaks corresponding to the backbone fragments a_4 (m/z 397), b_4 (m/z 425), y_4 (m/z 278) and y_3 (m/z 279). Their relative intensity distribution is in a good agreement with the action MS^2 obtained for the monomer molecule at the same energy (Figure 6.2a). It should be noted that m/z resolution of the action MS^2 for dimer molecule presented in Figure 6.6 is lower than in the case of MS^2 for monomer molecule presented in Figure 6.2a, due to requirements of extended mass range imposed by the dimer precursor mass. A broad peak at m/z 380 is probably associated with the formation of C-terminal peptide backbone ion z_4. Strong relaxation channels correspond to neutral losses from dimer precursor ions. Namely, water, carbon monoxide and carbon dioxide neutral losses are assigned to peaks at m/z 538, 528 and 512 respectively. Designated at m/z 448 we also observe the peak corresponding to the tyrosine side chain loss.

The photo-dissociation of dimer precursor below the IE leads to the formation of backbone fragments that are still bound to the monomer molecule (Figure 6.6c). More specifically, the fragmentation channels corresponding to the cleavage of the peptide backbone are assigned to peaks $[M+a_3]$ (m/z 805), $[M+y_2]$ (m/z 834), $[M+c_3]$ (m/z 850), $[M+y_3]$ (m/z 891), $[M+x_3]$ (m/z 917), $[M+y_4]$ (m/z 948) , $[M+a_4+1]$ (m/z 953) and , $[M+x_4]$ (m/z 975). We can also observe many other peaks associated with the extensive neutral losses from the dimer precursor ion. Particularly the most dominant peaks correspond to the tyrosine side chain loss $[2M+H]^+$-107 (m/z 1004) and phenylalanine side chain loss $[2M+H]^+$-91 (m/z 1020).

Like in the previous section, the investigation of the energy dependencies (photo-dissociation yields) of the selected fragment ions enables to reveal the electronic structure of the weakly bound dimer molecule, as well as its photostability towards VUV radiation. VUV photo-dissociation yields of the fragments originating from protonated Leu-enk dimmer precursor ion are presented in Figure 6.7 and Figure 6.8.

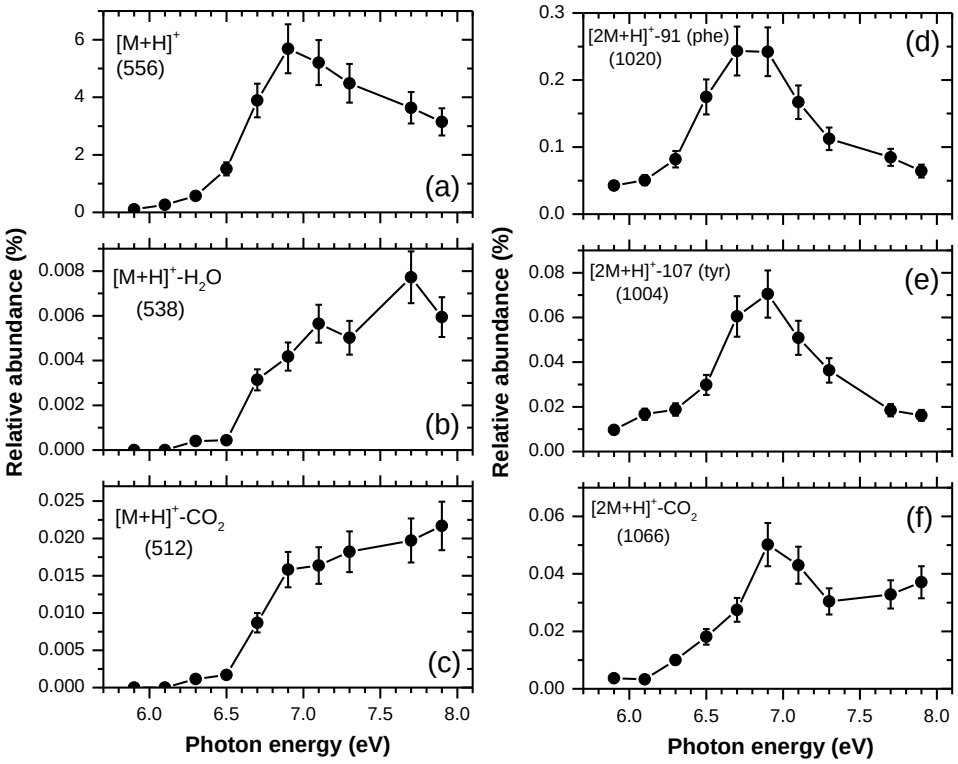

Figure 6.7 - Photo-dissociation yields of: (a) $[M+H]^+$ (m/z 556.1–556.4), (b) $[M+H]^+$-H_2O (m/z 538.08–538.38), (c) $[M+H]^+$-CO_2 (m/z 512.1–512.4), (d) $[2M+H]^+$-91 (phenyl) (m/z 1020.0–1020.3), (e) $[2M+H]^+$-107 (tyrosine) (m/z 1003.98–1004.28) and (f) $[2M+H]^+$-CO_2 (m/z 1066.0–1066.3) fragments.

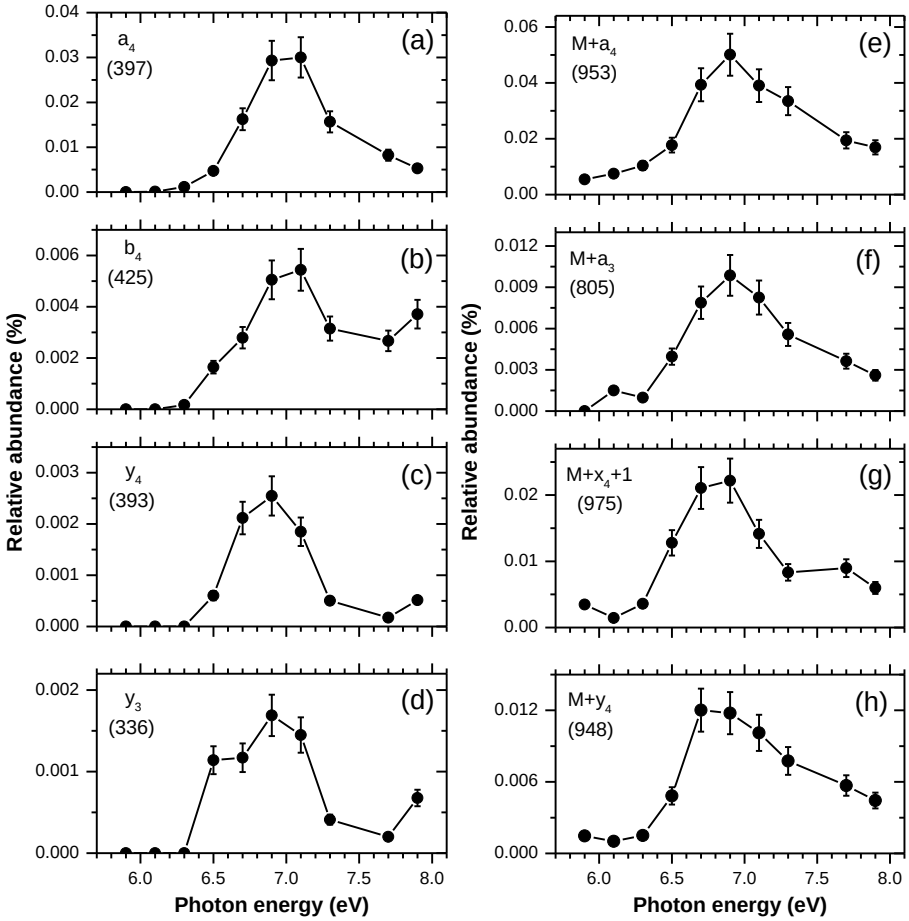

Figure 6.8 - Photo-dissociation yields of: (a) a_4 (m/z 397.05–397.35), (b) b_4 (m/z 425.08–425.38), (c) y_4 (m/z 393.0–393.3), (d) y_3 (m/z 336.0–336.3), (e) $M+a_4$ (m/z 952.92–953.22), (f) $M+a_3$ (m/z 805.05–805.35), (g) $M+x_4+1$ (m/z 975.0–975.3) and (h) $M+y_4$ (m/z 948.0–948.3) fragments.

The energy dependence of the fragment corresponding to the protonated monomer $[M+H]^+$ (Figure 6.7a) reaches a maximum at around 7 eV revealing a clear spectroscopic band. If we take the same consideration as in the previous section, suggesting that the peptide bond in small peptides can be approximated with the system containing four energy levels [15], [72–75], then the observed band can be associated with the transition $\pi_2\pi_3^*$ (*NV1*). A fast internal conversion to the hot ground state results in a dissociation of weak non-covalently bound dimer complex. The yields for fragments corresponding to H_2O (Figure 6.7b) and CO_2 (Figure 6.7c) neutral loss from the protonated monomer fragment, show an increase towards higher energies, suggesting that dissociation may also proceed with transition $\pi_1\pi_3^*$ (*NV2*). The spectroscopic band at 6.7 eV (*NV1* transition) seems to be more pronounced for fragments corresponding to the neutral amino acid losses, specifically tyrosine side chain loss (Figure 6.7e) and phenylalanine loss (Figure 6.7d). All fragment yields presented in Figure 6.8, show distinctive spectral band centered at 6.7 eV. Below the IE, the photo-dissociation of the protonated dimer precursor upon resonant VUV photon absorption proceeds with the electronic excitation, followed by a

fast internal energy redistribution to the hot ground state and finally scission of the weak non-covalent bonds as well as the peptide backbone.

Theoretical description of the protonated Leu-enk dimer has been performed by V. Cerovski [77] in order to put the experimental results into perspective. First, the geometries of conformers with the lowest energy are found as in [12] and optimized as suggested by [76] using the B3LYP/6-31+G(d,p) level of DFT. Previously calculated vertical ionization energy for this conformer was 9.31eV [12]. Figure 6.9 presents the lowest energy conformer for protonated dimer.

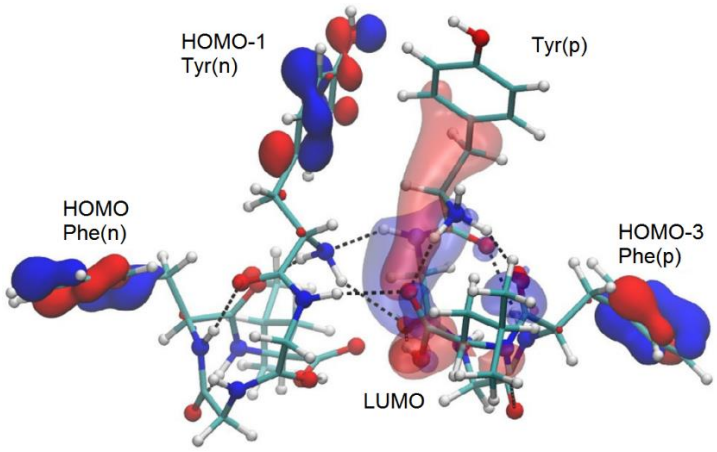

Figure 6.9 - Geometry of the lowest-energy CF found, shown together with several frontier orbitals, as indicated in the figure. HOMO-2 (not shown) is localized on Phe(n) just as HOMO. LUMO+1 and LUMO+2 (not shown) occupy the same part of the molecule as LUMO. (n) and (p) next to the group name indicate whether the group belongs to the neutral or protonated monomer, respectively.

The Leu-enk monomer units are bound by Hydrogen bonds indicated by dashed lines. The monomer molecule with the charge is labeled with (p), while the other neutral monomer molecule is labeled with (n). Four highest occupied molecular orbitals (HOMO) are localized around the aromatic groups (HOMO-2 is covered by the HOMO), while the lowest unoccupied molecular orbital (LUMO) is longitudinally spread across the peptide backbone. Two more orbitals LUMO+1 and LUMO+2 are also positioned across the peptide backbone, although with more density distributed towards tyrosine of the protonated precursor - Tyr(p) in Figure 6.9. Given the obtained electron densities the following transitions could be expected:

$$\mathrm{HOMO}-\mathrm{n}\rightarrow\mathrm{LUMO}+\mathrm{m}, \qquad (6.1)$$

where n=0, 1, 2, 3 and m=0, 1, 2. These transitions involve the charge transfer from the aromatic ring to the peptide backbone of the protonated monomer unit. Given the electronic stability of the aromatic ring, the charge transfer is weakening the peptide backbone of the protonated monomer due to the Coulomb repulsion. For this reason, the

protonated Leu-enk monomer in a dimer molecule is less stable in comparison with the neutral monomer.

Adenosine 5-monophospate (AMP)

DNA and RNA molecules strongly absorb UV light [78], making them sensitive to photo-induced alterations. Therefore, a large number of studies has been reported on the photo-physics of constituent molecules of DNA [79–82]. Particularly, in relevance to the present results S. Nielsen et al [83], investigated the fragmentation of protonated and deprotonated AMP molecule, induced by 266 nm photons.

Moreover, in nature biomolecules are surrounded by an aqueous environment, which affects their properties and biological functions. With modern experimental techniques, it has become possible to investigate an influence of the solvation on the stability of bio-molecules. Particularly, the effects of solvation at an extreme limit of only a few water molecules called micro- or nano-solvation can be investigated. Various studies have shown that nano-solvation with only one, two or three water molecules can strongly influence chemical reaction dynamics [84], the structure of peptides [85] or stability of a peptide dimer [12]. Dissociation of electrosprayed nanosolvated AMP nucleotides induced by high energy collisions with (Ne, Na) neutral atoms [86] and by electron capture [87], have also been studied.

In this section, our results of VUV action spectroscopy of protonated bare and hydrated AMP nucleotide [88] are presented. Figure 6.10 presents the chemical structural formula of the AMP nucleotide, were Hydrogen nucleus on the right side indicates the protonated singly charged ion $[AMP+H]^+$.

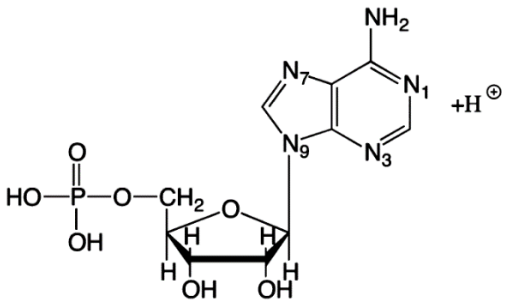

Figure 6.10 - Schematic representation of protonated Adenosine monophosphate molecule.

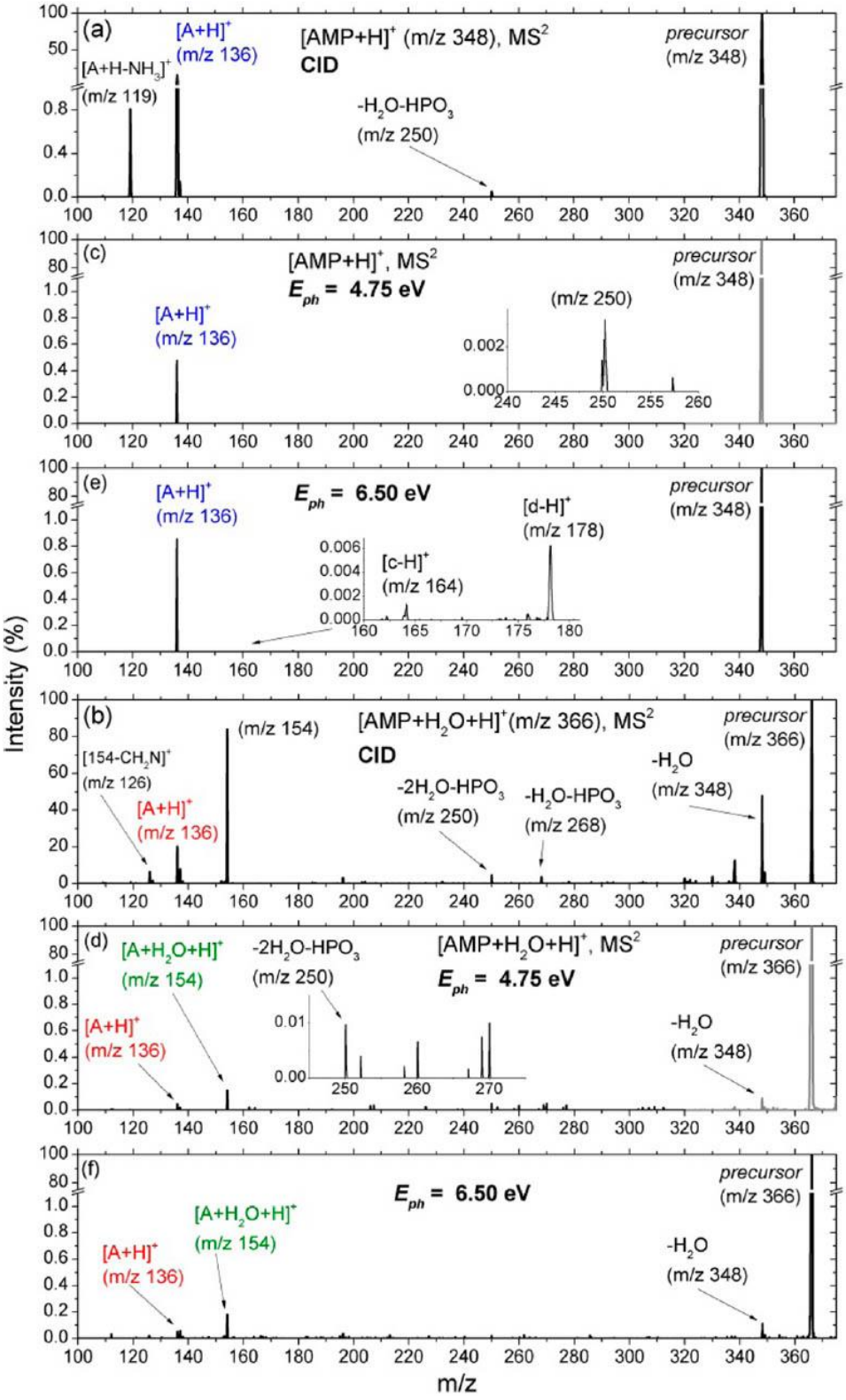

Figure 6.11 - Tandem mass spectrum of protonated $[AMP+H]^+$ and hydrated Adenosine monophosphate precursor ion $[AMP+H_2O+H]^+$, obtained for: (a,b) colission induced dissociation (CID); (c,d) VUV photo-induced dissociation at 4.75 eV and (e,f) VUV photo-induced dissociation at 6.5 eV.

Both bare $[AMP+H]^+$ (m/z 348) and hydrated $[AMP+H_2O+H]^+$ (m/z 366) AMP precursors were produced by nano-ESI and isolated in the ion trap. The selected precursors are subjected to UV photons from the DESIRS beamline. The action spectroscopy of the trapped precursors was performed by recording many action MS^2 for energies in the interval from 4 eV to 12.5 eV with 0.2 eV steps.

Figure 6.11a, b presents the action MS^2 of bare and hydrated precursor respectively, obtained with the collision induced dissociation (CID). The action MS^2 for bare and hydrated precursors irradiated at 4.75 eV, are presented in Figure 6.11c and d respectively. Action MS^2 obtained for both precursors at a photon energy of 6.5 eV are presented in Figure 6.11e and f.

In MS^2 from Figure 6.11b, we can see that dominant CID channel for the hydrated precursor is a water molecule loss, resulting in the formation of a fragment designated at m/z 348. It should be noted that a significant contribution to the intensity of the peak at m/z 348 comes from a thermal evaporation of the hydrated precursor, during the trapping time. Indeed, this peak can be observed in MS^2 with a relative intensity of around 0.15 %, even without any activation of the hydrated precursor.

The absorption of a photon below the IE leads to the cleavage of the glycosidic C-N_9 bond (see Figure 6.10). This bond scission results in a formation of a fragment at m/z 136, corresponding to protonated adenine base $[A+H]^+$, visible in both MS^2 in Figure 6.11c, e. Qualitatively good agreement is obtained with recent studies of protonated AMP, at 266 nm (≈4.7 eV) [89] and 260 nm (≈4.8 eV) [90]. Still, there are some differences compared with the fragmentation pattern reported by S. Pedersen et al [90]. More specifically, we observe lower abundances of the fragment at m/z 250 corresponding to the phosphate group loss. This difference can be attributed due to a longer fragmentation times of up to 500 ms in the present experiment, in relation to the sector based instruments. The increase of the activation energy to 6.5 eV leads to an increase of the protonated adenine peak at m/z 136.

The observed UV photo-induced fragmentation of the protonated precursor in the present experiment is fundamentally different from studies reported for a deprotonated anion $[AMP-H]^-$ [89, 91]. In those studies, a very rich fragmentation pattern was observed by S. Nielsen et al [91]. They have proposed the following fragmentation mechanism: the photon absorption leads to an electronic excitation into π^* state, accompanied by fast internal conversion to vibrationally excited electronic ground state, which finally decays through many fragmentation channels [80]. However, the lack of fragmentation channels in the present experiment indicates that the protonated cation $[AMP+H]^+$ probably undergoes a photo-dissociation through the cleavage of the glycosidic bond, via fast fragmentation channel directly from the excited π^* state.

In MS^2 from Figure 6.11d and f obtained for the hydrated precursor, we observe a significant (3-4 time fold) decrease in relative intensity of the peak at m/z 136, corresponding to protonated adenine base $[A+H]^+$. Also, one more additional fragment appears at m/z 154, which corresponds to the protonated adenine base bound to one water

molecule $[A+H_2O+H]^+$. Furthermore, CID of hydrated precursor (Figure 6.11b) results in an intensive water molecule loss (peak at m/z 348), compared to UV photo-induced dissociation (Figure 6.11d and f). These observations demonstrate the effects of nanosolvation with only one water molecule.

Theoretical calculations were performed by V. Cerovski for bare and hydrated AMP precursors in order to give more insights into the present experimental results. The geometries of conformers (CFs) with lowest energies were found by using the genetic algorithm approach with classical force field geometry optimization. DFT optimizations were then performed at M06-2X/6-311G(d,p) level [92], [93], where 50 lowest energy CFs were considered. Figure 6.12 presents the geometries of lowest energy CFs, CF1 for bare protonated precursor and two conformers CF1', CF2' for protonated hydrated precursor. All these three CFs have their HOMO and LUMO located on the adenine base, with a very small part of the electronic density spread across the rest of the cation. Two CFs are presented for the hydrated precursor, in order to point out two qualitatively different water hydrogen bondings: (1) to the phosphate group away from the adenine base (CF1') and (2) by forming a bridge between the phosphate group and the adenine base (CF2'). Therefore, upon UV photon absorption and scission of glycosidic bond, two main fragments are expected: bare protonated adenine base from CF1' and hydrated protonated adenine base from CF2', as confirmed by the present experimental findings (see Figure 6.11d and f). The calculated vertical ionization energies (VIEs) for CF1, CF1' and CF2' are 12.53 eV, 12.48 eV and 12.12 eV respectively. Binding energies of water hydrogen bonds for CF1' and CF2' are 69 kJ/mol and 69.5 kJ/mol respectively (≈0.72 eV).

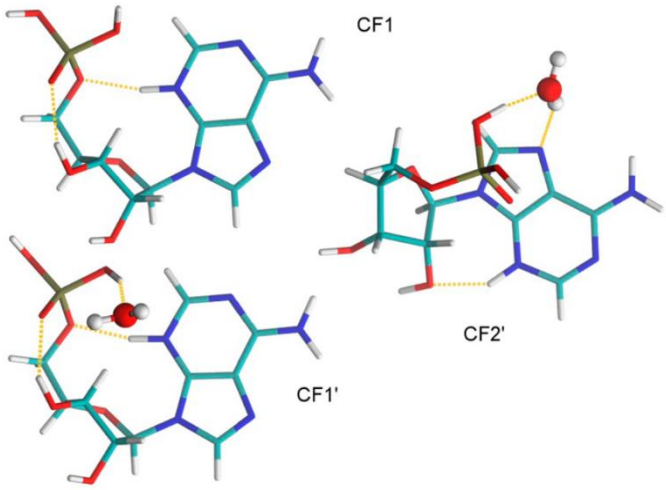

Figure 6.12 - Lowest energy conformers structure found for $[AMP+H]^+$ (CF1) and [AMP + H2O+H]$^+$ (CF1′, CF2′) at M06-2X/6- 311G(d,p) level of DFT. The protonated AMP (CF1) has the protonation site located at N_3 atom.

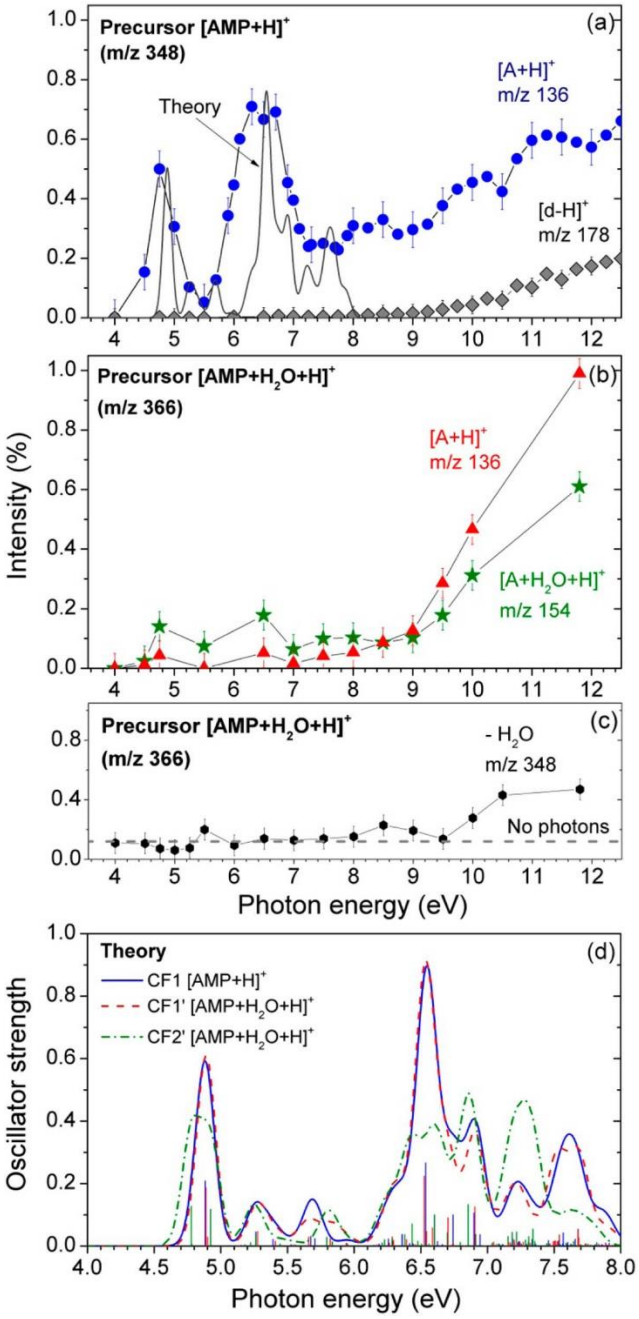

Figure 6.13 - Photodissociation yields of protonated adenine base $[A+H]^+$ (circles) and $[d-H]^+$ (diamonds) fragments from the bare protonated precursor $[AMP+H]^+$: (a) yield of $[A+H]^+$ (up triangles) from bare precursor; (b) yield of $[A+H_2O+H]^+$ (down triangles) from the hydrated precursor; (c) yield of $[AMP+H]^+$ fragment from hydrated precursor, corresponding to the loss of a single water. The dashed line marks the average water loss upon thermal evaporation from the ion precursor, without photon irradiation; (d) time-dependent B3LYP/6-31+G(d,p) calculated absorption spectra of conformers from Figure 6.12. Curves are obtained from the sticks by a 0.1 eV Gaussian convolution of the calculated transitions, providing a visual representation (the curve for CF1 is plotted as a full line, normalized to experiment at 4.75 eV).

The energy yields for fragments from bare precursors $[AMP+H]^+$ are presented in Figure 6.13a. The energy yield of protonated adenine base fragment, for bare precursor (circles in Figure 6.13a), shows distinctive resonant spectroscopic features, associated with absorption bands. One band is centered at about 4.75 eV (≈260 nm), which originates from the adenine base and is well known ππ* transition [78] also found in laser-based experiments. The observed spectral band is in a very good agreement with the absorption band of the protonated adenine base found at 4.7 eV by Pedersen et al [90]. We can also observe a second absorption band centered at about 6.5 eV, which is a dominant photodissociation channel for the bare precursor. Benchmark calculations reported by P. Szalay et al [94], using coupled-cluster methods to find oscillator strengths for adenine base, revealed transitions 3ππ* (6.5 eV) and 4ππ* (6.88 eV). The present experimental results are in a very good agreement with our theoretical absorption spectrum (Figure 6.13d), calculated by using the time-dependent density functional theory (TD-DFT), with B3LYP/6-31+G(d,p) basis set. The theoretical absorption spectrum is approximated by Gaussian convolution with 0.1 eV standard deviation, of calculated transition probabilities (oscillator strengths).

The fragmentation patterns of protonated AMP were reported by A. Bagag et al ([95] and references therein). The process requiring multiple bond cleavages is the mechanism of formation of the fragments $[d-H]^+$ (m/z 164) and $[c-H]^+$ (m/z 178), in MS^2 from Figure 6.11e. Therefore, the yield of the fragment $[d-H]^+$ starts increasing only at higher energies (diamonds in Figure 6.13a). It should be noted that in the present experiment conducted at room temperature, we do not have any control over the conformer formation and distributions. Also, the energies higher than the IE (resulting in a higher density and number of states) were not included in the TD-DFT calculation.

Figure 6.13b presents the energy yields of fragments originating from the hydrated precursor $[AMP+H_2O+H]^+$. The energy yields of fragments corresponding to protonated adenine base (stars) and the protonated adenine base bound with one water molecule (up triangles), also show the spectral features associated with ππ* transition after photon absorption. The theoretical absorption spectrum of the protonated hydrated precursor presented in Figure 6.13d, for CF1' (dashed line) is also in good agreement with the measured yield. However, we observe a significant reduction of the peak intensity for the fragment $[A+H]^+$ (Figure 6.11b). It should be noted that B. Liu et al [86] observed that the protection effects of nanosolvation for deprotonated adenine base upon collisions with sodium atoms starts for 10 added water molecules, while a significant dissociation reductions were observed above 13 added water molecules. In the electron capture dissociation (ECD) experiments the fragmentation was even increased with the addition of water molecules [87].

From the present findings, the photo-induced dissociation mechanisms of protonated bare and hydrated AMP nucleotide can be summarized as follows. The CID occurs on the ground electronic state, after statistical redistribution of the absorbed energy over the vibrational modes. UV photoexcitation can result in statistical and non-statistical fragmentation: (a) $[AMP-H]^-$ undergoes fast internal conversion to a vibrationally hot

electronic ground state, followed by a thermal (statistical) fragmentation [80]; (b) $[AMP+H]^+$ dissociates directly from excited electronic state (according to present findings and [89], [90]) and (c) $[AMP+H_2O+H]^+$, as we propose, also dissociates from the excited electronic states faster than intramolecular vibrational energy redistribution.

6.1.2 K-shell excitation and ionization of Ubiquitin protein

Proteins play a very important role in vital biological functions of living organisms. The folding - an arrangement of their constituent polypeptide chains in the three-dimensional space, is closely correlated with actual functions that they perform in the living organisms [96]. With the advancements and technological developments of the experimental techniques, an increasing number of studies of protein structures is reported [97]. An already established experimental technique for probing the spectral properties of a wide range of samples including biomolecules is near-edge X-ray absorption fine structure (NEXAFS) spectroscopy [98]. At first, NEXAFS was dedicated to probing samples (with low-Z numbers) prepared as thin films, in order to resolve the structure of molecules bound to surfaces. Recently, Y. Zubavichus and coworkers [99], reported a study where they probed the amino acids and proteins prepared as thin films with soft X-ray photons. In this method, incident SR X-ray photons excite core electrons, usually the ones closest to the nucleus (K-shell), into higher molecular orbitals. If the photon energy is high enough (above K-shell IE), direct transitions into the ionization continuum is also possible. It should be noted that transitions of core electrons into particular molecular excited states prefer certain photon polarizations. Since the polarization of SR produced in modern third generation synchrotrons is completely tunable, NEXAFS technique can be also highly selective. The sensitivity of the technique is also high, provided by the unmatched brilliance of the SR compared to any other X-ray source. An important aspect of the technique is that the incident photon energies are in the range from just slightly below up to 30 eV or so, above the ionization threshold of the molecular target. In this energy range, near-edge X-ray absorption fine structure is characterized by strong and distinctive features, similar to shape resonances [100]. Close inspection of such resonances reveals the electron structure of the target molecules.

With the advent of ESI technique it has become possible to isolate large biomolecular targets such as proteins in the gas phase. By subjecting the trapped biomolecular ions to soft X-ray photons with subsequent acquisition of action tandem mass spectra over near-edge energies, we can perform the action NEXAFS. A. Milosavljević et al [18] recently performed action NEXAFS of the Cytochrome C protein. Our results from the action NEXAFS study involving Ubiquitin protein [101] are presented in this Section.

By means of electrospray ionization, we produced the precursor ions of the Ubiquitin protein with charge states from +4 to +11, which were subjected to X-ray photons in the range of (282-304) eV for C-edge and (394-414) eV for N-edge.

In order to reveal the relaxation processes undergoing in a protein after soft X-ray photon absorption, Auger decay process has to be closely inspected below and above the inner-shell IE. Figure 4.1 presents the scheme for K-shell excitation/ionization of a protein followed by an Auger decay.

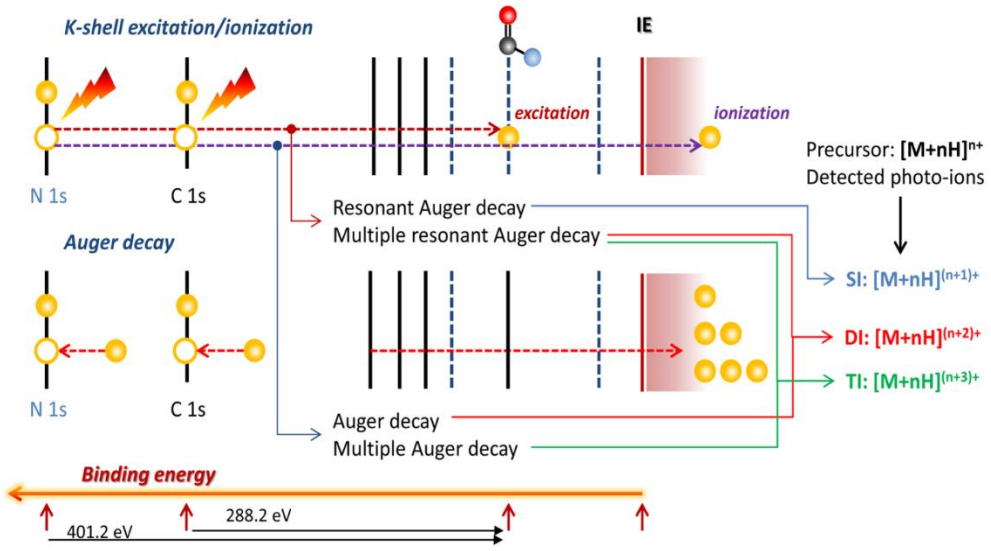

Figure 6.14 - Schematic representation of the K-shell excitation/ionization of a protein, followed by an Auger decay. Adopted from [101].

Below the IE, resonant absorption of a soft X-ray photon leads to excitation of the core electron from K-shell into an unoccupied, bonding molecular orbitals, forming a core hole. A valence electron fills the core hole in the order of femtoseconds and the system relaxes with an ejection of an electron. The process is called the resonant Auger decay [102]. It is possible that multiple valence electrons are ejected owing to a multiple Auger Decay [103]. However, the single ionization of the precursor ion is the most probable relaxation channel. In general, for n-time multiply charged protein precursor, resulting relaxation channels are represented by relation (6.2) [101]:

$$[M+nH]^{n+} + h\nu \rightarrow [M+nH]^{\bullet(n+k)+} + ke^{-}, \text{ where } k = 1,2,... \qquad (6.2)$$

Above the K-shell IE, a core electron is directly ejected into the ionization continuum creating a core hole, which triggers the normal Auger decay. In this process, the double or multiply ionized precursor ion is created. Relation (6.3) [101] describes the resulting process:

$$[M+nH]^{n+} + h\nu \rightarrow [M+nH]^{\bullet(n+1+k)+} + (k+1)e^{-}, \text{ where } k = 1,2,... \qquad (6.3)$$

MS^2 obtained at a photon energy of 288.2 eV, for 5+ precursor charge state of the Ubiquitin protein is presented in Figure 6.15. The spectrum was normalized to the intensity of precursor ion $[M+5H]^{5+}$ designated at m/z 1714. Dominant relaxation channels correspond to single (SI), double (DI) and tipple ionization (TI) of the precursor ions. They appear in the spectrum at mass-to-charge ratios of 1428, 1224 and 1071 respectively. It could also be seen that peaks corresponding to ionization are followed by clearly resolved low-mass neutral losses. All these relaxation channels are a consequence of the resonant Carbon ($1s \rightarrow \pi^*_{amide}$) X-ray photon absorption.

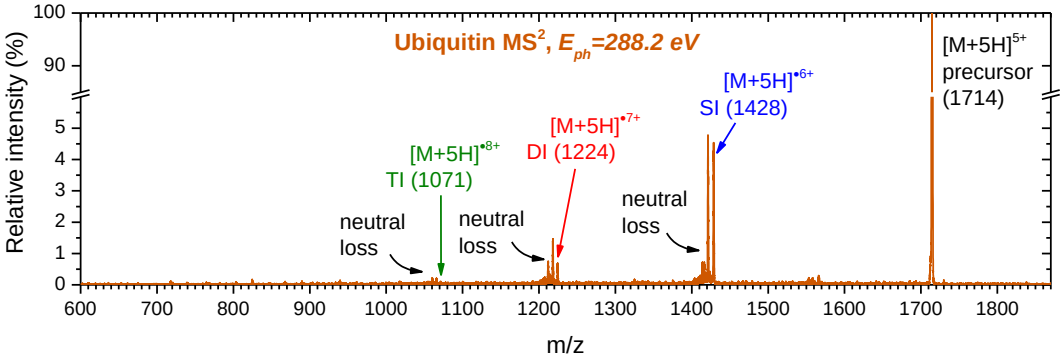

Figure 6.15 - Tandem ESI/photoionization mass spectrum of Ubiquitin protein, 5+ charge state precursor, obtained after photon impact at 288.2 eV. Adopted from [101].

The action K-shell NEXAFS around C-edge and N-edge energies of Ubiquitin protein was obtained by acquiring many action MS^2 around 300 eV and 400 eV photon energy regions respectively, with 0.2 eV energy steps. The ion yields for SI, DI and TI of Ubiquitin 5+ precursor $[M+5H]^{5+}$, were extracted from these MS^2 by integrating the area under the corresponding peaks, normalizing to the total ion current and the photon flux and finally by plotting against the photon energies. Figure 6.16 presents the obtained photoionization yields.

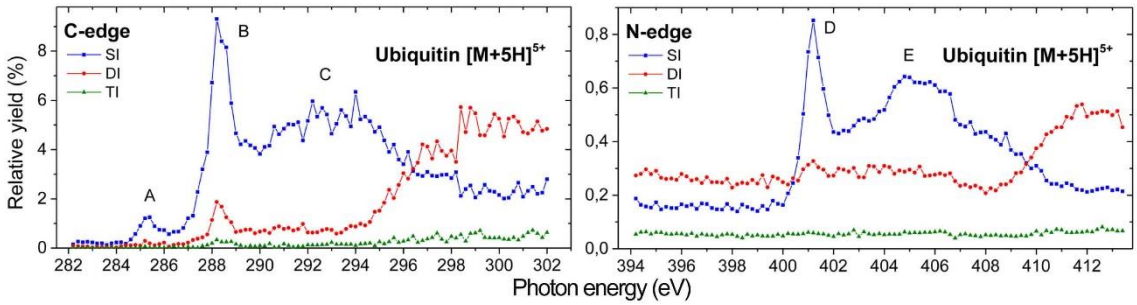

Figure 6.16 - K-shell photoionization energy yields of the Ubiquitin protein, 5+ charge state precursor: (a) C-edge and (b) N-edge. Peaks are integrated over the range $\Delta m/z=\pm 1$ around, SI - single ionization $[M+5H]^{\bullet 6+}$ (m/z 1428), DI - double ionization $[M+5H]^{\bullet 7+}$ (m/z 1224) and TI - triple ionization $[M+5H]^{\bullet 8+}$ (m/z 1071). Adopted from [101].

Prominent spectroscopic features (bands) are visible for SI yields in Figure 6.16. The clearly resolved bands are marked with letters A, B and D. Bands A and B are associated with excitations of Carbon core electron 1s, into molecular orbitals corresponding to $\pi^*_{C=C}$ (aromatic) at 285.3 eV and π^*_{C-N} (amide) at 288.2 eV, respectively. The excitation of Nitrogen 1s electron into molecular orbital corresponding to peptide bond π^*_{C-N} (amide) at 401.2 eV is associated with band D. Bands C and E originates from an overlap of many transition contributions mainly associated with σ^* resonances [18].

DI yields from Figure 6.16, show an increase at around 294 eV (C-edge) and 409 eV (N-edge) as a result of the opening of the direct double ionization channel. Since the yields are not background subtracted it should be noted that DI can still dominantly occur even below the IE thresholds due to multiple resonant Auger decay, initiated by resonant Carbon (or Nitrogen) core 1s electron excitation into bonding molecular orbitals. Looking at relation (6.2), if we take k=2 (for double Auger decay) and n=5 (5+ charge state), it would yield $[M+5H]^{\bullet 7+}$ with m/z 1224 - corresponding to DI peak. Considering the C-edge, both SI (from resonant Auger decay) and DI yields (from resonant double Auger decay) below the IE, are dominantly triggered by the same process C 1s→π^*_{amide}. Therefore, their shapes in this energy region should in principle be similar, which indeed is the case (see Figure 6.17).

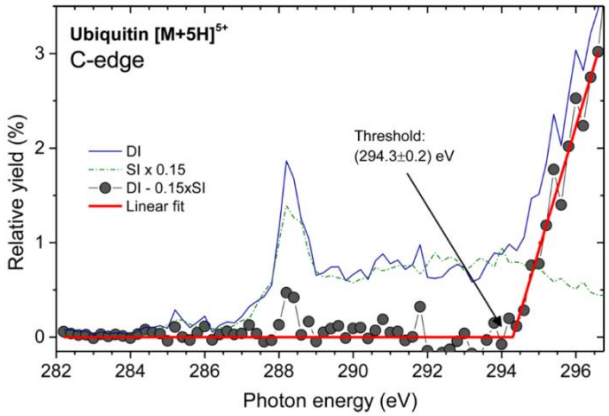

Figure 6.17 - Normalized single (SI, $[M+5H]^{6+\cdot}$ m/z 1427−1429) and double (DI, $[M+5H]^{7+\cdot}$ m/z 1223−1225) C K-edge photoionization yields of the 5+ charge state precursor $[M+5H]^{5+}$ of ubiquitin protein. Circles represent a difference DI − 0.15 × SI, resulting in normal Auger decay contribution of DI yields fitted to a linear threshold model (line). Adopted from [101].

In order to remove the multiple Auger contribution in DI yield, we performed the following procedure. By downscaling the SI with a factor of 0.15 and fitting the difference Δ=DI-0.15*SI with a linear threshold, we obtain the appearance energy (threshold) for DI. The obtained threshold curve (thick red line in Figure 6.17) now represents the contribution to direct K-shell ionization, which is possible only above IE. With this procedure we obtained the IE of 5+ charge state of Ubiquitin protein at (294.3±0.2) eV.

6.2 Electron experiments

6.2.1 Test measurements

Testing of the experimental setup is performed in two steps. The first step involves tuning the electrode voltages to optimal values and the characterization of the electron beam in the continuous mode. In the second step, the trapped ions are subjected to the pulsed beam of electrons of a defined energy during an optimal irradiation time, which has been defined previously.

In order to perform the optimization of the electrode voltages in the electron gun, the ion trap in the LTQ was temporarily modified, to allow for the electron current measurements. The electrical setup for the current measurement is presented in Figure 6.18. During the current measurements, all ion optics lenses including the ion trap and the detectors were turned off. Only the internal turbo pump has to be switched on.

The ion trap in the LTQ is equipped with two end disc plates, which appeared convenient for current measurement. The size of the aperture on both plates is 2 mm. This aperture was used for the beam profile measurement. The original wires in LTQ which supply the voltage to the front and back disc plates were disconnected from the ion trap. Two Teflon insulated Copper wires are connected instead, one on each plate of the ion trap. The front plate of the ion trap is grounded. The back plate is closed with the Aluminum foil, connected to the pico-ampere meter and polarized to +24 V relative to the ground, as depicted in Figure 6.18. The distance between the last electrode of the electron gun and the front plate of the ion trap is approximately 110 mm. The back plate is positioned at 65 mm from the front plate. Therefore, the final distance from the electron gun to the current measuring point was around[15] 175 mm.

[15] This distance is a close estimation, since flexible bellows position is changed during optimal alignment. Also, it can contract slightly once the pressure inside the vacuum manifold reaches ultra-high vacuum. For this reason, a final distance is estimated with uncertainty of up to 5 mm.

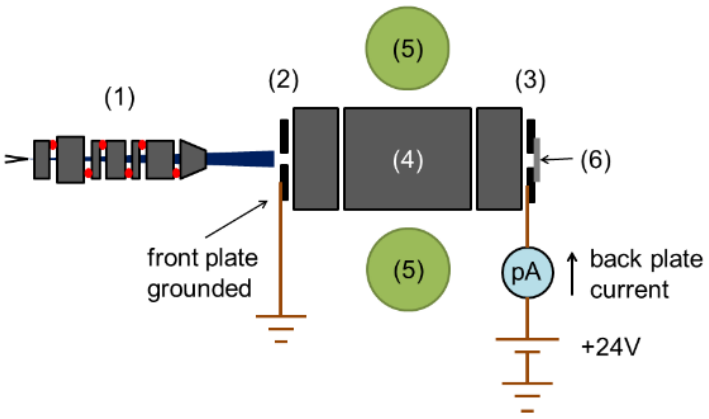

Figure 6.18 - An electrical scheme for the current measurement: 1) electron gun, 2) LTQ front plate - grounded, 3) LTQ back plate - connected to the pico-ampere meter, 4) ion trap, 5) ion detectors and 6) aluminum foil attached to back plate.

By measuring the continuous electron current on the back plate of the ion trap, optimal adjustment of the electrode voltages and characterization of the geometrical properties of the electron beam inside the ion trap was done. The results of the measurements are presented in Figure 6.19. The smallest spot size of the electron beam (or optimal focusing) on the back plate of the ion trap is indicated by the maximal back plate current reading. Optimal focusing, for a given electron energy is achieved by adjusting the voltage on the electrode V in the electron gun (for reference see Figure 4.34 or Figure 4.39). The back plate currents measured for different electron energies are presented in Figure 6.19a.

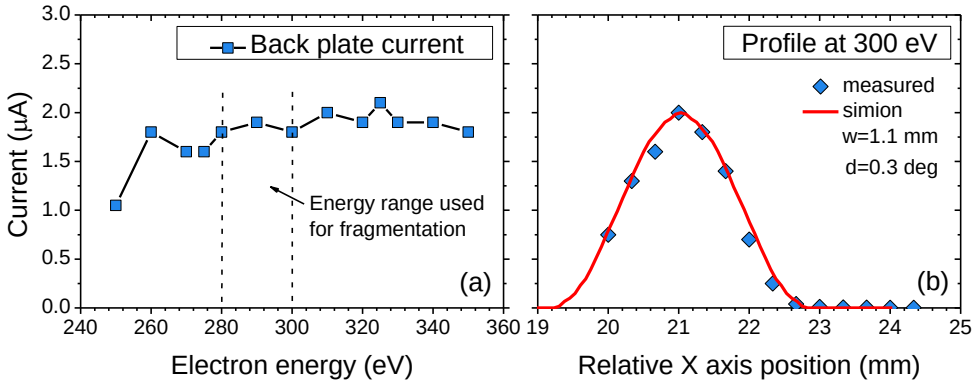

Figure 6.19 - Electron current measured at the back plate of the ion trap: a) plot of the back plate current versus the electron energy and b) electron beam profile. Simulated profile in SIMION is obtained for the beam width of 1.1 mm and pencil angle of 0.3 degrees and is in a good agreement with the measured profile.

The back plate current does not change significantly within the energy span of almost 100 eV. In particular, we were interested in a small energy range around 300 eV, corresponding to C K-shell edge. The mentioned energy range of (280-300) eV is

indicated by the dashed lines in Figure 6.19a. The current in this part of the energy range is practically constant around the value of 1.8 μA. Therefore, a normalization of the ion fragment intensities in the marked energy range was not necessary.

The electron beam profile is obtained by moving the LTQ mass spectrometer sideways relative to the vacuum assembly. The recorded profile for the electron energy of 300 eV is presented in Figure 6.19b. Due to the limitation in the maximal sideway extension of the flexible bellows, the measured profile is not fully completed. A programing code is written in PC program SIMION, in order to simulate the geometrical properties of the electron beam. The code is presented in Appendix 8.1. A good agreement with the measured beam profile is obtained for a simulated electron beam width of 1.1 mm and a pencil angle (divergence) of 0.3 degrees. According to the simulation, the electron beam width at the front plate of the ion trap is ≈2 mm. The obtained beam profile is very similar to the measured beam profiles for the same electron gun in the experimental setup UGRA from Belgrade. This was expected since no external electric fields from the ion trap are present during the electron current measurements. After the initial testing of the electron gun in the continuous mode, all original electrode connections of the ion trap were reverted back to its previous state.

The trapped molecular ions are activated in collisions with electrons, during the activation time. Part of the electron energy is absorbed by a molecular ion, which leads to the fragmentation and ionization. An important question is for how long activation time should last, before reaching a saturation of the signal intensity or even a detector damage?[16]. To establish optimal activation time under present experimental conditions, trapped molecular ions were probed with different electron beam pulse widths.

Prior to the ion activation, tests with lowered detector multiplier voltages were performed, in order to find their safe operating values. The beam of electrons was introduced in an empty ion trap, without selecting any ions. The detection and the mass spectrum acquisition was turned on, but with zero electron multiplier voltages on both detectors. For safety reasons, we decided to use only one detector. The electron multiplier voltages were gradually increased until normal values were reached, while constantly checking the mass spectrum. Since no abnormalities were present in the mass spectrum, typical working multiplier voltage of -1234 V (for positive ion mode) was set on the first detector, while the other one was kept at 0 V.

Precursor ions of Ubiquitin protein with charge state 7+ were produced by ESI and isolated in the ion trap. The trapped ions were subjected to short bursts of 300 eV electrons during a specified activation time (defined by the pulse width). An averaged tandem mass spectrum was recorded during 3 min for every pulse width. By this procedure, the MS^2 were obtained for pulse widths of: 2, 5, 10, 20, 50, 100, 200, 500 and 1000 ms. The MS^2 acquisition delay for each pulse width is presented in Table 6.1. The intensities of several selected ion fragments of the interest were extracted and plotted against pulse widths in

[16] See Section 4.3, for description of the LTQ mass spectrometer detection system.

Figure 6.20. An example of one of the action MS^2 obtained for 500 ms pulse width, is presented in Figure 6.21.

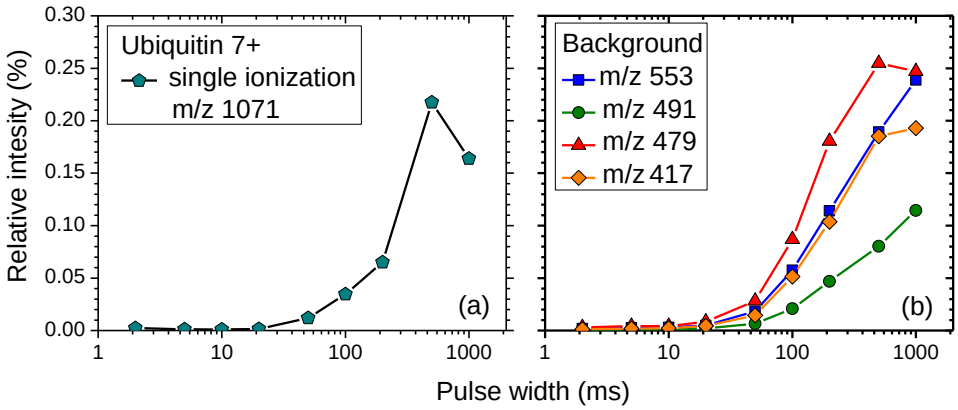

Figure 6.20 - Ion signal versus pulse width, measured for Ubiquitin 7+ precursor: a) peak at m/z 1071 corresponding to the single ionization of the parent ion and b) fragments originating from the electron background noise.

Table 6.1 - Acquisition parameters for the obtained MS^2 for Ubiquitin protein.

Pulse width [ms]	**2**	**5**	**10**	**20**	**50**	**100**	**200**	**500**	**1000**
Act. time [ms]	30	30	30	100	100	200	400	1000	2000
Acq. delay [ms]	28	25	20	80	50	100	200	500	1000

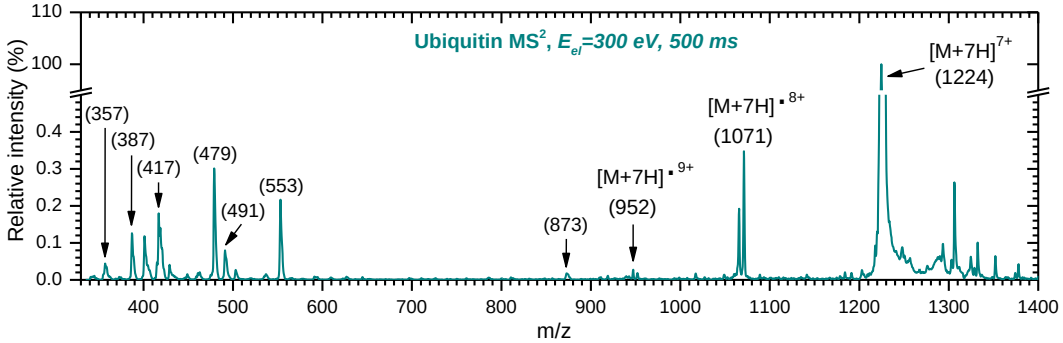

Figure 6.21 - Tandem mass spectrum recorded for Ubiquitin protein, precursor charge state 7+, for the electron energy of 300 eV and the pulse width of 500 ms. The spectrum was not background subtracted and contains both ion fragments and the noise signal.

The ion fragment designated at m/z 1071 in Figure 6.21 corresponds to the single ionization of the parent Ubiquitin precursor ion. The intensities of this ion fragment obtained for different pulse widths are presented in Figure 6.20a. The peaks in the low mass region in Figure 6.21 with mass-to-charge ratios 553, 479, 417, 387, 357 do not originate from the isolated precursor ion. The intensities of the background noise peaks

in relation to the pulse widths are presented in Figure 6.20b. They can be observed in the MS^2 even when no ions were isolated in the ion trap, thus we consider them as the noise signal. Both the ion fragments and the background start increasing for pulse widths higher than 10 ms, although the background is always slightly higher. Maximum of the intensity for ion fragment m/z 1071 is at 500 ms, while background continue to increase even further with increasing the pulse width. Therefore, based on the fragment intensity values presented in Figure 6.20, 500 ms is selected as optimal activation time (electron beam pulse width) for Ubiquitin protein.

6.2.2 MS^2 examples - Ubiquitin, Substance P and Melittin

Several large bio-molecular targets were introduced into the gas phase and activated in collisions with soft X-Ray energy electrons. In order to demonstrate the effectiveness of the electron activation method, MS^2 are presented for protein Ubiquitin, peptides Substance P and Melittin.

It should be noted that peaks with relatively high intensities appear in the low mass region in every MS^2. Their origin is not from the trapped precursor ions and they are regarded as the background noise. The most probable cause of the background could be the ionization of residual impurities on the ion trap electrode surface, as well as from ionization of neutral species produced by ESI. Another possibility could be the direct detection of reflected electrons by electron multipliers in the detectors. Increasing the acquisition delay reduces the background, but with an expense of a decrease in ion fragment intensities. Therefore, depending on the abundance of the produced precursor ions, both the electron beam pulse width and the acquisition delay have to be optimized. For the purpose of the background noise subtraction, MS^2 for each molecular target was recorded three times: a) electrons and ions, b) electrons only and c) ions only. The final MS^2 presented below were obtained by (b) from (a). Additionally, MS^2 obtained with electrons only is presented for each target, to reflect the slight change of the experimental conditions (regarding the neutral species content).

Ubiquitin, $[M+7H]^{7+}$

Ubiquitin is a small protein composed of 76 amino acids, which exists in almost all eukaryotic cells and has a molecular weight of 8565 g/mol.

The precursor ions with charge state 7+ from Ubiquitin protein, were selected in the ion trap and subjected to the electron impact at 288 eV electron energy. Figure 6.22 presents the MS^2 recorded without any ions produced, whereas Figure 6.23 presents the background subtracted MS^2 obtained for 288 eV electron energy.

The tandem mass spectrum presented in Figure 6.22 contains strong peaks designated at mass-to-charge ratios 360, 387, 401, 417, 479, 491, 553 and 873. The MS^2 is recorded for the electron energy of 288 eV, for 500 ms pulse width, 200 ms acquisition delay and is normalized to the intensity of the strongest peak at m/z 479. The mentioned peaks that

dominate the spectrum, along with all other visible peaks, represent the noise signal since there are no trapped precursor ions. Without a precise knowledge of the residual content in the ion trap, it is not possible to assign these peaks. Therefore, so far, their assignment remains unknown.

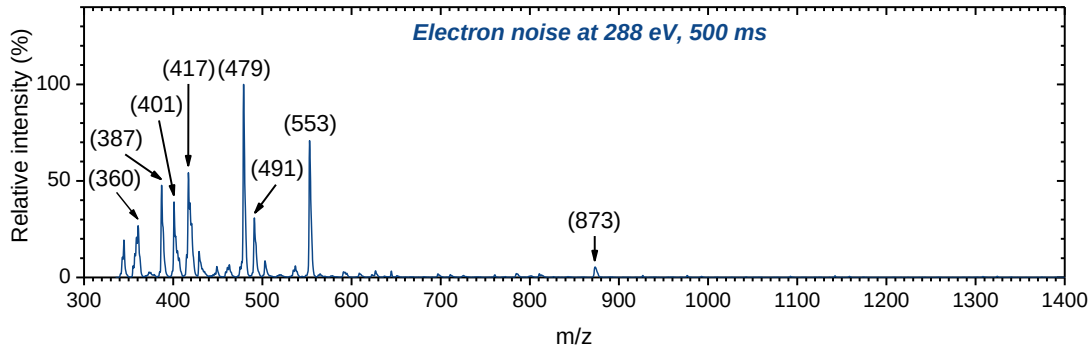

Figure 6.22 - Mass spectrum recorded with no isolated ions, for electron impact energy of 288 eV, 500 ms pulse width and 200 ms acquisition delay, acquired during 3 min.

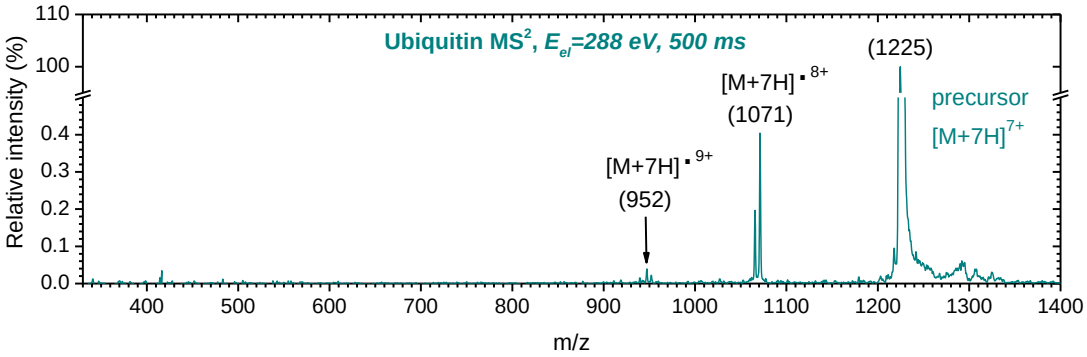

Figure 6.23 - Tandem mass spectrum recorded for 288 eV electron impact with protein Ubiquitin, 7+ charge state precursor. Electron beam pulse width is 500 ms, with acquisition delay of 200 ms, acquired during 3 min.

MS^2 presented in Figure 6.23 was acquired during 3 min, it is background subtracted and normalized to the intensity of the precursor ions designated at m/z 1225. Distinctive peaks are observed at mass-to-charge ratios 1071 and 952. They correspond to the single and double K-shell ionization of the precursor ions, respectively. More details are given in the Section 6.2.3.

Substance P, $[M+H]^+$

Consisted of 11 amino acids, Substance P is a neuropeptide with a molecular weight of 1347 g/mol. It acts as a neurotransmitter and neuromoderator. A comprehensive review of the Substance P was reported by S. Harrison at al [104].

The singly charged precursor ions of Substance P peptide are selected in the ion trap and subjected to electron impact at two energies. Figure 6.24 presents the MS^2 obtained with no ions selected, for 293 eV electron energy. Background subtracted MS^2 obtained for electron energies of 288 eV and 293 eV, are presented in Figure 6.26 respectively.

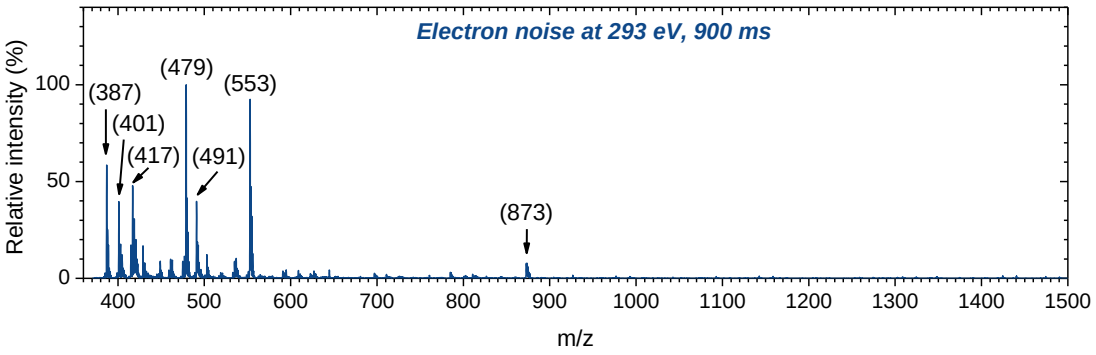

Figure 6.24 - Mass spectrum recorded with no isolated ions, for electron impact energy of 293 eV, 900 ms pulse width and 100 ms acquisition delay, acquired during 3 min.

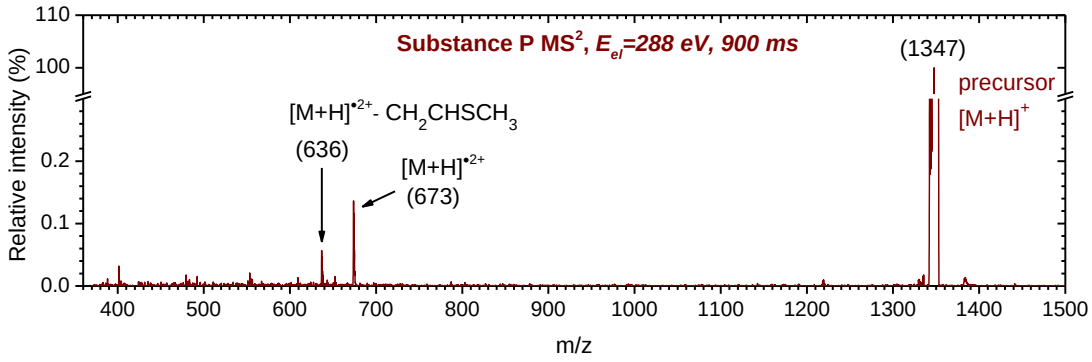

Figure 6.25 - Tandem mass spectrum recorded for 288 eV electron impact with peptide Substance P, singly charged precursor. Electron beam pulse width is 900 ms, with acquisition delay of 100 ms, acquired during 15 min.

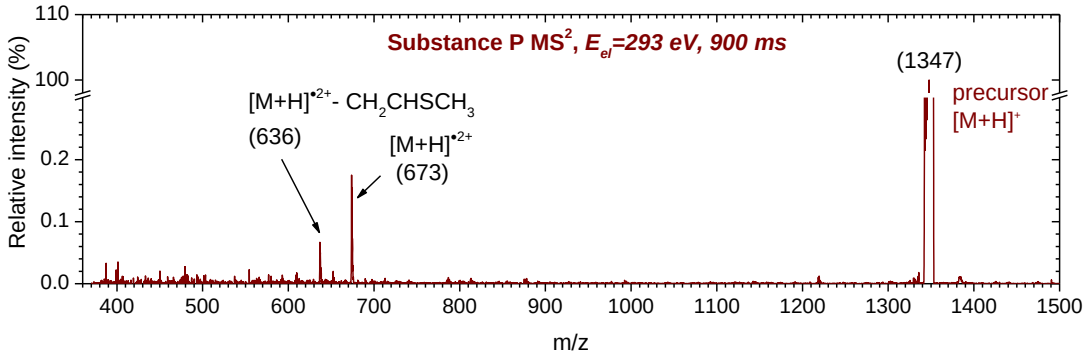

Figure 6.26 - Tandem mass spectrum recorded for 293 eV electron impact with peptide Substance P, singly charged precursor. Electron beam pulse width is 900 ms, with acquisition delay of 100 ms, acquired during 15 min.

Compared with the MS^2 presented in Figure 6.22, the same peaks corresponding to the noise signal dominate the lower mass region of the MS in Figure 6.24. A distribution of peak intensities is slightly different, given that the electron beam pulse width, the energy and the acquisition delay are also different. A decreased acquisition delay of 100 ms, yields higher overall noise. Unassigned noise peaks in Figure 6.24 with mass-to-charge ratios of 387, 553 and 873 show relative intensity increase, in comparison with the same peaks obtained at an electron energy of 288 eV (Figure 6.22).

Besides singly charged Substance P precursor ion $[M+H]^+$ designated at m/z 1374, the tandem mass spectra presented in Figure 6.25 and Figure 6.26 also reveal the ion fragments. In order to compensate for the low abundancy of precursor ions produced by ESI, the electron beam pulse width was increased to 900 ms and the MS^2 were acquired during 15 min. The peak at m/z 673 corresponds to the radical cation $[M+H]^{\bullet 2+}$ originating from the single ionization of the precursor ion, due to the Auger decay. After the neutral loss of CH_2CHSCH_3, part of the methionine residue usually present in proteins, radical cation $[M+H]^{\bullet 2+}$ forms the ion fragment with a mass-to-charge ratio of 636. This ion fragment is also reported by Canon et al [15], in a comprehensive fragmentation study of the trapped Substance P cations, activated with VUV photons from synchrotron radiation. Comparing the two MS^2 presented in Figure 6.25 and Figure 6.26, we observe a slight increase in the relative intensities of ion fragments at m/z 673 and 636, for the electron activation energy of 293 eV.

Melittin, $[M+2H]^{2+}$

Melittin peptide is present in the honey bee venom and is composed of 26 amino acids, with a molecular weight of 2846 g/mol.

Doubly charged precursor ions of Melittin peptide, are selected in the ion trap and subjected to the electron impact at the energy of 293 eV. Figure 6.27 presents the MS obtained with no ions selected, at 293 eV electron energy. A background-subtracted MS^2 obtained for electron energy of 293 eV is presented in Figure 6.28.

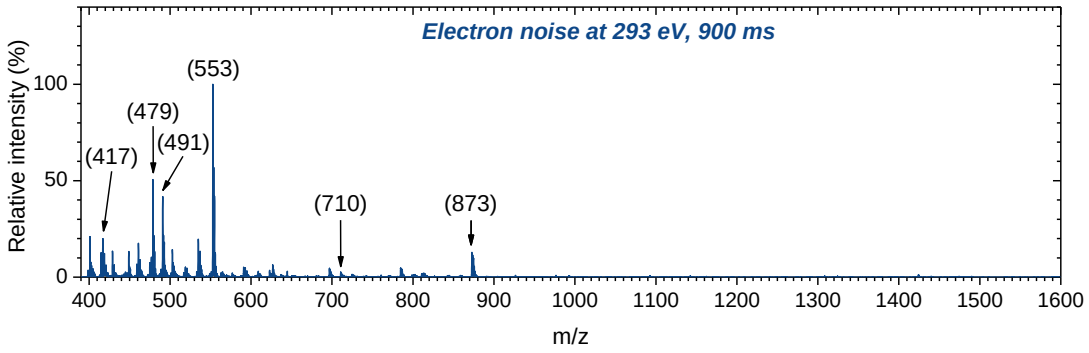

Figure 6.27 - Mass spectrum recorded with no isolated ions, for electron impact energy of 293 eV, 900 ms pulse width and 100 ms acquisition delay, acquired during 5 min.

The electron noise mass spectrum presented in Figure 6.27 is also characterized by the distinctive peaks in the low mass region. The peak designated at m/z 553 shows up as the strongest and followed by the peak at m/z 479. Even though the electron energy, the pulse width and the acquisition time are the same as for the Substance P in Figure 6.24, the distribution of the noise peak intensity is different. The different noise peak distributions suggest that experimental conditions are changed if a new analyte solution was injected into ESI, even though the precursor ions were not isolated in the ion trap. Compared with the electron noise obtained for Ubiquitin and Substance P, the noise peak observed at m/z 873 in Figure 6.27 appears with an increased intensity.

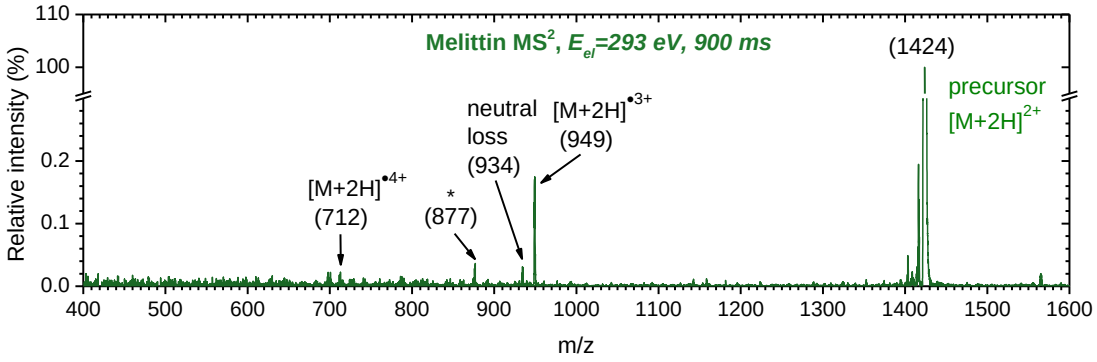

Figure 6.28 - Tandem mass spectrum recorded for 293 eV electron impact with peptide Melittin, doubly charged precursor. Electron beam pulse width is 900 ms, with acquisition delay of 100 ms, acquired during 25 min.

The tandem mass spectrum presented in Figure 6.28 shows a strong ion fragment at m/z 949, corresponding to the radical cation $[M+H]^{\bullet 3+}$. It is formed by single ionization of the precursor ion at m/z 1424 followed by an Auger decay. After a neutral loss of about 45 amu from the radical cation $[M+H]^{\bullet 3+}$, the peak with the mass-to-charge ratio of 934 is

formed. The radical cation $[M+H]^{\bullet 4+}$ that corresponds to double ionization of the Melittin precursor ion would appear in the spectrum at m/z 712. Although the MS^2 in Figure 6.28 is background subtracted, it is not entirely clear if the small peak observed at m/z 712 can be assigned to this radical cation. The electron noise MS^2 from Figure 6.27, does show a small noise peak at m/z 710. This noise peak is very close to the radical cation peak at m/z 712, thus there is a possibility that we observe a noise signal instead. Another peak at m/z 877 also remains unassigned so far. It might be assigned to a neutral loss from $[M+H]^{\bullet 3+}$, corresponding to 216 amu. However, the presence of a broad noise signal peak at m/z 873, clearly visible in the MS^2 from Figure 6.27, brings the ion origin of the peak at m/z 877 into question.

6.2.3 Electron induced action spectroscopy of Ubiquitin protein

Multiply charged precursor ions of Ubiquitin protein, with 7+ charge state were produced by electrospray ionization and activated with electrons. Electron energy was scanned near Carbon K-edge, from 280 eV to 300 eV. The same target was also probed with soft X-ray photons, by A. Milosavljevic et al [101]. The two obtained action MS^2 for practically the same incident energies of 288 eV, are compared in Figure 6.29 [105].

Figure 6.29a presents the action MS^2 obtained for the electron activation of the trapped precursor ions $[M+7H]^{7+}$ at m/z 1225, at the electron energy of 288 eV. The dominant relaxation channel corresponds to the single ionization of the precursor ion, thus forming the radical cation $[M+7H]^{\bullet 8+}$ with a mass-to-charge ratio of 1071. The triggering process of the Auger decay, in this case is the direct inner-shell excitation by the electron impact. A strong peak is observed near m/z 1066 corresponding to a neutral loss of about 42 amu from the radical cation $[M+7H]^{\bullet 8+}$. Given the reduced m/z resolution, we can tentatively assign the peak due to the amino acid side chain losses. A second strong channel is observed at m/z 952, corresponding to the formation of the radical cation $[M+7H]^{\bullet 9+}$, originating from the double ionization of the precursor ions. The intensive peak at m/z 947 is ascribed to the neutral loss (of about 42 amu) from the doubly ionized precursor ion. Other peaks with very low intensities are also present in the spectrum, although their assignments are not significant for the present study.

Figure 6.29b presents the action MS^2 obtained for the Ubiquitin 7+ precursor ions, at the photon energy of 288.2 eV. These action NEXAFS results are recently reported by A. Milosavljević et al [101]. The experiment is performed by coupling the same LTQ XL mass spectrometer to the soft X-ray beamline PLEIADES, at the synchrotron SOLEIL. It should be noted that m/z resolution of the X-ray action spectrum is higher than the one obtained for the electron activation. The energy of 288 eV, corresponds to a maximum in measured C 1s near-edge excitation function [101]. It could be seen that both fragmentation patterns are very similar. Indeed, in both cases, the ionization of the protein precursor ion, is the result of a resonant Auger decay process. It is triggered by the Carbon 1s electron excitation into higher unoccupied molecular orbitals, resulting in a core hole

formation. The system relaxes and an electron is ejected, resulting in a single ionization. Even though the triggering process of the Auger decay is entirely different (photons or electrons), the ionization pattern seems to be very similar.

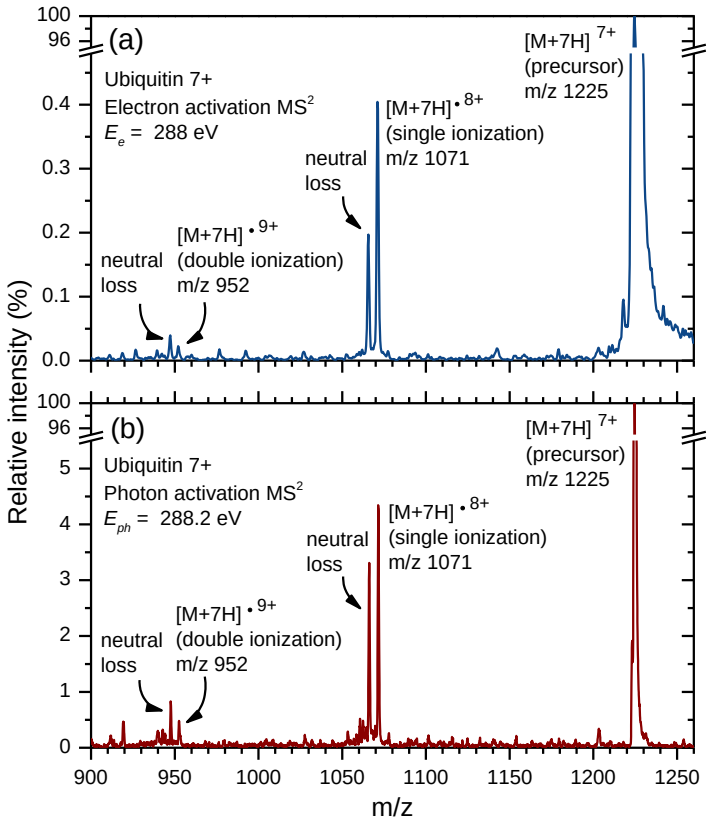

Figure 6.29 - Comparison of tandem mass spectra of Ubiquitin 7+ precursor, for energies near Carbon K-edge activated with: (a) electrons and (b) photons.

If the incident energy is lower than the ionization threshold, governed by the selection rules of a dipole transitions, the X-ray photon can be absorbed by the protein if its energy matches with the energy required by the core electron to undergo a transition from its ground state to the particular unoccupied bound excited state. In short, the photon absorption is a resonant process. In the case of the electron impact, the lower part of the incident electron energy is transferred to the core electron undergoing a transition. The remaining energy is carried away by the scattered electron, suffering the energy loss. Upon core hole formation valence electron fills the core vacancy in the order of femtoseconds [106] and an electron is ejected. In both cases, the process is called the resonant Auger decay, in which the single ionization of the protein precursor ion dominantly occurs. It should be noted that even below the ionization threshold the multiple resonant Auger decay can still occur [103, 107] in which system relaxes with more than one ejected electrons.

In the present experiment, the incident electron energy is only slightly above the transition energy. Thus, the excitation process is performed under so-called near-threshold conditions [108].

The acquisition of many action MS^2 spectra for different photon energies yields the action NEXAFS. In the case of the electron activation, action near-edge electron excitation function (NEEEF) is obtained. Figure 6.30 presents the obtained NEEEF action spectra, for the single and double ionization of the 7+ charge state precursor ions from Ubiquitin protein.

A comparison between the obtained NEEEF and NEXAFS action spectra, obtained for single ionization of the same Ubiquitin protein, is presented in Figure 6.31. The presented energy yields are extracted from MS^2, by normalizing the area under the corresponding peak in the mass spectrum to the total ion current and by plotting it against the incident energy. In the experiment involving photons, an additional normalization to the photon flux was performed. In order to preserve the electron beam geometry and keep the incident electron current constant, the electron gun was refocused for each energy point. The voltages required to refocus the electron gun were determined during the test measurements, prior to the experiment involving activation of trapped ions.

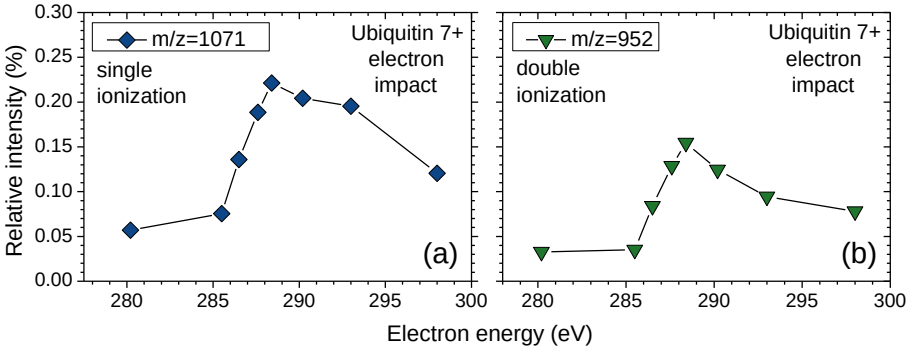

Figure 6.30 - Energy yields of single (a) and double (b) ionization of Ubiquitin protein, 7+ charge state precursor, obtained with electron impact.

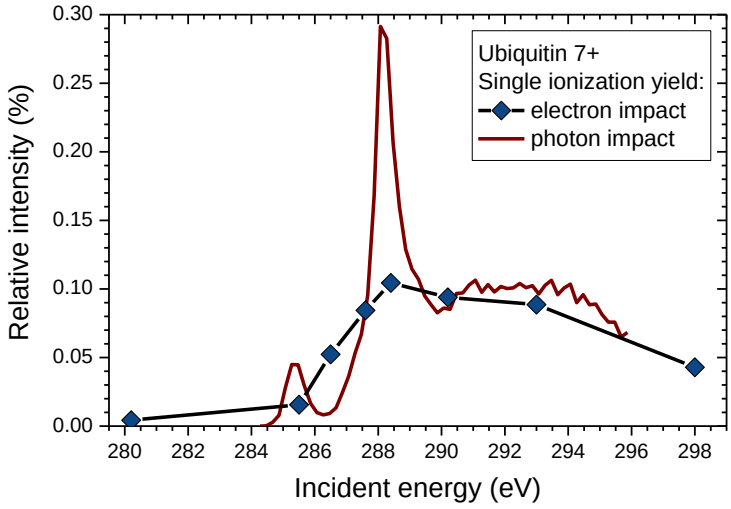

Figure 6.31 - Comparison of single ionization energy yields, obtained for Ubiquitin protein 7+ charge state precursor, for electron and photon impact.

In order to be able to compare the two energy yields from Figure 6.31, both yields are additionally normalized to the same area under the presented curves. The dashed line represents the NEXAFS spectrum, while diamonds represents the normalized NEEEF spectrum for the obtained single ionization (SI) of the Ubiquitin precursor ions. The clear spectroscopic feature appears for both SI yields. For the electron impact, the increase of the cross sections starts at the energy of 284.5 eV, corresponding to the Carbon 1s → $\pi^*_{C=C}$ (aromatic) transition. The maximum is reached at the energy of 288 eV, which corresponds to the Carbon 1s → π^*_{C-N} (amide) transition. Cross sections of both SI yields, decreases slowly with further increase of the incident energy.

SI yields presented in Figure 6.31 are in a very good agreement, even though the triggering process is intrinsically different. This fact could be of a high importance for the studies involving the radiation damage [109]. Furthermore, the similarity in the obtained action MS^2 (Figure 6.29) as well as in the ionization yields (Figure 6.31), is a proof of principle for our experimental setup for electron activation of trapped ions.

7 Conclusions

The work presented in this Thesis involved the gas-phase photon and electron action spectroscopy of trapped biopolymer ions, as well as bare and hydrated nucleotide ions. The activation of trapped ions was performed by either synchrotron radiation or electron beam produced by a custom designed electron gun. The photon action spectroscopy was performed using the previously developed setup and during the work on this Thesis, the experimental procedures have been improved and new interesting results have been collected and discussed. The experimental setup for coupling a focusing electron gun with the LTQ XL linear ion trap mass spectrometer has been developed during this Thesis. It allowed for performing, for the first time, the electron impact action spectroscopy of trapped macromolecular ions, in the C K-edge ionization region.

The energy dependent fragmentation study of protonated peptide Leu-enk in the VUV photon domain of (5.7-14) eV or (217.5-88.56) nm was performed. In the obtained fragment ion yields, we were able to observe the distinctive spectroscopic band centered at c.a. 6.9 eV ascribed to the peptide $\pi_2\pi_3^*$ (*NV1*) transition. For fragments b_2, b_3, b_4 and y_2 we could also observe the second spectral band centered at c.a. 9.6 eV ascribed to the $\pi_1\pi_3^*$ (*NV2*) transition. We propose that the photo-fragmentation below the IE threshold proceeds on the hot ground electronic state after an internal conversion, following the electronic excitation of the target. The measured photo-dissociation yields of the selected ionic fragments from Leu-enk dimer precursor reveal the absorption bands at about 6.7–7.1 eV (185–175 nm), which is similar to the monomer precursor.

The UV/VUV photo-dissociation of both bare and monohydrated protonated AMP nucleotide isolated in the gas phase, revealed spectral bands located at 4.75 eV and 6.5 eV. It should be noted that the band at 6.5 eV has not been directly measured previously and agree very well with our TD-DFT calculations. However, our studies also showed that the nanosolvation of the AMP nucleotide, with even one water molecule, significantly reduced the dissociation. This could be due to different absorption properties of the hydrated species, according to theoretical analysis.

The inner-shell X-ray action spectroscopy near C and N K-edge of multiply charged Ubiquitin protein (from +4 to +11 charge states) allowed to clearly distinguish the band at 284.5 eV, ascribed to Carbon 1s $\rightarrow \pi^*_{C=C}$ (aromatic) transition, as well as dominant strong absorption band at 288.2 eV corresponding to Carbon 1s$\rightarrow \pi^*_{C-N}$ (amide) transition. For the N-edge, the spectroscopic band was observed at 401.2 eV corresponding to Nitrogen 1s$\rightarrow \pi^*_{C-N}$ (amide) transition. IE for 5+ charge state precursor ion of Ubiquitin protein was measured at (294.3±0.2) eV.

Finally, we have presented the energy-tunable focused electron beam activation of m/z selected trapped protein ions by coupling an electron gun to a linear quadrupole ion trap mass spectrometer. We have shown that the electron and the X-ray activation of the charged precursor ion of Ubiquitin protein produce very similar MS^2 patterns, which is defined by the resonant Auger decay, regardless of the triggering process. We could also

measure the electron-induced single ionization ion yield, that revealed a maximum centered at about 288 eV, in the accord with the soft X-ray measurements. The performed experiments represent a proof of principle for an electron-impact activation method for MS^2 of trapped macromolecular ions, which can be also of interest for top-down protein sequencing.

8 Appendix

8.1 Faraday cup simulation in SIMION

This program was used to simulate and record the electron beam profile for the preset beam width and angle divergence. The final result is plotted in the graph in Microsoft Excel, although that part of the code is not necessary for the simulation. The main program code is contained in the LUA file. The geometry of the electrodes is contained in a separate geometry file (GEM), independent of the main LUA code. Definition of particles is also contained in an independent file (PARTICLES). All three pieces of the code are presented in the following sections.

8.1.1 Faraday cup - LUA code

```
simion.workbench_program()
--global adjustables
adjustable _y_range_mm          -- Y-axis range to scan [mm]
adjustable _points              -- number of data points
adjustable _dy_mm               -- electron beam initial width (window) [mm]
adjustable _da_deg              -- electron beam initial divergence (pupil angle) [mm]
 --Create Excel object (if not exist).
 local excel   -- Excel object
     if not excel then
       _G.excel = _G.excel or luacom.CreateObject("Excel.Application")
       excel = _G.excel
     end
 local wb = excel.Workbooks:Add()    -- Excel workbook
 local ws = wb.Worksheets(1)         -- Excel worksheet
 excel.Visible = false               -- don't show excel window
 -- create function for ploting graph in excel
 local function plot_chart()
  local chart = excel.Charts:Add()
  chart.ChartType = -4169  -- scatter XY
  chart.HasTitle = true
  chart.HasLegend = false
  chart.ChartTitle:Characters().Text = "Faradey cup simulation"
  local range = ws.UsedRange
  chart:SetSourceData(range, 2)
  chart.Axes(1,1).HasTitle = 1
  chart.Axes(1,1).AxisTitle:Characters().Text = "Y(mm)"
  chart.Axes(1,2).HasTitle = 1
  chart.Axes(1,2).AxisTitle:Characters().Text = "Transmission(%)"
 end
-- global help variables
local y_step = _y_range_mm / _points
local current_y = _y_range_mm
-- Counters.
local run=1
```

```
local num_particles
local num_hits
-- SIMION intialize segment.  Called for each particle construction.
function segment.initialize_run()
 assert(current_y)
 assert(y_step > 0)
 assert(_dy_mm > 0)
 assert(_da_deg > 0)
 -- Regenerate particle definitions
 local PL = simion.import 'particlelib.lua'
 PL.reload_fly2('particles.fly2', {
 --variables to pass to FLY2 file.
  current_y=current_y,
  y_step=y_step,
  _dy_mm=_dy_mm,
  _da_deg=_da_deg,
 })
 -- Reset the counter before each rerun
 num_hits = 0
 num_particles = 0
  if run == 1 then  -- when first particle in run is created.
     -- Print parameters used.
     print("Initial parameters:")
     print(string.format("dY=%g[mm], dA=%g[deg]", _dy_mm, _da_deg))
     print(" ")
     print("Y[mm] T[%]")
     print("----------")
  end
end
-- called on each particle initialization inside a PA instance...
function segment.initialize()
end
-- called on each particle termination inside a PA instance...
function segment.terminate()
 -- Count total number of particles
 num_particles = num_particles + 1
 -- Count particles that splat beyond some distance
 if ion_px_mm >= 75.5 then
    num_hits = num_hits + 1
 end
end
-- called on end of each run...
function segment.terminate_run()
 -- Count number of runs
 run=run+1
 -- Print summary and store some data at end of each run.
 local transmission = 100 * num_hits / num_particles
 if run > 2 then       -- skip the first run
 print(current_y+y_step, transmission)
 end
 -- set next y position to scan
 current_y = current_y - y_step
 --fill excel cells with data
```

```
 if run > 2 then       -- skip the first run
   ws.Cells(run,1).Value2 = current_y + 2*y_step
   ws.Cells(run,2).Value2 = transmission
 end
 -- rerun the ions
 sim_rerun_flym = 1
 -- stop reruns if enough data points are reached
 if run > 2*_points+2 then
 sim_rerun_flym = 0
 --Plot chart, make excel visible and reset number of runs
 excel.Visible = true
 plot_chart()  -- create chart
 run=0
 end
end
```

8.1.2 Faraday cup - GEM file

```
pa_define(1957,201,1,cylindrical,y_mirror)
  e(1) ;{fill{within{box(0,0,4,200)}          ;start disc
 locate(1105,0,0)
       {
        within{box(0,0,11,200)}               ;f.c.
        notin{box(0,0,11,8)}                  ;f.c. hole
        locate(663,0,0)
          {
           within{box(0,0,4,200)}             ;detector disc
           }}}}
```

8.1.3 Faraday cup - PARTICLES file

```
local var = _G.var or {}
local y0 = var.current_y
local y_step = var.y_step
local dy = var._dy_mm
local da = var._da_deg
particles {
 coordinates = 0,
 standard_beam {
  n = 121,
  tob = 0,
  mass = 0.00054857990946,
  charge = -1,
  x = 0.401,
  y = arithmetic_sequence
    {
     first = y0+(dy/2),
     step = -(dy/10),
     n = 11
    },
  z = 0,
  ke = 1,
  az = 0,
  el = arithmetic_sequence
```

```
        {
         first = da/2,
         step = -(da/10),
         n = 11
        },
       cwf = 1,
       color = 3
      }
     }
```

8.2 Simulation of the linear quadrupole RF+DC ion trap

This program was used to simulate the transmission of the electron beam through the linear quadrupole ion trap from the LTQ mass spectrometer. This simulation consists of few separate code segments. Particle definitions are used without special coding and are created through the user interface of the SIMION program. The main part of the code (LUA) is presented in the following section, while 3 geometry files with the information of electrode dimensions are given in the sections that follow next.

8.2.1 Ion trap - LUA file

```
simion.workbench_program()
-- Definition of variables.
adjustable DC_voltage_V = 100.0                    -- DC voltage [V]
adjustable RF_frequency_Hz = 1E+6                  -- RF frequancy [Hz]
adjustable RF_voltage_V = 400                      -- RF voltage [V]
adjustable phase_in_deg = 0                        -- Phase angle at ion entrance [deg]
adjustable phase_RF_deg = 180.0                    -- Phase angle between RF rods [deg]
adjustable disk_DC_voltage_V = 0                   -- Disk electrode DC voltage [V]
adjustable katode_V = 0                            -- Katode DCvoltage [V]
adjustable pe_update_each_usec = 0.0001            -- PE display update time step [usec]
adjustable time_step_min = 0.0001                  -- Min time step [usec]
-- Initialising static potentials on Disk electrodes and kathode in instances 1 and 3 only.
function segment.init_p_values()
   if ion_instance == 1 then      -- entrance PA
      adj_elect03 = disk_DC_voltage_V
      adj_elect04 = katode_V
    elseif ion_instance == 3 then  -- exit PA
      adj_elect03 = disk_DC_voltage_V
   end
 end
-- SIMION fast_adjust segment.  Called to override electrode potentials.
function segment.fast_adjust()
local omega = 2 * math.pi * RF_frequency_Hz * 1E-6
local phase_in = phase_in_deg * (math.pi/180)
local phase_RF = phase_RF_deg * (math.pi/180)
  -- Set electrode voltages.
  adj_elect01 = RF_voltage_V * sin (omega * Ion_Time_of_Flight + phase_in) + DC_voltage_V
  adj_elect02 = RF_voltage_V * sin (omega * Ion_Time_of_Flight + phase_in + phase_RF) -
DC_voltage_V
 end
```

```
-- SIMION other_actions segment. Called on each time-step.
local next_pe_update = 0   -- next time to update PE surface display [usec]
function segment.other_actions()
    -- Trigger PE surface display updates. If TOF reached next PE display update time...
  if ion_time_of_flight >= next_pe_update then
     -- Request a PE surface display update.
     sim_update_pe_surface = 1
     -- Compute next PE display update time (usec).
     next_pe_update = ion_time_of_flight + pe_update_each_usec
  end
end
-- SIMION segment called by SIMION to override time-step size on each time-step.
 function segment.tstep_adjust()

ion_time_step = min(ion_time_step, time_step_min)
end
```

8.2.2 Ion trap - front section GEM file

```
pa_define (72,72,232,p,xy,e,1)
locate(0,0,0,1,0,0)
{e(4) ; Cathode
{fill{within{box3d(-72,0,0,72,72,5) circle(0,0,10,10)}}}}
locate(0,0,155,1,0,0){e(3) ; Front plate disc
{fill{within{box3d(-72,0,0,72,72,6) circle(0,0,61,61)}
notin{box3d(-72,0,0,72,72,6) circle(0,0,6,6)}}}}
locate(0,0,166,1,0,0){
locate(0,0,0,1,0,0)
{e(1) ; Y-axis electrodes
{fill{within{box3d(-52,0,0,52,72,60) hyperbola(0,0,16,17)}}}}
locate(0,0,0,1,0,-90)
{e(2) ; X-axis elektrodes
{fill{within{box3d(-52,0,0,52,72,60) hyperbola(0,0,16,17)}}}
```

8.2.3 Ion trap - center section GEM file

```
pa_define (72,72,1,p,xy,e,1)
locate(0,0,0,1,0,0){
locate(0,0,0,1,0,0)
{e(1) ; Y-axis electrodes
{fill{within{box(-52,0,52,72) hyperbola(0,0,16,17)}}}}
locate(0,0,0,1,0,-90)
{e(2) ; X-axis electrodes
{fill{within{box(-52,0,52,72) hyperbola(0,0,16,17)}}}}}
```

8.2.4 Ion trap - back section GEM file

```
pa_define (72,72,82,p,xy,e,1)
locate(0,0,70,1,0,0)
{e(3) ; Detector disk
{fill{
within{box3d(-72,0,0,72,72,6) circle(0,0,61,61)}
notin{box3d(-72,0,0,72,72,6) circle(0,0,6,6)}}}}
locate(0,0,5,1,0,0){
locate(0,0,0,1,0,0)
```

```
{e(1) ; Y-axis electrodes
{fill{within{box3d(-52,0,0,52,72,60) hyperbola(0,0,16,17)}}}}
locate(0,0,0,1,0,-90)
{e(2) ; X-axis electrodes
{fill{within{box3d(-52,0,0,52,72,60) hyperbola(0,0,16,17)}}}}
```

9 References

[1] M. A. Śmiałek, P. Limão-Vieira, N. J. Mason, and A. V. Solov'yov, "Radiation damage of biomolecular systems: Nano-scale insights into Ion-beam cancer therapy. 2nd Nano-IBCT conference ∗," *Eur. Phys. J. D*, vol. 68, no. 10, 2014.

[2] I. Baccarelli, F. A. Gianturco, A. Grandi, R. R. Lucchese, and N. Sanna, "Electron-Driven Molecular Processes Induced in Biological Systems by Electromagnetic and Other Ionizing Sources," *Adv. Quantum Chem.*, vol. 52, no. 06, pp. 189–230, 2007.

[3] E. Alizadeh and L. Sanche, "Precursors of solvated electrons in radiobiological physics and chemistry," *Chem. Rev.*, vol. 112, no. 11, pp. 5578–5602, 2012.

[4] M. Yamashita and J. B. Fenn, "Electrospray Ion Source. Another Variation on the Free-Jet Theme," *J. Phys. Chem.*, vol. 434, no. 125, pp. 4451–4459, 1984.

[5] E. De Hoffmann and V. Stroobant, *Mass Spectrometry - Principles and Applications*, Third edit. John Wiley and Sons, Ltd, 2007.

[6] K. Hirsch, J. T. Lau, P. Klar, A. Langenberg, J. Probst, J. Rittmann, M. Vogel, V. Zamudio-Bayer, T. Möller, and B. von Issendorff, "X-ray spectroscopy on size-selected clusters in an ion trap: from the molecular limit to bulk properties," *J. Phys. B At. Mol. Opt. Phys.*, vol. 42, no. 15, pp. 154029–154036, 2009.

[7] R. Thissen, J. M. Bizau, C. Blancard, M. Coreno, C. Dehon, P. Franceschi, A. Giuliani, J. Lemaire, and C. Nicolas, "Photoionization Cross Section of Xe^+ Ion in the Pure $5p^5$ $^2P_{3/2}$ Ground Level," *Phys. Rev. Lett.*, vol. 100, no. 22, pp. 1–4, 2008.

[8] L. Nahon, N. De Oliveira, G. A. Garcia, J. F. Gil, B. Pilette, O. Marcouillé, B. Lagarde, and F. Polack, "DESIRS: A state-of-the-art VUV beamline featuring high resolution and variable polarization for spectroscopy and dichroism at SOLEIL," *J. Synchrotron Radiat.*, vol. 19, no. 4, pp. 508–520, 2012.

[9] A. R. Milosavljević, C. Nicolas, J. F. Gil, F. Canon, M. Réfrégiers, L. Nahon, and A. Giuliani, "VUV synchrotron radiation: A new activation technique for tandem mass spectrometry," *J. Synchrotron Radiat.*, vol. 19, no. 2, pp. 174–178, 2012.

[10] A. R. Milosavljević, A. Giuliani, C. Nicolas, J.-F. Gil, J. Lemaire, M. Réfrégiers, and L. Nahon, "Gas-phase spectroscopy of a protein," *J. Phys. Conf. Ser.*, vol. 257, no. 1, p. 012006, 2010.

[11] A. R. Milosavljević, C. Nicolas, J. Lemaire, C. Dehon, R. Thissen, J.-M. Bizau, M. Réfrégiers, L. Nahon, and A. Giuliani, "Photoionization of a protein isolated in vacuo.," *Phys. Chem. Chem. Phys.*, vol. 13, no. 34, pp. 15432–15436, 2011.

[12] A. R. Milosavljević, V. Z. Cerovski, F. Canon, L. Nahon, and A. Giuliani, "Nanosolvation-induced stabilization of a protonated peptide dimer isolated in the Gas phase," *Angew. Chemie - Int. Ed.*, vol. 52, no. 28, pp. 7286–7290, 2013.

[13] S. Bari, O. Gonzalez-Magaña, G. Reitsma, J. Werner, S. Schippers, R. Hoekstra, and T. Schlathölter, "Photodissociation of protonated leucine-enkephalin in the VUV range of 8-40 eV," *J. Chem. Phys.*, vol. 134, no. 2, pp. 6–10, 2011.

[14] O. González-Magaña, G. Reitsma, S. Bari, R. Hoekstra, and T. Schlathölter, "Length effects in VUV photofragmentation of protonated peptides.," *Phys. Chem. Chem. Phys.*, vol. 14, no. 13, pp. 4351–4354, 2012.

[15] F. Canon, A. R. Milosavljević, L. Nahon, and A. Giuliani, "Action spectroscopy of a

protonated peptide in the ultraviolet range," *Phys. Chem. Chem. Phys.*, vol. 17, no. 17, pp. 25725–25733, 2015.

[16] H. W. Jochims, M. Schwell, J. L. Chotin, M. Clemino, F. Dulieu, H. Baumgärtel, and S. Leach, "Photoion mass spectrometry of five amino acids in the 6-22 eV photon energy range," *Chem. Phys.*, vol. 298, no. 1–3, pp. 279–297, 2004.

[17] M. Schwell, H. W. Jochims, H. Baumgärtel, F. Dulieu, and S. Leach, "VUV photochemistry of small biomolecules," *Planet. Space Sci.*, vol. 54, no. 11, pp. 1073–1085, 2006.

[18] A. R. Milosavljević, F. Canon, C. Nicolas, C. Miron, L. Nahon, and A. Giuliani, "Gas-phase protein inner-shell spectroscopy by coupling an ion trap with a soft X-ray beamline," *J. Phys. Chem. Lett.*, vol. 3, no. 9, pp. 1191–1196, 2012.

[19] K. B. Shelimov, D. E. Clemmer, R. R. Hudgins, and M. F. Jarrold, "Protein structure in Vacuo: Gas-phase conformations of BPTI and cytochrome c," *J. Am. Chem. Soc.*, vol. 119, no. 9, pp. 2240–2248, 1997.

[20] B. A. Budnik, K. F. Haselmann, and R. A. Zubarev, "Electron detachment dissociation of peptide di-anions: An electron-hole recombination phenomenon," *Chem. Phys. Lett.*, vol. 342, no. 3–4, pp. 299–302, 2001.

[21] B. A. Budnik, Y. O. Tsybin, P. Häkansson, and R. A. Zubarev, "Ionization energies of multiply protonated polypeptides obtained by tandem ionization in Fourier transform mass spectrometers," *J. Mass Spectrom.*, vol. 37, no. 11, pp. 1141–1144, 2002.

[22] R. Uy and F. Wold, "Posttranslational covalent modification of proteins," *Science*, vol. 198, no. 4320, pp. 890–896, 1977.

[23] H. A. B. Johansson, "Fragmentation of Amino Acids and Microsolvated Peptides and Nucleotides using Electrospray Ionization Tandem Mass Spectrometry," Licentiate Thesis, Stocholm University, Stocholm, 2010.

[24] P. Roepstor and Fohlman J, "Proposal for a common nomenclature for sequence ions in mass-spectra of peptides," *Biomed. Mass Spectrom.*, vol. 26, no. 11, pp. 672–682, 1984.

[25] A. I. S. Holm, "Bare and Solvated DNA and Peptides. Spectroscopy and Mass Spectrometry," PhD Thesis, Aarhus University, Danemark, 2009.

[26] P. Rossmann, M. G.; Argos, "Protein Folding," *Annu. Rev. Biochem.*, vol. 50, p. 497−532, 1981.

[27] W. Kohn, "Electronic structure of matter - wave functions and density functionals - Nobel Lecture," vol. 71, no. 5, pp. 213–237, 1999.

[28] W. Kohn and L. J. Scham, "Self-Consistent Equations Including Exchange and Correlation Effects*," *Phys. Rev.*, vol. 140, no. 1951, 1965.

[29] M. Dole, L. L. Mack, and R. L. Hines, "Molecular beams of macroions," *J. Chem. Phys.*, vol. 49, no. 5, pp. 2240–2249, 1968.

[30] J. B. Fenn, M. Mann, C. K. A. I. Meng, S. F. Wong, and C. M. Whitehouse, "Electrospray Ionization for Mass Spectrometry of Large Biomolecules," *Science*, vol. 246, no. 6, 1989.

[31] V. Gabellca and E. De Pauw, "Internal energy and fragmentation of ions produced in electrospray sources," *Mass Spectrom. Rev.*, vol. 24, no. 4, pp. 566–587, 2005.

[32] V. Katta, D. T. Chow, and M. F. Rohde, "Applications of in-source fragmentation of protein ions for direct sequence analysis by delayed extraction MALDI-TOF mass

spectrometry.," *Anal. Chem.*, vol. 70, no. 20, pp. 4410–4416, 1998.

[33] S. Banerjee and S. Mazumdar, "Electrospray Ionization Mass Spectrometry: A Technique to Access the Information beyond the Molecular Weight of the Analyte," *Int. J. Anal. Chem.*, vol. 2012, pp. 1–40, 2012.

[34] G. Taylor, "Disintegration of Water Drops in an Electric Field," *Proceedings of the Royal Society A: Mathematical, Physical and Engineering Sciences*, vol. 280, no. 1382. pp. 383–397, 1964.

[35] L. Rayleigh, "On the equilibrium of liquid conducting masses charged with electricity," *Philisophical Mag.*, vol. 14, no. 87, pp. 184–186, 1882.

[36] P. Kebarle and U. H. Verkcerk, "Electrospray: From Ions in solution to Ions in the gas phase, what we know now," *Mass Spectrom. Rev.*, vol. 28, no. 6, pp. 898–917, 2009.

[37] J. V. Iribarne and B. A. Thomson, "On the evaporation of small ions from charged droplets," *J. Chem. Phys.*, vol. 64, no. 6, pp. 2287–2294, 1976.

[38] G. Schmelzeisen-Redeker, L. Bütfering, and F. W. Röllgen, "Desolvation of ions and molecules in thermospray mass spectrometry," *Int. J. Mass Spectrom. Ion Process.*, vol. 90, no. 2, pp. 139–150, 1989.

[39] J. B. Fenn and S. Nguyen, "Gas-phase ions of solute species from charged droplets of solutions," *Proc. Natl. Acad. Sci. U. S. A.*, vol. 104, no. 4, pp. 1111–1117, 2007.

[40] M. S. Wilm and M. Mann, "Electrospray and Taylor-Cone theory, Dole's beam of macromolecules at last?," *Int. J. Mass Spectrom. Ion Process.*, vol. 136, no. 2–3, pp. 167–180, 1994.

[41] M. Wilm and M. Mann, "Analytical properties of the nanoelectrospray ion source.," *Anal. Chem.*, vol. 68, no. 1, pp. 1–8, 1996.

[42] P. Wolfgang, "Electromagnetic traps for charged and neutral particles," *Rev. Mod. Phys.*, vol. 62, no. 3, 1990.

[43] J. E. Coutant and F. W. McLafferty, "Metastable ion characteristics," *Int. J. Mass Spectrom. Ion Phys.*, vol. 8, no. 4, pp. 323–339, 1972.

[44] S. Bari, O. Gonzalez-Magaña, G. Reitsma, J. Werner, S. Schippers, R. Hoekstra, and T. Schlathölter, "Photodissociation of protonated leucine-enkephalin in the VUV range of 8-40 eV," *J. Chem. Phys.*, vol. 134, no. 2, pp. 1–9, 2011.

[45] R. Zubarev, N. L. Kelleher, and F. W. McLafferty, "Electron capture dissociation of multiply charged protein cations. A Nonergodic Process," *J. Am. Chem. Soc*, vol. 120, no. 16, pp. 3265–3266, 1998.

[46] K. Biemann, "Four decades of structure determination by mass spectrometry: From alkaloids to heparin," *J. Am. Soc. Mass Spectrom.*, vol. 13, no. 11, pp. 1254–1272, 2002.

[47] T. Scientific, "LTQ Series Hardware Manual," *Revision A*, no. April. pp. 1–165, 2009.

[48] D. D. Pommeranchuck and I. Ivanenko, "On the maximal energy, obtainable in a betatron," *Phys. Rev.*, vol. 65, no. 11–12, p. 343, 1944.

[49] J. Schwinger, "Electron radiation in high energy accelerators," *Phys. Rev.*, vol. 70, p. 798, 1946.

[50] J. Schwinger, "On the Classical Radiation of Accelerated Electrons," *Phys. Rev.*, vol. 75, no. 12, pp. 1912–1925, 1949.

[51] D. Tomboulian and P. Hartman, "Ultraviolet radiation from the Cornell synchrotron,"

Phys. Rev., vol. 91, no. 6, pp. 1577–1578, 1953.

[52] K. Codling and R. P. Madden, "Characteristics of the 'synchrotron light' from the NBS 180-MeV machine," *J. Appl. Phys.*, vol. 36, no. 2, pp. 380–387, 1965.

[53] R. P. Madden and K. Codling, "Recently Discovered Auto-Ionizing States of Krypton and Xenon in the λ380–600-Å Region," *Phys. Rev. Lett.*, vol. 54, no. 2, pp. 268–269, 1964.

[54] R. P. Madden and K. Codling, "New autoionizing atomic energy levels in He, Ne, and Ar," *Phys. Rev. Lett.*, vol. 10, no. 12, pp. 516–518, 1963.

[55] C. Kuntz, E. Rowe, W. Gudat, A. Kotani, Y. Toyozawa, and K. Codling, *Synchrotron radiation techniques and applications*,. Berlin/Heidelberg/New York: Springer, 1979.

[56] "PLÉIADES beamline." [Online]. Available: http://www.synchrotron-soleil.fr/Recherche/LignesLumiere/PLEIADES. [Accessed: 05-Mar-2016].

[57] A. R. Milosavljević, C. Nicolas, J. F. Gil, F. Canon, M. Réfrégiers, L. Nahon, and A. Giuliani, "Fast in vacuo photon shutter for synchrotron radiation quadrupole ion trap tandem mass spectrometry," *Nucl. Instruments Methods Phys. Res. Sect. B Beam Interact. with Mater. Atoms*, vol. 279, pp. 34–36, 2012.

[58] A. R. Milosavljević, S. Madžunkov, D. Šević, I. Čadež, and B. P. Marinković, "Experimental determination of the differential cross-section surface for elastic electron–atom (molecule) scattering," *J. Phys. B At. Mol. Opt. Phys.*, vol. 39, no. 3, pp. 609–623, 2006.

[59] D. J. Manura and D. A. Dahl, "SIMION Version 8.0, User Manual." Idaho National Engineering and Environmental Laboratory, Scientific Instruments Services, 2007.

[60] J. C. Nickel, K. Imre, D. F. Register, and S. Trajmar, "Total electron scattering cross sections: I. He, Ne, Ar, Xe," *J. Phys. B*, vol. 18, pp. 125–133, 1985.

[61] D. Manura, "Additional Notes on the SIMION HS1 Collision Model Derivation of Mean Relative Speed," 2007.

[62] M. Pellegrini, E. M. Marcotte, M. J. Thompson, D. Eisenberg, and T. O. Yeates, "Assigning protein functions by comparative genome analysis: protein phylogenetic profiles," *Proc. Natl. Acad. Sci. U. S. A.*, vol. 96, no. 8, pp. 4285–4288, 1999.

[63] C. B. Anfinsen, "Principles that gouvern the folding of protein chains," *Science (80-.).*, vol. 181, no. 4096, pp. 223–230, 1973.

[64] M. Lj. Ranković, F. Canon, L. Nahon, A. Giuliani, and A. R. Milosavljević, "VUV action spectroscopy of protonated leucine-enkephalin peptide in the 6-14 eV range," *J. Chem. Phys.*, vol. 143, no. 24, p. 244311, 2015.

[65] Judit Sztaray, A. Memboeuf, L. Drahos, and K. Vekey, "Leucine Enkephalin - A Mass Spectrometry Standard," *Mass Spectrom. Rev.*, vol. 30, no. 298, 2011.

[66] V. S. Rakov, O. V. Borisov, and C. M. Whitehouse, "Establishing low-energy sequential decomposition pathways of leucine enkephalin and its N- and C-terminus fragments using multiple-resonance CID in quadrupolar ion guide," *J. Am. Soc. Mass Spectrom.*, vol. 15, no. 12, pp. 1794–1809, 2004.

[67] J. Laskin, "Energetics and dynamics of fragmentation of protonated leucine enkephalin from time-and energy-resolved surface-induced dissociation studies," *J. Phys. Chem. A*, vol. 110, no. 27, pp. 8554–8562, 2006.

[68] P. D. Schnier, W. D. Price, E. F. Strittmatter, and E. R. Williams, "Dissociation

energetics and mechanism of leucine enkephalin $(M+H)^+$ and $(2M+X)^+$ ions (X=H, Li, Na, K, and Rb) measured by blackbody infrared radiative dissociation," *J. Am. Soc. Mass Spectrom.*, vol. 8, no. 97, pp. 771–780, 1997.

[69] T. Tabarin, R. Antoine, M. Broyer, and P. Dugourd, "Specific photodissociation of peptides with multi-stage mass spectrometry," *Rapid Commun. Mass Spectrom.*, vol. 19, no. 20, pp. 2883–2892, 2005.

[70] N. C. Polfer, B. C. Bohrer, M. D. Plasencia, B. Paizs, and D. E. Clemmer, "On the dynamics of fragment isomerization in collision-induced dissociation of peptides," *J. Phys. Chem. A*, vol. 112, no. 6, pp. 1286–1293, 2008.

[71] K. Biemann, "Sequencing of peptides by tandem mass spectrometry and high-energy collision-induced dissociation.," *Methods Enzymol.*, vol. 193, no. 1981, pp. 455–479, 1990.

[72] L. Serrano-Andrés and M. P. Fülscher, "Theoretical study of the electronic spectroscopy of peptides. 1. The peptidic bond: Primary, secondary, and tertiary amides," *J. Am. Chem. Soc.*, vol. 118, no. 48, pp. 12190–12199, 1996.

[73] L. Serrano-Andrés and M. P. Fülscher, "Theoretical study of the electronic spectroscopy of peptides. III. Charge Transfer transitions in polypeptides," *J. Am. Chem. Soc.*, vol. 120, no. 9, pp. 10912–10920, 1998.

[74] L. Serrano-Andrés and M. P. Fülscher, "Theoretical study of the electronic spectroscopy of peptides. 2. Glycine and N-acetylglycine," *J. Am. Chem. Soc.*, vol. 118, no. 48, pp. 12200–12206, 1996.

[75] L. Serrano-Andrés and M. P. Fülscher, "Charge transfer transitions in neutral and ionic polypeptides: A theoretical study," *J. Phys. Chem. B*, vol. 105, no. 38, pp. 9323–9330, 2001.

[76] N. C. Polfer, J. Oomens, S. Suhai, and B. Paizs, "Infrared spectroscopy and theoretical studies on gas-phase protonated Leu-enkephalin and its fragments: Direct experimental evidence for the mobile proton," *J. Am. Chem. Soc.*, vol. 129, no. 18, pp. 5887–5897, 2007.

[77] A. R. Milosavljević, V. Z. Cerovski, M. L. Ranković, F. Canon, L. Nahon, and A. Giuliani, "VUV photofragmentation of protonated leucine-enkephalin peptide dimer below ionization energy," *Eur. Phys. J. D*, vol. 68, no. 3, p. 68, 2014.

[78] C. T. Middleton, K. de La Harpe, C. Su, Y. K. Law, C. E. Crespo-Hernández, and B. Kohler, "DNA Excited-State Dynamics: From Single Bases to the Double Helix," *Annu. Rev. Phys. Chem.*, vol. 60, no. 1, pp. 217–239, 2009.

[79] J. C. Marcum, A. Halevi, and J. M. Weber, "Photodamage to isolated mononucleotides--photodissociation spectra and fragment channels.," *Phys. Chem. Chem. Phys.*, vol. 11, no. 11, pp. 1740–51, 2009.

[80] J. C. Marcum, S. H. Kaufman, and J. M. Weber, "UV-photodissociation of non-cyclic and cyclic mononucleotides," *Int. J. Mass Spectrom.*, vol. 303, no. 2–3, pp. 129–136, 2011.

[81] V. Gabelica, F. Rosu, T. Tabarin, C. Kinet, R. Antoine, M. Broyer, E. De Pauw, and P. Dugourd, "Base-dependent electron photodetachment from negatively charged DNA strands upon 260-nm laser irradiation," *J. Am. Chem. Soc.*, vol. 129, no. 15, pp. 4706–4713, 2007.

[82] L. M. Nielsen, S. Ø. Pedersen, M. B. S. Kirketerp, and S. B. Nielsen, "Absorption by DNA single strands of adenine isolated in vacuo: The role of multiple chromophores," *J.*

Chem. Phys., vol. 136, no. 6, pp. 8–13, 2012.

[83] S. B. Nielsen, J. U. Andersen, J. S. Forster, P. Hvelplund, B. Liu, U. V. Pedersen, and S. Tomita, "Photodestruction of Adenosine 5'-Monophosphate (AMP) Nucleotide Ions in vacuo: Statistical versus Nonstatistical Processes," *Phys. Rev. Lett.*, vol. 91, no. 4, p. 048302, 2003.

[84] R. Otto, J. Brox, S. Trippel, M. Stei, T. Best, and R. Wester, "Single solvent molecules can affect the dynamics of substitution reactions.," *Nat. Chem.*, vol. 4, no. 7, pp. 534–8, 2012.

[85] N. S. Nagornova, T. R. Rizzo, and O. V. Boyarkin, "Interplay of intra- and intermolecular H-bonding in a progressively solvated macrocyclic peptide.," *Science*, vol. 336, no. 6079, pp. 320–3, 2012.

[86] B. Liu, S. B. Nielsen, P. Hvelplund, H. Zettergren, H. Cederquist, B. Manil, and B. A. Huber, "Collision-induced dissociation of hydrated adenosine monophosphate nucleotide ions: Protection of the ion in water nanoclusters," *Phys. Rev. Lett.*, vol. 97, no. 13, pp. 1–4, 2006.

[87] B. Liu, N. Haag, H. Johansson, H. T. Schmidt, H. Cederquist, S. B. Nielsen, H. Zettergren, P. Hvelplund, B. Manil, and B. A. Huber, "Electron capture induced dissociation of nucleotide anions in water nanodroplets," *J. Chem. Phys.*, vol. 128, no. 7, 2008.

[88] A. R. Milosavljević, V. Z. Cerovski, F. Canon, M. L. Ranković, N. Škoro, L. Nahon, and A. Giuliani, "Energy-dependent UV photodissociation of gas-phase adenosine monophosphate nucleotide ions: The role of a single solvent molecule," *J. Phys. Chem. Lett.*, vol. 5, no. 11, pp. 1994–1999, 2014.

[89] S. K. Kim, T. Ha, and J. Schermann, "Photoionization of 2-pyridone and 2-hydroxypyridine," *Phys. Chem. Chem. Phys.*, vol. 12, no. 14, pp. 3334–3335, 2010.

[90] S. Ø. Pedersen, K. Støchkel, C. S. Byskov, L. M. Baggesen, and S. B. Nielsen, "Gas-phase spectroscopy of protonated adenine, adenosine 5'-monophosphate and monohydrated ions.," *Phys. Chem. Chem. Phys.*, vol. 15, no. 45, pp. 19748–19752, 2013.

[91] S. B. Nielsen and T. I. Sølling, "Are conical intersections responsible for the ultrafast processes of adenine, protonated adenine, and the corresponding nucleosides?," *ChemPhysChem*, vol. 6, no. 7, pp. 1276–1281, 2005.

[92] Y. Zhao and D. G. Truhlar, "A new local density functional for main-group thermochemistry, transition metal bonding, thermochemical kinetics, and noncovalent interactions," *J. Chem. Phys.*, vol. 125, no. 19, pp. 1–18, 2006.

[93] M. Valiev, E. J. Bylaska, N. Govind, K. Kowalski, T. P. Straatsma, H. J. J. Van Dam, D. Wang, J. Nieplocha, E. Apra, T. L. Windus, and W. A. De Jong, "NWChem: A comprehensive and scalable open-source solution for large scale molecular simulations," *Comput. Phys. Commun.*, vol. 181, no. 9, pp. 1477–1489, 2010.

[94] P. G. Szalay, T. Watson, A. Perera, V. F. Lotrich, and R. J. Bartlett, "Benchmark studies on the building blocks of DNA. 1. Superiority of coupled cluster methods in describing the excited states of nucleobases in the Franck-Condon region," *J. Phys. Chem. A*, vol. 116, no. 25, pp. 6702–6710, 2012.

[95] A. Bagag, A. Giuliani, and O. Laprévote, "Atmospheric pressure photoionization mass spectrometry of nucleic bases, ribonucleosides and ribonucleotides," *Int. J. Mass Spectrom.*, vol. 264, no. 1, pp. 1–9, 2007.

[96] M. G. Rossmann and P. Argos, "Protein Folding," *Annu. Rev. Biochem.*, vol. 50, pp.

497–532, 1981.

[97] N. Jones, “Crystallography: Atomic secrets,” *Nature*, vol. 505, pp. 602–603, 2014.

[98] G. Hähner, “Near edge X-ray absorption fine structure spectroscopy as a tool to probe electronic and structural properties of thin organic films and liquids.,” *Chem. Soc. Rev.*, vol. 35, no. 12, pp. 1244–1255, 2006.

[99] Y. Zubavichus, A. Shaporenko, M. Grunze, and M. Zharnikov, “NEXAFS spectroscopy of biological molecules: From amino acids to functional proteins,” *Nucl. Instruments Methods Phys. Res. Sect. A Accel. Spectrometers, Detect. Assoc. Equip.*, vol. 603, no. 1–2, pp. 111–114, 2009.

[100] G. J. Schulz, “Resonance in the elastic scattering of electrons in helium,” *Phys. Rev. Lett.*, vol. 10, no. 3, pp. 104–105, 1963.

[101] A. R. Milosavljević, C. Nicolas, M. Lj. Ranković, F. Canon, C. Miron, and A. Giuliani, “K-Shell Excitation and Ionization of a Gas-Phase Protein: Interplay between Electronic Structure and Protein Folding,” *J. Phys. Chem. Lett.*, vol. 6, no. 16, pp. 3132–3138, 2015.

[102] O. Travnikova, C. Miron, M. Bässler, R. Feifel, M. N. Piancastelli, S. L. Sorensen, and S. Svensson, “Resonant Auger decay study of C1s → π* core-excited OCS,” *J. Electron Spectros. Relat. Phenomena*, vol. 174, no. 1–3, pp. 100–106, 2009.

[103] L. Journel, R. Guillemin, A. Haouas, P. Lablanquie, F. Penent, J. Palaudoux, L. Andric, M. Simon, D. Céolin, T. Kaneyasu, J. Viefhaus, M. Braune, W. B. Li, C. Elkharrat, F. Catoire, J. C. Houver, and D. Dowek, “Resonant double Auger decay in carbon K -shell excitation of CO,” *Phys. Rev. A - At. Mol. Opt. Phys.*, vol. 77, no. 4, pp. 1–14, 2008.

[104] J. S. Gillespie, “Substance P,” *J. Neurol. Neurosurg. Psychiatry*, vol. 40, no. 11, p. 1126, 1977.

[105] M. Lj. Ranković, A. Giuliani, and A. R. Milosavljević, “Electron impact action spectroscopy of mass / charge selected macromolecular ions : Inner-shell excitation of ubiquitin protein,” *Appl. Phys. Lett.*, vol. 108, p. 064101, 2016.

[106] C. Nicolas and C. Miron, “Lifetime broadening of core-excited and -ionized states,” *J. Electron Spectros. Relat. Phenomena*, vol. 185, no. 8–9, pp. 267–272, 2012.

[107] A. P. Hitchcock, “Core Excitation and Ionization of Molecules,” *Phys. Scr.*, vol. T31, pp. 159–170, 1990.

[108] A. P. Hitchcock, “Inner shell excitation spectroscopy of molecules using inelastic electron scattering,” *J. Electron Spectros. Relat. Phenomena*, vol. 112, no. 1–3, pp. 9–29, 2000.

[109] B. Boudaïffa, P. Cloutier, D. Hunting, M. A. Huels, and L. Sanche, “Resonant formation of DNA strand breaks by low-energy (3 to 20 eV) electrons.,” *Science*, vol. 287, no. 5458, pp. 1658–1660, 2000.

Biography

Ranković Miloš was born in 17.06.1986. Belgrade, Serbia. He attended the elementary school and electro-technical high school “Nikola Tesla” in Belgrade, Serbia. In the year of 2005. Miloš started his academic studies in physics at Faculty of Physics, University of Belgrade, at the group ”Applied physics and informatics”. In July 2012. he graduated with the average score 8.97 (out of 10) and scored 10 (out of 10) for the B.Sc. Diploma Work with the title “The application of acoustic measurements in volumetric analysis” (written in Serbian). Miloš started his Ph.D. studies in December 2012. at Faculty of Physics, University of Belgrade, at the group “Physics of atoms and molecules”. In April 2013. he has been accepted as the research associate at the Institute of Physics Belgrade and joined the project ОИ 171020 with the title “The physics of collisions and photo-processes in atomic, (bio) molecular and nano-dimensional systems”, financed by the Ministry of Education, Science and Technological Development of Serbia. Miloš is currently a research assistant and works in the “Laboratory for Atomic Collision Processes” at the Institute of Physics Belgrade.

Publications

I Papers and letters in international journals

(a) The papers that came out as contributions from this Ph.D. Thesis:

P7. **M. Lj. Ranković**, A. Giuliani and A. R. Milosavljević, "Design and performance of an instrument for electron impact tandem mass spectrometry and action spectroscopy of mass/charge selected macromolecular ions stored in RF ion trap",
Eur. Phys. J. D **70**, 7 (2016).

P6. **M. Lj. Ranković**, A. Giuliani and A. R. Milosavljević, "Electron impact action spectroscopy of mass/charge selected macromolecular ions: inner-shell excitation of ubiquitin protein",
Appl. Phys. Lett. **108**, 064101 (2016).

P5. **M. Lj. Ranković**, F. Canon, L. Nahon, A. Giuliani, and A. R. Milosavljević, "VUV action spectroscopy of protonated leucine-enkephalin peptide in the 6-14 eV range",
J. Chem. Phys. **143**, 244311 (2015).

P4. A. R. Milosavljević, C. Nicolas, **M. Lj. Ranković**, F. Canon,
C. Miron and A. Giuliani, "K-Shell Excitation and Ionization of a Gas-Phase Protein: Interplay Between Electronic Structure and Protein Folding",
J. Phys. Chem. Lett. **6**, 16 (2015).

P2. A. R. Milosavljević, V. Z Cerovski, F. Canon, **M. Lj. Ranković**, N. Škoro, L. Nahon and A. Giuliani, "Energy-Dependent UV Photodissociation of Gas-Phase Adenosine Monophosphate Nucleotide Ions: The Role of a Single Solvent Molecule",
J. Phys. Chem. Lett. **5**, 11 (2014).

P1. A. R. Milosavljević, V. Z. Cerovski, **M. Lj. Ranković**, F. Canon, L. Nahon, and A. Giuliani, "VUV photofragmentation of protonated leucine-enkephalin peptide dimer below ionization energy",
Eur. Phys. J. D **68**, 68 (2014).

(b) Papers outside of the topic of this Ph.D. Thesis:

P3. A. R. Milosavljević, **M. Lj. Ranković**, D. Borka, J. B. Maljković, R.
J. Bereczky, B. P. Marinković and K. Tőkési, "Study of electron transmission through a platinum tube",
Nucl. Instr. Meth. **B** (2015).

II Invited lectures at international conferences

IT2. M. Lj. Ranković, A. Giuliani and A. R. Milosavljević, "Design and performance of an instrument for gas phase electron spectroscopy of trapped molecular ions", *The 3rd CELINA* (*Chemistry for Electron-Induced nanofabrication*) Meeting, 18 may - 20 may 2016, Kraków, Poland, STSM report (Oral presentation and abstract).

IT1. M. Lj. Ranković, F. Canon, L. Nahon, A. Giuliani and A. R. Milosavljević, "Photodissociation of protonated Leucine-Enkephalin peptide in the VUV range", *Proc. XXIX ICPEAC15 International Conference on Photonic, Electronic and Atomic Collisions,* 22 July - 28 July 2015, Toledo, Spain, Special report (Oral presentation and abstract).

III Contributions at international conferences

CI9. M. Lj. Ranković, F. Canon, L. Nahon, A. Giuliani and A. R. Milosavljević, "Photoinduced fragmentation of gas-phase protonated leucine-enkephalin peptide in the VUV range", *Journal of Physics: Conference Series* **635**, 012034 (2015).

CI8. I. Bačić, M. Lj. Ranković, F. Canon, V. Cerovski, C. Nicolas, A. Giuliani and A. R. Milosavljević, "Gas-phase X-ray action spectroscopy of protonated nanosolvated substance P peptide around O K-edge", *Proc. WG2 Expert Meeting on Biomolecules, COST Action CM1204, XLIC - XUV/X-ray Light and fast Ions for ultrafast Chemistry*, 27-30 April 2015, Poster presentation P08, p.71.

CI7. M. Lj. Ranković, V. Cerovski, F. Canon, L. Nahon, A. Giuliani and A. R. Milosavljević, "VUV action spectroscopy of bare and hydrated protonated leucine-enkephalin peptide", *Proc. WG2 Expert Meeting on Biomolecules, COST Action CM1204, XLIC - XUV/X-ray Light and fast Ions for ultrafast Chemistry*, 27-30 April 2015, Poster presentation P07, p.69.

CI6. M. Lj. Ranković, J. Rackwitz, I. Bald and A. R. Milosavljević, "Optimization of a Low-Energy Electron Gun by Electron Ray-Tracing Simulations", *Proc. 27th Summer School and Int. Symp. on Physics of Ionized Gases* – SPIG 2014, 26th - 29th August 2014, Belgrade, Serbia, Poster Presentation 1.10, pp.58-61.

CI5. A. R. Milosavljević, C. Nicolas, M. Lj. Ranković, F. Canon, C. Miron and A. Giuliani, "N K-Shell X-Ray Tandem Mass Spectrometry of Gas-Phase Ubiquitin Protein", *Proc. 27th Summer School and Int. Symp. on Physics of Ionized Gases* – SPIG 2014, 26th - 29th August 2014, Belgrade, Serbia, Poster Presentation 1.9, pp.54-57.

CI4. J. B. Maljković, M. Lj. Ranković, R. J. Bereczky, B. P. Marinković, K. Tőkési, A. R. Milosavljević, "Electron transmission through a metallic capillary", *Proc. 26th International Conference on Atomic Collisions in Solids* (ICACS-26), 13th – 18th July 2014, Debrecen, Hungary, Poster presentation P23, p.59.

CI3. A. R. Milosavljević, J. B. Maljković, R. J. Bereczky, M. Lj. Ranković, B. P. Marin ković and K. Tőkési, "Transport of electrons through a long metallic microcapillary: characterization of the outgoing low-energy electron beam",
Proc. The First Annual Meeting of COST Action CM1301 (CELINA), 19-22 March 2014, Erlangen, Germany, Poster presentation P22, p.47.

CI2. A. R. Milosavljević, M. Lj. Ranković, J. B. Maljković, R. J. Bereczky, B. P. Marinković and K. Tökési, "Kinetic Energy Distribution of Electrons Scattered Inside a Platinum Tube at the Incident Energy of 200 eV",
Proc. 27th Summer School and Int. Symp. on Physics of Ionized Gases – SPIG 2014, 26th - 29th August 2014, Belgrade, Serbia, Poster Presentation 2.11, pp.210-213.

CI1. A. R. Milosavlievć, F. Canon, V. Z. Cerovski, M. Lj. Ranković, L. Nahon, A. Giuliani, "VUV photodissociation of bare and nanosolvated protonated nucleotide isolated in the gas phase",
Proc. 2nd NANO-IBCT Conference 2013 (Radiation Damage in Biomolecular Systems: Nanoscale Insights into Ion-Beam Cancer Therapy), 20-24 May 2013, Sopot, Poland, Poster presentation p.91.

Прилог 1.

Изјава о ауторству

Потписани-а Милош Ранковић

број уписа D29/2012

Изјављујем

да је докторска дисертација под насловом

Фотонска и електронска акциона спектроскопија трапираних биомолекуларних јона: од изолованих до наносолватисаних честица

- резултат сопственог истраживачког рада,
- да предложена дисертација у целини ни у деловима није била предложена за добијање било које дипломе према студијским програмима других високошколских установа,
- да су резултати коректно наведени и
- да нисам кршио/ла ауторска права и користио интелектуалну својину других лица.

Потпис докторанда

У Београду, 15.04.2016.

Ранковић Милош

Прилог 2.

Изјава о истоветности штампане и електронске верзије докторског рада

Име и презиме аутора Милош Ранковић

Број уписа D29/2012

Студијски програм Физика атома и молекула

Наслов рада Фотонска и електронска акциона спектроскопија трапираних биомолекуларних јона: од изолованих до наносолватисаних честица

Ментор др Александар Милосављевић

Потписани Милош Ранковић

изјављујем да је штампана верзија мог докторског рада истоветна електронској верзији коју сам предао/ла за објављивање на порталу **Дигиталног репозиторијума Универзитета у Београду.**

Дозвољавам да се објаве моји лични подаци везани за добијање академског звања доктора наука, као што су име и презиме, година и место рођења и датум одбране рада.

Ови лични подаци могу се објавити на мрежним страницама дигиталне библиотеке, у електронском каталогу и у публикацијама Универзитета у Београду.

Потпис докторанда

У Београду, 15.04.2016.

Ранковић Милош

Прилог 3.

Изјава о коришћењу

Овлашћујем Универзитетску библиотеку „Светозар Марковић“ да у Дигитални репозиторијум Универзитета у Београду унесе моју докторску дисертацију под насловом:

Фотонска и електронска акциона спектроскопија трапираних биомолекуларних јона: од изолованих до наносолватисаних честица

која је моје ауторско дело.

Дисертацију са свим прилозима предао/ла сам у електронском формату погодном за трајно архивирање.

Моју докторску дисертацију похрањену у Дигитални репозиторијум Универзитета у Београду могу да користе сви који поштују одредбе садржане у одабраном типу лиценце Креативне заједнице (Creative Commons) за коју сам се одлучио/ла.

1. Ауторство

2. Ауторство - некомерцијално

3. Ауторство – некомерцијално – без прераде

4. Ауторство – некомерцијално – делити под истим условима

5. Ауторство – без прераде

6. Ауторство – делити под истим условима

(Молимо да заокружите само једну од шест понуђених лиценци, кратак опис лиценци дат је на полеђини листа).

Потпис докторанда

У Београду, 15.04.2016.

Ранковић Милош

1. Ауторство - Дозвољавате умножавање, дистрибуцију и јавно саопштавање дела, и прераде, ако се наведе име аутора на начин одређен од стране аутора или даваоца лиценце, чак и у комерцијалне сврхе. Ово је најслободнија од свих лиценци.

2. Ауторство – некомерцијално. Дозвољавате умножавање, дистрибуцију и јавно саопштавање дела, и прераде, ако се наведе име аутора на начин одређен од стране аутора или даваоца лиценце. Ова лиценца не дозвољава комерцијалну употребу дела.

3. Ауторство - некомерцијално – без прераде. Дозвољавате умножавање, дистрибуцију и јавно саопштавање дела, без промена, преобликовања или употребе дела у свом делу, ако се наведе име аутора на начин одређен од стране аутора или даваоца лиценце. Ова лиценца не дозвољава комерцијалну употребу дела. У односу на све остале лиценце, овом лиценцом се ограничава највећи обим права коришћења дела.

4. Ауторство - некомерцијално – делити под истим условима. Дозвољавате умножавање, дистрибуцију и јавно саопштавање дела, и прераде, ако се наведе име аутора на начин одређен од стране аутора или даваоца лиценце и ако се прерада дистрибуира под истом или сличном лиценцом. Ова лиценца не дозвољава комерцијалну употребу дела и прерада.

5. Ауторство – без прераде. Дозвољавате умножавање, дистрибуцију и јавно саопштавање дела, без промена, преобликовања или употребе дела у свом делу, ако се наведе име аутора на начин одређен од стране аутора или даваоца лиценце. Ова лиценца дозвољава комерцијалну употребу дела.

6. Ауторство - делити под истим условима. Дозвољавате умножавање, дистрибуцију и јавно саопштавање дела, и прераде, ако се наведе име аутора на начин одређен од стране аутора или даваоца лиценце и ако се прерада дистрибуира под истом или сличном лиценцом. Ова лиценца дозвољава комерцијалну употребу дела и прерада. Слична је софтверским лиценцама, односно лиценцама отвореног кода.